

The University of Adelaide

Faculty of Sciences

School of Physical Sciences

Department of Earth Sciences

**Process Constraints on the Giant IOCG Mineral System of the Eastern
Gawler Craton, Australia**

Cheng Lin Yang

PhD Thesis

Submitted on 12 February 2018

Declaration of Originality

I certify that this work contains no material which has been accepted for the award of any other degree or diploma in my name, in any university or other tertiary institution and, to the best of my knowledge and belief, contains no material previously published or written by another person, except where due reference has been made in the text. In addition, I certify that no part of this work will, in the future, be used in a submission in my name, for any other degree or diploma in any university or other tertiary institution without the prior approval of the University of Adelaide and where applicable, any partner institution responsible for the joint-award of this degree.

I give consent to this copy of my thesis, when deposited in the University Library, being made available for loan and photocopying, subject to the provisions of the copyright Act 1968.

I also give permission for digital version of my thesis to be made available on the web, via the University's digital research repository, the Library Search and also through web search engines, unless permission has been granted by the University to restrict access for a period of time.

Signature:

Name: Cheng Lin Yang

Date: 12 February 2018

Supervisors

Prof. David Giles

School of Physical Sciences, University of Adelaide, South Australia 5005, Australia

Deep Exploration Technologies Cooperative Research Centre

Strand Leader, Minerals and Resources Engineering

Future Industries Institute | University of South Australia

Building X, X1-09 | Mawson Lakes Campus | Mawson Lakes SA 5095

Dr. Caroline Forbes

School of Physical Sciences, University of Adelaide, South Australia 5005, Australia

Deep Exploration Technologies Cooperative Research Centre

Mr. Adrian Fabris

Geological Survey of South Australia, Department of State Development, 101 Grenfell St, Adelaide. DET CRC Project Leader.

Acknowledgments

Why do the PhD in my age? New migrants cannot find a job in Australia although I had the bachelor degree from the Centre South University, Changsha, China in 1985. I applied the PhD in the University of Adelaide in 2005 and transfer to Master degree and completed in 2008. I applied the HCh models in Dos version for albitisation but unsuccessful during master degree. I do the PhD for the HCh models.

Thanks to Prof. John Foden and Nigel Cook give me a chance to find the PhD project with DET CRC. Difficult is to find the reference people for AGC requirements. The previous supervisor Andreas Schmidt Mum was in Saudi Arabia and Joel Burger was moving to Monash University at Jan 2014.

Thanks to Prof. Joel Brugger and Dr. Bao Hong (DSD) as my reference people.

Thanks to DET CRC for financial supports and DSD for the best information system.

Thanks Benjamin Wade and Aoife McFadden of the Adelaide microscopy staff for accompanying the analysis.

Thanks Groom David and Groom Keryn (Dmitre) for support my samplings.

Thanks my team for support (ioGAS) whenever I needed (Dr. Stephanie Fleurance, Benjamin van der Hoek, Laura Anne Rollison; Katherine Stoate; Charlotte Mitchell; Eline Baudet; Keryn Dianne Wolff) and all staff in the Department of Earth Sciences.

Thanks to Dr. Bastrakov Evgeniy has sold the HCh software via Geoscience Australia from Moscow University.

Thanks Joel Brugger had made me practiced the DOS HCh models for albitisation in 2007.

Thanks the IT people set up the HCh software in my computer.

Thanks to Alan Collins introduce the microscopy in the Mawson Building in Adelaide.

Thanks to Prof. Graham Heinson and Dr. Rosalind King encourage me to do it always.

Thanks to the old staff: Dr. Rowl Twidale and Victory who is the volunteer working in the University of Adelaide and looking after me.

Thanks my family, my daughter is studying the PhD in same stage of me in the National University, Canberra and my wife have supported me all times including seated outside of the office in Mawson Lakes

I acknowledge the support I have received for my research of Australian Postgraduate Award.

Specifically thanks to Dr. Dana A Thomesn from the University of Adelaide for editing my thesis for 4 months works and once a week.

Specific thanks to Fabris, Adrian (DSD) to make the decision of sampling a section in Emmie Bluff and one mineralisation hole GHDD4. Fabris edited one publishing “trace element” in the AESC conference.

Specific thanks to Caroline Forbes, who is my co-supervisor and coming to everything when I needed her.

Specific thanks to David Giles, who is my principal supervisor and has friendly talked about the petrogenesis and trace element and put the extremely effort in the HCh models. David Giles is a great geoscientist.

ABSTRACT

The aim of this thesis is to map the distribution of alteration minerals and pathfinder elements from deposit to regional-scale within the IOCG mineral system of the eastern Gawler Craton, South Australia, and understand fluid-rock interactions that control that distribution. I present geochemistry, petrology and mineral chemistry from a range of metasomatically altered rocks including four protolith types; siliciclastic metasedimentary rock, calc-silicate metasedimentary rock, granite and mafic magmatic rock. Techniques employed included; transmitted light microscopy, electron microprobe analyses (EM), scanning electron microscopy (SEM) and laser ablation inductively coupled plasma mass spectroscopy (LA-ICPM). Thermodynamic modelling using the HCh software was then applied in order to further understand the temperature, pressure, fO_2 and fluid-rock ratio conditions responsible for a range of alteration types

Multiple, overprinting paragenetic relationships and unusual alteration textures in four contrasting protolith rocks from the central eastern Gawler Craton can be interpreted within the framework of five paragenetic stages (protolith; skarn; stage 1, K-feldspar-magnetite; stage 2, hematite-chlorite-muscovite, including the major Cu-ore minerals; stage 3, post mineralization) corresponding to different mineral assemblages in the four protolith types. The paragenesis is consistent with successive periods of Fe-K-metasomatism, with early higher temperature, more reduced (magnetite stable) alteration being consistently overprinted by lower temperature, more oxidized (hematite stable) alteration and with the bulk of Cu-sulphide mineralization occurring at close to the transition from magnetite to hematite.

Minerals that pre-date the main sulphide phase (namely from the protolith, skarn and stage 1 assemblages) typically have major and trace element concentrations within expected ranges for comparable rock types outside the eastern Gawler Craton mineral province. Hematite associated with stage 2 assemblages has higher average concentrations of Ba, Cu, Mo, Nb, Pb, Th, Ta, U and Σ REE compared to magnetite (between 1 and 2 orders of magnitude higher). In addition hydrothermal hematite contains elevated concentrations of Cu, U, Sb and Bi compared to the average crustal abundance. Hematite is the main host of Sb even when there are co-existing sulphide phases in the rock. Where sulphide minerals are present most chalcophile pathfinder elements (e.g. Ag, As, Bi, Cu, and Se) are dominantly deported in the sulphides, even at low concentrations, far from mineralisation. Pyrite is the most common sulphide, with chalcopyrite increasing in abundance closer to mineralisation. The pyrites are p-type, with S/Fe_{atom} ratios of > 2 and Co/Ni ratios ranging between 0.4 and 10, but mostly above 1. This is consistent with a moderate-temperature hydrothermal origin for the pyrite. Concentrations of Co, As, Bi, Se, Te and Au in pyrite reach 2 to 3 orders of magnitude above crustal abundance. The chalcopyrite grains show variable enrichment in pathfinder elements and are most enriched in Bi, Se, Te and Ag, with values ranging between 1 and 4 orders of magnitude above crustal abundance. At elevated whole rock concentrations, within altered rocks, the REE are deported in hydrothermal apatite. This is consistent with the extreme capacity of the hydrothermal system to mobilise, and locally accumulate, even the most refractory elements. REE enrichment (up to 2604 ppm) is a good proximity indicator to ore, since it only occurs around the mineral system.

Thermodynamic modelling was conducted using the HCh software to calculate equilibrium mineral assemblages predicted for model granite and calc-silicate protoliths mixed with a range

of model hydrothermal fluids. Fluid compositions were consistent with fluid inclusion studies from the eastern Gawler Craton. Models were created in the C-H-O-Cl-S-Na-K-Mg-Fe-Si-Al-Cu-Ca-Mn chemical system at temperatures from 150⁰ to 500⁰C, fO₂ of -34 to -26 and fluid-rock ratios from 10⁻³ to 10⁴. The modelling provides semi-quantitative constraints for mineral assemblages associated with IOCG mineral systems of the eastern Gawler Craton. The transition from protolith assemblages to magnetite-K-feldspar assemblages to chlorite-magnetite-K-feldspar assemblages to hematite-chlorite-muscovite assemblages with decreasing temperature, increasing fluid-rock ratio and increasing logfO₂. This is consistent with the petrologic observations presented in this thesis, namely the consistent overprinting of stage 1, magnetite-K-feldspar alteration by stage 2, hematite-chlorite and muscovite alteration. Although Cu-sulphides are predicted to be stable over a range of temperature and fO₂ conditions, they are predicted to be most abundant between temperatures of ~300⁰ to 250⁰C, fO₂ of -26 to -34 and at fluid-rock ratios >10. This corresponds to alteration assemblages at the magnetite and hematite boundary, with abundant chlorite and muscovite alteration.

The distribution of pathfinder elements (measured in whole rock chemistry) within the central eastern Gawler Craton IOCG province can be predicted by combining petrological observations with mineral chemistry and thermodynamic modelling and are consistent with the observations of Fabris (2012, 2013). Elements associated with hematite alteration (notably Sb and W) are expected to have a wide geographic footprint. Elements enriched in pyrite (notably As, but also S and Se) are likely to have a broad geographic distribution in line with the presence of pyrite in both magnetite and hematite stable alteration assemblages. Elements most enriched in copper sulphides (Cu, Ag and Au) are largely restricted to within <5 km of known deposits.

Table of Contents

1	Introduction	11
1.1	Iron-oxide copper gold deposits	11
1.2	Unresolved questions	15
1.3	Background Geology, the eastern Gawler Craton.....	19
1.4	Thesis structure	25
2	Spectrum of fluid/rock alteration in the IOCG system of eastern Gawler Craton, Australia.....	27
2.1	Introduction.....	28
2.2	Characteristics of IOCG mineralisation	28
2.3	Mineralisation of the Gawler Craton.....	29
2.4	Methods.....	31
2.4.1	Sample selection	31
2.4.2	Geochemistry	31
2.4.3	Petrography	32
2.4.4	Scanning Electron Microscopy (SEM – XL30)	32
2.5	RESULTS	32
2.5.1	Whole Rock Geochemistry	32
2.5.2	Petrography	36
2.6	Discussion.....	51
2.6.1	Interpreted petrogenesis	51
2.6.2	Summary and alteration stages.....	56
2.6.3	Nature of the hydrothermal fluids	60
2.7	Conclusions.....	61
3	Mineral chemistry mapping within an IOCG system, Olympic Cu-Au Province, South Australia.....	62
3.1	Introduction.....	63
3.1.1	Mineral department of trace elements as exploration tools	63
3.1.2	Geological background	64
3.2	Methods.....	66
3.2.1	Mineral abundance estimation	68
3.2.2	Scanning Electron Microscopy	68

3.2.3	Electron Microprobe Analysis	69
3.2.4	LA-ICPMS analysis	69
3.2.5	Bulk rock calculation	71
3.3	Results	71
3.3.1	Pyrite (FeS ₂)	71
3.3.2	Cu-sulphides.....	74
3.3.3	Magnetite	76
3.3.4	Hematite	76
3.3.5	Feldspars	79
3.3.6	Chlorite.....	82
3.3.7	Biotite.....	84
3.3.8	Muscovite.....	87
3.3.9	Carbonate	88
3.3.10	Apatite and Nine other Minerals	90
3.4	Discussion	91
3.4.1	Significance of pyrite chemistry	91
3.4.2	Trace element deportment.....	92
3.4.3	Relationship between trace elements and fluids	96
3.4.4	Significance of trace element patterns	97
3.4.5	Mineral Contributions to Whole Rock Chemistry	98
3.4.6	Relationship between paragenesis and fluid/rock interactions	104
3.5	Conclusion	105
4	HCh thermodynamic models of IOCG systems of the eastern Gawler Craton, South Australia	106
4.1	Introduction.....	107
4.1.1	Background Geology	108
4.1.2	Models of ore formation for the Gawler Craton IOCG deposits.....	109
4.2	Methods.....	111
4.2.1	HCh modelling General Method.....	112
4.2.2	Choice of System	112
4.2.3	Modelling conditions	113

4.2.4	Rock and fluid composition	113
4.2.5	HCh Models	119
	<i>Granite HCh models</i>	119
4.3.1	Model Granite equilibrated with Cu-rich model fluid A (35 wt % NaCl equiv)	119
4.3.3	Model Granite equilibrated with model fluid B1 (16.2 wt % NaCl equiv. no sulphur). 125	
4.3.5	Model Granite equilibrated with model fluid C (Mg-rich, 30 wt % NaCl equiv).....	126
	<i>Calc-silicate HCh models</i>	128
4.3.6	Model calc-silicate -fluid B.....	128
4.4	Discussion.....	131
4.5	Conclusions and recommendations.....	137
5	Thesis conclusions.....	138
6	References	141
7	Appendixes	153
	Appendix 1: The summary of work	153
	Appendix 2: The Handheld X-ray Data	157
	Appendix 3: The Electron Microprobe Data.....	160
	Appendix 4: The LA-ICPMS Analysed Data	174
	Appendix 5: The multiple elements of minerals contributed to whole rock assay	202
	Appendix 6: The element substitution of sulphur minerals, hematite, chlorite, muscovite and K-feldspar.....	208
	Appendix 7: Fluid components and symbols used in HCh models.....	211

1 Introduction

1.1 IRON-OXIDE COPPER GOLD DEPOSITS

Iron-oxide copper gold (IOCG) deposits are an important type of copper (Cu), gold (Au), uranium (U) and rare earth element (REE) mineralisation (Ferris et al., 2002; Espinoza, 2002; Naslund et al., 2002; Billström et al., 2010; Corriveau et al., 2010; McLellan et al., 2010; Porter 2010; Rusk et al., 2010; Xavier et al., 2010; McPhie et al., 2011). South Australian IOCG deposits account for 6% of global Cu resources, 8% of Au resources and 19% of U resources (Porter, 2010; Kathleen et al., 2014; Senior, 2016; NEA/IAEA, 2016).

The IOCG deposit type, first recognised by Hitzman et al. (1992), includes deposits with a range of morphologies (e.g. veins, hydrothermal breccias, tabular replacement bodies and composite deposits comprising two or more of the preceding) characterised by Cu-Au mineralisation associated with abundant iron-oxide minerals. IOCG deposits are commonly associated with crustal-scale hydrothermal systems and high volume magmatic systems. IOCG deposits are classified separately to porphyry Cu deposits, as IOCG deposits display substantial accumulations of iron-oxide minerals, association with sodium-calcium (Na-Ca) rich felsic-intermediate intrusives, and lack of complex element zonation and alteration mineral assemblages commonly associated with porphyry Cu deposits (Hitzman et al., 1992). There is often little internal metal zonation within recognised examples of IOCG deposits. The relatively simple Cu-Au ± U ore assemblage is distinct from the wide spectrum of porphyry Cu deposits. IOCG deposits tend to accumulate within faults as epigenetic mineralisation distal to coeval intrusions, whereas porphyries are proximal to intrusive bodies. IOCG deposits are defined as ‘iron-oxide alkaline altered’ by Porter (2010) in reference to the common observation of large-scale Na and K alteration of country rocks in IOCG districts.

IOCG deposits have widespread geographic distribution and occur in rocks of Archaean to Cainozoic age (Figure 1, Table 1), (e.g. Williams et al., 2005; Groves et al., 2010; Porter, 2010). The inferred age of IOCG deposits cluster in five periods of Earth history: 2.4 to 2.8 Ga, 1.45 to 1.6 Ga, 0.75 to 0.85 Ga, 0.51 to 0.57 Ga and 0.095 to 0.165 Ga.

Some authors (e.g. Gandhi, 2003 and 2004; Corriveau, 2006) have defined IOCG sub-type classifications, and in many cases use an individual deposit as the type-case for classification (e.g. Olympic Dam-type, Cloncurry-type, Kiruna-type, Palabora-type, Bayan Obo-type). However, Porter (2010) subdivided the full spectrum of IOCG deposits into four sub-types on the basis of host rock, type of alteration and commodity elements, as follows:

1. **IOCG sensu stricto deposits** have significant hematite and/or magnetite enrichment and extensive alkali alteration. These deposits contain Cu and/or Au as the principal economic commodity and commonly contain elevated concentrations of REE (e.g. Olympic Dam, Earnest Henry). Williams et al. (2005) describes a further sub-division of this class as being iron-oxide skarn deposits that have significant volumes of calc-silicate minerals as gangue (e.g. Hillside, Emmie Bluff).
2. **Iron-oxide-apatite IOCG deposits** are rich in phosphorous and typically contain abundant apatite. These deposits tend to have lower grades of Cu and Au than IOCG sensu stricto deposits (e.g. Kiruna).

Table 1. Global IOCG sub-types and age, size and commodities (data are extracted from Porter, 2010 and from the South Australian Resources Industry Geoserver (SARIG) website).

Deposit	Location	Age of host rock	Age of deposit	Size Resource	Main commodities	Sub-type
Olympic Dam	Australia	1590 Ma	1590 Ma	9080 Mt (0.87% Cu, 0.32ppm Au, 0.27kg/t U ₃ O ₈)	Cu-Au-U	1
Carrapateena		1857±6 Ma	1.59-1.57Ga	203 Mt (Cu 1.31%, Au 0.56ppm, 0.27Kg/t U ₃ O ₈)	Cu-Au-U	1
Prominent Hill		1760 to ~1740 Ma	1.59-1.57Ga	283 Mt (Cu 0.89%, Au 0.81ppm, Ag 2.48ppm)	Cu-Au-Ag	1
Emmie Bluff		1760-1730 Ma	1595 Ma	25 Mt (Cu 1.3%)	Cu-Co-Ag-Zn	1
Oak Dam		~1850 Ma	1.57-1.59 Ga	~560 Mt (Fe 41-56 wt %)	Cu-Au-U	1
Khamsin		1860-1841 Ma	1595 Ma?	202 Mt (Cu 0.6%, Au 0.1 ppm, Ag 1.t ppm)	Cu-Au-Ag	1
Punt Hill		1850 Ma	1580 Ma	122 Mt (Cu 0.47%, Zn 0.38%, Ag 6.6%, Au0.1ppm)	Cu-Zn-Ag-Au	1
Ernest Henry		1760-1660 Ma	1525 Ma	226 Mt (Cu 1.1%, Au 0.51ppm)	Cu-Au	1
Mount Eliot		1890 to 1610 Ma	1.55-1.50Ga	570 Mt (Cu 0.44%, Au 0.26ppm)	Cu-Au	1
Osborne		1695-1650 Ma	1595 Ma	27 Mt (Cu 1.4%, Au 0.8ppm)	Cu-Au	1
Roseby Corridor		Mesoproterozoic	Unclear	132 Mt (Cu 0.7%, Au 0.06ppm)	Cu	1
North Portia		1703Ma	1605 Ma	11.3 Mt (Cu 0.89%, Au 0.64 ppm)	Cu-Au	3
Warrego		1920±60 Ma	Unclear	6.95 Mt (Cu 2%, Au 6.6ppm, Bi 0.32%)	Au-Cu-Bi	1
Candelaria		Chile	116-114 Ma	120-112 Ma	470 Mt (Cu 0.95%, Au 0.22ppm, Ag 3.1ppm)	Cu-Au
El soldado	116-114 Ma		108- 95 Ma	>200 Mt (Cu 1.4%, Ag 6ppm)	Cu	1
Manto Verde	116-114 Ma		120-112 Ma	410 Mt (Cu 0.58%, Au0.11ppm)	Cu-poor Au	1
Raul Condestable	Peru	177 to 95 Ma	Unclear	>32 Mt (Cu 1.7%, Au 0.3ppm, Ag 6ppm)	Cu-Ag	3
Mina Justa		177 to 95 Ma	108- 95 Ma	347 Mt (Cu 0.71, Au 0.03ppm)	Cu	3
Marcona		177 to 156 Ma	162-156 Ma	1.9 Gt (Fe 55.4%, Cu 0.12%)	Fe-poor Cu	3
Cristalino	Brazil	2.76-2.51 Ga	2.74-2.57 Ga	~500 Mt (Cu 1%, Au 0.3ppm)	Cu-poor Au	1
Salobo		2.76-2.51 Ga	2.74-2.57 Ga	986 Mt (Cu 0.82%, Au 0.49ppm)	Cu-Au	1
Sossego		2.76-2.51 Ga	2.74-2.57 Ga	245 Mt (Cu 1.1%, Au 0.23ppm)	Cu-Au	1
Pea Ridge	USA	Mesoproterozoic	1.48-1.45 Ga	Unclear	Fe-Apatite	2
Wernecke	Canada	Proterozoic	1.6 Ga	Unclear	Cu-Au-U	1
Sue Dianne		1.9-1.8 Ga	1.9-1.8 Ga	8.4 Mt (Cu 0.8%, Au 0.07ppm)	Cu	3
NICO		1.9-1.8 Ga	1.9-1.8 Ga	31.7 Mt (Au 0.91ppm, Co 0.12%, Bi 0.16 %)	Au-Co-Bi	4
Cerro de Mercado	Mexico	30.8-30.1 Ma	30.8-30.1 Ma	Unclear	Fe-apatite	2
Bayan Obo	China	Proterozoic	555-420Ma	40 Mt (REE 3.5-5.4%, F 130ppm)	Fe-REE-Nb	3
Palabora	South	2.05 Ga	2.05 Ga	1200 Mt (Cu 0.59%, Au U PGE recovered)	Cu	3
Vergenoeg	Africa	2.05 Ga	2.05 Ga	Unclear	Fe-F-REE	4
Shimiyoka	Zambia	2.7-2.5 Ga	Unclear	Unclear	Fe-P	2
Mumbawa		2.7-2.5 Ga	535 Ma	87 Mt (Cu 0.94%, Au 0.05ppm)	Cu	2
Kiruna	Sweden	1.90-1.88 Ga	Unclear	Unclear	Fe-P	2
Kiirunavaara		1.9-1.8Ga	1.9-1.8Ga	Unclear	Fe-Apatite	2

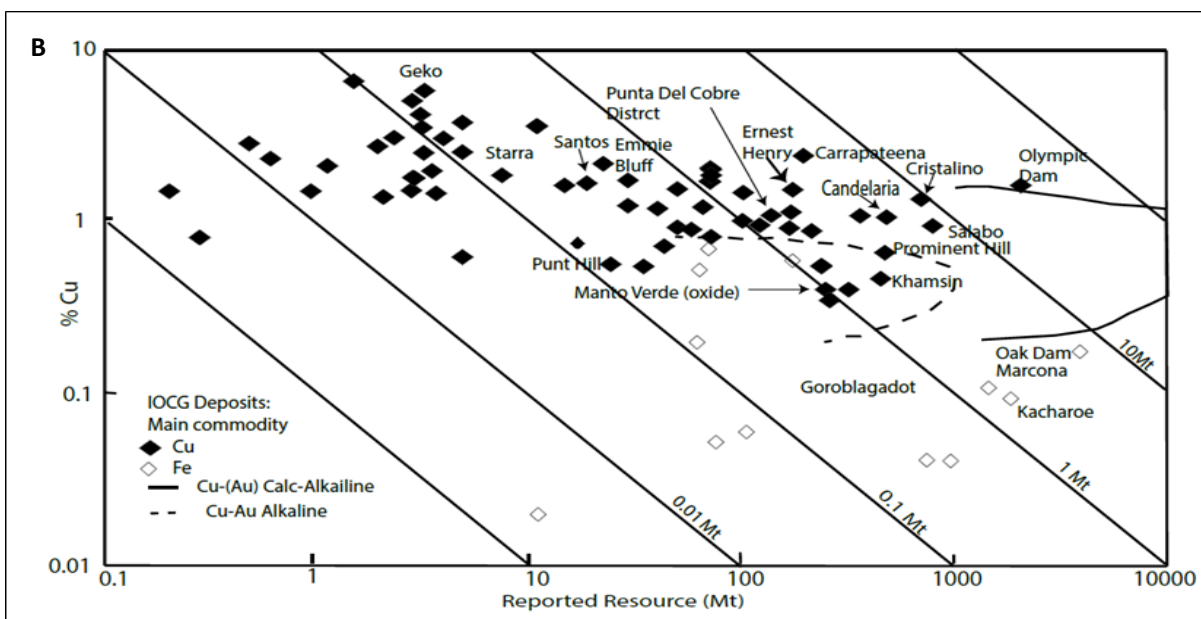
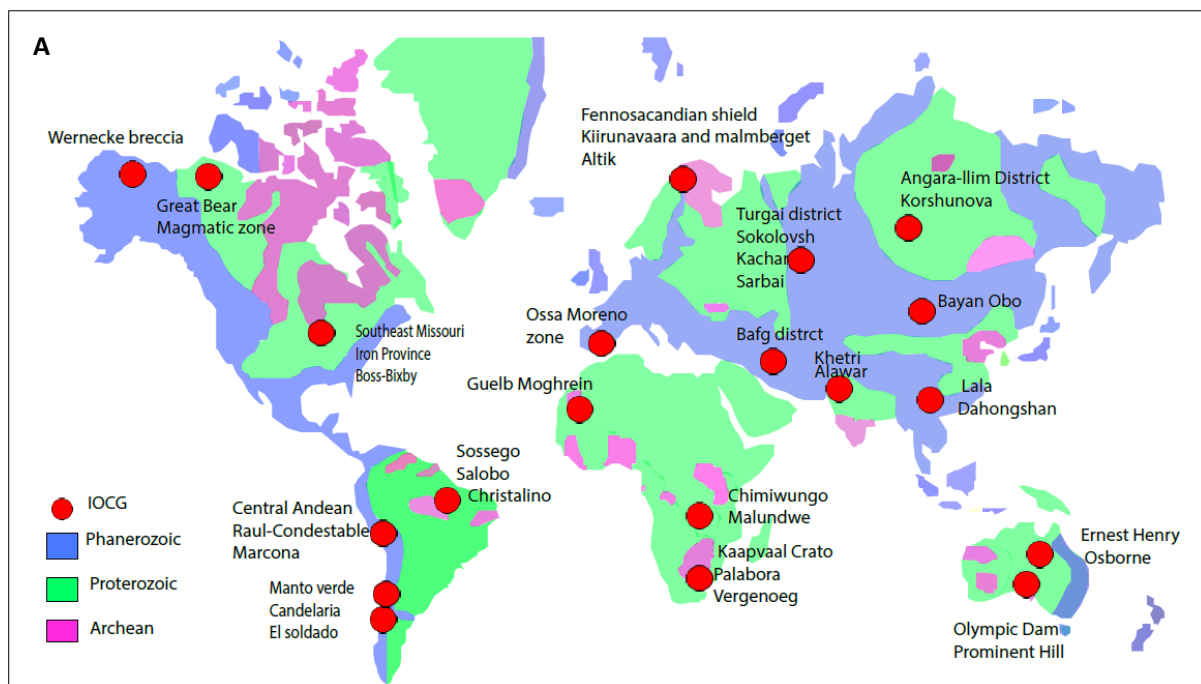


Figure 1. A) Global location of major IOCG districts (Modified from Groves et al., 2010 and Porter, 2010). B) Grade-tonnage diagram displaying reported resource (Mt) vs copper (%). Modified from William et al. (2005) after Seedorff et al. (2005).

3. **IOCG deposits directly associated with carbonate and alkaline or alkali altered intrusives** are typically REE-rich and Cu and Au poor (e.g. Palabora, Bayan Obo, Raul Condestable, Sue Dianne).
4. **Overlap and miscellaneous IOCG deposits** contain some aspects of the IOCG class (e.g. large proportion of Fe-oxide minerals, alkali alteration, Cu and/or Au enrichment), but do not fall easily within the other three categories and may overlap in characteristics with other recognised ore types (e.g. Vergenoeg, Andean mantos).

Alteration

IOCG mineral provinces are typified by kilometre-scale alkali alteration that is classified into four main types: muscovite-chlorite-hematite associated with core zones of IOCG sensu stricto deposits; K-feldspar-biotite-magnetite associated with core zones of some IOCG deposits and often observed as a pre-ore alteration assemblage in muscovite-chlorite-hematite altered IOCGs; calc-silicate alteration and regional Na-Ca alteration (e.g. Mark, 2004). Na-Ca alteration is generally centred on major transcrustal faults over tens to hundreds of kilometres, or within regionally pervasive zones controlled by complex fault networks (e.g. Gawler Craton), or by lithological and structural permeability (Punta del Cobre, Chile).

The spatial distribution and type of alteration assemblages preserved differs between deposits. The Candelaria deposit in Chile displays vertical zonation, ranging from Na-K at depth and grading up to a dominantly K-rich suite (Robert et al., 2002). Chlorite-sericite alteration occurs in upper sections of the IOCG system, with vertical zonation in Fe-oxides from magnetite to hematite, the latter of which only appears in the upper most parts of the system. In Punta del Cobre and Mantoverde, Chile, regional Na-Ca alteration has produced albite and scapolite bearing assemblages which spatially coincide with K-feldspar-magnetite alteration (Benavides et al., 2007; Baton et al., 2010). Ernest Henry, in northwest Queensland, is accompanied by potassic-iron alteration as early intense biotite-magnetite, followed by K-feldspar and sulphides (Cleverly and Oliver, 2005; Rusk et al., 2010). Olympic Dam, South Australia, is characterised by hematite-sericite alteration in combination with fluorite, barite and Cu sulphides, which typically overprint earlier magnetite-carbonate-chlorite-pyrite±Cu sulphide assemblages (Gow et al., 1994, 1996; Haynes et al., 1995; Kathy et al., 2012).

Inferred tectonic setting

When the IOCG deposit class was first described in 1992 no particular tectonic setting was identified (Hitzman, 1992). The distribution and scale of IOCG deposits suggests that the processes responsible for their formation should be considered on a crustal- to lithospheric-scale (Groves et al., 2010; Porter, 2010). The IOCG deposit sub-types, as described above (Porter, 2010), have tectonic settings ranging from Mesozoic suprasubduction zones (e.g. Andean IOCG deposits) to Proterozoic intracontinental with no plate margin recognised (e.g. Olympic Dam) (e.g. Groves et al., 2010). Depths of formation have been estimated between < 2 km (Olympic Dam) to ~12 km (Salobo) with alteration zones >1000 km² (Skirrow et al., 2002). Recently, a near plate margin setting was proposed for Olympic Dam (Hand et al., 2007) and there is growing consensus that plate margin processes influence the geodynamics of ore deposition (shown in Figure 2) (Williams et al., 2005; Groves et al., 2010). Major IOCG systems appear to be spatially related to crustal to lithospheric-scale structures (Skirrow et al., 2002; Xavier et al., 2010), implying that lithospheric-scale tectonic processes have a strong influence on the mineral system (Groves et al., 2010). In a majority of IOCG provinces there is demonstrated spatial and temporal coincidence of mineralisation with voluminous batholithic complexes, composed of anorogenic granitoids and mantle related mafic to

intermediate magmatic rocks in varying proportions. All are characterised by numerous and widespread small juvenile mafic dykes, sills and stocks, while some include layered mafic complexes that range from small to giant (Williams et al., 2005; Groves et al., 2010; Porter, 2010). Qiuyun et al. (2016) suggested the mafic components of the Gawler Range Volcanics generally have higher Zr contents and Zr/TiO₂ ratios than those of high-Mg basalts and picrites produced in variable tectonic settings worldwide, possibly reflecting continental crustal components involved in their mantle source.

Skirrow et al. (2007) used the link between magmatic rocks and isotopic data from IOCG deposits in South Australia to argue the importance of mantle input into IOCG systems. IOCG systems are associated with magmatic and volcanic activity where vertical depth is determined by mantle heating sources and presence or absence of metal sources, and high temperature processes causing K-feldspar and magnetite alteration. Although Olympic Dam likely formed at < 250°C (Haynes et al., 1995), heat was the initial driver for the alteration sequence. Other tectonic settings of IOCG systems are related to tectonic thickening of the upper plate during collision, symmetric rifting and asymmetric rifting events.

1.2 UNRESOLVED QUESTIONS

There are a number of unresolved questions regarding the formation of IOCG deposits. This thesis focuses on three pertinent areas of research: source of fluids and metals, mechanism of precipitation and nature of, and controls on, district-scale alteration. These issues are briefly introduced below.

Source of fluids and metals

The source of metals and fluids responsible for transporting them in IOCG systems is a subject of debate. Hypersaline fluids are considered responsible for forming IOCG deposits. For instance, the major difference between barren breccia pipes and IOCG mineralisation in the Cloncurry district is an absence of multiphase high salinity, high temperature fluid inclusions in the former, suggesting that these factors are critical in the genesis of IOCG deposits (Bertelli, 2007).

Five potential fluid sources for IOCG deposits have been proposed:

1. Fluid released from a fractionating mantle or from intraplate intrusive rocks. Johnson (1995) noted the correlation of Cu grade with primitive Nd isotope signatures in the Olympic Province, and suggested a direct link to mantle derived magmas or mantle metasomatism. Groves (2010) inferred that ultrabasic to basic intrusions were the ultimate driving force and fluid source based on high salinity ore fluids and available stable and radiogenic isotope data.
2. Exsolved from large intermediate to felsic intrusions and associated with early widespread K and Fe metasomatism. Metasomatism is manifest as orthoclase and magnetite alteration of granitoid and volcanic rocks (Benavides et al., 2007).
3. Produced by high temperature metamorphism (Clark et al., 2005; Conor, 2006; Oliver

et al., 2008; Yang, 2009).

4. Sedimentary formation / basinal water ultimately of meteoric origin (Benavides et al., 2007). For example, Monteiro et al. (2008) indicated that hot metalliferous fluid (> 500°C) mixed with meteoric fluids may be the main mechanisms responsible for deposition of metals transported as metal chloride complexes in orebodies of the Sossego deposit.
5. Surface derived bittern brines or re-dissolved evaporite. Such fluids are typically hypersaline and have the potential to leach a range of elements Ni, Co, Cr, Mn, Mo, Cu, Pb, Zn, Ba, Sr, U and REE and result in widespread albite alteration (Yang, 2009).

Various authors have proposed multiple fluid models in which mixing between fluids of different sources is an important mechanism for ore deposition (e.g. Haynes et al., 1995; Bastrakov et al., 2007). As an example, Hou et al. (2017) proposed that the Vergenoeg deposit was formed during two stages, the first dominated by CO₂-rich magmatic hydrothermal fluids and the second involving a mixture of magmatic and oxidised meteoric water. Barton (2010)

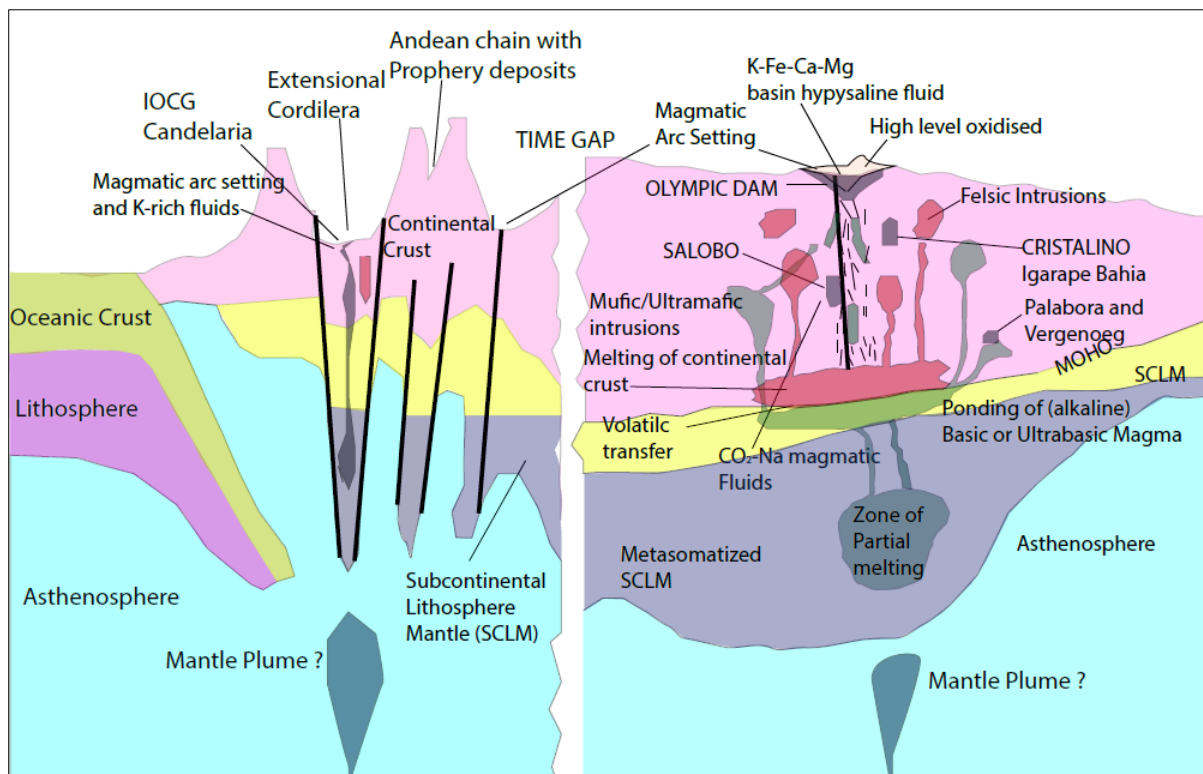


Figure 2. Schematic diagram showing tectonic and lithospheric setting of IOCG deposits in Precambrian cratons and extensional parts of Cordilleran arcs. The Candelaria and Vergenoeg have a proposed metamorphosed mantle source and subcontinental lithospheric mantle source, respectively. Modified after Groves et al. (2010).

proposed a model for Candelaria which involves mixing of magmatic derived fluids with sedimentary-meteoric fluids. Conversely, other authors suggest that only one fluid type was involved in IOCG mineralisation. For example, Sillitoe (2003) argues that fluids involved in the formation of Andean IOCG deposits were derived from mafic magmas, and that mixing

with other fluids (e.g. metamorphic, evaporitic, seawater, meteoric) is circumstantial.

Mechanism of metal precipitation

A number of models have been proposed to explain deposition of ore minerals in IOCG systems (Figures 3 and 4) (Haynes et al., 1995; Bastrakov et al., 2007). These models typically involve successive periods of mineralisation during fluid-rock interactions with variations based on relative importance of fluid-rock chemistry, temperature, fO_2 and pH.

- Bastrakov et al. (2007) proposed a model for the Emmie Bluff IOCG deposit in which early magnetite-sulphide mineralisation was replaced by hematite with coincident upgrading of ore minerals (Figure 3).
- Groves et al. (2010) proposed that a range of IOCG deposits with slightly varying metal content, morphology and alteration signatures could be formed from magmatic source rock fluids with variable interaction with fluids derived from country rock.
- Benavides et al. (2007) and Monteiro et al. (2008) proposed a mixing model where Na-Ca alteration is overprinted and mixed with meteoric water as the major metal precipitation process.
- Haynes et al. (1995) proposed a fluid mixing model for the Olympic Dam IOCG deposit in which a high-temperature, metal-rich fluid ($>300^\circ\text{C}$) mixed with a low temperature fluid ($<150^\circ\text{C}$) to cause metal precipitation (Figure 4).
- Porter (2010) proposed that the Palabora IOCG deposit was a result of fluid mixing or fluid-rock reactions, rather than changes in temperature or pressure.

The above models commonly show that temperature and pressure variations have minimal influence on ore deposition and that changes in fluid chemistry (in particular fO_2) driven by fluid-rock or fluid mixing interactions are paramount in IOCG deposit formation.

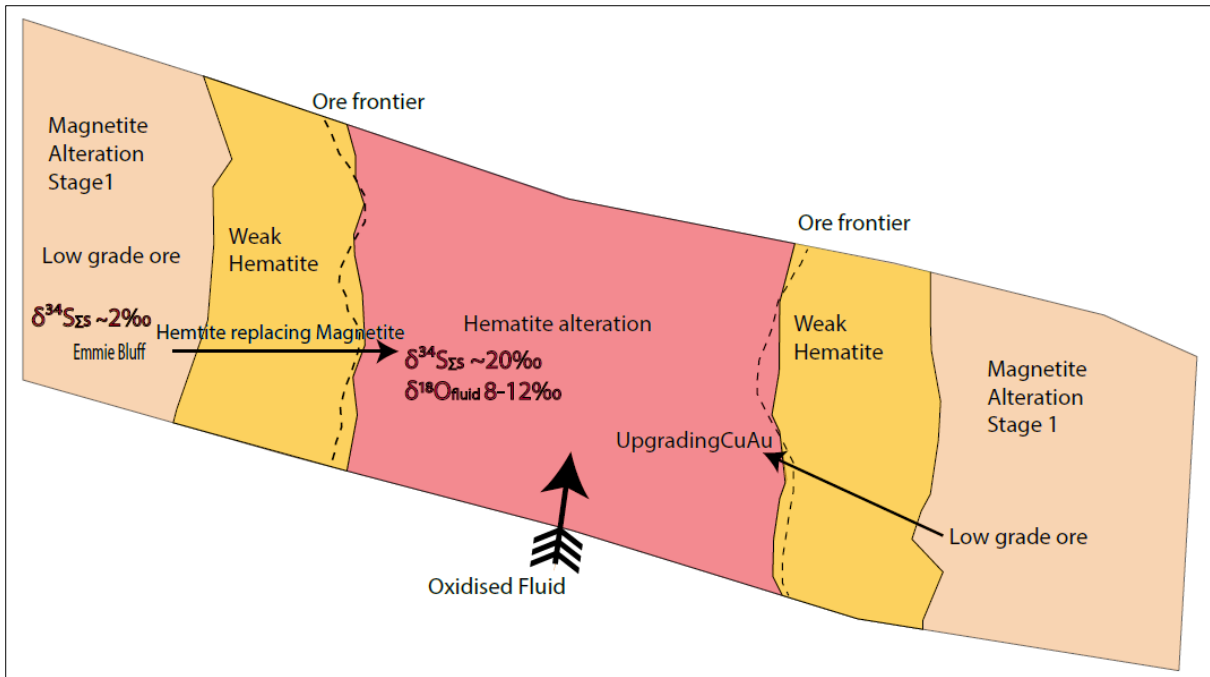


Figure 3. Fluid-rock interaction model for Cu and Au precipitation in IOCG systems. Copper precipitation occurs by reduction of a copper gold-bearing oxidised (hematite-stable) fluid interacting with a magnetite bearing assemblage. Modified from Bastrakov et al. (2007).

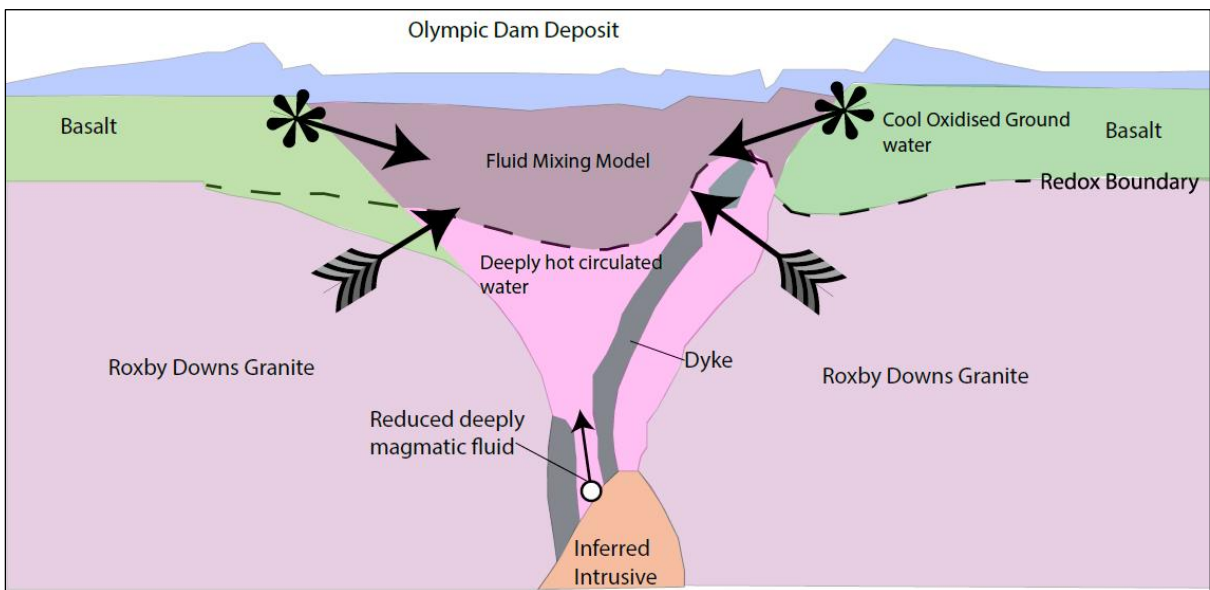


Figure 4. Fluid mixing model showing generation of the Olympic Dam deposit from mixing of a deeply sourced, reduced magmatic fluid or hot circulating fluids and oxidised cooler ground water/meteoric fluids. Modified after Haynes et al. (1995).

Nature of district-scale alteration

A broad link between the range of deposit-scale alteration features of IOCG mineralisation (e.g. K-feldspar-biotite, hematite-sericite-chlorite alteration) and Na-Ca regional alteration is recognised (Gow et al., 1996; Haynes et al., 1995; Bastrakov et al., 2007). However, there is relatively little information on the distribution of alteration minerals and elemental

geochemistry, and a poor understanding of the processes controlling alteration mineral distribution, in particular, the links between IOCG deposit and regional-scale geochemistry. As a result, the geoscience community does not have a good understanding of the whole IOCG mineral system or how to use geochemistry and alteration mineralogy to explore within the system.

Fabris (2012, 2013) conducted research in the Olympic Dam region, the same study region as examined in this research, to develop an empirical index that utilises pathfinder elements as the vector to orebodies, ranging from distal to proximal to the orebody. Ten pathfinder elements were selected for the index - Au, Ag, As, Bi, Cu, Mo, S, Sb, Se and W. Fabris (2012, 2013) applied a threshold value of ten times average crustal abundance for each of the ten elements, then divided the number of elements above the threshold by the number of elements below the threshold to generate the index. Calculated index values thus range from 0 (no elements $> 10 \times$ crustal abundance) to 10 (all ten elements $> 10 \times$ crustal abundance). The index appears to have a spatial correlation, whereby higher values occur more proximal to mineralisation and lower values more distal. This led Fabris (2012, 2013) to propose that the IOCG element index might have value as a mineral exploration tool, with the potential to vector toward mineralisation using geochemical data.

An important unknown in the work of Fabris (2012, 2013) is which minerals host the various pathfinder elements and in what way those minerals are associated with the IOCG alteration system. Empirical observations of mineralogical controls on element distribution are required as well as understanding of the processes involved in element Alteration systems evolve during multiple stages over a range of conditions and with varying degrees and types of fluid-rock interactions. These processes may lead to local enrichment or depletion of pathfinder elements and minerals. Empirical observations of mineralogical controls on element distribution are required as well as understanding of the processes involved in element department.

This thesis addresses a series of questions related to the nature of, and controls on, district-scale alteration in IOCG systems using the central eastern Gawler Craton of South Australia as a case study. This study uses a sample set outside of known mineral deposits that incorporates a range of alteration types and abundances of potential pathfinder elements to understand the breadth of fluid-rock interactions in the mineral system. Thus, this work provides insight to potential mechanisms of ore deposition (within the smaller, often uneconomic satellite deposits as well as well-known larger deposits) and potential sources and evolution of mineralising fluids.

1.3 BACKGROUND GEOLOGY, THE EASTERN GAWLER CRATON

The Gawler Craton is a globally important IOCG province, containing the prospective Olympic Domain in the east of the Craton (Figure 5). This area contains numerous economic and sub-economic occurrences of IOCG mineralisation, including the supergiant Olympic Dam and giant Prominent Hill deposits (McPhie et al., 2011; Schlegel and Heinrich, 2015). The Olympic

Dam deposit is the world's fourth largest Cu resource, fifth largest Au resource and the world's largest U resource in a single deposit (BHP, 2012). The IOCG system preserves extensive alkaline and iron-oxide alteration, and mineralisation is often recognised as being structurally controlled (Williams et al. 2005; Groves et al. 2010). Many studies of mineralization in the Olympic Domain have focused on deposit-scale issues (e.g. Oreskes and Einaudi 1990; Gow et al., 1994; Davidson et al., 2007). Relatively fewer studies have focused on regional alteration (Johnson and McCulloch 1995; Skirrow et al., 2007). The IOCG deposits themselves are only a small part of the system, and are often used to understand the alteration core. Therefore, to develop holistic models, and in particular to increase our understanding of the broad geochemical footprint related to the IOCG deposits, there is a need to understand regional fluid-rock interactions, even at low fluid-rock ratios.

The area studied in this research covers approximately 1200 km² and is located ~40 km south of the giant Olympic Dam IOCG deposit and ~240 km north of the Hillside deposit. The region is within the middle of the Olympic Domain of the eastern Gawler Craton, which hosts numerous economic IOCG deposits and prospects (Figure 6). Exploration within the Olympic Domain is hampered by deep cover and has relied on sparse drilling into potential field geophysical anomalies, which are proxy measures for IOCG systems. The interpreted geographic extent of the Olympic Domain (~600 km x 200 km), the clustering of mineralisation (Belperio et al., 2007; Porter, 2010; Skirrow et al., 2007) and the diversity of protoliths that host IOCG deposits (Gow et al., 1994; Hand et al., 2007; Fairclough, 2005) point to a hydrothermal mineralising system of significant scale and intensity.

The Palaeoproterozoic basement rocks of the Olympic Domain are poorly exposed, and are extensively overlain by Neoproterozoic to Cambrian cover sequences of the Adelaide Rift Sequence and Stuart Shelf (e.g. Drexel and Preiss, 1995). The oldest rocks recognised in the eastern Gawler Craton are the c. 1850 Ma Donington Suite (Reid et al., 2008) and the c. 1760-1730 Ma Wallaroo Group (Cowley et al., 2003). These units were emplaced at a time of rift-basin development and deposition of a series of volcanosedimentary packages throughout the Gawler Craton (Hand et al., 2007; Reid and Hand, 2012). Basin development was terminated by the c. 1730-1690 Ma Kimban Orogeny (Hoek and Schaefer, 1998; Hand et al. 2007), which involved extensive magmatism, high-grade metamorphism, crustal-scale shearing and transpressional deformation (e.g. Reid and Hand, 2012). The extent and intensity of Kimban Orogeny deformation within the Olympic Domain is not entirely resolved (e.g. Mount Woods Domain: Betts et al., 2003).

The Kimban orogeny was followed by a period of extensive magmatism and localised sedimentation mostly within the central Gawler Craton. The next major tectonothermal event within the Gawler Craton occurred between c. 1640-1550 Ma, and is broadly termed the Kararan Orogeny (Daly et al., 1998; Hand et al., 2007). The Kararan Orogeny involved a complex history including high-temperature metamorphism, intense deformation, voluminous magmatism and extensive mineralisation (e.g. Stewart and Foden 2003; Johnson and Cross, 2005; Hand et al. 2007; Skirrow et al. 2007; Forbes et al. 2011; Morrissey et al. 2014). Magmatism included emplacement of shallow level intrusions of the felsic-dominated Hiltaba Suite (c. 1595-1575 Ma) and extrusion of the Gawler Range Volcanics (1593-2592 Ma) (e.g. Johnson and Cross 2005; Jagodzinski 2014). The most precise zircon U-Pb ages for Hiltaba

Suite granitoids in the study area cluster around c. 1588 to 1596 Ma (Johnson and Cross, 1995). Mafic intrusions of comparable age have been increasingly identified in the Olympic Dam district (Johnson and Cross, 1995; Jagodzinski, 2005).

Widespread NW-SE contractional deformation occurring at the time of the Hiltaba Suite is expressed by the formation and/or reactivation of shear zones ranging up to crustal scale. Deformation of the Hiltaba Suite granites and GRV (Gawler range volcanics) in the early Mesoproterozoic, during IOCG formation, was restricted to local brittle-style fracturing, brecciation and faulting (Direen and Lyons, 2007; Hand et al. 2007). Extensive IOCG mineralisation was emplaced throughout the eastern Gawler Craton at c. 1590 Ma, including the Olympic Dam, Prominent Hill and Carrapateena deposits (e.g. Johnson and Cross 2005; Skirrow et al. 2007; Reid et al. 2011) (Figure 5). Northwest-trending structures, such as those in the vicinity of the Olympic Dam deposit, are likely to have accommodated dilation associated with strike-slip movements. Intersection between these structures and NE-trending contractional faults, c.1590 to 1580 Ma, may have formed suitable structural traps for mineralisation within the eastern Gawler Craton.

In addition to IOCG mineralisation, Au-only mineralisation was emplaced within the 'Central Gawler Gold Province', and includes the Tunkillia, Tarcoola and Barns deposits (Budd and Fraser, 2004; Fraser et al. 2007) (Figure 5). The IOCG and Au-only provinces preserve lithospheric compositional differences that are indicated by modern-day heat flow in the IOCG province which is significantly higher ($90 \pm 10 \text{ mWm}^{-2}$) compared to the Au-dominated province ($54 \pm 5 \text{ mWm}^{-2}$) (Hand et al., 2007). This is interpreted to possibly reflect deposition of Au occurring prior to IOCG in craton assembly (Hand et al., 2007). Qiuyue et al. (2017) suggested that at least two time-punctuated hydrothermal events have occurred at Olympic Dam and both generations of mafic rocks could provide copper to the deposit.

IOCG mineralisation is hosted within a range of basement rock types including the c. 1850 Ma Donington Suite granite (Carrapateena: Fairclough, 2005; Sawyer, 2013), Mesoproterozoic granites (e.g. Roxby Downs granite at Olympic Dam: Johnson and Cross, 1995) and sedimentary rocks (e.g. Emmie Bluff: Gow et al., 1994). The dominant lithology hosting IOCG mineralisation in the eastern Gawler Craton is hematite breccia. Ore minerals commonly include chalcopyrite, bornite and chalcocite. Hydrothermal alteration includes chlorite, K-feldspar, hematite alteration (Bastrakov et al., 2007) and carbonate alteration of various basement protoliths including granite and calc-silicate rocks.

This study is focussed on the area of the eastern Gawler Craton that includes the Carrapateena, Punt Hill, Emmie Bluff, Khamsin and Oak Dam deposits (Figures 5 and 6). The eastern Gawler Craton IOCG system contains a range of alteration types related to fluid-rock interactions, with three broadly defined end-members (Skirrow et al., 2002): calc-silicate-alkali feldspar-magnetite (CAM), magnetite-biotite (MB) and hematite-sericite-chlorite-carbonate (HSCC) alteration. Typical CAM assemblages include magnetite-actinolite-K-feldspar-pyrite-dolomite \pm apatite (Skirrow et al., 2002). Mineralisation at Punt Hill and Emmie Bluff exhibits magnetite and calc-silicate alteration of carbonate bearing metasedimentary rocks of the Wallaroo Group (Gow et al., 1994; Reid et al., 2008; Daly and Rowett, 2007). At Emmie Bluff there are four recognised alteration stages in which early

magnetite alteration was overprinted by hematite, late-stage veins and sericite alteration. (Gow et al., 2004). Cu-Au-REE mineralisation at Carrapateena is associated with intense HSCC alteration of the host Donington Suite granite (Figure 6). Magnetite bearing (CAM and MB) alteration has been linked to high temperature, hypersaline (>30% NaCl equivalent), Cu-rich fluid inclusions (Bastrakov et al., 2007) and inferred to have formed at temperatures of 350° to 500°C. In contrast, hematite bearing (HSCC) alteration has been linked to low salinity (1-7 wt % NaCl equivalent) fluids and inferred to have formed at temperatures below 300°C (Bastrakov et al., 2007).

HCh models have previously been used to establish relationships between the three mineralisation styles of CAM, MB and HSCC and to model ore genesis. I used samples of the three mineralisation styles to run C-H-O-Cl-S-Na-K-Mg-Fe-Si-Al-Cu-Ca-Mn hydrothermal system experiments using the HCh thermodynamic numeric computing calculation for alteration. Our approach was different to previous modelling, as I used true rocks and fluids from the study area. As about 40% of fluid in the study area is hypersaline, and HCh modelling requires about < 35 wt % equiv fluid, I selected fluid samples within the range suitable for HCh modelling. I applied temperatures between 500° and 150°C within the temperature-pressure (T-P) grid (P=8*T-1100 bar) and examined additional models out of the T-P grid for 300°-400°C and 390°-200°C with 4000 bar isothermal models generated. Sulphur (S) is important to HCh modelling of ore minerals, whether S is derived from fluids or rocks.

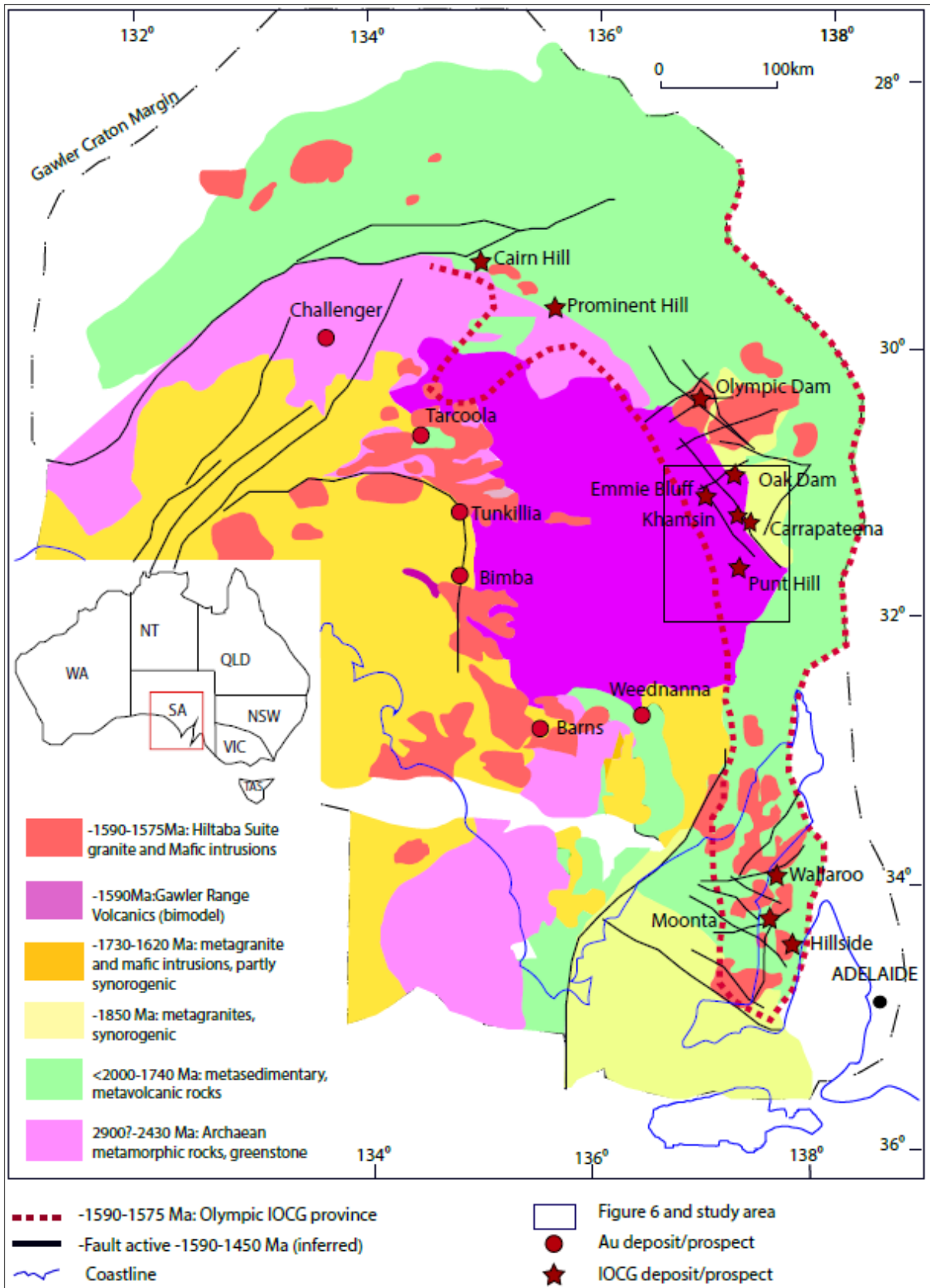


Figure 5. Simplified geological map of the Gawler Craton, South Australia (modified from Geoscience Australia and SARIG) showing major geological units and location of IOCG and Au deposits/prospects. The location of the study area in the eastern Gawler Craton is shown.

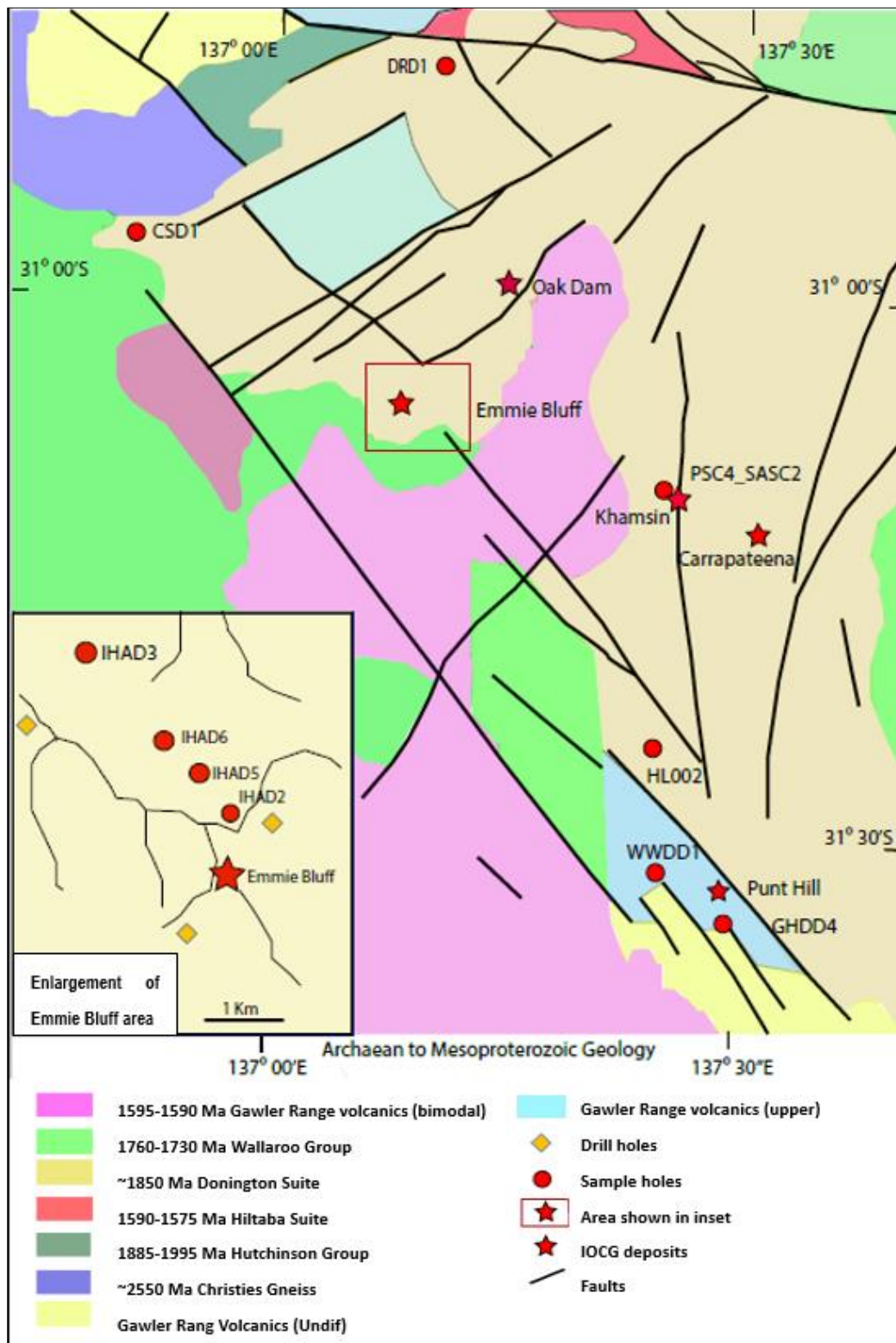


Figure 6. Simplified solid geology map of the eastern Gawler Craton study area showing basement geology and location of IOCG deposits and prospects. Locations of drill holes sampled in this study are also shown. The location of the study area is shown in Figure 5 (Modified from SARIG: <https://sariq.pir.sa.gov.au/Map>).

Thesis aim

The aim of this thesis is to map the distribution of alteration minerals and pathfinder elements

from deposit to regional-scale within the IOCG mineral system of the eastern Gawler Craton and understand fluid-rock interactions that control that distribution.

Research findings may allow mineral explorers to better understand mineral assemblages and geochemical patterns observed from drillholes within the context of a regional mineral system. In turn, findings inform decision making during the exploration process, such as determining drillhole location to improve exploration success.

Three related objectives were important to addressing the thesis aim:

1. Establish the mineralogical characteristics of altered rocks within the mineral system including: A) a range of protolith rocks collected from a broad geographic area, B) a range of alteration type characteristics of the IOCG mineral system and C) a range of alteration intensity as measured by concentration of commodity and pathfinder elements.
2. Understand the mineral deportment of trace elements, including commodity and pathfinder elements, within alteration assemblages as a means of reconstructing fluid-rock interactions driving regional geochemical patterns.
3. Model thermodynamic constraints on the nature of fluid-rock interactions.

1.4 THESIS STRUCTURE

This thesis contains five chapters: Chapters 1 and 5 are general introduction and conclusions, respectively. Chapters 2 to 4 contain new data and interpretations relating to the three objectives stated above. Chapters 2 to 4 have been prepared such that they can be easily reformatted for submission to a journal and thus have a stand alone introduction with elements that may be repeated in each chapter.

Chapter 1: Introduction

In chapter 1, I present a review of IOCG deposits, in particular the eastern Gawler Craton deposit, study outline, general aims, thesis structure and modelling method. The chapter includes a brief introduction of background geology of the eastern Gawler Craton.

Chapter 2: Spectrum of fluid/rock alteration in the IOCG system of eastern Gawler Craton, Australia

In chapter 2, I present geochemical and petrological data that characterises the spectrum and intensity of alteration types within the eastern Gawler Craton mineral system. This chapter presents whole rock geochemistry and HyLogger hyperspectral mineralogy from 2276 samples of drill core. Of these, 44 samples were selected for detailed petrology representing a range of protolith types (e.g. granite, amphibolite, calc-silicate metasediment and siliciclastic metasediment), alteration types (e.g. K-feldspar, magnetite, calc-silicate, chlorite and hematite) and variable concentrations of Cu, Au, U and REE, and pathfinder elements proposed as a measure of alteration intensity (Fabris, 2013). The petrologic study was underpinned by transmitted and reflected light microscopy, focusing on mineral textures and paragenesis. Of

44 petrology samples, 11 were selected for scanning electron microscopy (SEM) as a means of observing micron-scale textures and mapping elemental concentrations within individual mineral phases.

Chapter 3: Mineral chemistry mapping within an IOCG system, Olympic Cu-Au Province, South Australia

In chapter 3, I present elemental chemistry of single mineral phases within the context of alteration mineralogy and textures identified in Chapter 2. The aim of this chapter is to establish the trace element budget within each studied sample and use those data to understand fluid/rock interactions responsible for trace element deportment. Mineral chemistry was analysed by electron microprobe and laser ablation inductively coupled mass spectrometry (LA-ICPMS) on the same 11 samples chosen for SEM. Electron microprobe analyses were conducted on 234 individual minerals, with concentrations of selected elements used to calibrate subsequent LA-ICPMS analyses on the same minerals. Discussion of mineral chemistry focusses on:

- Fe/S and Co/Ni ratios in pyrite as a means of identifying geological processes responsible for pyrite growth.
- REE patterns as a means of identifying protolith types and quantifying REE mobility due to alteration.
- Trace element abundances and patterns of enrichment as a means of characterising nature and intensity of alteration.

In samples with sufficient trace element data from minerals that constitute a significant volume of the rock, trace element data combined with estimated mineral abundances was used to calculate a 'model' trace element budget for comparison with whole rock data from the same sample intervals.

Chapter 4: HCh thermodynamic models of IOCG systems of the eastern Gawler Craton, South Australia

In chapter 4, I present results of thermodynamic modelling, describing constraints on physical (temperature, pressure, fluid/rock ratios) and chemical (fO_2 , pH, fluid composition and rock composition) conditions at which alteration assemblages described in Chapters 2 and 3 were formed. Rather than attempting to contrive a series of models describing paragenesis of individual samples, this research instead used model protoliths (representing generic unaltered granite and generic unaltered calc-silicate rock) mixed with a model fluid (of a composition consistent with fluid inclusions from across the eastern Gawler Craton) at a range of fluid/rock ratios, temperatures and pressures. Outcomes are presented as a model volume in which equilibrium alteration mineral assemblages and fluid compositions were mapped against three parameters considered by previous authors to be important in IOCG systems: A) combined temperature and pressure, B) fO_2 and C) fluid/rock ratio.

Chapter 5: Conclusions

In chapter 5, I summarise and highlight major findings of the research project and broader implications for hydrothermal processes and mineral exploration.

2 Spectrum of fluid/rock alteration in the IOCG system of eastern Gawler Craton, Australia

ABSTRACT

In this chapter, I present petrology and geochemistry from a range of metasomatically altered rocks collected from the central eastern Gawler Craton of South Australia. Rock samples used in this study represent four protolith types: siliciclastic metasedimentary rock, calc-silicate metasedimentary rock, granite and mafic magmatic rock. Multiple, overprinting paragenetic relationships can be interpreted within the framework of five paragenetic stages, with characteristic mineral assemblages in the four protolith types summarized as follows:

- Protolith assemblages include; quartz and K-feldspar in siliciclastic metasedimentary rocks; dolomite in calc-silicate (carbonate) metasedimentary protoliths; quartz, K-feldspar, plagioclase, biotite and ilmenite in granitic protoliths, and; quartz and amphibole in mafic magmatic protoliths.
- Skarn assemblages include anhydrous calc-silicate minerals garnet, pyroxene and actinolite and occur exclusively in calc-silicate protoliths. Skarn assemblages most commonly occur early during the paragenesis.
- Stage 1: K-feldspar, magnetite and chlorite assemblages with pyrite and minor Cu-sulphides. These assemblages correspond to MB (magnetite, biotite \pm K-feldspar) and CAM (chlorite, alkali feldspar and magnetite) alteration styles as previously reported on the eastern Gawler Craton by Skirrow et al. (2002).
- Stage 2: Hematite, chlorite and muscovite assemblages with Cu-sulphides. This represents the main Cu-mineralisation phase and corresponds to the HSCC (hematite, sericite, chlorite and carbonate) alteration style of Skirrow et al. (2002).
- Stage 3: Post-mineralisation assemblages which include hematite, chlorite, carbonate, apatite, quartz and manganite.

The paragenesis is consistent with successive periods of Fe-K-metasomatism, with early higher temperature, more reduced (magnetite stable) alteration being consistently overprinted by lower temperature, more oxidized (hematite stable) alteration and with the bulk of Cu-sulphide mineralization occurring at close to the transition from magnetite to hematite. It is possible that variable overprinting (e.g. Bastrakov et al., 2007) and/or mixing (e.g. Haynes et al., 1995) of two discrete fluids was responsible for the observed paragenesis. However it is also possible that an initially highly-saline, hot and reduced fluid evolved toward a cooler, lower-salinity and more oxidized fluid as it migrated through the crust. In all rock types, alteration intensity was greatest in samples with breccia textures, intermediate in samples with veining and micro-fractures and least in samples with little evidence of deformation. These observations are consistent with a link between alteration intensity and increased fluid-rock ratios due to transient structurally controlled permeability.

2.1 INTRODUCTION

Iron-oxide copper gold (IOCG) deposits are important global copper gold uranium and REE resources. While there has been considerable study of these systems (Ferris et al., 2002; Espinoza, 2002; Naslund et al., 2002; Billström et al., 2010; Corriveau et al., 2010; McLellan et al., 2010; Porter, 2010; Rusk et al., 2010; Xavier et al., 2010; Kontonikas-charos et al., 2014 and 2017; Verdugo-Ihl et al., 2017), there remains uncertainty regarding the geodynamic setting of deposits and specific controls on mineralisation. Importantly, there is a need to better understand the nature and source of mineralising fluids and how they interact with various rock types as they pass through the crust. Johnson (1995) suggested that mineralising fluids have chemistry consistent with a mantle source, while Barton (2010) contended that mixing with sedimentary (meteoric fluids) is important to IOCG formation. Bastrakov and Skirrow (2007) found two fluids present in samples from the eastern Gawler Craton: a high-temperature, metal-rich fluid and a low temperature fluid. But there remains a need to understand how these fluids interacted with each other and the suite of rocks in the district.

In the chapter, I use a combination of petrology and SEM element mapping to show that the two fluids recognised by Bastrakov et al. (2007) could be responsible for the range of alteration and mineralisation styles observed in the eastern Gawler Craton mineralised province. Whole rock geochemistry is used to characterise alteration trends associated with the IOCG mineral system. There is an important relationship between ore mineral phases and alteration mineral phases in rock sequences, classified by an alteration spectrum.

2.2 CHARACTERISTICS OF IOCG MINERALISATION

IOCG deposits have been found on every continent (except Antarctica), in a variety of host rocks, over a range of geologic time (with a concentration in the Proterozoic), in a variety of interpreted tectonic settings (convergent margins to 'intracratonic' basins) and have a range of proposed mechanisms of formation (Benavides, 2007; Monteiro, 2008; Groves et al., 2010; Porter, 2010). Consistent elements of these models include; 1) IOCG mineral systems are associated with significant lithospheric-scale fluxes of heat and fluid, including coincident magmatism, potentially linking to mantle processes; 2) that IOCG systems are controlled by lithospheric-scale fluid pathways (faults and shear zones) that are located in dynamic tectonic settings (eg. at the margins of continental plates, or in actively deforming intracratonic areas; 3) that local structure intersections are common emplacement sites of IOCG orebodies and that the orebodies typically contain evidence of complex, syn-mineralisation structural reworking and brecciation (Fairclough, 2005; Daly and Rowett, 2007; Huntington et al., 2006); 4) that the dominant IOCG processes are hydrothermal, with a variety of characteristics that vary according to location (Ferris et al., 2002; Espinoza, 2002; Naslund et al., 2002; Billström et al., 2010; Chen, 2010; McLellan et al., 2010; Rusk et al., 2010; Xavier et al., 2010; Ismail et al., 2014); 5) that these processes result in a spectrum of deposit styles and alteration products related (amongst other things) to a range of formation depths between 2-15 km depth (Ferris et al., 2002; Espinoza, 2002; Porter, 2010); that the key alteration feature is abundant iron-oxide minerals (dominantly hematite and magnetite), both within the ore envelope and in widespread regional alteration.

IOCG mineral systems display a range of alteration styles that have been interpreted to represent complex interactions between various protolith rocks with fluids of different origin (magmatic, metamorphic, meteoric and surface derived brines) over a wide range of crustal depths (eg. Hitzman et al., 1992; Bastrakov et al., 2007; Porter, 2010; Rusk et al., 2010; Kontonikas-charos et al., 2014 and 2017; Verdugo-Ihl et al., 2017). One potential source of magmatic fluids are I-type and A-type granites that are often observed to be coincident with IOCG mineralisation (Benavides et al., 2007; Porter, 2010). Such fluids have been implicated in regional Na-alteration (albitisation) and proximal K-alteration in IOCG systems (Cleverley et al., 2005; Yang 2009). Fluid inclusions in ore minerals point to hot brines (>30 wt % NaCl equiv) that were progressively cooled and diluted by low-salinity fluids (<10 wt % NaCl) (Xavier et al., 2010). Hence, incursion of evaporite-sourced basinal brines, or seawater, has been proposed as a prerequisite for IOCG deposits (Chen, 2010). Hypersaline fluids from above 550°C decrease to below 300°C during fluid mixing, accompanied by a fO₂ increase from magnetite-chalcopyrite to hematite-bornite (Xavier et al., 2010). Low temperature (~300°C) muscovite and biotite may have influenced IOCG mineralisation in the Gawler Craton (Hand et al., 2007), similar to the function of chlorite, at below 300°C, in the Sossego IOCG deposit (Monteiro et al., 2008). GRV and HS (Hiltaba Suite) are high temperature magmatic and metamorphic geological systems (Hand et al., 2007) link to the sodic–calcic event at ~500 °C (1.4 kbar) (Monteiro et al., 2008).

2.3 MINERALISATION OF THE GAWLER CRATON

The largest IOCG deposits in the eastern Gawler Craton IOCG system are, from north to south, Prominent Hill, Olympic Dam and Carrapateena (Figure 5). In addition there are numerous known mineral occurrences including Emmie Bluff, Oak Dam and Punt Hill. Mineralisation occurs in a range of host rocks including granite, felsic volcanic rocks and metasedimentary rocks (particularly calc-silicate metasediments). Common to all deposits is the intimate association of iron-oxides, dominantly hematite, with mineralization. Heterolithic, hematite-rich breccia being consistently associated with sulphide mineralisation in the largest known deposits (Olympic Dam, Prominent Hill and Carrapateena). This association with iron-oxides has informed previous exploration efforts on the eastern Gawler Craton which have focused on testing magnetic and gravity anomalies (Fairclough, 2005; Belperio et al., 2007). Ore minerals contained within hematite breccia include chalcopyrite, bornite and chalcocite. Hydrothermal alteration associated with iron-oxides and sulphide mineralisation has resulted in widespread K-feldspar, biotite, chlorite, muscovite and carbonate alteration (eg. Bastrakov et al., 2007; Verdugo-Ihl et al., 2017). Skirrow et al. (2002) subdivided alteration associated with the IOCG mineral system on the eastern Gawler Craton into three end-members:

- Magnetite-Biotite (BM): Syn- to post-compressional district- to deposit-scale magnetite-rich alteration characterized by Fe⁺² metasomatism and generally minor Cu-Au mineralization (magnetite, K-feldspar or biotite, actinolite, quartz, apatite, pyrite, chalcopyrite).

- Calc-silicate, Alkali feldspar and Magnetite (CAM): Related to calc-silicate protolith and alkali environments and also minor Cu-Au mineralisations and
- Hematite–Sericite–Chlorite–Carbonate (HSCC): above magnetite-bearing zones; higher grade uranium mineralization is generally associated with gold-rich and/or more oxidized mineral assemblages. Combinations of hematite, chlorite, sericite, carbonate, pyrite, gold, chalcopyrite, bornite, chalcocite, barite and various REE and phosphate minerals.

The host rock of Carrapateena is a brecciated granite complex of Donington Suite (Figure 5; Fairclough, 2005). Silicate mineral assemblage varies from plagioclase, feldspar, biotite, and hornblende, K-feldspar, quartz assemblages variably altered to chlorite, sericite. Carrapateena Breccia Complex is cut at its centre by an EW- to ENE-trending complex zone of faulting. A near vertical pipe chalcopyrite with sulphidic vein-fill and blebs related to a hematite-rich breccia (Fairclough, 2005). Host rock is a strongly brecciated granite complex (granitoid, variably foliated, sheared gneissic quartz-granite and quartz-diorite) of Palaeoproterozoic Donington Suite (Ca. 1857±6 Ma) (Figure 6). Alteration is HSCC style, hematite, sericite, chlorite and carbonate alteration with abundant quartz and (siderite and/or ankerite), and secondary barite, monazite, anatase, magnetite, apatite, fluorite and zircon (Fairclough, 2005). Ore is vertically downward from bornite to chalcopyrite-bornite to chalcopyrite to chalcopyrite-pyrite. Chalcopyrite-bornite zone contains U-REE (Ce-La) minerals and chalcocite, covellite, trace sphalerite and galena and digenite. Mineralisation zone is from upper hematite-rich zone, to a lower magnetite-rich zone. Apatite occurs at hang wall and foot wall, stratabound characteristics.

The host rock of Emmie Bluff is Wallaroo Group sandstone, a stratabound zone of metasedimentary rocks (1760-1730Ma). Silicate mineral assemblage is amphibole, clinoproxene, K-feldspar, sericite, chlorite and quartz (Bastrakov et al., 2007; Gow et al., 1994). Alteration is CAM and HSCC multiple alteration styles with late-stage veins (carbonate or magnesite) (Gow et al., 1994). Ore is chalcopyrite ± bornite ± covellite with significant silver, cobalt and minor zinc credits. Mineralisation is zoned vertically from an upper hematite-rich zone, with chalcopyrite–bornite–covellite mineralisation, to a lower magnetite-rich zone (Huntington et al., 2006). Apatite at hang wall and foot wall, stratabound characteristics.

The host rock of Punt Hill is brecciated Gawler Range Volcanics (1596-1590Ma) and altered metasedimentary rocks of Wallaroo Group (1760-1730 Ma) (Reid et al., 2008; Daly and Rowett, 2007). Silicate minerals are garnet, pyroxene, biotite, feldspars, sericite, chlorite, diopside, amphibole, epidote and tourmaline (Reid et al., 2011). Alteration is chlorite-rich CAM style and hematite- sericite-rich HSCC style (Skirrow et al., 2007). Ore is chalcopyrite, sphalerite, chalcocite and bornite. Top of ore is rich-bornite. In addition to copper mineralization Punt Hill contains elevated concentrations of Ag, Zn, Au, Pb and REE, with elevated Au and Pb occurring over wider than the Cu-rich core zone and elevated REE occurring vertically above the Cu-rich core zone.

2.4 METHODS

I used a combination of petrological and geochemical techniques on selected samples from the central eastern Gawler Craton (Figure 6) to establish patterns of alteration and paragenetic relationships.

2.4.1 Sample selection

To characterise alteration throughout the central eastern Gawler Craton, I selected 44 samples from 10 drillholes (see appendix 1) surrounding the Carrapateena, Emmie Bluff and Punt Hill prospects, within an area of $\sim 120 \times 100 \text{ km}^2$ and over a vertical depth extent of 400-1200m (Figure 6). The samples were distributed to represent different protolith types, as well as different styles and intensity of alteration. Samples were initially chosen based on previous logging recorded in the online South Australian Resources Industry Geoserver (SARIG) database (Fabris, 2013). For many samples, there is uncertainty regarding protolith classification due to widespread metamorphic recrystallisation, metasomatic alteration and textural overprinting. Thus protolith classification decisions for the 44 selected samples were also based on detailed re-logging of drillholes by the author and reference to multi-element geochemistry (see below), HyLogger data and handheld XRF geochemistry (see appendix 2). This selection process ensured variation in protolith types (where protolith could be identified) and degrees of alteration intensity of the 3D space in the eastern Gawler Craton.

2.4.2 Geochemistry

Whole rock geochemical data were obtained from the SARIG database (<https://sarig.pir.sa.gov.au/Map>). The SARIG database contains data from one meter intervals taken every tenth meter for approximately 600 drillholes in the eastern Gawler Craton. A small proportion of drillholes have been completely analysed, i.e. each one meter interval, to provide additional data (e.g. IHAD5). Six analytical methods were consistently used to determine whole rock geochemistry for 65 elements (Table 2). Ten major elements were reported at % level, with Au, Pd and Pt trace elements reported at ppb level and another 42 elements reported at ppm level.

I examined whole rock geochemical data using ioGasTM software to determine rock types and alteration trends and to inform selection of the 44 representative samples from the central eastern Gawler Craton. Ternary plots of major elements (Figures 7 and 8), in particular, provided a useful means of characterizing various protolith and alteration trends.

Table 2. Six data analysis methods used to examine 65 elements reported in the SARIG database

Method	Description	Elements
FB6/OE	Lithium borate fusion, ICP-OES	SiO ₂ Al ₂ O ₃ CaO Fe ₂ O ₃ K ₂ O MgO MnO TiO ₂ P ₂ O ₅ Na ₂ O V Cr Sc
FA25/MS	Lead collection fire assay 25g charge, ICP-MS	Au Pd Pt
FB6/MS	Lithium borate fusion, ICP-MS	Ba Zr Rb Sr Ce La Nd Y Ga Th Nb Pr Hf Sm U Gd Dy Sn W Be Yb Er Eu Ta Ho Tb Tm Lu
FC7/SIE	Carbonate fusion, Selective Ion Electrode	F
4A/OE	Four acid digests, ICP-OES	S Cu Zn Ni Pb
4A/MS	Four acid digests, ICP-MS	Co Li Cs Se Mo Bi Ge Sb Tl As In Te Ag Re Cd

2.4.3 Petrography

Polished thin sections were prepared Adelaide Petrographics Laboratories for all 44 of the selected samples. The thin sections were prepared from 2 cm × 4 cm subsamples and polished to a consistent thickness of 40-45µm. Petrographic observations were conducted using a petrographic microscope under plane and polarized, transmitted and reflected light. The thin sections were examined to determine mineralogy, structures (including micro faults and veins), textures (including mineral filling and replacement textures) and paragenetic overprinting relationships. Reflected and transmitted light photomicrographs were taken of key textures and petrogenetic relationships. I took particular care to identify and document textural overprinting relationships, at scales ranging from 2 mm to 10 µm, between mineral phases to establish a mineral paragenesis for each sample (Appendix 1).

As a result of petrographic observations 11 of 44 samples were selected as representative of various protoliths, alteration styles and intensity of IOCG alteration on the central eastern Gawler Craton and prepared for more detailed semi-quantitative microanalysis (see chapter 1.2, chapter 3.2 and appendix 1).

2.4.4 Scanning Electron Microscopy (SEM – XL30)

For the 11 representative samples selected above, semi-quantitative elemental mapping was conducted using scanning electron microscopy (SEM) at Adelaide Microscopy. The SEM instrument used was a Philips XL30 FEG SEM - with EDX detector, mapping capability, Oxford CT1500HF Cryo stage and HKL Channel 5 Electron BackScatter Diffraction System (EBSD). The XL30 instrument has the ability to identify 1-5 µm size minerals because the thin film EDS detector allows X-ray analysis. Quality images are produced at 100 µm scale where an electron beam is focused onto a small spot to give 2 nm resolution and magnification of up to $\times 10^6$. Major element compositions can be determined from the SEM data with effective limits of detection of ~1% within ~10% errors.

A number of single element SEM maps at a magnification of $\times 100$ and covering areas with side lengths ~2-3 mm size are reproduced in this chapter. The SEM images are a useful reference for identification and confirmation of minerals at grain sizes down to ~5µm, for recognition of chemical zonation within minerals and for detailed textural relationships between minerals of varying chemistry.

2.5 RESULTS

2.5.1 Whole Rock Geochemistry

There is considerable overlap in the major element chemistry between rocks identified in the SARIG database as belonging to four common protolith types (granites, calc-silicate metasedimentary rocks, otherwise unclassified metasedimentary rocks and mafic rocks). “Metasedimentary” protoliths include a large proportion of CaO-MgO-rich samples that

overlap with the dominant population of “calc-silicate” protoliths. The extent to which this subset of the metasedimentary protoliths reflects intermixing of carbonate sedimentary lithologies or overprinting of carbonate alteration can not be determined from the ternary plot. SiO₂ and Al₂O₃-rich metasedimentary protoliths have considerable overlap with the dominant population of “granitic” protoliths. Whilst the granitic protoliths also have a subpopulation drawn toward the CaO+MgO apex, which likely reflects carbonate alteration. For all protolith types there is a clear trend toward the Fe₂O₃ apex consistent with widespread and locally intense iron-oxide alteration (Figure 7).

Each of the four protolith types have a prominent subpopulation that can be inferred to represent the range of “least altered” examples of the protolith type (Figure 7). Least altered granites plot as a coherent geochemical group (Al₂O₃ > 50 and CaO+MgO < 20 in Figure 7) which corresponds to whole rock chemistry of SiO₂ (72-78 wt %), Al₂O₃ (12-20 wt %) and K₂O+Na₂O+CaO (8-12 wt %). The least altered calc-silicate metasedimentary protoliths occur within an area bound by Al₂O₃ > 10, Fe₂O₃ > 20 and CaO+MgO > 60 on Figure 7. The metasedimentary rocks include a significant subpopulation with CaO+MgO < 10, 45 < Al₂O₃ > 70 on Figure 7 and with whole rock SiO₂ of > 70%. This subpopulation of “siliciclastic” metasediments represent a mixture between quartz rich (silica dominated) metasediments and arkosic or shale end-members with similar whole rock chemistry to granites. The dominant population of “mafic” protoliths occupies a region between 25 < Al₂O₃ > 40 and 25 < Fe₂O₃ > 55 on Figure 7. A discrete group of high-Al₂O₃ and high-SiO₂ samples, logged as “mafic” may represent a discrete, more felsic magmatic rock type.

Whole rock sulphur is a measure of the sulfide (and sulphate) component of the mineralogy. Elevated Sulphur concentrations occur in all protolith types in the SARIG database but are more common in the metasedimentary and calc-silicate protoliths than in the granitic and mafic protoliths. The whole rock geochemistry illustrates a tendency for iron-rich rocks (those dragged toward the Fe₂O₃ apex by Fe-alteration) and carbonate-rich rocks (with an unknown mixture of sedimentary and alteration carbonate) to have elevated sulphur contents, in some cases exceeding 10 wt % (Figure 8). In contrast the region of Figure 8 corresponding to the least altered granite and metasedimentary protoliths, centred on approximately 75% Al₂O₃, 25% Fe₂O₃ and 10% CaO + MgO, is characterized by low sulphur concentrations.

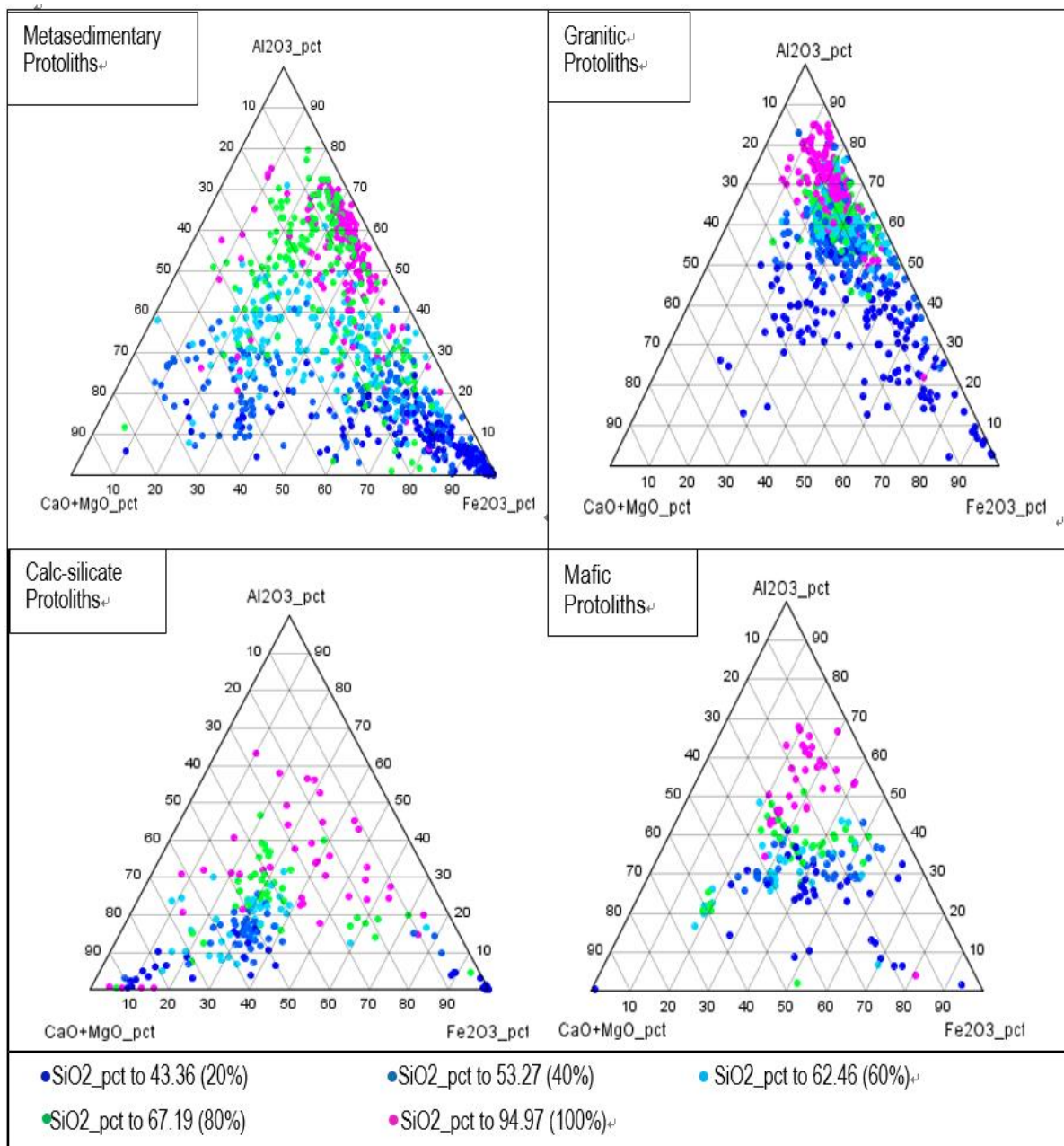


Figure 7. Ternary plots of Al₂O₃ vs CaO + MgO vs Fe₂O₃ and coloured for SiO₂ content, for four common protolith types (as identified in the SARIG database) of the central eastern Gawler Craton.

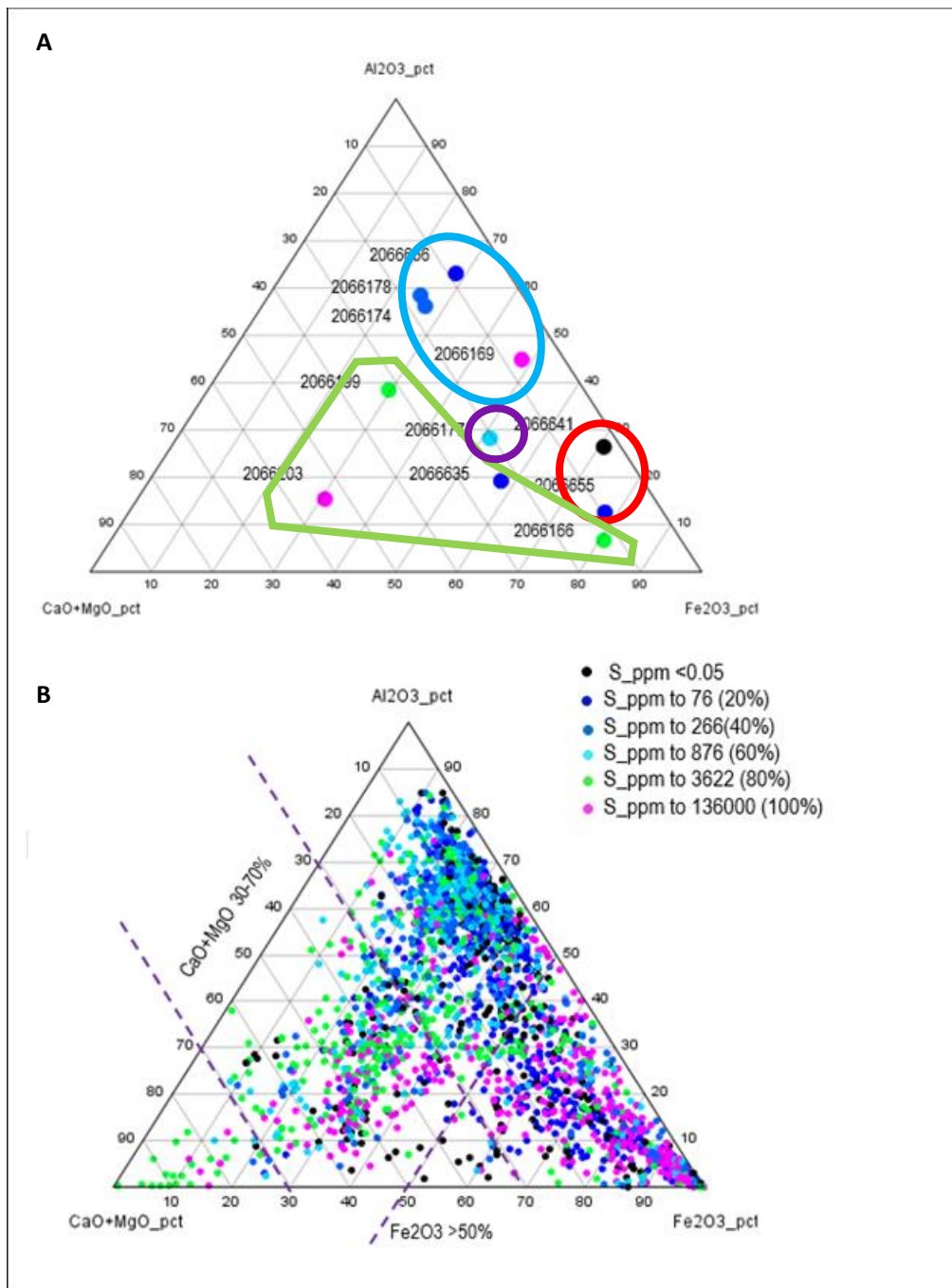


Figure 8. Whole rock geochemistry from four common rock types from the central eastern Gawler Craton coloured for sulphur (S) content. **A.** The eleven samples selected for detailed petrography and SEM analysis. Blue outlined samples = granite protoliths (2066656, 2066178, 2066174 and 2066169), green = calc-silicate (2066166, 2066199, 2066635 and 2066203), red = metasedimentary rocks (2066641 and 2066655) and purple = mafic rock (2066177). **B.** All data shown in Figure 7. Note that consistently highest sulphur contents occur in association with Fe-rich and CaO+MgO rich rocks at two areas.

2.5.2 Petrography

Siliciclastic metasedimentary protoliths

In this research, identification of siliciclastic protolith samples was based on visual recognition of sedimentary textures and dominant quartz and aluminosilicate mineralogy. The siliciclastic grouping included a range of protoliths with varying mixtures of quartz and clay (psammitic to pelitic) at varying metamorphic grade. Many drill core samples identified as siliciclastic metasedimentary protolith also contained significant proportions of carbonate minerals and iron-oxides, which may represent combinations of primary sedimentary mineralogy and alteration. Variable proportions of carbonate, similar to calc-silicate protolith samples (discussed below), demonstrate a continuum between siliciclastic and calc-silicate protolith end-members. Siliciclastic protolith samples grouped by original visual logging in the SARIG database were retained in this grouping, except for two samples (2066166 and 2066199) which were regrouped as calc-silicate.

A hematite-altered metasediment sample (2066641) was selected for further investigation. This sample was taken from a depth of 799.8 m in drillhole IHAD3 (Figure 9), within a 58 m intersection of metasediment logged as Wallaroo Group in the SARIG database. The interval has a distinctive dark brown colour due to abundant hematite. The sample contains ~ 25% hematite, 35% quartz, 20% chlorite, 10% K-feldspar and 10% minor phases including fine-grained micas, goethite, manganite and apatite. The sample has two broad domains: K-feldspar+chlorite-rich and hematite-rich, with a diffuse gradual boundary of 5mm width in the centre of the sample (Figure 9). Elongate irregular blebs of quartz 0.5-0.8 cm length and 0.2-0.3 cm width occur within the K-feldspar+chlorite zone. Hematite (+ minor apatite) veins of ~200 μm width cut through K-feldspar+chlorite domain and are in turn cross cut by manganite veins (50 μm) and quartz veins (10 μm) cut manganite veins.

Detailed investigation was conducted on sample 2066655, a brecciated chlorite-altered metasediment taken from a depth of 1016.6 m in drill core IHAD5, located ~1.5 km north of the Emmie Bluff prospect (Figure 10). The sample was taken from within a 159 m wide intersection of metasedimentary rocks logged as metasandstone and assigned to the Wallaroo Group in the SARIG database. The entire Wallaroo Group interval in IHAD5 has a distinctive green colour due to abundant chlorite. The sample was taken from a zone cross cut by 0.1-1 cm scale carbonate veins. The sample contains ~30% chlorite, 25% quartz, 20% hematite, 15% K-feldspar, 5% dolomite and 5% minor phases including calcite, magnetite, pyrite and chalcopyrite. The sample contains sub-millimeter grains of quartz, K-feldspar, pyrite and magnetite overprinted by fine-grained intergrown hematite and chlorite with minor chalcopyrite (Figure 10A). Elongate hematite partially replace a K-feldspar at the lower left corner of Figure 10A and the blocky shape of hematite and chlorite zones also imply replacement of feldspar. The sample includes distinctive ~millimetre-scale ring textures within a zone of fine grained chlorite, K-feldspar and hematite (Figure 10B). Hematite grains form the outer zone of the ring texture and display inward-growing space-filling textures. The hematite grains are overgrown by chlorite. The inner zone of the ring texture consists of chalcopyrite with complex discontinuous and embayed margins with the surrounding chlorite and containing ~10 μm inclusions of quartz and chlorite.

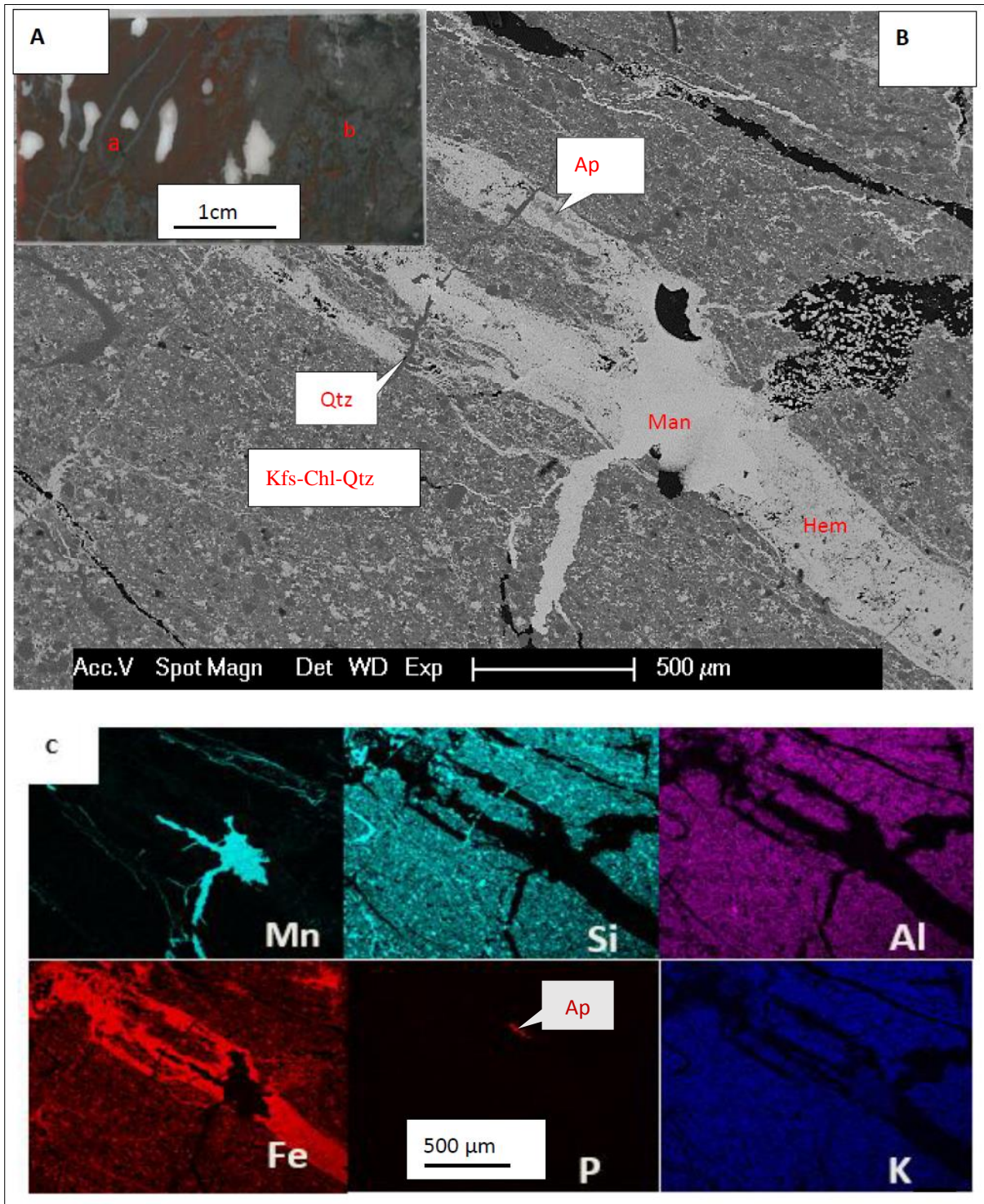


Figure 9. Petrographic images from the hematite-rich metasedimentary sample 2066641. **A.** Photograph of the entire thin section. Left hand side of the image (labelled a) is K-feldspar+chlorite rich with fine-grained hematite, irregular quartz blebs and narrow (grey) hematite veins. Right hand side (labelled b) is hematite-rich dominated. **B.** Backscatter SEM image from location (a) highlighting vein overprinting relationships in the K-feldspar+chlorite rich domain. Ap = apatite, Chl = chlorite, Hem = hematite, Kfs = K-feldspar, Man = manganite, Qtz = quartz. **C.** Mn, Si, Al, Fe, P and K SEM element maps from location a.

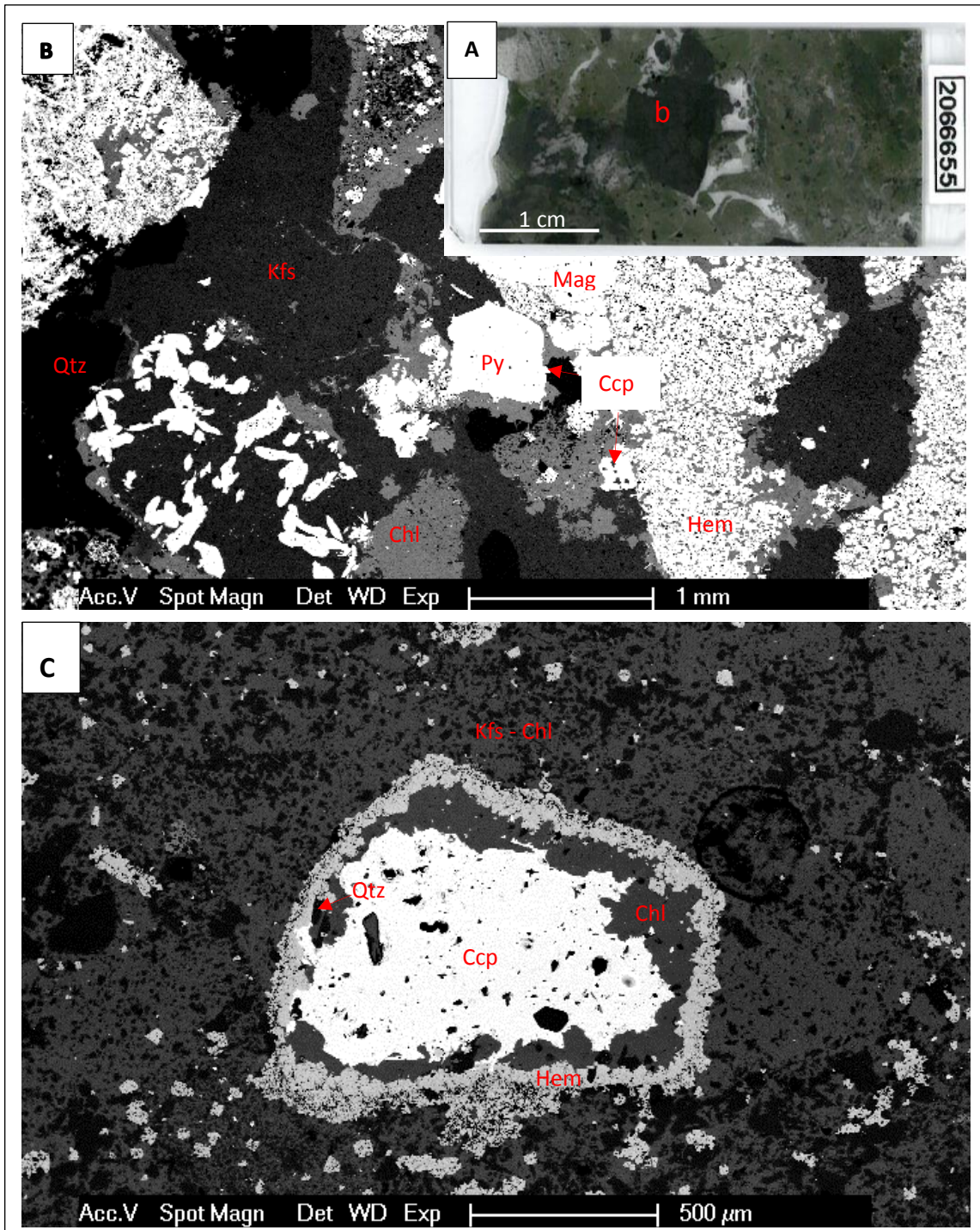


Figure 10. Petrographic images from the chlorite-rich metasedimentary sample 2066655. **A.** Photograph of the entire thin section. Labels b and c show the locations of Figure 10B and 10C respectively. **B.** Fine grains intergrowth hematite + chlorite replace a blocky rectangular mineral. Chlorite decorates margins of intergrown chlorite + hematite; and has irregular boundaries and partly replaces K-feldspar grains at their margins. Pyrite (euhedral) is surrounded by chlorite. Anhedronal magnetite occurs as the inclusions in hematite-chlorite zones. Chalcopyrite (5 μm) occurs at the margins of pyrite (0.5 mm). **C.** Millimetre-scale ring texture of chalcopyrite, with inclusions of chlorite and quartz; chlorite and hematite within a matrix of fine grained chlorite, K-feldspar and hematite. Mineral abbreviations: Kfs=K-feldspar, Chl=chlorite, Hem=hematite, Mag=magnetite, Py=pyrite, Ccp=chalcopyrite.

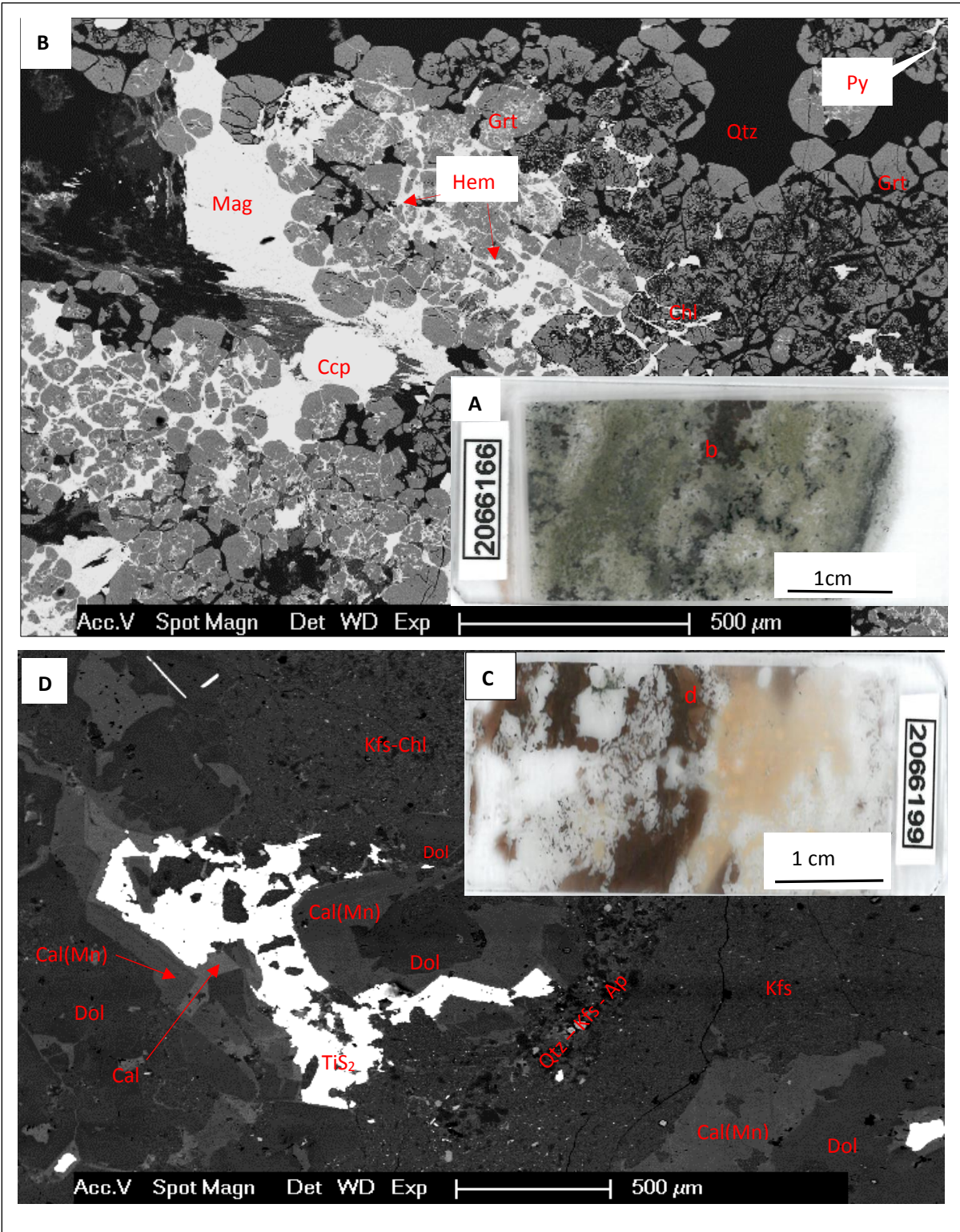
Calc-silicate protoliths

Identification of calc-silicate protoliths in drill core was based on visual recognition of sedimentary textures and dominant carbonate and calc-silicate mineralogy. The grouping includes a range of protoliths with varying mixtures of carbonate and calc-silicate (garnet, pyroxene and amphibole) and at varying metamorphic grade. Many of the samples contain significant proportions of chlorite and iron-oxides. A proportion of rocks classified as generic metasedimentary rocks in the SARIG database contain high concentrations of CaO + MgO (chapter 2.5.1; Figure 7) and abundant calc-silicate minerals and have been reclassified as calc-silicate protoliths in this study. These include samples 2066166 and 2066199.

The calc-silicate sample 2066166 was taken from drill core CSD1, ~40 km northwest of Emmie Bluff prospect (Figure 6), at a depth of 970.6m. The sample was taken from within a 128 m wide intersection of metasedimentary rocks logged as metasiltstone and assigned to the Wallaroo Group in the SARIG database. The entire Wallaroo Group interval in drill core CSD1 has a distinctive dark grey colour with an abundance of carbonate, chlorite, calc-silicate minerals (e.g. garnet) and magnetite. The sample contains ~30% quartz, 30% chlorite, 20% magnetite, 10% hematite, 10% carbonate and trace pyrite (Figure 11). Euhedral garnet (50 μm size) is intergrown with quartz and overprinted by magnetite and chalcopyrite (Figure 11B). Chlorite and hematite occur as fine-grained replacement of magnetite and garnet at grain boundaries and in a network of complex internal fractures within grains of garnet.

Sample 2066199 is a K-feldspar bearing calc-silicate rock taken from drill core WWDD1, ~12 km NWW of the Punt Hill prospect (Figure 6), at a depth of 683.8m. The sample was taken from within a 190 m intersection of sandstone/siltstone assigned to the Wallaroo Group. The Wallaroo Group interval in WWDD1 is characterized by interbedded layers of grey dolomite, light brown K-feldspar rich metasediment and green chlorite-rich metasediment at scales of ~1 cm thickness. The sample contains ~10% quartz, 20% K-feldspar, 20% chlorite, 9% hematite, 20% dolomite, 10% calcite and 11% accessory minerals including apatite, biotite, muscovite and rutile. The sample has two mineralogical zones, a K-feldspar and hematite-rich zone and a carbonate-rich zone separated by a ~500 μm hematite-rich band at the transition.

Dolomite grains (~200 μm) are overprinted by manganese-rich calcite (the latter containing dolomite inclusions (lower right hand corner of Figure 11D), and thence by K-feldspar with irregular embayed boundaries. K-feldspar contains numerous 10 μm scale inclusions of chlorite, quartz and apatite. In the left hand side of Figure 10D manganese-rich calcite nucleates on dolomite grains and exhibits space filling textures growing radially toward the centre of irregular shaped sub-millimetre cavities. Manganese-rich calcite is subsequently overgrown by manganese-poor calcite and then by TiS_2 which fills the centre of the cavity. The TiS_2 contains numerous inclusions of K-feldspar, dolomite and calcite with highly irregular grain boundaries (Figure 11D).



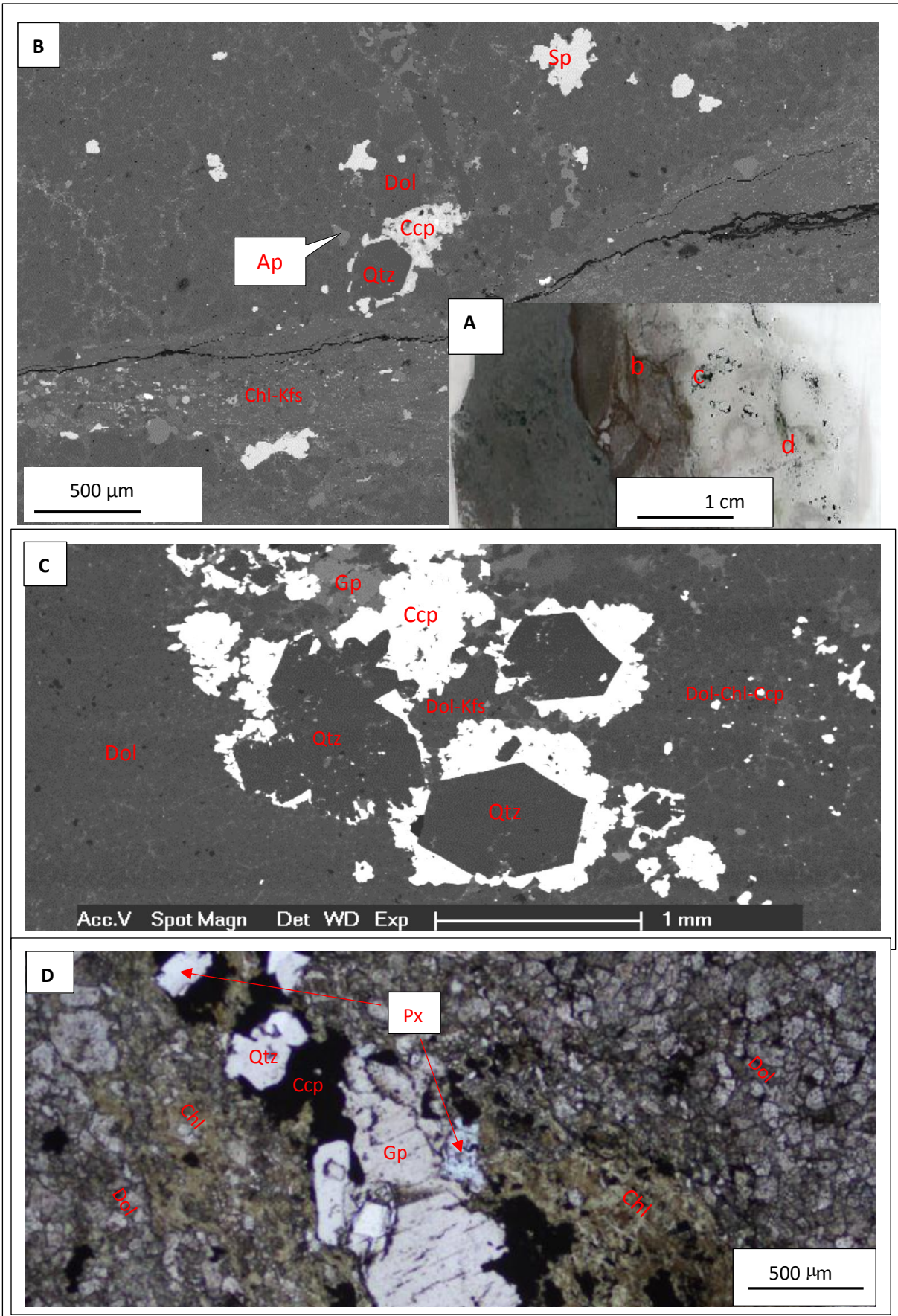


Figure 11 (page 40). Petrographic images from the calc-silicate metasedimentary samples 2066166 and 2066199. **A.** Photograph of the entire thin section of sample 2066166. Label b shows the location of figure 11B. Patchy, diffuse mineralogical zones are chlorite rich (olive green), carbonate-rich (pale) and magnetite-hematite rich (dark grey). **B.** Backscatter SEM image from location b in 2066166, see text for description. **C.** Photograph of the entire thin section of sample 2066199. Label d shows the location of Figure 11D. The thin section has two zones; K-feldspar and hematite-rich on the left hand side and carbonate-rich on the right hand side, with an ~500 μm hematite-rich area at the transition. **D.** Backscatter SEM image from location d in 2066199, see text for description. Mineral abbreviations: Ap = apatite, Cal= calcite, Cal(Mn) = manganese-rich calcite, Dol = dolomite, Grt = garnet, Chl = chlorite, Hem = hematite, Mag = magnetite, Ccp = chalcopyrite, TiS_2 = titanium disulfide.

Figure 12 (Page 41). Petrographic images from the calc-silicate metasedimentary sample 2066635. **A.** Photograph of the entire thin section. Labels b, c and d show the location of Figures 12B, 12C and 12D respectively. The sample has three zones: hematite-rich on the left hand side, K-feldspar and chlorite-rich breccia zone in the centre and a carbonate-rich zone on the right hand side. **B.** Backscatter SEM image from location (b) in Figure 12A. Lower half of the image is representative of textures from the central mineralogical zone and the upper half of the image is representative of the carbonate-rich zone. **C.** Backscatter SEM image from location (c) in Figure 12A showing detail of a quartz, gypsum and chalcopyrite 'patch'. **D.** Transmitted light photomicrograph from location (d) in Figure 12A centred on a pyroxene, gypsum, quartz and chalcopyrite vein with chlorite alteration selvage within the carbonate-rich zone. Mineral abbreviations as for Figure 11 with the addition of Gp = gypsum, Px = pyroxene, Sp = sphalerite.

Sample 2066635 is a hematite-altered calc-silicate which was taken from drill core IHAD6, located ~2 km north of Emmie Bluff prospect (Figure 6) at a depth of 855.8 m. The sample was taken from within a 38m wide intersection of carbonate-bearing metasedimentary rock assigned to the Wallaroo Group in the SARIG database. The entire Wallaroo Group interval in IHAD6 has a distinctive brown colour with variable abundance of chlorite, carbonate, mica and hematite. The sample contains ~25% quartz, 20% hematite, 20% dolomite, 10% K-feldspar, 15% chlorite and 10% accessory minerals including apatite, bornite and gypsum. The sample has three mineralogical zones (Figure 12A): a grey hematite-rich zone (left hand side of Figure 12A), a central zone exhibiting breccia textures and containing a mixture of K-feldspar, chlorite, hematite and carbonate and a pale carbonate-rich zone with minor chlorite and apatite (right hand side of Figure 12A). Narrow veins and irregular millimeter-scale 'patches' within the carbonate-rich zone contain pyroxene, gypsum, quartz and chalcopyrite and are surrounded by a selvage of chlorite which overprints interlocking dolomite grains in the carbonate matrix (Figure 12D). Well-formed euhedral quartz crystals occur in the centre of some of these patches and are surrounded by inclusion-rich chalcopyrite (Figures 12B and 12C). Sphalerite with space filling texture also occurs in ~100 μm scale patches. In the central zone fine-grained K-feldspar and chlorite, along with apatite, pyroxene and sulphide minerals (lower half of figure 12B) are texturally distinct from more coarse-grained dolomite bearing assemblages of the carbonate zone (upper half of Figure 12B). The hematite zone is near monomineralic with fine-grained interlocking hematite and no sulphide minerals.

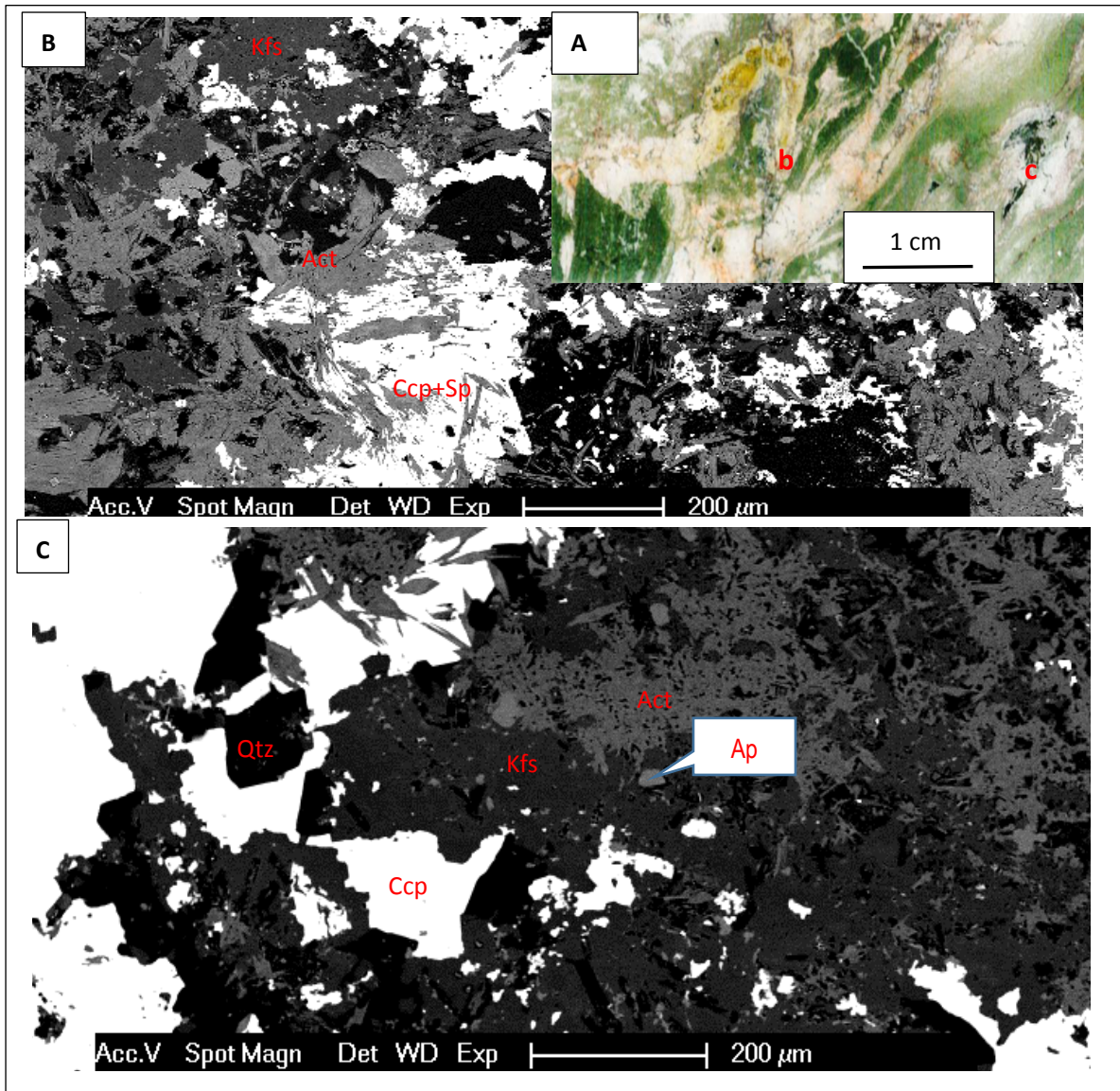


Figure 13. Petrographic images from the calc-silicate metasedimentary sample 2066203. **A.** Photograph of the entire thin section. Labels b, c show the location of Figures 13B and 13C respectively. Folded and faulted banding is defined by variable proportions of K-feldspar+hematite (pale brown), actinolite (dark green), chlorite (mid-green) and pyroxene (pale green). **B.** Backscatter SEM image from location (b) in Figure 13A. Randomly oriented actinolite blades are overprinted by K-feldspar, quartz and chalcopyrite, with mutual inclusions. **C.** Backscatter SEM image from location (c) in Figure 13A. Apatite, chalcopyrite and inclusion-rich K-feldspar overprint actinolite. Euhedral quartz grains exhibit space filling textures and are surrounded by coarse-grained chalcopyrite. Mineral abbreviations as for Figures 11 and 12 with the addition of Act = actinolite.

Sample 2066203 is a chlorite-altered calc-silicate sample which was taken from drill core GHDD4, located ~2 km SW of the Punt Hill prospect (Figure 6), at a depth of 854 m. The sample was taken from within a 155 m intersection of carbonate bearing metasedimentary rocks logged as “skarn” and assigned to the Wallaroo Group in the SARIG database. The drill core has a distinctive light grey and green colour due to an abundance of chlorite and carbonate. The

sample is composed of ~25% quartz, 20% chlorite, 15% K-feldspar, 15% actinolite, 8% calcite, 8% hematite, 3% pyroxene and 5% accessory minerals including apatite, pyrite, chalcopyrite and sphalerite. Discontinuous mineralogical banding at 3-5mm scale is defined by variable proportions of carbonate, calc-silicate minerals and hematite and is tightly folded and offset by microfractures (Figure 13A). Randomly oriented ~100 μm scale blades of actinolite are texturally overprinted by K-feldspar, quartz and sulphide minerals, including chalcopyrite (Figure 13B). K-feldspar, quartz and chalcopyrite all contain ~10 μm scale of inclusions of actinolite and have mutual overprinting relationships, each containing inclusions of the other two minerals (Figure 3B). In other parts of the sample (Figure 13C) K-feldspar and apatite overprint actinolite, with later euhedral quartz grains exhibiting space-filling textures and subsequently surrounded by coarse-grained inclusion poor chalcopyrite.

Granitic protoliths

Rocks identified as 'granite' within the SARIG database (see chapter 2.5.1) include a range of protoliths with varying mixtures of quartz and feldspar (granite to granodiorite) and varying degrees of alteration. Many of the identified granite protoliths contain significant proportions of carbonate minerals and iron-oxides, which are likely products of IOCG alteration. This variable mineralogy can create difficulty in distinguishing granite and calc-silicate protoliths. Thus, for the purposes of this study I deferred to the SARIG classification regardless of the intensity of alteration and sought to confirm that classification based on visual recognition of igneous textures (in some cases pseudomorphed by other minerals) and observed or inferred quartz, feldspar and biotite protolith mineralogy.

Sample 2066178 was taken from drill core HL002, located ~25 km SSW of Carrapateena deposit (Figure 6), at a depth of 529.2 m and within a 70 m intersection of granite assigned to the Donington Suite. Sample 2066178 is composed of ~35% quartz, 30% K-feldspar, 25% biotite, 5% plagioclase and 5% accessory minerals including chlorite, magnetite and pyrite (Figure 14A). At hand specimen scale the sample appears to be little effected by alteration. However, in thin section K-feldspar aggressively replaces biotite and relict plagioclase grains with complex, embayed grain boundaries. Minor magnetite occurs as ~50 μm grains included within K-feldspar. K-feldspar (along with biotite and plagioclase) is overprinted by fine-grained intergrown chlorite and hematite, with 50-100 μm size euhedral apatite occurring within the chlorite-hematite zones and at the grain boundaries of biotite (Figure 14B).

Sample 2066656 was taken from drillhole IHAD2, located ~ 1 km north of Emmie Bluff prospect (Figure 6), at a depth of 819.6 m, within a 134 m intersection of granite assigned to the Donington Suite in the SARIG database. The Donington Suite interval within IHAD2 contains abundant submillimetre-scale white mica, K-feldspar and hematite, cross cut by 1 mm carbonate veinlets, giving the rock a distinctive mottled white and brown appearance. The sample contains ~20% quartz, 20% muscovite, 20% K-feldspar, 15% hematite, 10% chlorite, and 5% ilmenite (Figure 14C). Fine-grained (<10 μm) intergrown randomly oriented muscovite and hematite combine to produce pale brown/orange patches in the thin section. Within zones of muscovite, hematite alteration ilmenite grains of ~200 μm size (potentially a magmatic

mineral in Donnington Suite granites) are aggressively replaced by hematite, with ragged grain boundaries (Figure 14D).

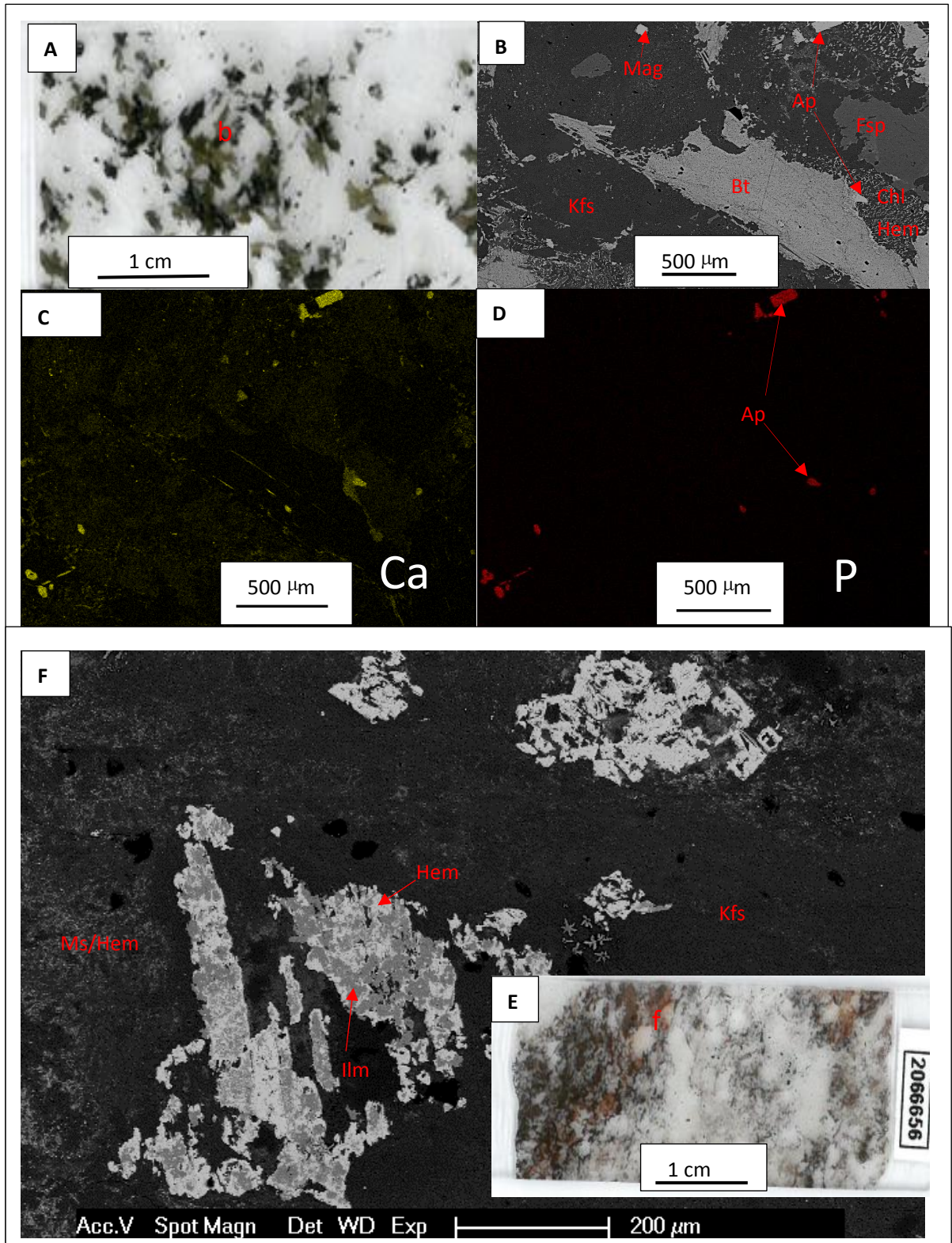


Figure 14 (previous page). Petrographic images b shows the location of Figures 14B. The coarse-grained green mineral is biotite, pale zones contain quartz, K-feldspar and lesser plagioclase. **B.** Backscatter SEM image from point b in sample 2066178. **C.** Ca element map showing the same field of view of Figure 14B. **D.** P element map showing the same field of view of Figure 14B. **E.** Photograph of the entire thin section of sample 2066656. Label f shows the location of Figures 14F. Areas of intense muscovite-hematite alteration are coloured brown to orange. **F.** Backscatter SEM image from location f in Figure 14E. Hematite aggressively replaces ilmenite. Mineral abbreviations as for Figures 11, 12 and 13 with the addition of Bt = biotite, Fsp = Feldspar, Ilm = ilmenite, Ms = Muscovite.

Sample 2066174 was taken from drill core PSC4_SASC2, located ~10 km NWW of Carrapateena deposit (Figure 6), at a depth of 539.5 m. The sample was taken from within a 29.5 m intersection of granodiorite assigned to the Donington Suite in the SARIG database. The Donington Suite interval within PSC4_SASC2 is composed dominantly of quartz, white mica, chlorite and hematite, cross cut by K-feldspar veinlets and dolomite veins, giving the rock a distinctive mottled pink and green-grey appearance. Sample 2066174 is comprised of ~30% quartz, 15% K-feldspar, 10% biotite, 20% chlorite, 15% dolomite, 5% hematite and 5% apatite. The sample is centred on a 2mm wide hematite-rich alteration zone, this zone occurs within a 2.5cm wide zone where fine-grained chlorite and hematite incompletely replace K-feldspar (Figure 15). This zone gives way to a zone of less intense chlorite alteration at the margins of the sample. These alteration zones are cross cut by a ~1mm wide dolomite vein with a selvage of elongate apatite crystals exhibiting space filling textures on the vein wall.

Sample 2066169 was taken from drill core DRD1, located ~40 km north of Emmie Bluff prospect (Figure 6), at a depth of 1139.4 m and within a 121 m wide intersection of granite assigned to the Donington Suite in the SARIG database. The entire interval of granite in DRD1 contains abundant submillimetre-scale chlorite and white mica in roughly equal proportions, cross cut by numerous hematite-rich veinlets and alteration zones, giving the rock a distinctive mottled green and orange appearance. Sample 2066169 is composed of ~20% quartz, 5% feldspar, 5% muscovite, 35% chlorite, 30% hematite and 5% pyrite. The sample is centred on an irregular centimeter-scale mass of mixed pyrite and hematite (Figure 16A). Millimetre-scale pyrite grains in this mass are completely mantled by inclusion-rich hematite and contain 10-50 μm sized chalcopyrite grains along internal fractures. Quartz grains at the margins of the sulphide-hematite masses have euhedral form, with well-faceted projections facing radially inward toward the mass. These textures imply a close genetic relationship between hematite and pyrite and are reminiscent of reaction rims between porphyroblasts and wall rocks in metamorphic settings.

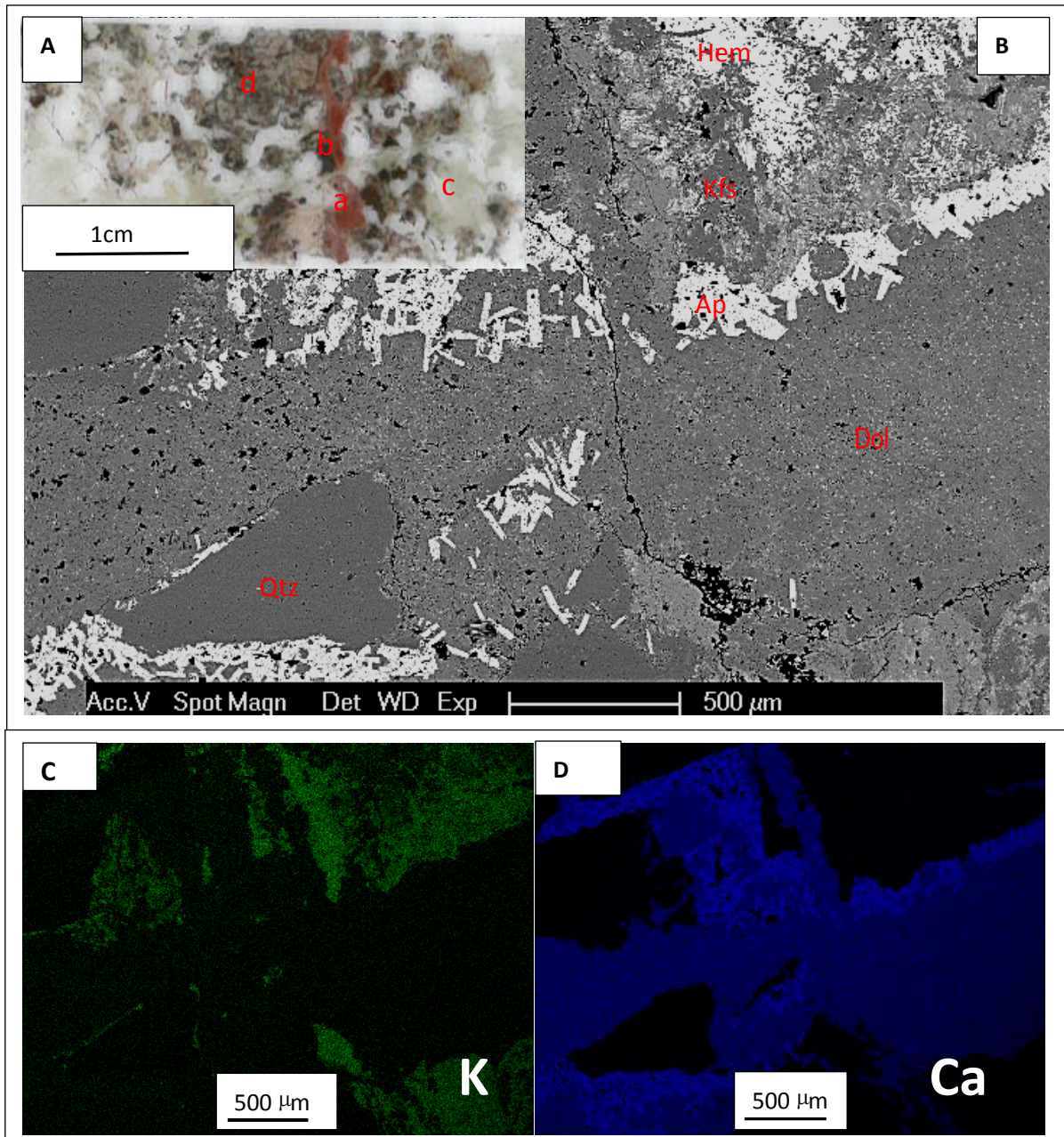


Figure 15. Petrographic images from the granite protolith sample 2066174. Points of a, b are dolomite vein fault K-feldspar, K-feldspar fault hematite respectively, c and d are chlorite and mica alteration respectively. **A.** Photograph of the entire thin section. Label b shows the location of Figure 15B. Narrow hematite-rich zone is surrounded by hematite-chlorite and weak chlorite alteration zones. **B.** Backscatter SEM image located at b in Figure 15A. Fine-grained hematite and chlorite overprint K-feldspar and are cross cut by a ~1mm wide dolomite vein with apatite selvage. **C.** K element map showing the same field of view as Figure 15B and highlighting the distribution of K-feldspar (overprinted by fine-grained chlorite and hematite) in the wall rock of the dolomite vein. **D.** Ca element map showing the same field of view as Figure 15B and highlighting the late dolomite vein with apatite selvage.

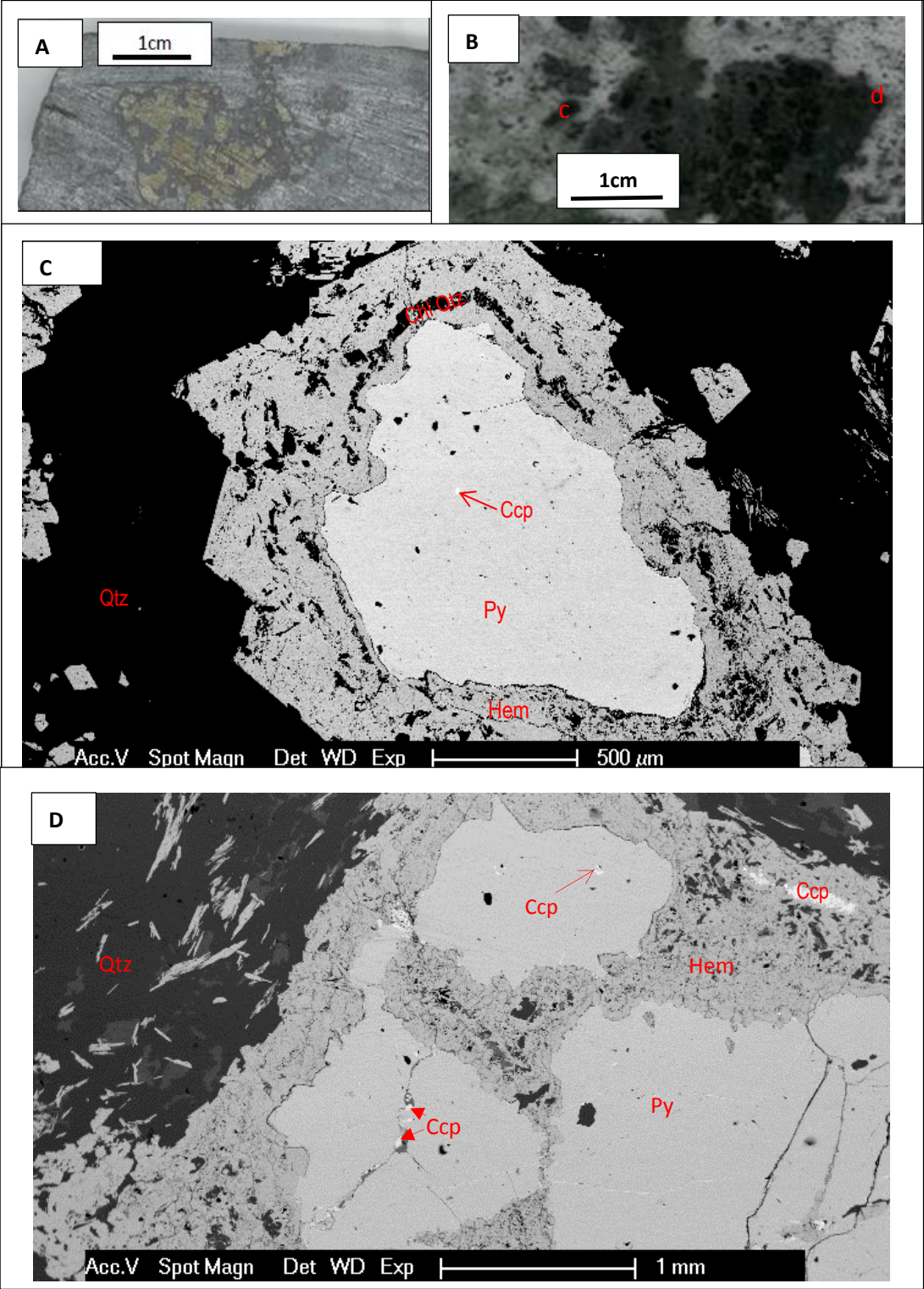


Figure 16 (previous page). Petrographic images from the granite protolith sample 2066169. **A.** Hand specimen of quarter drill core from which the thin section was made. **B.** Photograph of the entire thin section. Labels c and d show the location of Figures 16C and 16D respectively. The central part of the thin section features an irregular centimeter-scale zone of millimeter sized sulphide minerals completely enclosed by hematite. **C.** Backscatter SEM image located at c in Figure 16B. Well-faceted quartz grains at the margins of the sulphide-hematite mass project inward. Hematite contains numerous quartz inclusions arranged in concentric rings. Pyrite-hematite grain boundaries are irregular and embayed consistent with disequilibrium between these phases. **D.** Backscatter SEM image located at d in Figure 16B. Textures are comparable to Figure 16C with the additional observation of hematite needles within the wall rock and location of fine grained chalcopyrite associated with the hematite 'mantle' of the sulphide-hematite mass and within microcracks within pyrite.

Mafic protoliths

The 'mafic' protolith grouping in SARIG includes varying mixtures of amphibolite at varying metasomatic grade. Many mafic protolith samples contain significant proportions of carbonate minerals and iron-oxides, which may represent combinations of primary amphibolite mineralogy and alteration. Variable proportions of carbonate, reaching abundance comparable to samples recognised as calc-silicate rocks, demonstrates a continuum between mafic and calc-silicate protolith end-members. For the purposes of this study samples included in the mafic grouping were consistent with original visual logging recorded in SARIG, with additional confirmation attained by visual recognition of igneous textures and mafic mineralogy by the author.

Sample 2066177 was taken from drill core HL002 (the same drillhole as sample 2066178), located ~25 km SSW of Carrapateena deposit (Figure 6), at a depth of 471.2 m. The sample was taken from within a 0.45m intersection of mafic intrusive rock, logged as amphibolite and assigned to the Donington Suite. The interval contains abundant chlorite and amphibole, cross cut by complex carbonate and hematite veins. The sample is composed of ~30% chlorite, 20% calcite and 50% of fine-grained intergrown amphibole, hematite, quartz, and K-feldspar (Figure 17). The bulk of the sample is dominated by fine-grained chlorite which overprints and replaces minor relict quartz, pyroxene and garnet. The complex veins contain calcite, dolomite, hematite, pyroxene, K-feldspar, biotite and traces of rutile, gypsum and apatite. (Figure 17).

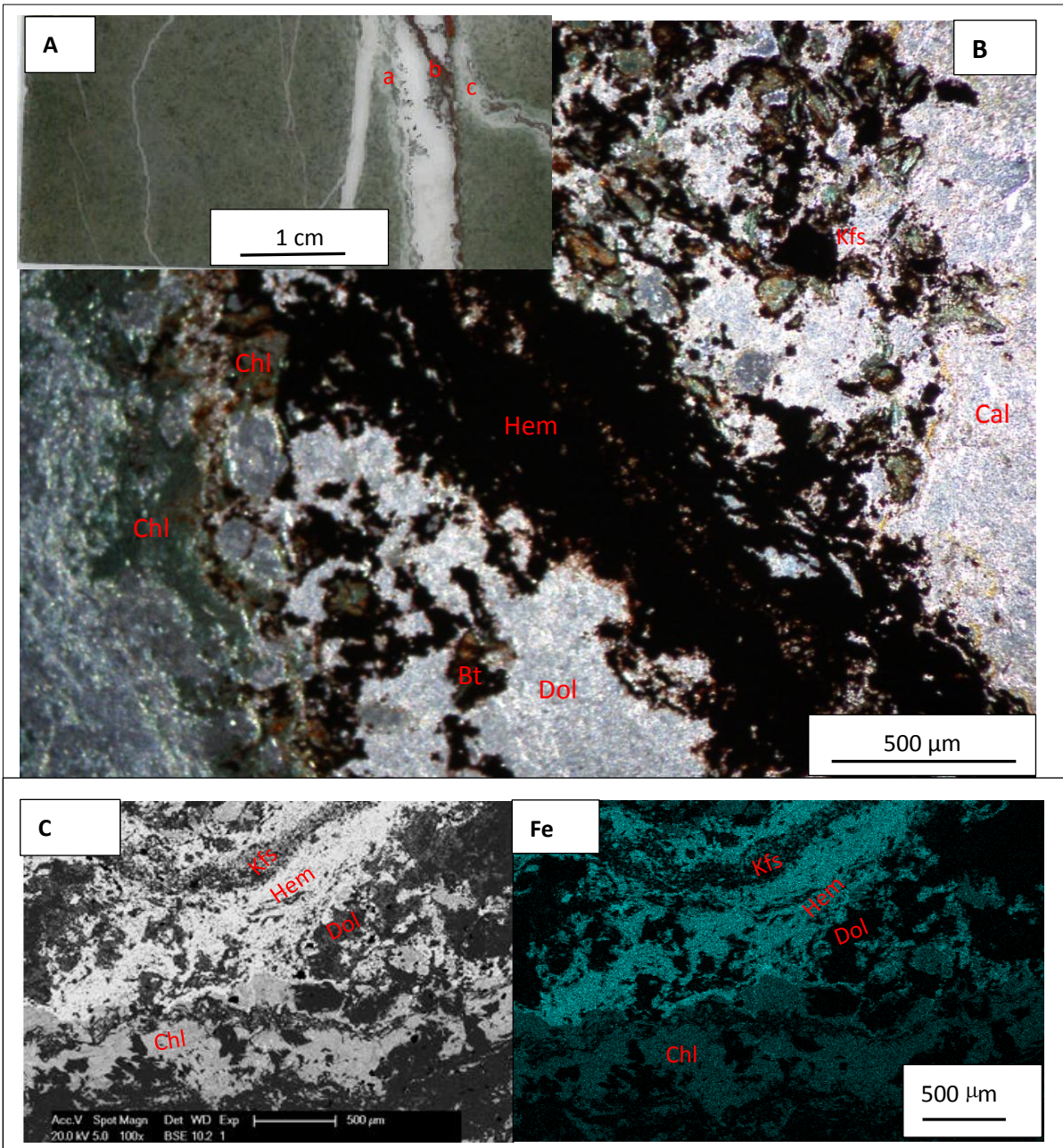


Figure 17. Petrographic images from the mafic protolith sample 2066177. **A.** Photograph of the entire thin section. Labels b and c show the location of Figures 17B and 17C respectively. Labels a, b and c are carbonate vein, hematite vein and boundary between calcite and amphibole respectively. **B.** Transmitted light photomicrograph from the margin of a carbonate-hematite vein at location b in Figure 17A. **C.** Backscatter SEM image from location b. **D.** Fe element map of the same location. Note that Figure 17C and 17Fe are rotated 90° counter-clockwise in comparison to Figure 17B.

2.6 DISCUSSION

2.6.1 Interpreted petrogenesis

Siliciclastic metasedimentary protoliths

Interpreted paragenesis for the two metasedimentary protolith samples 2066641 and 2066655 is summarised in Figure 18. There is little evidence of primary minerals or mineral textures in either of these highly altered rocks. Quartz grains are the most likely relicts of the sedimentary mineralogy and the smaller grain size of quartz in 2066641 compared to 2066655 might reflect grain sizes in the protolith rock - 2066641 coming from a Wallaroo Group sequence logged as metasediments and 2066655 from metasandstone.

Textural evidence in 2066641 (Figure 9) is consistent with intense Fe-K-metasomatism involving mobilization of silica. The fine-grained hematite+K-feldspar+chlorite-rich domain is cross cut by numerous hematite veins varying in width from 200 μm to $<10 \mu\text{m}$. Larger veins bifurcate into smaller veins. Although having a preferred orientation (top left to bottom right in Figure 9B) the smaller veins have contorted geometry, wrapping around boundaries of 10s of micron scale quartz grains. This implies a transition from high fluid/rock ratio fracture controlled (larger hematite veins) to pervasive grain-scale fluid flow (resulting in pervasive hematite, K-feldspar and chlorite alteration in the matrix) during the same alteration event. In this context, the hematite-rich domain in this sample does not necessarily represent a second, overprinting alteration event but rather a zone of higher fluid/rock ratio within the same alteration event. The irregular, elongate quartz blebs within the hematite+K-feldspar+chlorite-rich domain illustrate that silica was a mobile phase during this period of alteration. The form of the quartz 'blebs' quartz is not consistent with deposition in crack-seal veins but rather deposition within cavities created by dissolution of pre-existing minerals. Manganite and quartz veins cross cut hematite veins at a high angle and represent the final paragenetic stage in this sample.

Sample 2066655 exhibits intense chlorite alteration and brecciation with quartz filling cavities between angular breccia clasts (Figure 10A). Approximately 1mm sized, euhedral grains with 90° crystal faces occur within a 1cm sized breccia clast and have been pseudomorphed by K-feldspar and hematite (lower left of Figure 10B) and fine-grained mixtures of hematite and chlorite (Figure 10B). I interpret that selective hematite alteration within these grains indicates a Fe-rich precursor mineral, likely to be pyroxene. The spaces between these grains comprise a mixture of quartz, K-feldspar, pyrite and magnetite which are overgrown and replaced at grain boundaries by fine-grained chlorite (and lesser hematite). Texturally equivalent fine-grained chlorite also mantles the hematite and chlorite pseudomorphs. Chalcopyrite occurs within masses of fine-grained chlorite and at pyrite-grain boundaries. Distinctive ring textures in the chlorite-rich matrix of the breccia (Figure 10C) are reminiscent of reaction rims formed around porphyroblasts in metamorphic rocks and are interpreted to be evidence of disequilibrium between the core phase (chalcopyrite) and fluids within the matrix of the rock. Chalcopyrite within the core contains numerous inclusions of quartz and chlorite with comparable grain size to material in the surrounding matrix. In contrast the complex, embayed outer margin of the chalcopyrite demonstrates that the sulphide mineral

was destabilized during a later phase of chlorite alteration. The outer rim of hematite exhibits space filling textures consistent with nucleation on the matrix wall and growth toward the center of the ring. These textures indicate a paragenesis in which chalcopyrite post-dated a significant phase of chlorite alteration and in turn was post-dated and remobilized by a phase of chlorite+hematite alteration. Similar textures have recently been reported from the Emmie Bluff prospect by Uvarova et al. (2018) and interpreted to be the result of reaction with a late, oxidized and Cl-rich fluid which dissolved chalcopyrite and resulted in local deposition of the Cu-chloride mineral atacamite.

In combination the observations from 2066641 and 2066655 are consistent with three main stages of alteration (Figure 18). The first stage (quartz, K-feldspar, magnetite, pyrite stable) is only evident in 2066655. The second stage is dominant in both samples and includes abundant chlorite and hematite. Chalcopyrite is associated with this stage and appears relatively late in the paragenesis (contains chlorite inclusions). I have grouped chlorite and hematite, which post-dates chalcopyrite in 2066655, and late-paragenetic manganite and quartz in 2066641 into Stage 3 (effectively “post-mineralisation”). However there are no specific timing constraints minerals occurring in the different samples.

















Minerals	Protolith*	Stage1	Stage2	Stage 3
Quartz				
K-feldspar				
Magnetite				
Pyrite				
Chlorite				
Hematite				
Apatite				
Chalcopyrite				
Manganite				

Figure 18. Composite paragenetic summary for metasedimentary samples 2066641 (blue) and 2066655 (red).

Calc-silicate protoliths

The interpreted paragenesis of the four calc-silicate protolith samples is summarised in Figure 19. A consistent theme of the paragenesis is that dolomite, anhydrous calc-silicate minerals (including garnet, pyroxene and actinolite) and anhydrite occur early in the paragenesis (High T Skarn stage) and are overprinted; firstly by a combination of quartz, calcite, K-feldspar, chlorite, apatite, magnetite and various sulphide minerals (Stage 1) and secondly by a combination of chlorite and hematite (Stage 2). Textures in all samples are consistent with aggressive, although incomplete, replacement of pre-existing minerals along grain boundaries and internal fractures, dissolution of pre-existing phases with later phases exhibiting space-filling textures and focused fluid flow in veins.





















Minerals	Protolith*	High T skarn	Stage1	Stage 2
Dolomite				
Quartz				
Garnet				
Pyroxene				
Actinolite				
Calcite (Mn)				
K-feldspar				
Apatite				
Magnetite				
TiS ₂				
Chalcopyrite				
Sphalerite				
Gypsum				
Hematite				
Chlorite				

Figure 19. Composite paragenetic summary for calc-silicate metasedimentary samples 2066166 (blue), 2066199 (red), 2066635 (green) and 2066203 (orange).

I interpret the zoning in sample 2066635 (Figure 12) to be an alteration front recording the interaction of a Fe-K-rich fluid with a dolomite dominated metasedimentary rock. The carbonate zone in this sample is dominated by 50 - 100 µm interlocking grains of dolomite, with small patches and veinlets of gypsum, pyroxene, quartz and sulphide minerals (including chalcopyrite and sphalerite) surrounded by millimeter-scale zones of chlorite alteration. Sulphide-rich ‘patches’ (Figures 12B and 12C) commonly contain well-faceted euhedral quartz crystals surrounded by a moat of sulphide. These textures are reminiscent of daughter crystals grown in fluid inclusions and are interpreted here to indicate that the quartz and sulphide were deposited in a cavity produced by dissolution of a pre-existing (carbonate) phase. The brecciated central zone of this sample is more intensely overprinted by fine-grained chlorite,

K-feldspar and hematite, with partial destruction of the pre-existing interlocking dolomite textures. Compositional banding in this zone (which is highlighted by variable proportions of alteration minerals) is interpreted to be sedimentary. The hematite zone is close to monomineralic with complete destruction of pre-existing textures and compositional banding.

Space-filling, dissolution – precipitation textures are also characteristic of the sulphides present in 2066199 (TiS₂) and 2066203 (chalcopyrite). Such textures are common in skarn mineral systems, in which acidic hydrothermal fluids destabilize and locally dissolve pre-existing carbonates, stabilize calc-silicate minerals and/or iron oxides and deposit sulphides (Uvarova et al., 2018). The characteristic of skarn deposits to display early high-temperature phases (\pm magnetite), overprinted by lower temperature, hydrous phases (\pm hematite) (Ismail et al., 2014) is also comparable to the paragenesis observed here.

Granite protoliths

The interpreted paragenesis of the four granite protolith samples is summarised in Figure 20. All of the granite samples display preservation of protolith textures with 200 to 500 μ m interlocking quartz, biotite and feldspar grains – the latter variably altered by combinations of hematite, chlorite and muscovite. I also interpret relict ilmenite in sample 2066656 as a protolith phase. Ilmenite is a common accessory in granites of the Donnington Suite (Reid et al., 2011)).

K-feldspar is both a magmatic protolith phase and an alteration phase in these samples. In 2066178 K-feldspar (plus minor magnetite) replaces biotite and plagioclase, with plagioclase persisting as relict cores and inclusions within second stage K-feldspar (Figure 20B). Minor fine-grained intergrown chlorite and hematite, accompanied by apatite, overprints hydrothermal K-feldspar in 2066178. In sample 2066656 K-feldspar is the only remaining feldspar phase and locally is overprinted by fine-grained muscovite, hematite and chlorite. Ilmenite in these parts of the sample is aggressively replaced and pseudomorphed by hematite.

The unusual pyrite+hematite masses in sample 2066169 have comparable textures to the above mentioned sulphide ring structures in sample 2066655. In the case of 2066169 irregular masses of millimeter-scale pyrite grains are completely mantled by fine-grained hematite with numerous inclusions of quartz and chlorite. In Figure 16C, quartz with inward-projecting space-filling textures occurs at the margin of the pyrite-hematite mass. Chalcopyrite occurs within the hematite mantle, at the grain boundaries of pyrite and within internal fractures of the pyrite. These textures are consistent with pyrite being an early paragenetic phase with a reaction rim forming at the pyrite margins (pyrite being replaced by hematite with coincident chalcopyrite deposition). Chlorite and hematite alteration within the matrix of 2066169 are interpreted to be part of the same alteration event.

In addition to Fe and K metasomatism in the form of K-feldspar, hematite and chlorite, sample 2066174 provides an example of carbonate alteration of a granite protolith. The latest paragenetic stage in this sample is a dolomite vein, with apatite selvages) which clearly cross cuts an earlier hematite alteration zone (Figure 15). The carbonate and phosphate components of this vein must have been sourced external to the granite. Nearby highly altered carbonate

rocks with ample evidence of dissolution provide a potential source for these components in the fluid.









Minerals	Protolith*	Stage 1	Stage 2	Stage 3
Quartz				
K-feldspar				
Plagioclase				
Biotite				
Ilmenite				
Magnetite				
Pyrite				
Chlorite				
Hematite				
Muscovite				
Apatite				
Chalcopyrite				
Dolomite				

Figure 20. Composite paragenetic summary for granite samples 2066178 (blue), 2066656 (red), 2066174 (green) and 2066169 (orange).

From the combination of these observations I interpret the alteration petrogenesis in the granites to consist of four stages; magmatic, with variably preserved quartz, K-feldspar, plagioclase, biotite and ilmenite; Stage 1, dominated by K-feldspar but also including magnetite and possibly pyrite; Stage 2, characterized by widespread chlorite, hematite and muscovite alteration and including chalcopyrite and; Stage 3 late carbonate veining (Figure 20).

Mafic protolith

In comparison to the other samples examined here, the paragenetic sequence in the mafic sample 2066177 is relatively simple. The standout feature of this sample is intense chlorite alteration. I interpret relict quartz and amphibole in the sample matrix to be earlier phases. These are potentially magmatic and/or metamorphic phases and I make no attempt to differentiate between those options. The complex, multi-mineralic veining in this sample is dominated by carbonate minerals (both dolomite and calcite) but also includes hematite, K-feldspar, pyroxene, biotite and chlorite. Chlorite occurs along the vein margins, in with a transition to pervasive chlorite alteration in the matrix. This relationship suggests that carbonate veining was synchronous with chlorite alteration. Pyroxene and biotite are concentrated toward the vein margins and I interpret them to be the result of partial equilibration of the vein fluid with wall rocks. Thus the observations from 2066177 are consistent with one stage of veining and alteration. In Figure 21, I have labelled this “Stage 2” alteration because the intense chlorite alteration and presence of hematite cut through calcite to “Stage 3” alteration from the metasedimentary, calc-silicate and granite protoliths.

Minerals	Protolith*	Stage1	Stage2	Stage 3
Quartz	■			
Amphibole	■			
Calcite			■	
Dolomite			■	
Pyroxene			■	
Biotite			■	
Hematite				■
Chlorite			■	
K-feldspar			■	

Figure 21. Paragenetic summary for the amphibolite sample 2066177.

2.6.2 Summary and alteration stages

Multiple, overprinting paragenetic relationships and unusual alteration textures in four contrasting protolith rocks from the central eastern Gawler Craton can be interpreted within the framework of five paragenetic stages, with characteristic mineral assemblages summarized as follows:

Protolith assemblages

Mineral assemblages identified as being inherited from the protolith rock were interpreted here on the basis of:

1. They are the first group of minerals in the paragenetic sequence;

2. They have textures consistent with those expected in the inferred protolith rock, and;
3. They are consistent with mineral assemblages expected from the inferred protolith rock.

The minerals which fulfil these requirements were different for the four protolith rock types examined these were:

Quartz and K-feldspar and siliciclastic metasedimentary rocks, quartz, K-feldspar, plagioclase, biotite and ilmenite in granites, dolomite in calc-silicate rocks and quartz and amphibole in mafic rocks.

Skarn assemblages

Skarns are rocks rich in calc-silicate minerals including garnets, pyroxenes, amphiboles and epidote. In this study skarn assemblages occur only in calc-silicate protoliths. Skarn minerals include quartz, garnet, pyroxene and actinolite. In 2066166 garnet intergrown with quartz are the earliest minerals in the paragenesis. In 2066203 pyroxene and quartz are the earliest minerals in the paragenesis but are overprinted by actinolite, demonstrating that 'skarn' alteration can involve multiple stages. In 2066635 pyroxene occurs as a vein mineral associated with chlorite alteration of a dolomite-rich protolith. In this case the skarn mineral occurs relatively late in the paragenesis. These observations suggest that there is no particular skarn stage of alteration but that skarn minerals form due to processes that could occur over a range of conditions at different stages of the paragenesis.

Einaudi et al. (1981) discuss three processes for the formation of skarn mineral assemblages; metamorphism of impure carbonate rocks, diffusion metasomatism between rocks of contrasting mineralogy (typically silica-rich and carbonates) and reaction between silica-rich (and often iron-rich) hydrothermal fluids and carbonate rocks. Skarn mineral deposits are most often formed by the latter process. In these deposits skarn mineral assemblages are strongly influenced by rock and fluid chemistry (importantly the concentration of CO₂) which can lead to the formation of anhydrous, calc-silicate minerals over a range of temperatures and pressures. Ismail et al. (2014) describe skarn assemblages similar to those observed here (garnet, pyroxene, actinolite with the addition of clinozoisite) at the Hillside IOCG prospect on the Yorke Peninsular in South Australia. Ismail et al. (2014) interpreted such assemblages to be part of a multistage fluid/rock system which evolved from temperatures of ~660°C (garnet and pyroxene), through decreasing temperatures (actinolite and clinozoisite) to a post-skarn ore deposition phase estimated to occur at a temperature of ~100°C.

Overprinting of dolomite-rich protolith rocks by iron bearing calc-silicates (garnet, pyroxene and actinolite) in this study is consistent with alteration by a silica and iron-rich hydrothermal fluid.

Stage 1: K-feldspar+magnetite+chlorite assemblages

This stage is characterized by K-feldspar and magnetite assemblages in all protolith types, with the addition of chlorite as a major alteration mineral in calc-silicate rocks. K-feldspar and magnetite alteration is evident in granite protoliths even when there is little visual evidence of

alteration at hand-specimen scale (e.g. sample 2066178). In calc-silicate rocks chlorite occurs in close association with K-feldspar (e.g. 2066199) and as an alteration product of pre-existing iron-bearing calc-silicate minerals (e.g. 2066166). Magnetite occurs in abundances of ~ 1 to 20 %, which are relatively low compared to hematite associated with Stage 2 alteration (see below). Pyrite is the dominant sulphide phase but there is also minor chalcopyrite.

K-feldspar, magnetite and chlorite bearing assemblages in this study correspond to the MB and CAM styles of alteration described by Skirrow et al. (2002). Skirrow et al. (2002) described that CAM (350-550°C) having calc-silicate-alkaline feldspar -magnetite and MB having magnetite-biotite ±Cu-Au minerals. MB and CAM were major mineralisation in some case (Porter, 2010; Barton et al., 2010) are consistent with Skirrow et al. 2002).

Bastrakov et al. (2007) also identified these styles of alteration in the central eastern Gawler Craton and attributed a generation of high-salinity 'Type C' fluid inclusions to this phase of alteration. Type C fluid inclusions contained multiple daughter minerals (including, halite, iron-oxides and silicates), high concentrations of Fe, K and Cu (up to percent levels) and decomposition temperatures of ~450°C.

These data are consistent with K-feldspar, magnetite and chlorite alteration occurring as the result of infiltration of a relatively high temperature (>400°C) and relatively reduced (magnetite and pyrite stable) fluid.

Stage 2: Hematite+chlorite+muscovite assemblages

Summary observations

This stage is characterized by locally intense chlorite, hematite and muscovite alteration. Muscovite is abundant in the granite protoliths and rare in the other rock types, whereas chlorite and hematite are ubiquitous. Some altered rocks are dominated by hematite and it is a common vein mineral. Chalcopyrite mineralization is most commonly associated with Stage 2 and occurs in four paragenetic scenarios:

1. Filling voids in carbonate rocks along with quartz, gypsum and pyroxene. (Sphalerite also occurs in this context) (e.g. 2066635).
2. At grain boundaries and within internal fractures if pre-existing pyrite (e.g. 2066655, 2066169).
3. As sub-millimeter grains within intergrown hematite and chlorite alteration zones (e.g. 2066635)
4. At the center of complex ring structures, in which the chalcopyrite both overprints previously chlorite alteration and is in turn overprinted (and dissolved at its margins) by later chlorite and hematite (e.g. 2066655).

Hematite, chlorite and muscovite bearing assemblages in this study correspond to the HSCC style of alteration described by Skirrow et al. (2002). Skirrow et al. (2002) described that HSCC contained hematite-sericite- chlorite-carbonate ± Cu- Au-U minerals at <300°C. These HSCC may overprinted the CAM (350-550°C) and MB. Skirrow et al. (2002) described that HSCC overprinted CAM and MB in Moonta-Wallaroo and Mt Woods Inlier; and HSCC

overprinted CAM (calc-silicate -K-feldspar-muscovite-apatite).

Hematite-chalcopyrite-pyrite \pm chlorite-carbonate assemblage observed in hematite alterations showed that chalcopyrite mineralisation (Bastrakov et al., 2007; Xavier et al., 2010). More oxidized (hematite vs magnetite) occurred at a lower temperature <300°C.

My observations are consistent with those of Skirrow et al. (2002) (Gow et al., 1994 and 1996; Bastrakov et al., 2007) and I interpret that stage 2 alteration involved the infiltration of a relatively oxidized (hematite vs magnetite stable), lower temperature fluid than stage 1 alteration. Although hematite replacement of magnetite is commonly observed (e.g. 2066166), the occurrence of abundant magnetite in the protolith or in previous alteration assemblages is not a pre-requisite of hematite alteration. Sample 2066635 provides an example of intense hematite alteration of a carbonate protolith without pre-existing magnetite - or indeed any pre-existing Fe-rich phase. These observations demonstrate that significant amounts of iron were introduced during Stage 2 alteration - the presence of hematite is a reflection of Fe-metasomatism and the relative abundance of hematite is a measure of high fluid-rock ratios.

Although sulphide minerals including chalcopyrite are commonly associated with Stage 2 alteration, intense Stage 2 alteration can occur without sulphide minerals (e.g. 2066641, 2066656). This is consistent with hydrothermal fluids that contain the elements necessary for sulphide mineralisation (Fe, Cu and S), for example the Type C fluids described by Bastrakov et al. (2007), but for which sulphide saturation only occurs in specific circumstances. The four paragenetic scenarios for chalcopyrite suggest that these specific circumstances include; solution-precipitation reactions between the hydrothermal fluid and carbonate protoliths; reactions between the hydrothermal fluid and pre-existing sulphur bearing phases (particularly pyrite); transient periods of sulphide stability within the fluid-rock evolution which correspond to the transition from magnetite to hematite stable redox conditions.

Stage 3: Final stage (post-mineralisation) assemblages

These assemblages include hematite, chlorite, quartz, manganite, dolomite and apatite, commonly occurring as veins which overprint pre-existing mineral assemblages. In samples which contain sulphide minerals Stage 3 assemblages post-date the sulphides. In samples without sulphide minerals Stage 3 assemblages post-date hematite-chlorite alteration.

An interesting aspect of the paragenesis presented here is that hematite and chlorite occur broadly synchronous with sulphides (in Stage 2 assemblages) and also post-date sulphide mineralization - sometimes in the same sample (Figure 10C, 2066655). Dissolution of chalcopyrite at grain boundaries and deposition of chlorite and hematite demonstrates that the late-stage hydrothermal fluid was capable of remobilizing copper. The presence of intense hematite alteration (without sulphide mineralization) adjacent to less intense hematite+chlorite alteration of carbonate (with sulphide mineralization) in sample 2066635, suggests that the same fluid could be responsible for both sulphide deposition and remobilization. Close to the boundary of intense Fe-metasomatism sulphides are deposited as a result of solution-precipitation reactions, but with more intense alteration and oxidization the sulphide minerals are unstable. This suggests that post-mineralisation assemblages may not post-date

mineralization by a long period of time, but rather might represent the evolution of the hydrothermal fluid immediately subsequent to the mineralizing phase.

This is similar to the late stage paragenesis described at Emmie Bluff by Uvarova et al. (2018). Uvarova et al. (2018) interpreted chalcopyrite dissolution, associated with late Mn-rich chlorite, and local precipitation of the Cu-chloride mineral atacamite to be the result of the infiltration of late-stage highly oxidized fluids.

2.6.3 Nature of the hydrothermal fluids

The paragenetic stages discussed above suggest a broad evolution from higher temperature, more reduced (magnetite stable) alteration to lower temperature, and more oxidized (hematite stable) alteration over time. This could be achieved in three ways: 1) Evolution of the same hydrothermal fluid, from hotter and reduced to cooler and oxidized, as it migrated through the crust. Cooling might simply have been a function of transport from deeper hotter rocks toward shallower, cooler rocks. Oxidisation might have occurred via interaction with oxidized rocks and/or fluids, however simple cooling could also be responsible for the fluid crossing the magnetite-hematite redox buffer. 2) Variable mixing of a hotter, reduced fluid with a cooler, oxidized fluid. 3) Separate hydrothermal fluids, not interacting, but overprinting the same volume of rock with the cooler, oxidized fluid consistently post-dating the hotter, reduced fluid.

Bastrakov et al. (2007) identified three types of fluid inclusions in their study of alteration in the eastern Gawler Craton. Type A are vapour-rich high temperature fluid inclusions, Type B are medium to low temperature liquid vapour inclusions and Type C are high-temperature hypersaline, multiphase fluid inclusions. Type A and C inclusions were documented within magnetite-bearing assemblages at Titan (BD1), Torrens (TD2), and Emmie Bluff (SAE7). Type A and type C inclusions survive in quartz grains overprinted by hematitic assemblages (e.g. Torrens). Type B inclusions are ubiquitous in association with hematitic assemblages but also occur as trails of secondary inclusions in quartz of magnetite-bearing assemblages. Bastrakov et al. (2007) described that fluid inclusion temperature type B <300°C and Type C in microthermometric studies, complete homogenization was not attained and decrepitated at temperatures $\geq 400^\circ\text{C}$.

Even though the fluids associated with Stage 1 alteration had high copper - they didn't result in abundant copper mineralization. I interpret that the physical conditions associated with Stage 1 alteration were such that copper was soluble and remained in the fluid phase. In contrast, fluids associated with extensive hematite alteration, and commonly containing copper bearing minerals, do not contain high concentrations of copper. I interpret that the physical conditions associated with hematite alteration resulted in low copper solubility and the precipitation of copper into solid phases.

An alternative to the fluid mixing ore deposit model of Haynes (1995) and the upgrading model of Bastrakov et al. (2007) is that the various stages of alteration presented here were the result of the evolution of the same fluid. The fluid began as a high temperature ($>450^\circ\text{C}$), hypersaline, reduced fluid with percent level concentrations of Fe, K and Cu. This fluid

produced widespread Fe-K-metasomatism manifest as K-feldspar and magnetite assemblages but only low grade Cu-mineralisation. As the fluid cooled, it crossed the magnetite-hematite buffer resulting in deposition of voluminous hematite, which has low solubility in hydrothermal fluids compared to magnetite. This redox reaction resulted in co-precipitation of sulphide minerals (Cleverley and Oliver, 2005) close to the magnetite-hematite buffer. The evolving fluid would have lower overall salinity and decreased concentrations of Cu, S, Fe and K and would resemble the Type B fluid inclusions of Bastrakov et al. (2007). In this context I raise the possibility that the Type B fluids that are ubiquitous in hematite alteration in the eastern Gawler Craton are effectively 'spent' fluids from the mineralizing phase - which would have had the potential to dissolve pre-existing mineralization.

2.7 CONCLUSIONS

Iron-oxide Cu-Au deposits form through successive periods of Fe-K-metasomatism, where alteration stages represent reactions that occur at progressively lower temperature and more oxidized conditions. While alteration intensity is controlled by the degree of fluid-rock interaction, alteration mineralogy is largely controlled by fluid composition rather than protolith. Although carbonate-rich protoliths lead to skarn assemblages, certain alteration minerals are common to all protoliths observed in this study, namely siliclastic metasediments, calc-silicate, granite and amphibolite. Three main alteration stages were recognized in this study and are consistent with observations of previous studies in the Olympic Cu-Au Province. Stage 1 involved K-feldspar, magnetite and chlorite alteration with minor Cu-sulfides, and occurred as a result of a relatively high-temperature ($>400^{\circ}\text{C}$) and relatively reduced (magnetite and pyrite stable) fluid. Stage 2 involved locally intense chlorite, hematite and muscovite alteration in more oxidized and lower temperature ($<300^{\circ}\text{C}$) conditions. Although hematite replacement of magnetite is common, abundant magnetite in the protolith or in previous alteration assemblages is not a pre-requisite of hematite alteration and demonstrate that significant amounts of iron were introduced during Stage 2 alteration. Although sulfide minerals including chalcopyrite are commonly associated with Stage 2 alteration, intense Stage 2 alteration can occur without sulfide minerals indicating that sulfide saturation only occurs where hydrothermal fluids interacted with either carbonate protoliths, pre-existing sulfur bearing phases, or during transient periods of sulfide stability which correspond to the transition from magnetite to hematite stable redox conditions. In this context, cooled fluids in these systems are effectively 'spent' fluids from the mineralizing phase and have the potential to dissolve pre-existing mineralization. The final stage of alteration includes hematite, chlorite, quartz, manganite, dolomite and apatite, commonly occurring as veins which overprint pre-existing mineral assemblages. This third alteration phase causes dissolution of sulfides and remobilization of copper.

3 Mineral chemistry mapping within an IOCG system, Olympic Cu-Au Province, South Australia

ABSTRACT

In this chapter I present the results of optical microscopy, Scanning Electron Microscopy (SEM), Electron Microprobe (EM) and Laser Ablation Inductively Coupled Plasma Mass Spectrometry (LA-ICPMS) analyses on selected samples from the eastern Gawler Craton iron-oxide-copper-gold (IOCG) system in South Australia. I use these data to comment on the mineralogical deportment of trace pathfinder elements that hold potential to map 10s of kilometer-scale exploration vectors within the IOCG system. Early silicate mineral assemblages are either magmatic (granites), metamorphic (amphibolites and metamorphosed siliciclastic sedimentary rocks) or high-T metasomatic (skarn altered metasedimentary rocks). Hydrothermal mineral assemblages associated with the main sulphide stage of the petrogenesis are dependent in part on the protolith but typically include hematite, chlorite, and muscovite \pm K-feldspar \pm pyrite \pm chalcopyrite. Minerals that pre-date the main sulphide phase typically have major and trace element concentrations within expected ranges for comparable rock types outside the eastern Gawler Craton mineral province. Abundant hydrothermal hematite, overprinting all previous mineral assemblages, is a characteristic feature of the sulphide stage of petrogenesis. Where hematite and magnetite occur in the same rock, hematite consistently overprints magnetite in the paragenesis and has higher average concentrations than magnetite (between 1 and 2 orders of magnitude higher) of Ba, Cu, Mo, Nb, Pb, Th, Ta, U and Σ REE (Rare Earth Elements). Hydrothermal hematite contains elevated concentrations of Cu, U, Sb and Bi compared to the average crustal abundance. Petrologic overprinting provides evidence for two stages of hydrothermal chlorite growth; prior to and subsequent to chalcopyrite deposition. Hydrothermal chlorite contains elevated concentrations of Cu, S and a range of chalcophile “pathfinder” elements including As, Bi, Mo and Sb. The first stage of chlorite has relatively lower concentrations of Cu (up to ~80 ppm) and S (~ 500 ppm) than the second stage of chlorite (up to ~7500 ppm Cu and ~1000 ppm S). Second stage chlorite contain Cu mineral inclusions.

Where sulphide minerals are present most chalcophile pathfinder elements (e.g. Ag, As, Bi, Cu, and Se) are dominantly deported in the sulphides, even at low concentrations, far from mineralisation. Pyrite is the most common sulphide, with chalcopyrite increasing in abundance closer to mineralisation. The pyrites are p-type, with S/Fe_{atom} ratios of > 2 and Co/Ni ratios ranging between 0.4 and 10, but mostly above 1. This is consistent with a moderate - temperature hydrothermal origin for the pyrite. There is considerable chalcophile trace element enrichment within pyrite. Concentrations of Co, As, Bi, Se, Te and Au reach 2 to 3 orders of magnitude above crustal abundance. Cu, Bi, Te, Au, Ag and Pb display large variations in concentration (up to 4 orders of magnitude for Bi) and are most abundant in hydrothermally altered rocks of metasedimentary protoliths. The chalcopyrite grains show variable enrichment in pathfinder elements and are most enriched in Bi, Se, Te and Ag, with values ranging between 1 and 4 orders of magnitude above crustal abundance. At elevated whole rock concentrations, within altered rocks, the REE are deported in hydrothermal apatite. This is consistent with the extreme capacity of the hydrothermal system to mobilise, and locally accumulate, even the most refractory elements. REE enrichment (up to 2604 ppm) is a good proximity indicator to ore, since it only occurs around the mineral system. Semi-quantitative mass balance calculations show that Cu, Ag, Au, As, Bi, Se and Te are dominantly contributed by sulphide minerals with pyrite particularly important for As and the Cu-sulphides important for Cu and Ag. Antimony preferentially occurs in iron-oxide phases, even if sulphides are present. If sulphides are not present the chalcophile elements are distributed in a range of oxide and

silicate alteration minerals at low concentrations.

3.1 INTRODUCTION

The iron-oxide–copper–gold (IOCG) mineral province of the eastern Gawler Craton plays host to economically important large to giant mineral deposits and has potential to host additional, as yet undiscovered resources. Exploration in the province is hampered by deep cover and has relied on sparse drilling into potential field geophysical anomalies, which are proxy measures for IOCG systems at best (measuring hematite and magnetite rather than copper and gold). The geographic extent of the Gawler Craton IOCG province (~600 km×200 km), the clustering of mineralisation ages at ~1590 Ma (e.g. Belperio et al., 2007; Skirrow et al., 2007; Porter, 2010) and the diversity of protoliths that host mineralisation (e.g. Gow et al., 1994; Fairclough, 2005; Hand et al., 2007) point to a hydrothermal mineralising system of significant scale and intensity. Such a system can be expected to result in fluid-rock interactions with a measurable mineralogical and chemical footprint much larger than the economic concentrations of commodity elements. In this study we ask what can we learn from the mineralogy and chemistry of the sparsely distributed drillholes within the eastern Gawler Craton that can inform us about the nature and size of the IOCG mineralising system, and how can we use that to improve our chances of exploration success?

The study area covers a 100×120 km region and is located within the eastern Gawler Craton in South Australia (Figure 5). The northern boundary of the study area is ~40 km south of the supergiant Olympic Dam deposit. The area includes a number of known, as yet unexploited IOCG occurrences (Carrapateena, Emmie Bluff, Punt Hill and Oak Dam) located beneath Late Proterozoic to Quaternary cover sequences of between 250 m and 1070 m thickness. The South Australian Geological Survey open file data repository available via SARIG contains information from ~600 drillholes that intersect the prospective basement rocks within the study area for an average density of drilling of 1 hole per 20 km². Many of the drillholes are tightly clustered around the known mineral occurrences, such that the drilling density for much of the area is considerably less than this.

Previous research has focused on the characteristics of known prospects and regional whole rock analysis using available drillholes (e.g. Oreskes and Einaudi, 1992; Haynes et al., 1995; Williams and Skirrow, 2002; Skirrow et al., 2002, 2007 and 2010; Williams et al., 2010; Porter et al., 2002 and 2010). Fabris et al. (2012) has shown that these drillholes intersect rocks with concentrations of a number of commodity and potential pathfinder elements that are commonly well in excess of average crustal abundances. Further, there appears to be a broad spatial pattern within the element distribution, even within these sparsely distributed holes, that hints at their potential use as geochemical vectors within the IOCG system. However, it is not yet clear to what extent the geochemical signatures recognised by Fabris et al. (2012, 2013) are related to the IOCG mineralising system. It is therefore necessary to establish the mineralogical controls of the geochemical signatures and relate those to an alteration paragenesis that is recognisable and characteristic of IOCG systems.

3.1.1 Mineral deportment of trace elements as exploration tools

Trace element concentrations within alteration minerals have the potential to be used as measures of hydrothermal activity and as exploration tools (McIntire, 1963; Bajwah et al., 1987, McDonough and Sun, 1995; Clark et al., 2004; Carew et al., 2006; Cook et al., 2009; Yang, 2009; Schmidt et al., 2010; Zhao et al., 2011; Tauson et al., 2013; Cook et al., 2013b; Ismail et

al., 2014). Much of this previous work has focused on trace element deportment in pyrite, which is the most abundant sulphide mineral commonly occurring peripheral to ore in many mineral systems (Abraitis et al., 2004; Clark et al., 2004; Carew et al., 2006; Benavides, 2007; Monteiro, 2008; Cook et al., 2009; Grove et al., 2010; Ye et al., 2011; Cook et al., 2013). Co/Ni ratios have been used to differentiate between an inferred sedimentary, magmatic or hydrothermal origin of pyrite (Abraitis et al., 2004; Clark et al., 2004). In hydrothermal systems n-type pyrite, with $Fe/S_{atom} > 0.5$, forms at high temperatures (250-500°C) and p-type pyrite, $Fe/S_{atom} < 0.5$, forms at lower temperatures (100-350°C) (Ares et al., 1998; Gomes et al., 2003; Abraitis et al., 2004). Elevated Te, Se and As (Abraitis et al., 2004; Zhao et al., 2011) incorporated within the lattice of pyrite are considered to be an indication of low temperature (190-250°C) hydrothermal processes (Ares et al., 1998; Gomes et al., 2003). High-As pyrite (and arsenopyrite) often have a spatial association with Au mineralisation (Abraitis et al., 2004; Zhao et al., 2011; Cook et al., 2013a). Large et al. (2014), Cook et al. (2013a) and Deditius et al. (2014) have shown that hydrothermal pyrite can incorporate a range of trace elements (e.g. As, Au, Bi, Cu, Hg, Pb, Sb, Tl, Ti and Zn) either within the crystal lattice or as micro-inclusions of other minerals. These pyrites commonly dominate the budget of chalcophile elements within the rock and may display internal zonation which can be used to infer the evolution of fluid-rock relationships (Abraitis et al., 2004; Clark et al., 2004).

Other minerals that have been assessed for trace element deportment in mineral systems include iron-oxides, apatite, chlorite, epidote and sulphide phases other than pyrite (McIntire, 1963; Nakamura, 1974; Monteiro et al., 2008; Yang, 2009; Ye et al., 2011; Cook et al., 2013b). Cook et al. (2011) suggested that Cu-sulphide minerals with elevated concentrations of Ag, Bi, Te and Se but poor Co, Ni, Ga and Ge are characteristic of a broad suite of Cu-sulphide deposits (12 deposits of syn-metamorphic Cu-vein systems in Norway, and skarn, porphyry and epithermal systems in SE Europe). Trace element concentrations within chlorite have been applied as vector tools in exploration for Cu porphyry deposits by Cooke et al. (2014) and Wilkinson et al. (2015). Ti, V and Mg decrease exponentially in concentration with increasing distance and Mn and Zn display a maximum in chlorite at a distance of ~1.3 km from the mineral deposit. In the case of IOCG mineral systems, which are characterized by enrichment in a wide range of elements (Groves, 2010), the potential mineralogical hosts of the geochemical signature are diverse. Carew et al. (2006) identified trace element-rich magnetite (with detectable Sc, Co, Ni, Cu, Zn, Ga, Sn, Pb, Mn and Mo) at the Ernest Henry IOCG deposit in North Queensland, and suggested that elevated concentrations of Mo and Sc in particular have potential as proximity indicators to economic mineralisation. In addition, Zhang et al. (2009) suggested that the concentration of V and Ni in magnetite could be used as a vector toward mineralisation in the area around Ernest Henry. Andrea et al. (2010) suggested the high concentration of fluorine and other complexing agents in this phase allowed trace elements to be transported in solution. Ismail et al. (2014) found that REE patterns of apatite have the potential to be used as vectors toward mineralisation in the LREE enriched IOCG system of the southern Gawler Craton.

In this study I assess the deportment of a range of trace elements in silicate, oxide and sulphide phases from a lithologically and spatially diverse sample set collected in the vicinity of known IOCG deposits and prospects in the eastern Gawler Craton. I seek to characterise the deportment of trace elements, particularly potential pathfinder elements, and determine to what extent they may be a measure of hydrothermal processes related to the IOCG mineral system.

3.1.2 Geological background

Eastern Gawler Craton

Basement rocks of the eastern Gawler Craton are Archaean to Early Mesoproterozoic age (Hand, 2008; Reid, 2008; Reid and Hand, 2012) (Figure 5) and are extensively overlain by Neoproterozoic, Cambrian, and younger sedimentary rocks of variable thickness (commonly >500m) (see Chapter 1.3 and Chapter 2.3). The distribution of basement rock has been interpreted from potential field data and relatively sparse drilling (e.g. Direen and Lyons, 2007).

The oldest rocks in the eastern Gawler Craton belong to the Archaean aged Christies Gneiss, which is a diverse suite of metamorphic rocks including quartzite, schist, dolomite, iron formations, calc-silicate metasediments, marble and amphibolite. These are overlain by the Hutchison Group metasedimentary package, which contains psammite and pelite with minor carbonate and iron formation, deposited between 1885 and 1995 Ma (Daly et al., 1998). This was intruded by granitoids of the Donington Suite (c.1850 Ma) (Reid and Hand, 2008) including quartz-gabbro-norite, hypersthene gneissic granite, syenogranite, monzogranite, granodiorite, tonalite and megacrystic granitoid gneiss (Reid et al., 2008). These were overlain by metasedimentary and metavolcanic rocks of the Wallaroo Group deposited between c. 1760 and 1730 Ma (Cowley et al. 2003). The Wallaroo Group contains schist, argillite, and carbonate bearing sedimentary rocks, siltstone, sandstone, felsic volcanics, amphibolite, dolerite and basalt. The Gawler Range Volcanics have widespread distribution in the study area, and were extruded between 1593-1592 Ma (e.g. Fanning et al., 1988; Jagodzinski, 2014). The Gawler Range Volcanics are volumetrically dominated by dacite and rhyolite with lesser andesite and basalt (e.g. Blissett et al., 1993; Daly et al., 1998). Intrusion of the Hiltaba Suite granites occurred at c. 1595-1575 Ma (e.g. Fanning et al., 1988; Johnson and Cross, 2005; Fanning et al., 2007). The granites are K-feldspar rich and include quartz syenite to quartz poor phases as well as hornblende bearing monzodiorite and quartz monzonite in the Olympic Dam area (Creaser, 1989; Reeve et al., 1990). Hiltaba Suite granites are typically described as A-type granites (Drexel et al. 1993) and show evidence of deformation (e.g. Stewart and Foden, 2003). Dating of alteration and ore phases associated with IOCG mineralization at numerous locations within the eastern Gawler Craton indicates that primary mineralization formed at approximately 1590 Ma (e.g. Johnson and Cross, 2005; Skirrow et al., 2007; Reid et al., 2011) broadly synchronous with the Hiltaba Suite Granites and Gawler Range Volcanics and metamorphism.

The IOCG Mineral System

IOCG deposits are globally distributed with ages ranging from Archean to Cainozoic, but with most occurrences of Precambrian age (Williams et al. 2005; Groves et al., 2010; Porter, 2010). IOCG deposits are characterized by (e.g. Williams et al. 2005; Groves et al., 2010; Porter, 2010):

1. Abundant iron-oxide (hematite or magnetite) mineralogy;
2. Cu-Au as the main commodity elements but also potentially including U and REE;
3. Widespread hydrothermal alteration which is characterised by hematite-sericite-chlorite-carbonate (HSCC), calc-silicate-alkaline feldspar-magnetite (CAM) and magnetite-biotite (MB) mineral assemblages;
4. Emplacement depths of between the surface and 15 km;

5. Links to the mantle as a source of heat, magma and potentially fluids;
6. Conjectural fluid and metal sources, with the possibility of multiple fluids of varying salinity, temperature, redox and composition (Haynes et al. 1995; Bastrakov et al. 2007; Groves et al. 2010). However there is increasing evidence that metal-rich fluids were hypersaline and relatively high-temperature, see chapter 2.6.3 (Williams et al., 2005; Bastrakov et al., 2007).

The eastern Gawler Craton is a globally important IOCG province which contains the supergiant Olympic Dam deposit and the giant Prominent Hill deposit as well as numerous as yet unexploited prospects including Carrapateena, Punt Hill, Oak Dam and Emmie Bluff (Figure 5 and 6). Studies of hydrothermal alteration associated with the eastern Gawler Craton IOCG deposits have identified a spectrum of mineral assemblages related to fluid-rock interactions (Haynes et al., 1995; Johnson et al., 1995; Bastrakov et al., 2007), with three broadly defined end-members (Skirrow et al., 2002).

Calc-silicate, alkali feldspar and magnetite assemblages (CAM): Typical minerals within the CAM alteration type include magnetite, actinolite, K-feldspar, dolomite, apatite and pyrite. These assemblages are inferred to have been formed from carbonate-rich sedimentary protoliths (Ismail et al., 2014) and contain hypersaline (> 30% NaCl equivalent), Cu-rich fluid inclusions with homogenization temperatures of 350°-500°C (Bastrakov et al., 2007).

Magnetite-biotite assemblages (MB): These assemblages also often include pyrite and chalcopyrite. Biotite in these assemblages is iron-rich (tending toward end-member annite) compared to biotite from unaltered granites in the eastern Gawler Craton which is phlogopitic (Skirrow et al., 2002). The magnetite-biotite is inferred to form at temperatures of 460°-500°C due to the constraints of magnetite - actinolite -biotite formation at ~500°C and biotite-K-feldspar formation at 460°C (Porter, 2010).

Hematite-sericite-chlorite-carbonate assemblages (HSCC): The HSCC style of alteration is commonly associated with the main phase of Cu-sulphide mineralization (pyrite, chalcopyrite, chalcocite, and bornite) and consistently overprints MB and CAM assemblages. HSCC alteration ranges from incipient (hematite dusting of feldspars) to intense (near complete replacement of previous mineralogy and textures, brecciation). Incipient hematite alteration is a widespread phenomenon on the eastern Gawler Craton, whereas greater intensity HSCC tends to occur in the core zones of economic deposits (e.g. Olympic Dam, Prominent Hill). This style of alteration is associated with relatively low salinity (1-7 wt % NaCl equivalent) fluid inclusions with homogenization temperatures of <300°C.

IOCG deposits of the eastern Gawler Craton display variable components of these end member alteration assemblages. Mineralisation at the Carrapateena deposit (Figure 5) is hosted by Donington Suite granite that is strongly overprinted by HSCC alteration (Skirrow 2002). Alteration minerals include secondary barite, monazite, anatase, magnetite, apatite, fluorite and zircon (Cleverley et al., 2005). Punt Hill mineralisation occurs in brecciated Gawler Range Volcanics and Wallaroo Group metasedimentary rocks (Daly and Rowett, 2007; Reid et al., 2008) which are overprinted by CAM and HSCC alteration (Skirrow et al. 2007). Emmie Bluff mineralisation occurs in stratabound magnetite-skarn of the Wallaroo Group and includes examples of both CAM and HSCC alteration, typically with hematite alteration occurring vertically above magnetite alteration (Gow et al., 1994; Huntington et al., 2006).

3.2 METHODS

Our approach is to take a spatially diverse suite of samples representing a range of protoliths,

alteration types and alteration intensity from within the eastern Gawler Craton mineral system. By determining the mineral department of pathfinder trace elements in these samples I aim to link whole rock geochemistry to particular alteration assemblages. By mapping trends in the alteration paragenesis throughout the system I may then be in a position to utilise whole rock geochemistry as a proxy for alteration intensity at the key mineralising stage of the system (and thus evaluate using whole rock geochemistry in assessing proximity to mineralisation).

Contributions to elemental whole rock chemistry depend on concentrations of the elements in the individual minerals and the modal abundance of the mineral in the rock (Table 3). From our larger set of forty-four samples (see chapter 2.4.1) I chose eleven samples for detailed mineralogy and mineral chemistry based on the following criteria:

- Broad spatial distribution (Figure 6) including a 2.5 km geological cross section through the Emmie Bluff deposit (four samples);
- Four protolith rocks, including granite, carbonate bearing metasediment-calc-silicate rocks, siliciclastic metasediment and amphibolite;
- Variable alteration intensity as identified by petrologic examination and HyLogger observation (see chapter 2);
- Having 10 pathfinder elements at concentrations over ten times average crustal abundance as index Au, Ag, As, Bi, Cu, Mo, S, Sb, Se and W. The pathfinder elements are defined by the whole rock IOCG alteration index of Fabris et al. (2013). Of 11 samples selected, there were 2 samples with 1 pathfinder element, 3 samples with 2 pathfinders, 2 sample with 3 pathfinders, 1 sample with 4 pathfinders, 2 sample with 6 pathfinders and 1 sample with 9 pathfinders that were over ten times natural crustal abundance (also see chapter 2).

The location of the eleven samples is shown in Figure 6. Detailed mineralogy is given in Table 3.

Table 3. Mineralogical, alteration and lithological details for the eleven samples used in this study.

Sample	2066641	2066655	2066169	2066178	2066656	2066174	2066166	2066203	2066635	2066199	2066177
DH	IHAD3	IHAD5	DRD1	HL002	IHAD2	PSC4_SASC2	CSD1	GHDD4	IHAD6	VVDD1	HL002
From	799.8	1016.7	1139.4	529.13	819.61	539.46	970.6	854	855.87	683.75	471.1
To	799.88	1016.8	1139.5	529.27	819.76	539.53	970.7	854.15	855.99	683.86	471.26
Alteration	HSCC	CAM	HSCC	MB	HSCC	HSCC	CAM	HSCC	HSCC	CAM	MB
Rock type	Metasediment		Granite				Calc-silicate				Amphibolite
Quartz%	35	25	15	35	10	30	30	25	25	10	10
K-feldspar%	10	15	5	30	20	15		15	10	20	10
Chlorite%	20	30	25	2	10	20	30	20	15	20	20
Hematite%	25	20	30	1	15	5	10	8	20	9	9
Magnetite%		1		1			20				1
Dolomite%		3				15			20	20	
Calcite%		2						10		10	20
Pyrite%		3	20				1	2			
Chalcopyrite%		1					1	3	2 Bn		
Apatite%	1			1		5		1	3	5	
Mica%	Bt5		Ms5	Bt25	Ms40	Bt 10				Ms 1	
Rest %				An 5			Gr 8	Act15			Am 30
Other%	Man4				Ilm 5			Sp 1	Gp 5	Rt 5	

Act=actinolite, An=anorthoclase, Am=amphibole, Bn=bornite, Bt=biotite, Gp=gyypsum, Grt=garnet, Ilm=ilmenite, Man=manganosite, Ms=Muscovite, Rt=rutile, Sp=sphalerite.

3.2.1 Mineral abundance estimation

Mineral abundances in each sample were estimated from polished thin sections using a petrological microscope in combination with Scanning Electron Microscopy (SEM) over selected areas. The 60×20 mm polished thin sections were prepared commercially by Pontifex and Associates with an average thickness of 40-45 µm. The SEM provides detailed textural analysis combined with mineral identification and semi-quantitative element concentrations.

3.2.2 Scanning Electron Microscopy

Eleven samples were used for electron back scatter imaging and semi-quantitative elemental mapping using the SEM at Adelaide Microscopy. Polished thin sections were coated with 3-5 nm of carbon prior to analysis. A Philips XL30 FEG SEM - with EDX detector, mapping capability was used. Maps of sample surface (2-3 mm dimensions) were created by rastering the electron beam over the sample using a 2 nm beam size. The EBSD system provided a high-resolution image that is dependent on the mean atomic mass of the surface atoms and allows mineral identification and observation of sub-micron textures. Elemental maps were constructed with a resolution of 1-5 µm using an EDS detector.

3.2.3 Electron Microprobe Analysis

Petrological analysis combined with the SEM elemental mapping were used as a guide to select 234 analysis points from 22 mineral grains from the eleven samples for quantitative elemental analysis using a Cameca SXFive Electron Microprobe equipped with five WDS detectors housed at Adelaide Microscopy, University of Adelaide. Analysed mineral phases included pyrite, chalcopyrite, bornite, hematite, magnetite, feldspar, chlorite, muscovite and biotite. The analytical suite included Si, Zr, Ti, Zn, Al, V, Cr, Fe, Mn, Mg, Ca, Ba, Na, K, P, Cl, F, O and H measured with detection limits of 0.01%. Individual mineral grains were analysed using a primary electron beam accelerated to 1.5×10^3 eV. A current of 15kV and 20nA was used for silicates and oxides. For sulphides, a current of 20 kV and 20nA was used. Spot sizes of 3-5 μm were used for all analyses. Major element concentrations were calibrated against reference materials which were analysed at the beginning of each analytical session. Silicates and oxides were calibrated against the same standard allowing for concentrations to be determined for a suite of 18 elements (Al-Astimex garnet, Ba-Astimex Barite, Ca-Astimex plagioclase, Cr-Astimex, Chromium metal, Cl-Astimex Tugtupite, F-P&H Developments Apatite, Fe-Astimex garnet, Mg-Astimex garnet, Na-Astimex albite, O-calculate oxygen from the stoichiometry of the cations, Si-Astimex albite, P-P&H Developments Apatite, K-Astimex Sanidine, Ti-P&H Developments Rutile, Mn-Astimex Rhodonite, V-Astimex Vanadium metal, Zn-Astimex Willemite, Zr-Taylor zircon). Sulphide minerals utilised pyrite package: S-Astimex marcasite, As-P&H Developments Gallium Arsenide, Fe-Astimex marcasite, Cu-P&H Developments Chalcopyrite, Bi-P&H Developments Bismuth Selenide, Co-Astimex Cobalt metal), providing concentrations of 6 elements (Co, Cu, Fe, S, As and Bi). The results are presented in Table 4 and Appendix 3.

3.2.4 LA-ICPMS analysis

Individual minerals identified by SEM and analysed using the electron microprobe were further analysed by Laser Ablation Inductively Coupled Plasma Mass Spectrometry (LA-ICPMS) to collect trace element data to lower detection limits (ppm to ppb) than the microprobe for a wide range of trace elements including Ag, As, Au, Bi, Cu, S, Sb, Se, Mo, W and REE. As the LA-ICPMS data requires calibration based on major element concentrations, which can be provided by electron microprobe data, the approach was to co-locate electron microprobe and LA-ICPMS analytical spots where possible. 290 analyses were collected. An Agilent 7500cx with attached New Wave UP-213NdYag solid state laser ablation system at Adelaide Microscopy, University of Adelaide was used. The laser was operated under conditions of 0.47 to 0.53 mJ, 5Hz and 6.63-7.62 J/cm³ with a spot size of 30 μm . The depth of ablation was dependent on the laser pulse parameter, and the thermal conductivity and density of analysed minerals. Sample ablation and analysis involved two stages. The first stage of ~28 seconds was used to measure the background; the second stage of ~67 seconds analysed the plasma produced by the laser ablation.

A total of 290 LA-ICPMS analyses were conducted in this study, including 218 analyses that were conducted at the same location as a previous electron microprobe analysis of the same minerals. Three standards for sulphide minerals (Mass-01), silicate minerals (Nist 612) and

oxide minerals (BHVO-1) were routinely analysed along with the unknowns. However, due to the potential for matrix dependent elemental fractionation during LA-ICPMS analyses it is desirable to calibrate against a robust independent concentration measurement from the same mineral and same analytical location. As such, the LA-ICPMS trace element concentrations reported here were calibrated relative to the content of selected major elements as measured by electron microprobe analysis at the same location. In 72 cases where there was not a matching electron microprobe analysis the LA-ICPMS data were calibrated using the average concentration of the selected elements for the mineral in question (Table 4).

Table 4. Minerals analysed by electron microprobe and LA-ICPMS, showing the number of grains analysed by electron microprobe, the elements used for LA-ICPMS calibration and the average concentration of those elements determined by electron microprobe analyses and used to calibrate LA-ICPMS in cases where there was no matching electron microprobe analysis.

Minerals	No. of EM analyses	Calibration Element 1	WT %	Calibration Element 2	WT %	Minerals	No. of EM analyses	Calibration Element 1	WT %	Calibration Element 2	WT %
Apatite	9	P	18	Ca	40	K-feldspar	18	Si	30	Al	10
Biotite	25	Si	20	Al	9	Magnetite	6	Fe	71	O	30
Calcite	9	O	11.	Ca	41	Manganosite	4				
Bornite	7	S	20	Fe	11	Monazite	2				
Chlorite	34	Si	12	Al	10	Muscovite	8	Si	22.5	Al	15
Dolomite	17	O	12	Ca	21	Pyrite	11	Fe	42	S	
Plagioclas	4	Al	13.	Si	27.5	Pyroxene	10	Si	23	Ca	8.2
Garnet	2	Si	17	Ca	23	Rutile	2				
Gypsum	1					Quartz	1				
Hematite	47	Fe	66	O	29	Sphalerite	3				
Ilmenite	3					Chalcopyrite	11	Fe	29	Cu	33
Subtotal	158						76			Total	234

Note: 14 minerals were calibrated as: K-feldspar, plagioclase, biotite, muscovite, chlorite, pyroxene magnetite, hematite, apatite, calcite, dolomite, pyrite, bornite and chalcopyrite. The GLITTER software program was used to obtain a uniform signal for the remaining 8 minerals.

Data review and calibrations were conducted using the GLITTER software program. The data review allowed checking analytical times and ensuring that the analytical signal was stable over the period of analysis. A suite of 29 elements are reported for sulphide elements (Na, Si, S, V, Cr, Mn, Fe, Co, Ni, Cu, Zn, Ga, As, Se, Mo, Ag, Cd, In, Sn, Sb, Fe, Ba, W, Ir, Au, Hg, Tl, Pb and Bi), whereas silicates and oxides have a broader suite of 55 elements (Na, Mg, Si, Al, P, S, K, Ca, Ti, V, Cr, Mn, Fe, Co, Ni, Cu, Zn, Ga, Ge, As, Se, Rb, Sr, Y, Zr, Nb, Mo, Ag, Cd, Sn, Sb, Te, Ba, Hf, Ta, W, Au, Hg, Pb, Bi, Th, U; La, Ce, Pr, Nd, Sm, Eu, Gd, Tb, Dy, Ho, Er, Tm, Yb, Lu). Results are given in Appendix 4.

Note that as a result of the relatively large size (30 μm) and finite depth of the LA-ICPMS spots compared to the electron microprobe spots (<5 μm) there is potential for inclusion of internal compositional variations and/or additional phases in the LA-ICPMS data (for example by overlap onto other minerals, inclusions at a scale below detection by SEM or drilling into a new phase during laser ablation). Analytical sites were carefully selected in an attempt to avoid

this. However a number of analyses, particularly of the iron oxide phases, displayed large variations from the expected chemistry which indicate contamination by other phases.

Selected trace element abundances in individual minerals are presented in spider diagrams (figures 25, 27, 30, 33, 36, 38, 41) in which each element is normalized to average upper crustal abundance as reported by Taylor and McLennan (1985). I chose to normalize to average upper crustal abundance in order to provide a sense of the relative contribution to whole rock geochemistry that each of the examined minerals might make. For example, a mineral occurring at an abundance of ~1% in the rock but having an element at a concentration of ~100 times crustal abundance could account for the entire whole rock budget of that element and should be considered an important host for that element.

3.2.5 Bulk rock calculation

In most instances mineral exploration geochemistry will be collected by whole rock analysis. A relevant question for explorers, with the potential to help interpret processes and rank geochemical anomalies, is which minerals control the whole rock concentrations of ore and pathfinder elements? By multiplying estimated mineral abundances by elemental concentrations of the mineral phases I have derived a “calculated whole rock chemistry” which can be used to make first order comparisons with the measured whole rock geochemistry. There are some obvious limitations to the approach. Foremost is that the material submitted for whole rock analysis (typically 1 m intervals of half drill core) is of greater volume than the thin section chosen to represent it and may contain different proportions of minerals (and indeed different minerals) compared to the thin section. Trace minerals, most notably the sulphides and apatite in this study, will be particularly susceptible to estimation errors. As a result, the most robust results of this study relate to elements deployed within the abundant alteration minerals (silicates and oxides) with less quantitative results for elements deposited in sulphides (see chapter 2.5.2).

3.3 RESULTS

Sulphides

3.3.1 Pyrite (FeS₂)

Electron microprobe analysis

Twelve pyrite grains in three samples were analysed using an electron microprobe to measure elemental concentrations of Fe, S, Cu, Co, As and Bi. The sample from drillhole IHAD5 (2066655) contains siliciclastic metasediment with CAM alteration. The sample from drillhole IHAD6 (2066635) contains calc-silicate rocks with HSCC alteration, and from drillhole DRD1 (2066169) the sample contains granite with HSCC alteration (Figure 6). In the granite sample, six analyses were conducted on two grains of pyrite (2 mm) with three analyses per grain: one site at the centre of the grain, one site toward the margin and another site between them. Three analyses were conducted independently on pyrite grains in metasediments and calc-silicate samples respectively. Tabulated results for Fe, S, Cu, Co, As and Bi are provided in Appendix 3, however I found that the S and Fe concentrations were the most useful for classifying pyrite

chemistry. S/Fe atomic ratios are close to the stoichiometry of ideal pyrite (~2) for all samples, but almost all pyrite analysed are slightly Fe deficient (Figure 22), placing them within the field of pyrites which typically display p-type semiconducting properties (Abraitis et al., 2004).

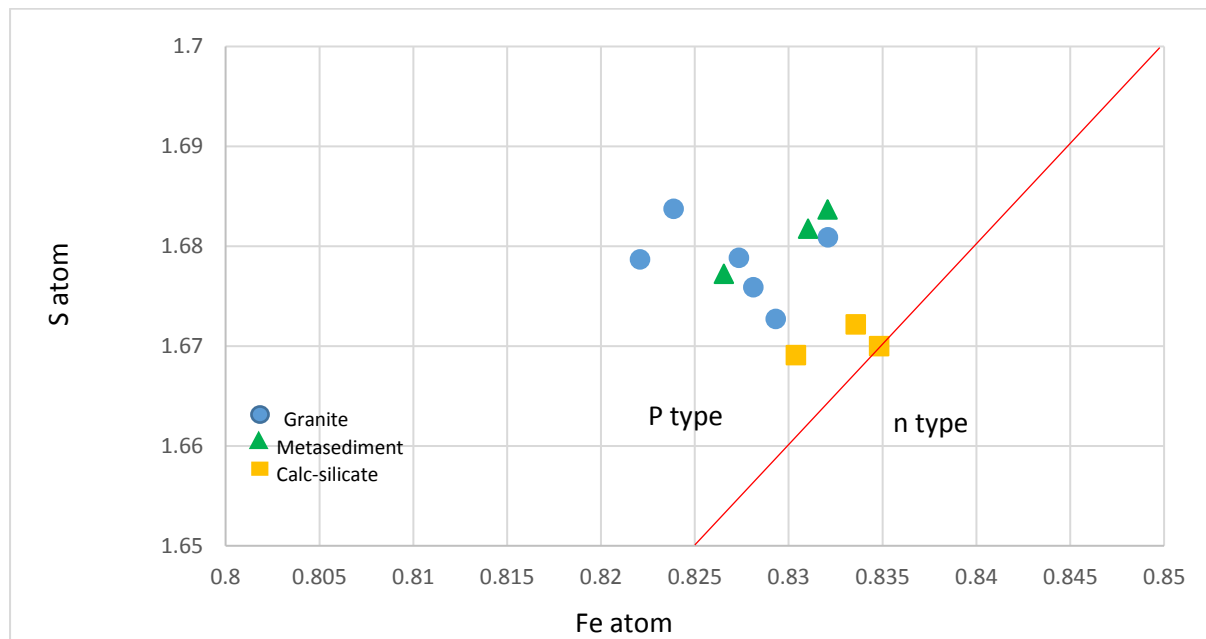


Figure 22. S vs Fe plot for pyrite grains from various protoliths analysed by electron microprobe in this study. The red line indicates ideal pyrite stoichiometry. Slight Fe deficiency is displayed in the majority of analyses, and is typical of pyrites that are p-type semiconductors (Abraitis et al., 2004).

LA-ICPMS analysis

Thirteen pyrite analyses were collected on three rock samples (granite, metasedimentary and calc-silicate) using LA-ICPMS to measure trace element abundance. Six analyses were conducted at the same sites as electron microprobe analyses for granite sample 2066169. Five analyses were conducted on metasedimentary sample 2066655, three at the same sites as electron microprobe analyses and two duplicate analyses to check internal consistency of pyrite grains. Two additional pyrite analyses from calc-silicate sample 2066166 are shown in Figure 23, and were calibrated based on average Fe concentrations of pyrite in the electron microprobe data.

LA-ICPMS analysis on the samples described above showed 17 elements are present in concentrations above detection limits (Appendix 4). Co and Ni concentrations vary significantly between the three rock types and are higher in the granite than metasedimentary protoliths (Figure 23). Co/Ni ratios are <1 for calc-silicate, between 0.75 and 9.75 for siliciclastic metasedimentary rock and between 0.18 and 7.1 for granite (Figure 23). Two pyrite grains from granite sample 2066169 show differing Co/Ni ratios, with grain 2066169B having Co/Ni ratio between 2.2 and 7.1, and grain 2066169A having Co/Ni ratio between 0.18 and 0.42. For the two calc-silicate rock samples the Co/Ni ratio is 0.25 and 0.43.

The trace element pattern identified in this study is similar for pyrite in granite, metasedimentary and calc-silicate rock types. Se, Te, Co, As, Ni and Au content of pyrite is considerably above average crustal abundance (Figure 25A). Se, Te, Co and As content of pyrite 1-3 orders of magnitude higher compared to average crustal abundance. All other trace elements show high variation from well below to well above crustal abundance (see Appendix

4).

With the exception of Co, Ni, Se and Hg, other trace elements are consistently more abundant in pyrite hosted within calc-silicate and siliciclastic metasedimentary rock than in granite, with the most pronounced enrichments in Cu, Bi, Te, Au and Ag. Ag and Bi are above average crustal abundance in siliciclastic metasediment and below crustal abundance in the calc-silicate and granite. Zn, In, Sn, Sb, Tl, Ba and Pb are below average crustal abundance in all analyses. Hg preserves concentrations approximating average crustal abundance.

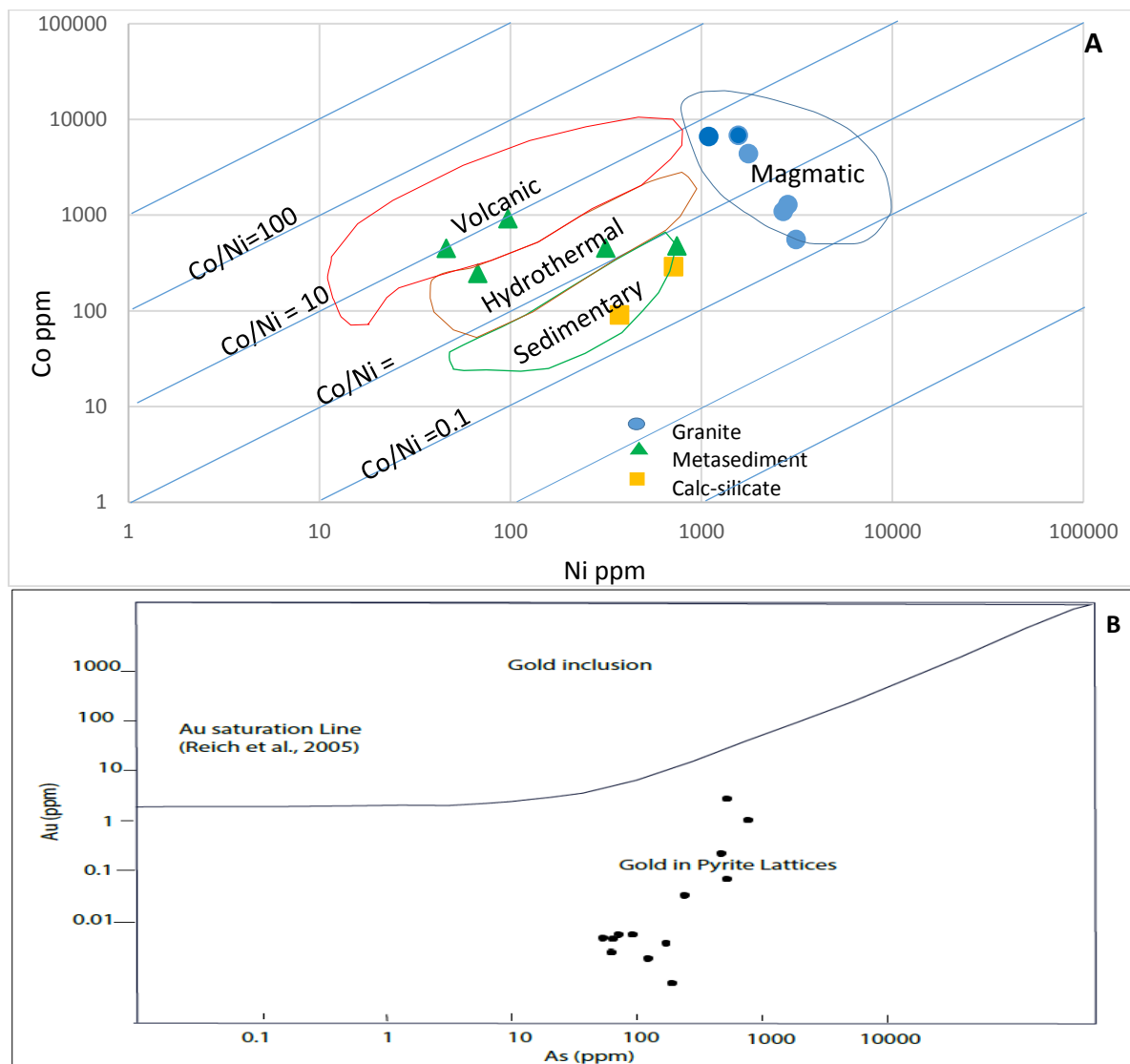


Figure 23. A) Plot of Co versus Ni for pyrite from granitic, calc-silicate and metasedimentary samples. The blue lines depict the Co/Ni ratios that have been used as an indicator of the origin of pyrite (e.g. Bralía et al., 1979; Bajwah et al., 1987; Bettina 1989; Abraitis et al., 2004; Clark et al., 2004). The red, brown, green and blue circles outline the fields identified by Xiao-wen et al. (2015) within which pyrite of volcanic, hydrothermal, sedimentary and magmatic origin respectively will fall. For this study, pyrite in granite is of magmatic origin. Pyrite from metasediments is a mixed sedimentary, hydrothermal and volcanic origin, depending on which interpretation of Co/Ni ratios is used. Pyrite in calc-silicate is of sedimentary origin. B) Plot of Au and vs As from the pyrite samples analysed in this study. The Au saturation line is from Reich et al. (2005). The chemistry of pyrite is consistent with Au incorporated within the crystal lattice of pyrite, rather than Au inclusions.

3.3.2 Cu-sulphides

Electron microprobe analysis

Fifteen Cu-sulphide grains from four samples (one siliciclastic metasediment, two calc-silicate and one granite) were analysed using an electron microprobe. The samples included siliciclastic metasediment with CAM alteration (2066655, from drillhole IHAD5), calc-silicate metasediment with HSCC alteration (2066635, from drillhole IHAD6), granite with HSCC alteration (2066169A, from drillhole DRD1) and calc-silicate with strong CAM/HSCC alteration (2066203, from drillhole GHDD4) (Figure 24). Analytical sites were chosen with reference to petrological observations reported in Section 2.6.2. Seven analytical sites on calc-silicate metasediment with HSCC alteration (2066635) show Cu between approximately 49 and 58 wt %, Fe between approximately 10 and 13 wt % and S between approximately 19 and 24 wt %, consistent with the stoichiometry of bornite (Cu_5FeS_4). Eight sites analysed for the other three samples show Cu between 25 and 34 wt %, Fe between 24 and 29 wt % and S between 23 and 37 wt %, broadly consistent with the stoichiometry of chalcopyrite (CuFeS_2) (Figure 24).

LA-ICPMS analysis

Thirty-six Cu-sulphide grains were analysed by LA-ICPMS. Twelve analyses returned data inconsistent with the target minerals and were presumed to contain significant inclusions of other mineral phases. Of the 24 remaining analyses, six are bornite and eighteen are chalcopyrite. In addition to high Cu concentration, trace element patterns for bornite and chalcopyrite are similar, showing consistent enrichment in Bi, Se, Te, Au and Ag of 1 to 4 orders of magnitude above average crustal abundance (Figure 25B, C) and variable enrichment in In, As and Sb.

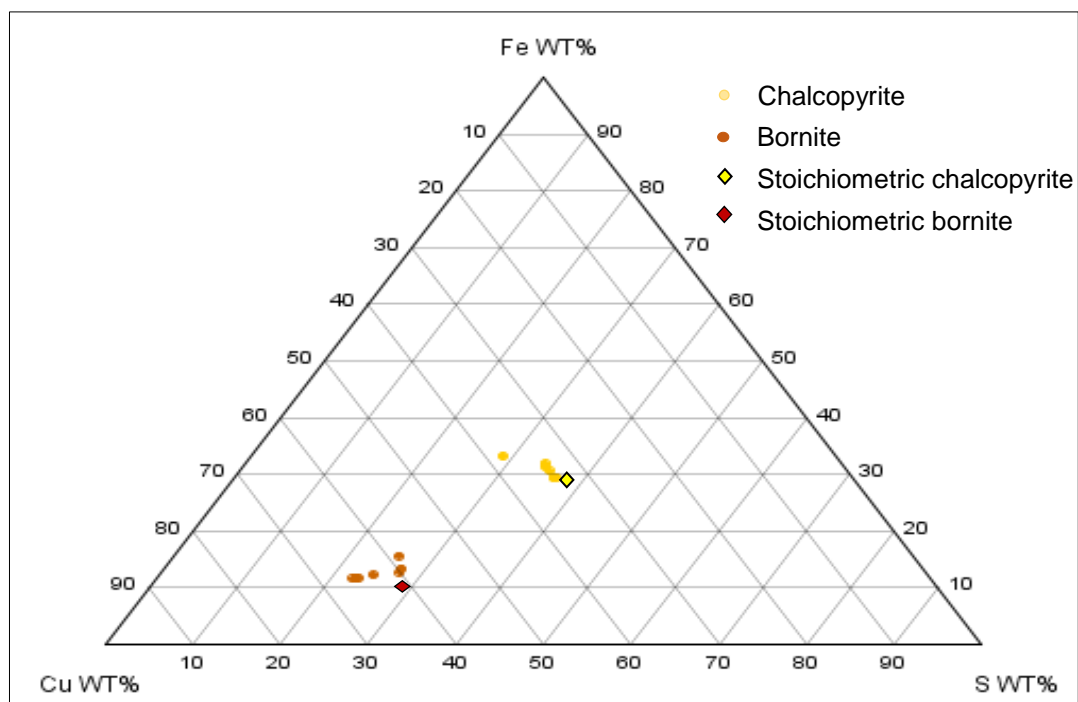


Figure 24. Fe-Cu-S ternary diagram showing the chemistry of the 8 analysed chalcopyrite (CuFeS_2) and 7 bornite (Cu_5FeS_4) grains.

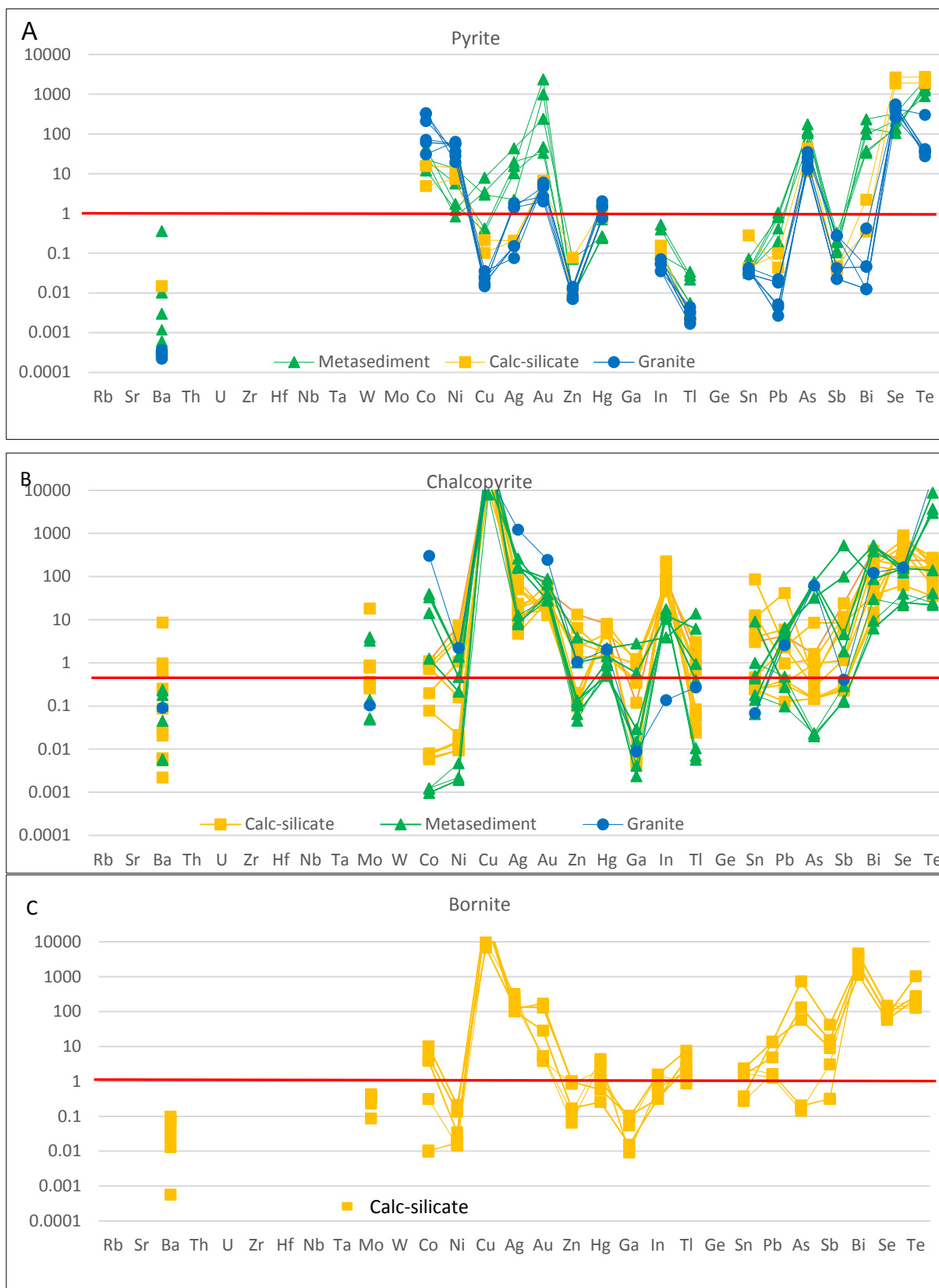


Figure 25. Trace element abundances normalized to average upper crustal abundance in A) pyrite; B) chalcopyrite; and C) bornite analysed in this study and coloured by protolith. Normalisation to average upper crustal abundance provides a comparable measure for all elements from which to determine the likelihood of the mineral being a significant host of each element in the rock.

Oxides

3.3.3 Magnetite

Electron microprobe analysis

Six magnetite grains from two samples were analysed by electron microprobe (Figure 26A), namely calc-silicate rock with CAM alteration (2066166, from drillhole CSD1) and an unaltered granite with incipient MB alteration (2066178, from drillhole HL002). Analysis of two magnetite grains show significant concentrations of Si and Al and low Fe (40 to 50% calculated as Fe_2O_3). These analyses presumably overlapped with silicate inclusions. The remaining four analyses are consistent with magnetite. These grains contain detectable concentrations of a number of trace elements, including 0.43-0.48 F wt %, as well as Si, Ti, Zn, Al, V, Cr, Mn, Mg, Ca, Ba, Na, K, P and Cl at <0.1 wt %.

LA-ICPMS analysis

Eleven magnetite sites were analysed for 48 elements. Four sites (two sites of calc-silicate 2066166, two sites of granite 2066178) show Fe concentrations between 70.3 and 71.3 wt % Fe with low Al, Si, Mg and Ca content, consistent with magnetite (Figure 27). Remaining analyses show significant concentrations of other major elements (Si, Al, Mg and K) indicating the sites overlapped with silicate mineral inclusions. W, Sn, Sb and Bi are preserved at concentrations slightly above average crustal abundance in the calc-silicate sample. All other elements are at or below average crustal abundance (Figure 27). All are below Post Achaean Average Shale (PAAS, Figure 28) with slight LREE depletion compared to HREE.

3.3.4 Hematite

Electron microprobe analysis

Hematite grains from 10 samples were analysed at 53 sites (Figure 26, Appendix 3). Fourteen analyses were not used as they had Fe concentrations less than 55.6 wt %, indicating significant Si and Mn alteration and silicate inclusions. In total, 39 hematite grains from 10 samples were included. Nineteen grains hosted in granite were used, including eight grains from granite with HSCC alteration (2066169, from drillhole DRD1), five grains from granite with HSCC alteration (2066174, from drillhole PAS_SASC2), three grains from unaltered granite (2066178, from drillhole HL002), and three grains from granite with CAM/HSCC alteration (2066656, from drillhole IHAD2). Five grains from calc-silicate samples were analysed, including one from a calc-silicate with CAM alteration (2066199, from drillhole WWDD1), one from calc-silicate with HSCC alteration (2066635, from drillhole IHAD6) and three from calc-silicate with HSCC alteration (2066203, from drillhole GHDD4). Six grains from metasediment with CAM alteration (2066655, from drillhole IHAD5) and six grains from metasediment with HSCC alteration (2066641, from drillhole IHAD3) were analysed. Three analysed grains were from amphibolite with MB alteration (2066177, from drillhole HL002). Hematite grains preserve Fe concentrations between 55.6 wt % and 69.5 wt % (Appendix 3). A number of elements are at detectable concentration, including F averaging 0.29 wt %; Si, Mn, Al and Ti averaging between 0.2 and 0.5 wt %; and Cr, Zn, Ba and P at <0.1 wt %.

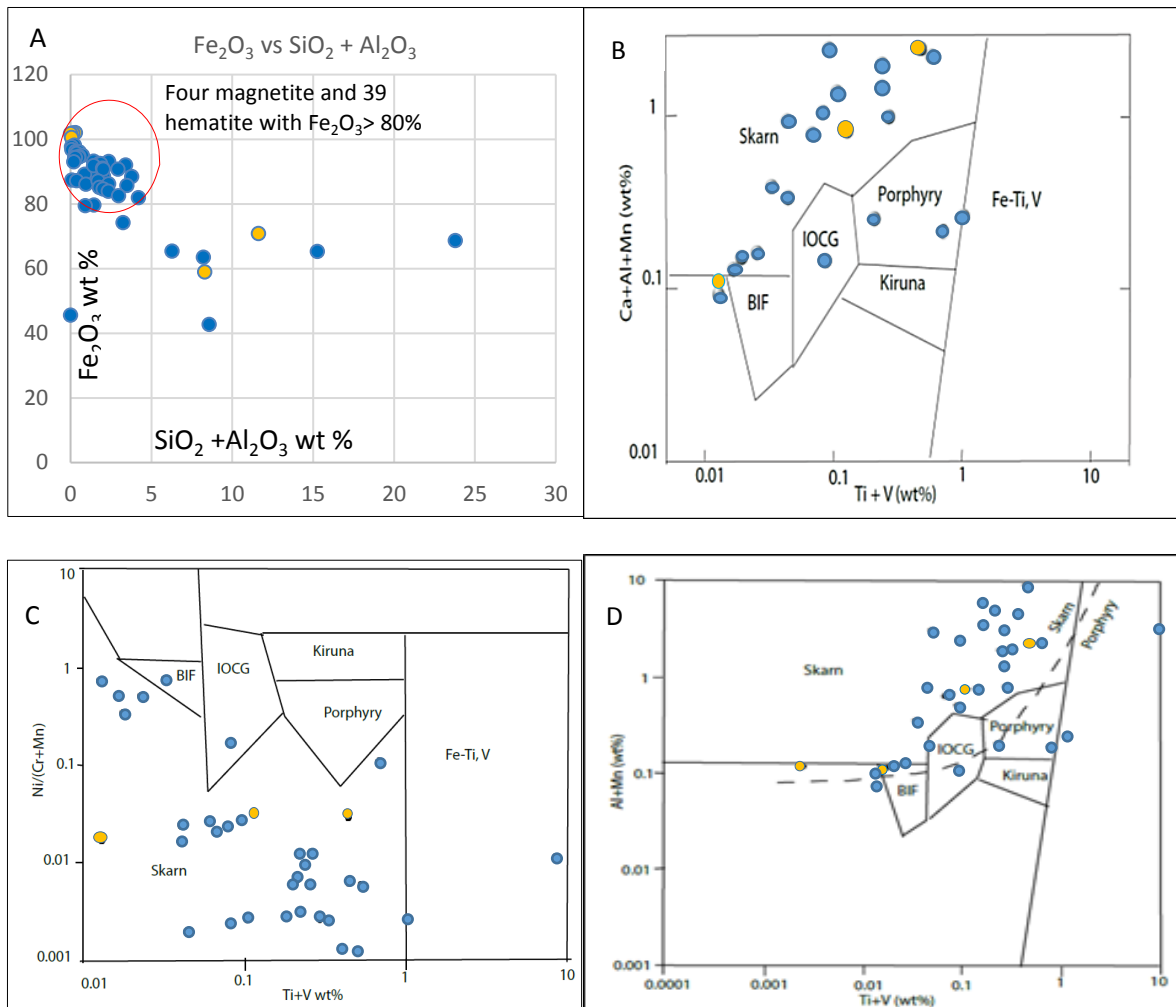


Figure 26. A) Fe_2O_3 vs $\text{SiO}_2 + \text{Al}_2\text{O}_3$ plot of 53 LA-ICPMS analyses of magnetite (yellow) and hematite (blue) from the study area. The spread toward high $\text{SiO}_2 + \text{Al}_2\text{O}_3$ (>5%) reflects silicate inclusions in the iron-oxide whereas $\text{SiO}_2 + \text{Al}_2\text{O}_3 < 5\%$ is consistent with matrix substitutions in the iron oxide framework. B) $\text{Ca} + \text{Al} + \text{Mn}$ vs $\text{Ti} + \text{V}$ diagram for iron oxides analysed in this study. With fields of common iron oxide bearing mineral deposits determined from the empirical data of Dupuis and Beaudoin (2011). Most analyses fall within the skarn field. C) $\text{Ni}/(\text{Cr} + \text{Mn})$ vs $\text{Ti} + \text{V}$ wt% diagram after Dupuis and Beaudoin (2011) and D) $\text{Al} + \text{Mn}$ wt% vs $\text{Ti} + \text{V}$ wt% after Nadoll et al., (2014). In Figure 26 C) and D) most analyses also lie in the skarn field.

LA-ICPMS analysis

Ninety sites from hematite in 10 samples were analysed by LA-ICPMS. Analyses were conducted on sites previously analysed by electron microprobe. Data with high concentrations (> 2 wt %) of Al, Si, Ca or Mg were omitted due to potential contamination from phases other than hematite (e.g. silicate or carbonate inclusions). As a result, only 24 hematite analyses (those with $\text{Al} + \text{Si} < 4$ wt %) are presented here. Of these 24 hematite analyses, one is from a calc-silicate sample (2066635), seven are from a granite sample (2066169), three are from a granite sample (2066656), five are from a metasediment sample (2066641) and eight are from a metasediment sample (2066655) (Figure 27, Appendix 4).

Concentrations of trace elements normalised to crustal abundance show a general increase

based on the periodic table from alkali metals (left) to metalloids (right) (Figure 27). High concentrations of Nb and Ta in one granite sample may reflect an inclusion of a Ti-rich phase, with Nb and Ta being common substitutes for Ti. Hematite shows consistently elevated concentrations of Mo, W, Co, Cu, Sn, Sb, Pb and Bi up to two orders of magnitude greater than average crustal abundance (Figure 27).

REE concentrations in hematite are almost exclusively below PAAS with similar patterns of LREE depletion and flat HREE for all samples (Figure 28). Hematite grains in granite and metasedimentary samples have variable positive Eu anomalies. No Eu anomaly is evident in the three hematite grains host in calc-silicate rock.

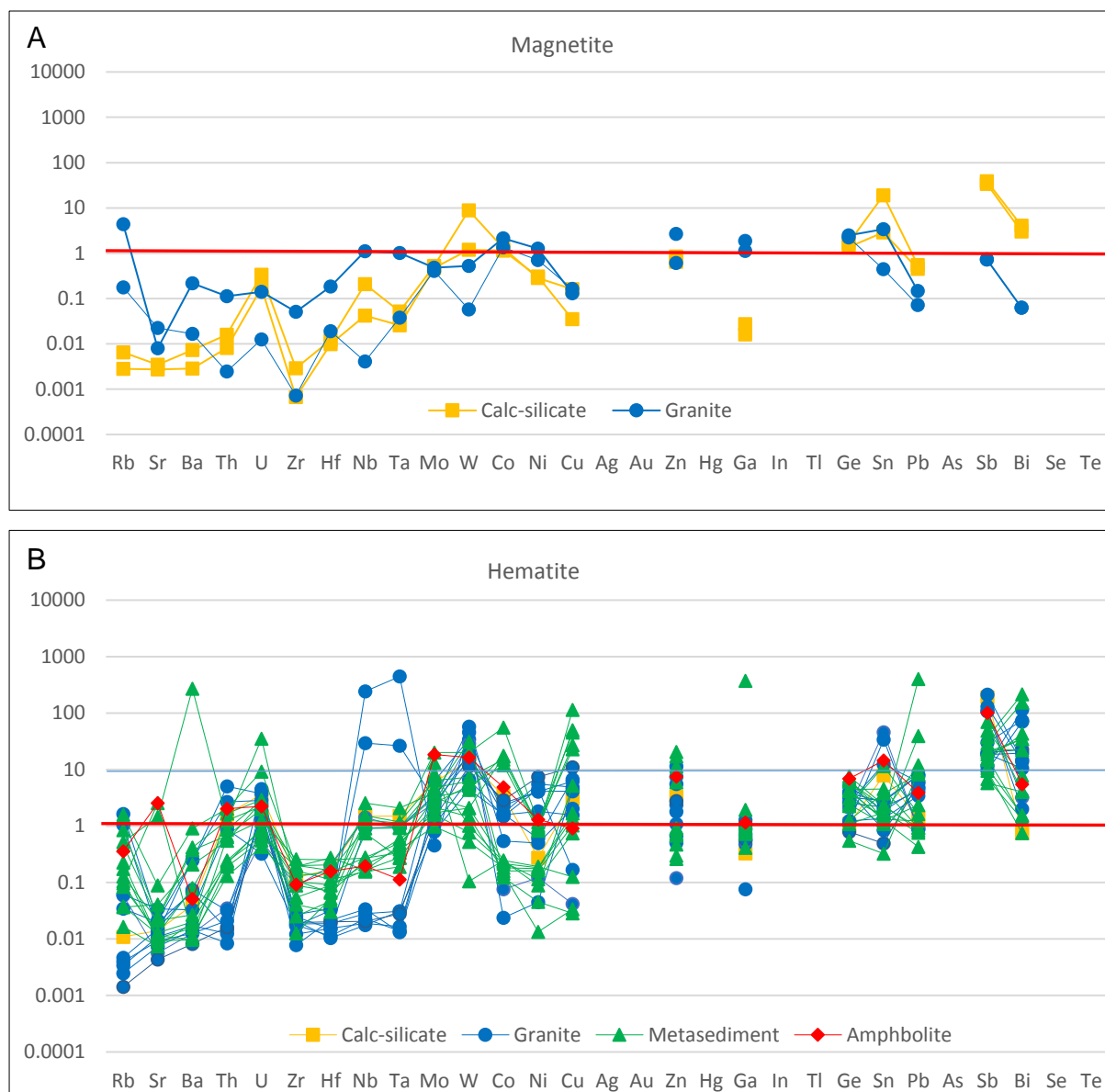


Figure 27. Multi-element diagrams for A) magnetite; and B) hematite normalised to average upper crust. Four magnetite grains preserve high Ge and Sb contents and variable Zn, Ga, Bi, W, Sn, Cu and U contents. Co and Ga are enriched in the granite magnetite. Ge, Sb, Bi, W and Sn are enriched in calc-silicate magnetite. Ba, Sr, Zr, Hf, Pb and Th are depleted in magnetite within calc-silicate rock and granite. As, Se and Ag are below the detection limit. Hematite (24 grains) contains elevated Sb, Bi, and Sn concentrations, variable Ni, Pb, W, U and Th, and low Ba, Rb, Sr, Zr, and Hf. Cu is present in granite (up to 10 times average upper crustal abundance) and metasediments (up to 100 times average crustal abundance).

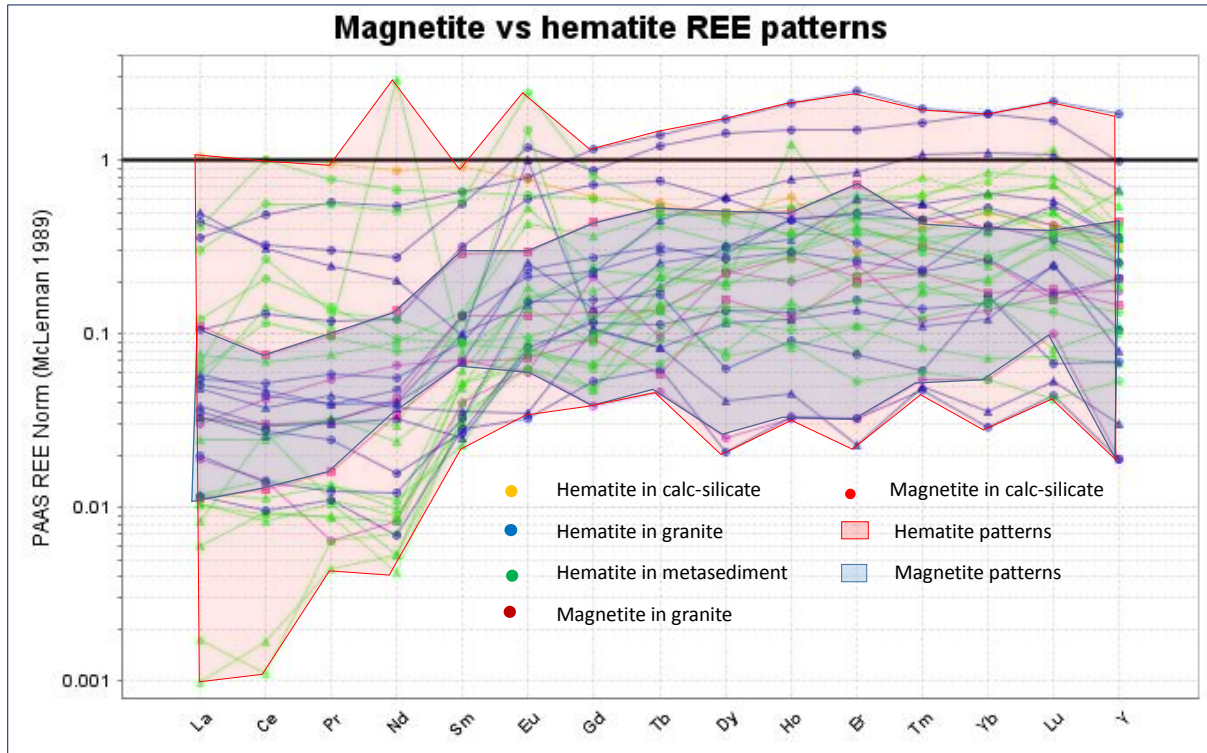


Figure 28. REE patterns of hematite and magnetite. Magnetite in granite has less REE than magnetite host in calc-silicate rock. REE are depleted in hematite from metasandstone, granite, calc-silicate rock. Overall, magnetite has lower REE concentration relative to hematite.

3.3.5 Feldspars

Electron microprobe analysis

Twenty-two feldspar grains were analysed by electron microprobe. Five grains are from granite with HSCC alteration (2066174, from drillhole PSC4_SASC2), and five grains are from unaltered granite with very little MB alteration (2066178, from drillhole HL002). Seven grains are from calc-silicate with HSCC alteration (2066203, from drillhole GHDD4), and four grains are from calc-silicate with CAM alteration (2066199, from drillhole WWDD1). One grain is from mafic rock (amphibolite) with MB alteration (2066177, from drillhole HL002).

Eighteen of the 22 feldspar grains analysed are K-feldspar, two are sanidine and two are andesine (Figure 29). The K-feldspars show a narrow range of major element concentrations (29-31 wt % Si, 9-10 wt % Al, 12-14 wt % K), with an average chemical formula of $K_{0.91}Al_{1.03}Si_{3.03}O_{8.12}$. The exception is one grain from 2066199 with 30.2 wt % Si, 11.8 wt % Al, 8.1 wt % K, 1.3 wt % Fe and 0.51 wt % Mg. The two sanidine and two andesine grains from granite sample 2066178 contain 13.1-15.0 wt % Al, 26.5-29.7 wt % Si, 3.6-6.4 wt % Na, 0.59-3.8 wt % K and 0.65-2.9 wt % Ca. Other elements in feldspar grains with concentrations in the range of 10-30 % of rock included Ba, Na, Fe, Ca, Mg and Cl (Appendix 3). Concentrations of Ba, Na, Ca and Fe show considerable variation independent of protolith types.

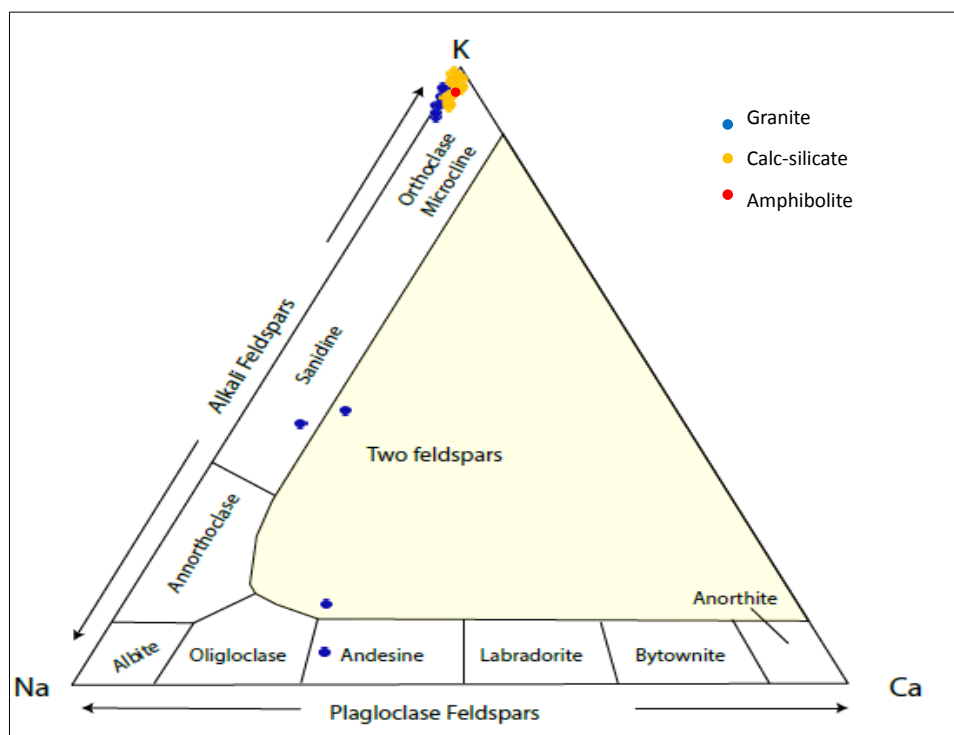


Figure 29. K-Na-Ca ternary diagram showing the composition of the eighteen K-feldspar and four sanidine-andesine grains analysed.

LA-ICPMS analysis

Twenty-four feldspar grains were analysed by LA-ICPMS with the beam focused on the location of previous electron probe analyses. Seven analyses have Al and Si concentrations inconsistent with the stoichiometry of feldspar or had high Mg and Ca content. These analyses presumably contained significant volumes of inclusions smaller than the scale of the laser ablation beam and were not included in the results presented here. Of the remaining seventeen analyses, twelve are K-feldspar (7.8-14.6 wt % K, 0.03-1.04 wt % Na and 0.09-1.1 wt % Ca), two sanidine (3.8-4.6 wt % K and 4.6-5.3 wt % Na, 0.4-0.7 wt % Ca), two andesine (2.0-2.7 wt % K and 5.7-6.2 wt % Na, 1.4-1.5 wt % Ca) and one anorthite (1.3 wt % K and 6.2 wt % Na, 2.4 wt % Ca).

The sanidine, andesine and anorthite grains show similar trace element patterns (Figure 30) with all elements at or below average crustal abundance. The K-feldspar grains show a similar pattern to other feldspars at low concentrations, but had large variance from average crustal abundance compared to other feldspars for all elements (including REE) except Sr and Ag. In K-feldspar, the majority of elements show concentrations between 0.01 and 10 times crustal abundance. One analysis shows Cu at two orders of magnitude above crustal abundance.

Of the ten pathfinders identified by Fabris et al. (2013) (Au, Ag, As, Bi, Cu, Mo, S, Sb, Se and W), K-feldspar can only accommodate significant concentrations of Sb and to a lesser extent Sn. The K-feldspar characteristically preserves slightly higher REE concentrations compared to other feldspar (sanidine, andesine and anorthite). In some samples, K-feldspar displayed LREE enrichment (Figure 31).

The REE patterns for sanidine, andesine and anorthite feldspars are similar, showing

concentrations for most elements well below PAAS, flat HREE, variable LREE depletion relative to HREE and a consistent, pronounced positive Eu anomaly (Figure 31). The K-feldspar shows a similar pattern to other feldspars at low concentrations of REE, but has greater variance at higher concentrations. At higher total REE (particularly in calc-silicate samples), the patterns changed, tending toward LREE enrichment without an Eu anomaly (Figure 31).

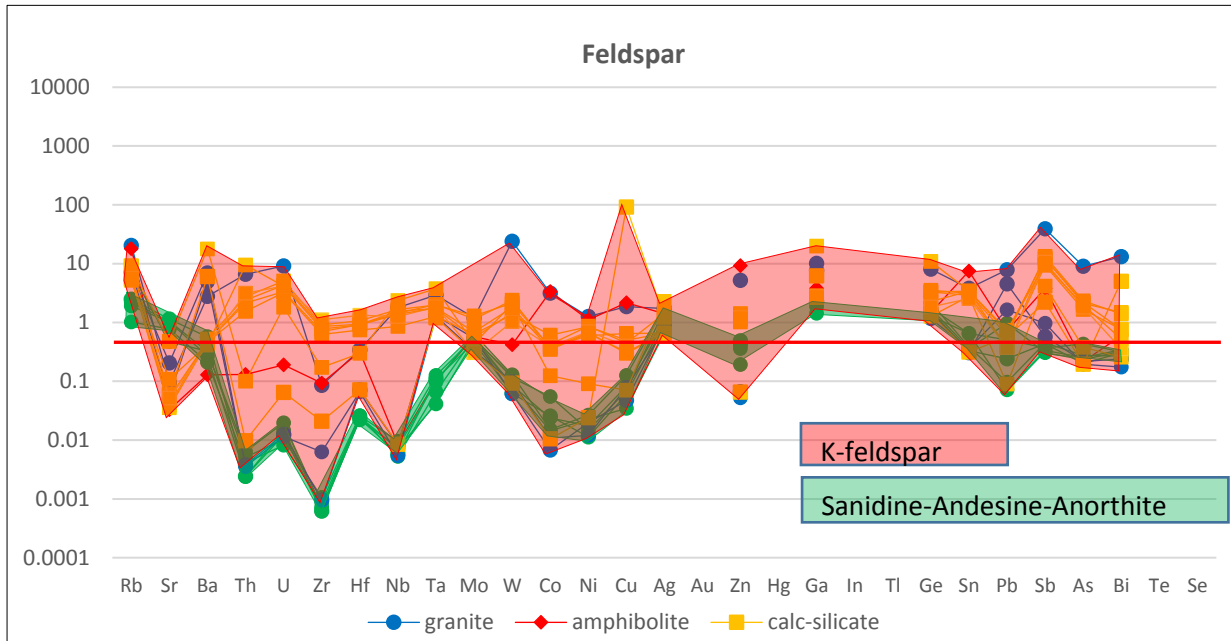


Figure 30. Multi-element plot for analysed feldspar normalised to the upper crust. Analyses below detection limits are represented at half the detection limit. Relevant detection limits are Zr = 0.12-0.17 ppm, Nb = 0.06-0.11 ppm, Mo = 0.5-0.7 ppm, Ag = 0.07-0.19 ppm, Hf = 0.12-0.14 ppm and Bi = 0.04-0.05 ppm).

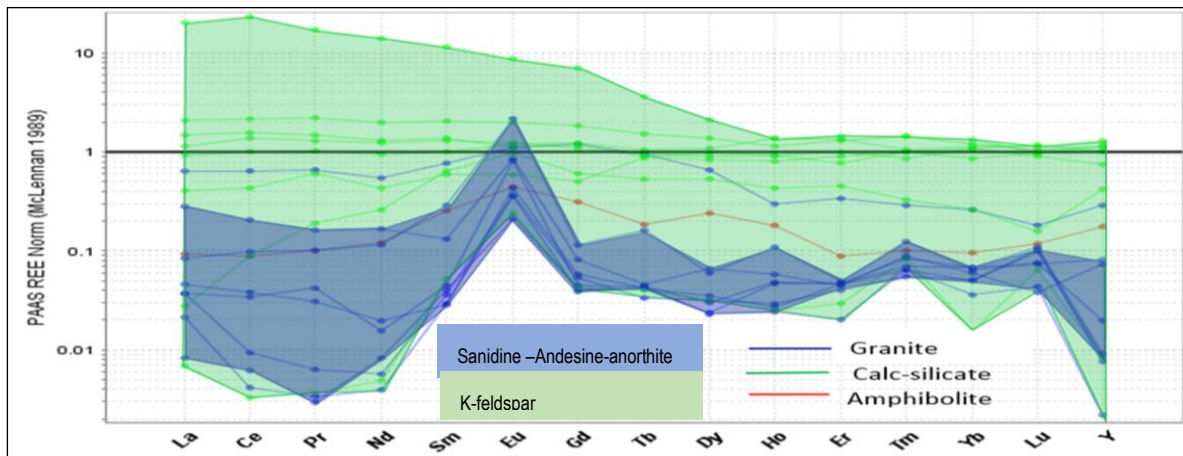


Figure 31 (previous page). REE patterns for analysed feldspar grains.

3.3.6 Chlorite

Electron microprobe analysis

Thirty-two chlorite grains were analysed by electron microprobe. Two grains effected by Fe and Ca alteration are not presented here. Eleven grains are from a metasediment sample with CAM alteration (2066655, from drillhole IHAD5), eleven grains are from amphibolite with MB alteration (2066177, form drillhole HL002), five grains are from calc-silicate, two grains are from CAM alteration (2066166, from drillhole CSD1) and three grains are from calc-silicate with HSCC alteration (2066635, from drillhole IHAD6). Five grains are from granite; four grains are from HSCC alteration (2066169, from drillhole DRD1) and one grain is from granite with CAM/HSCC alteration (2066656, from drillhole IHAD 2). Analysis of chlorite grains show Fe:Mg:Al compositions ranging between 40:30:30 to 70:10:20 with few out of the range. Three calc-silicate chlorite grains have slightly higher Mg and one granite chlorite and one amphibolite chlorite have slightly lower Al (Figure 32).

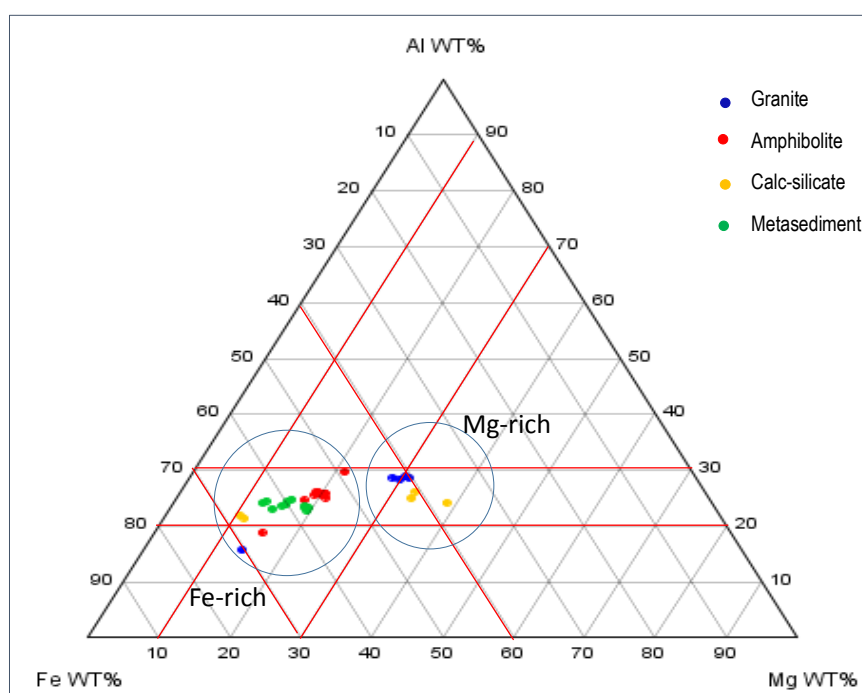


Figure 32. Al-Fe-Mg ternary diagram showing analytical results for chlorite hosted in granite, amphibolite, calc-silicate and metasediment. The Fe-rich and Mg-rich groups are circled. Fe-rich chlorite is preserved within all rocks. Mg-rich chlorite is preserved within granite and calc-silicate. Red lines showed the limits of the Fe:Mg:Al ratios used.

LA-ICPMS analysis

Fifty-six chlorite sites were analysed by LA-ICPMS, including all sites of previous electron probe analyses. Thirty-two analyses show major element stoichiometry consistent with chlorite. Twenty-four analyses show elevated concentrations of Ca, K, Na, Al, Si or Mn, indicating significant inclusions of other minerals and are not included in the data presented below.

Trace element patterns are similar for all chlorite analyses despite the diversity of rock type. The granite and amphibolite samples show a narrow range of trace element abundance, whereas there is a broader range of data for calc-silicate and metasediments (Figure 33). Chlorite from

granite contains Co, Ni and Zn at an order of 1-2 magnitudes above average crustal abundance. In granite and amphibolite, most trace element patterns are at or below average crustal abundance. Calc-silicates and metasediments show higher trace element content compared to granite and amphibolite, except for Ni and Zn.

The highest concentration of Cu is in chlorite host within metasediments and calc-silicate rock. Chlorite in granite preserves the highest enrichment of Ni at >10 times that of chlorite in other lithologies (Figure 33). Ag concentration is highest in metasediments. Higher Cu, As, Mo, Sb, W and Bi is observed in some calc-silicate samples. Cu and Ag are high in siliciclastic metasediment.

Chlorite REE patterns in calc-silicate samples show flat HREE patterns with relative enrichment in LREE (Figure 34). Chlorite REE patterns for granite, metasediment and amphibolite samples all show lower concentration than for calc-silicate rocks, with granite being the lowest, then metasediment, then amphibolite at close to PAAS. Concentrations of trace elements and REE appear to be related to alteration intensity with more intensely altered rocks (in this case calc-silicate protoliths) being consistently enriched in trace elements and REE.

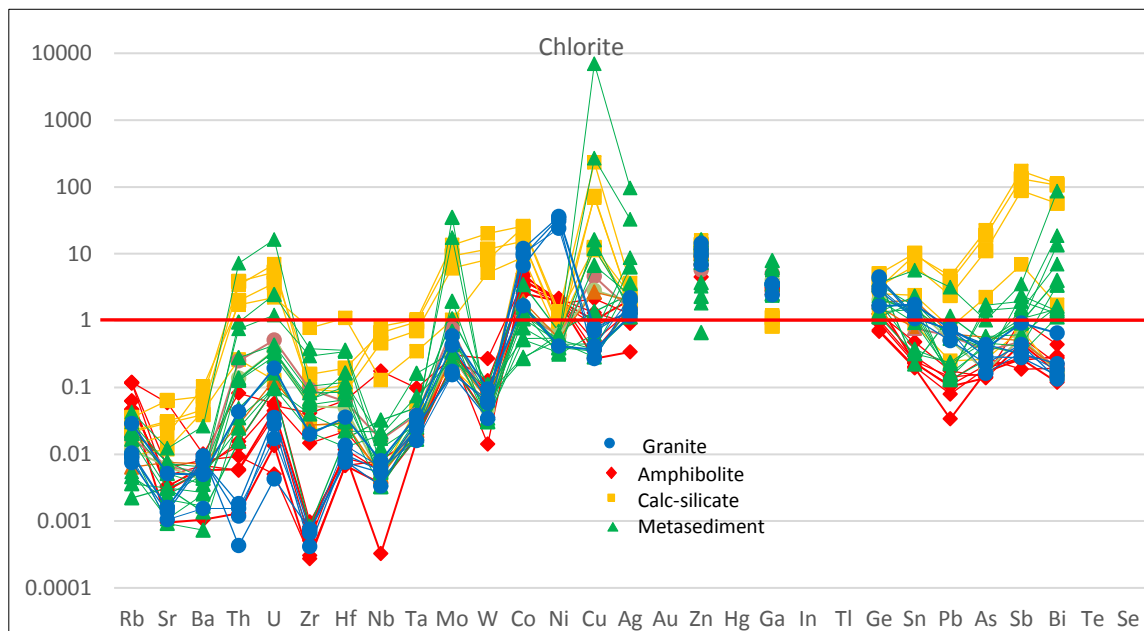


Figure 33. Multi-element diagram for chlorite normalised to the upper crust. Chlorite is elevated in Co, Cu, Zn, Ga, Ge, Ag, Sb and Bi in all four rock types. Twenty-two elements were richer in calc-silicate rock except Ga, and Ag is highest in metasediments. Ni is highest in the granite and is 10 times higher than amphibolite, calc-silicate and metasediments. Cu is elevated in metasediments and calc-silicate rock.

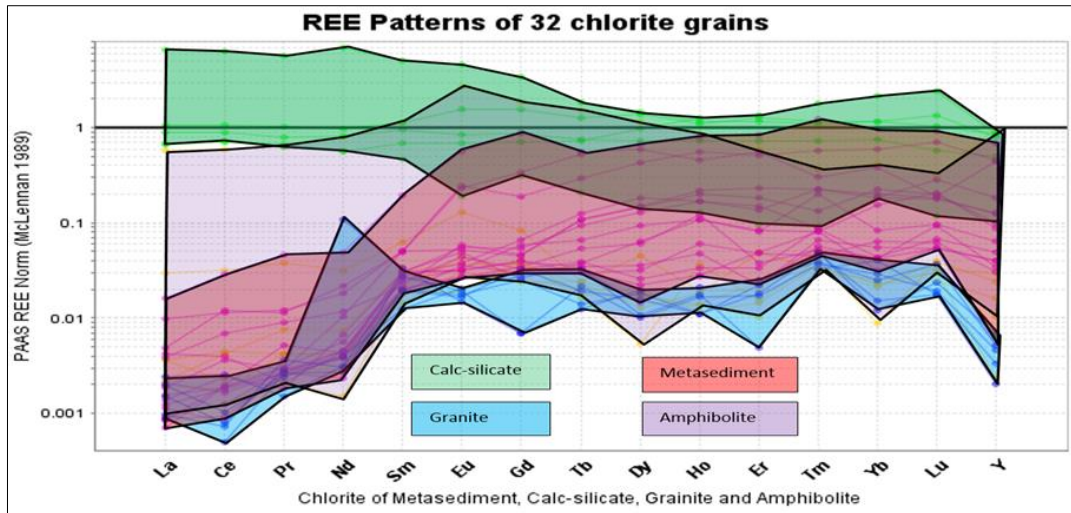


Figure 34. REE patterns for chlorite in the four rock types.

Micas

3.3.7 Biotite

Electron microprobe analysis

Fourteen biotite grains were analysed by electron microprobe. Two grains show evidence of Fe and chlorite alteration were excluded. Eleven grains are from unaltered granite (2066178) and one grain from amphibolite with MB alteration (2066177). The 12 biotite grains show a narrow range of major element concentrations (15.9-17.2 wt % Si, 8.2-8.9 wt % Al, 15.4-22.8 wt % Fe, 1.5-6.4 wt % Mg and 5.0-8.0 wt % K; Figure 35 and Appendix 3). The average biotite chemical formula is $\text{KMg}_{1.1}\text{Fe}_{1.6}\text{Al}_{1.7}\text{Si}_{3.1}\text{O}_{25}$, which is comparable to the standard biotite formula of $\text{K}(\text{MgFe})_3(\text{AlSi}_3\text{O}_{10})(\text{OH})_2$. Biotite grains contain high Ti, Mn and F (up to 1.7 wt % Ti, 0.28 wt % Mn and 1.4 wt % F); moderate Ca, Na, Cl and V (0.08 wt % Ca and Na, 0.03 wt % Cl and 0.04 wt % V average concentration) and low Zr, Cr, P and Zn (0.01-0.02 wt % average).

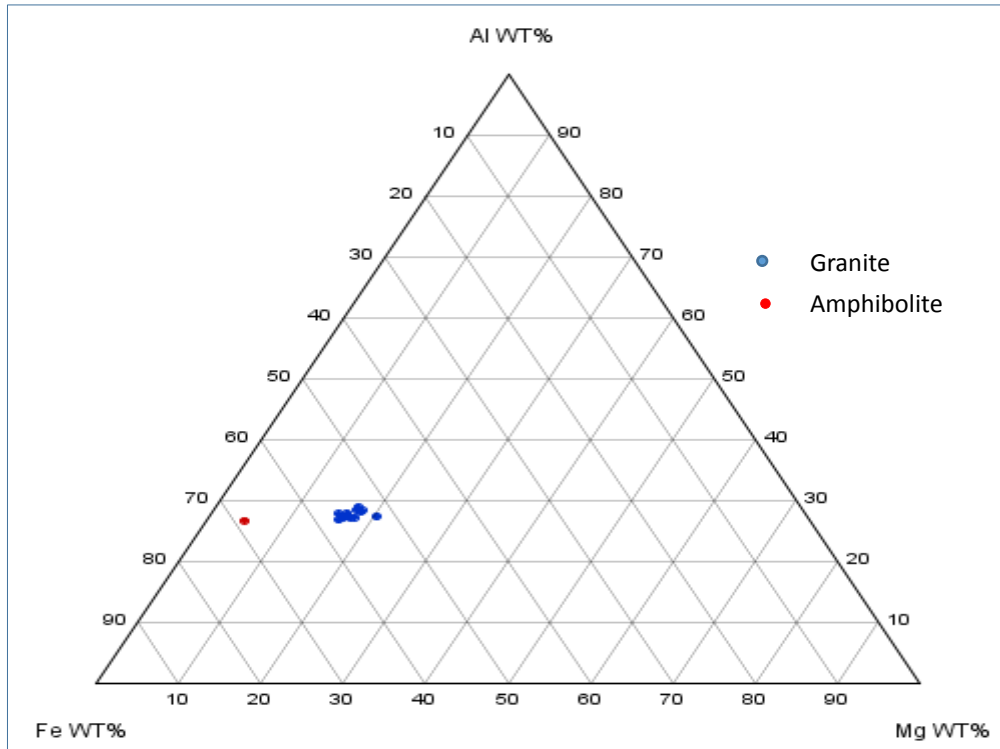


Figure 35. Al-Fe-Mg plot of biotite from granite and amphibolite samples showing the Fe- and Mg-rich nature of the biotite.

LA-ICPMS analysis

Twenty-one biotite grains from granite were analysed by LA-ICPMS with the beam focused on the sites of previous electron probe analyses. Fourteen analysis sites have Al and Si concentrations inconsistent with the stoichiometry of biotite or have high Mg, Ca, P and Mn content beyond the control of Al and Si calibration, thus data for these sites were not included in analysis. The remaining seven biotite grains show average Al 8.8 wt % and Si 16.3 wt % under Al and Si calibration.

The granite biotite shows relatively tight distribution patterns. In one grain of biotite, Au is present at 0.075 ppm. The As and Mo content of biotite are below average crustal abundance. Sr and Zr are well below average crustal abundance, indicating that bulk rock chemistry concentrations for these elements are not controlled by biotite. Biotite has Rb, Ta and Sn at 1-2 orders of magnitude above average crustal abundance. For Th and U content of biotite, there were two groups: one group is below 0.1 and another group is equivalent to or above average crustal abundance, with the highest abundance being 1-2 orders of magnitude. The Hg, Se, Ag and Te content of biotite is below detection limits (Figure 36).

Two REE patterns are observed in the biotite grains. The first shows high concentration of La to Sm, and the second shows low concentration of La to Sm with an order of magnitude difference (Figure 37). REE concentrations are all below PAAS. LREE depletion is observed in biotite from granite samples. The biotite from granite shows a pattern of flat REE depletion and another pattern of generally low REE concentration and extreme LREE depletion. The total REE contents are generally depleted in biotite from within granite.

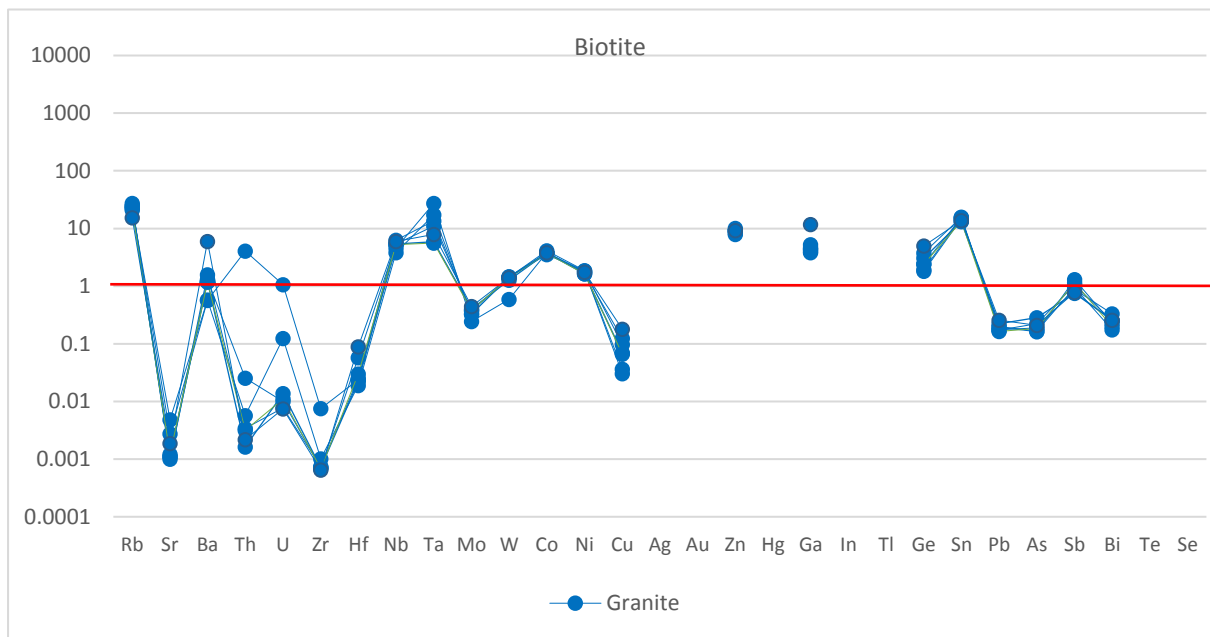


Figure 36. Trace elements for biotite grains within granite (7 grains-2066178) normalised to the upper crust. Ag, Se and Te are below the detection limits of 0.08-0.15 ppm, 12-20 ppm and 0.005 ppm respectively. Cu, As, Sr, Bi, Zr, Hf, Th and U are depleted and Rb, Nb, Ta, Zn, Ga, Ge and Sn enriched in the biotite grains.

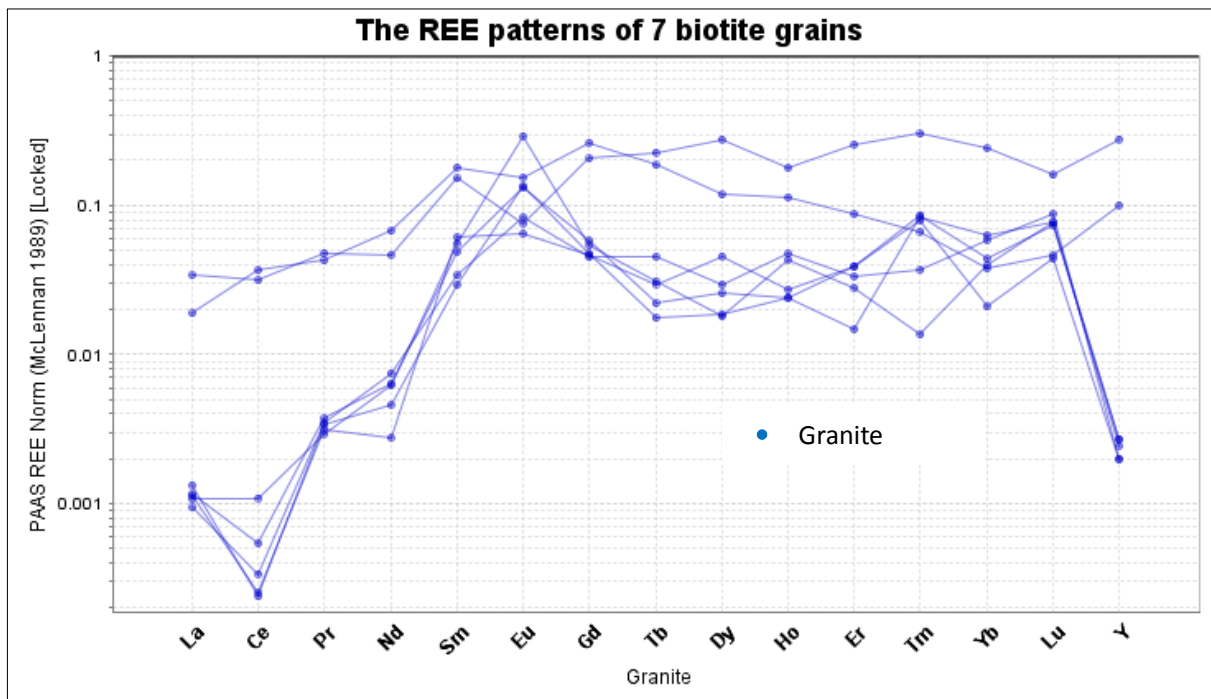


Figure 37. REE patterns for biotite showing two general patterns. The first pattern is flat with higher LREE content. The second shows significantly lower LREE contents. All REE concentrations are below PAAS.

3.3.8 Muscovite

Electron microprobe analysis

Nineteen muscovite grains were analysed by electron microprobe. Nine grains are from granite, one grain is from an unaltered granite (2066178, from drillhole HL002), four grains are from a HSCC/CAM alteration (2066656, from drillhole IHAD 2), and four grains are from a granite with HSCC alteration (2066174, from drillhole PSC4_SASC2). Eight grains are from a calc-silicate rock with MB alteration (2066199, from drillhole WWDD1). One grain is from a metasediment with HSCC alteration (2066641, from drillhole IHAD3) and one is from amphibolite (2066177, from drillhole HL002).

Eight muscovite grains preserve slightly broader range of major element concentrations (20.4-26.3 wt % Si, 11.3-17.8 wt % Al, 2.1-8.9 wt % Fe and 4.9-7.9 wt % K) relative to biotite (Appendix 3). The muscovite chemical formula is $\text{KFe}_{0.39}\text{Al}_{1.2}(\text{Al}_{1.2}\text{Si}_{4.8}\text{O}_{13.8})(\text{F},\text{OH})_2$, which is similar to the standard muscovite $\text{KAl}_2(\text{AlSi}_3\text{O}_{10})(\text{F},\text{OH})_2$ but less K and Fe-rich. The muscovite grains preserve high Mg, Ti, Ca and Ba (up to 1.7 wt % Mg, 0.9 wt % Ti, 0.2 wt % Ca and 0.3 wt % Ba), moderate Na, Mn and F (0.09 wt % Na, 0.08 wt % Mn and 0.19 wt % F on average) and low Zr, Zn, Cr, V and Cl (0.01-0.02 wt % on average). P averaged below 0.01 wt %. These data imply muscovite is Mg, Ca and Ba rich and P-poor.

LA-ICPMS analysis

Fifteen muscovite grains were analysed by LA-ICPMS with the beam focused on the location of previous electron probe analyses. The grains have 4.9-17.1 wt % Al, 20-30 wt % Si and 3.4-8.7 wt % K and 0.8-17.1 wt % Fe in granite, calc-silicate and metasediment rocks. Au, Ag, Hg, Ge and Te are below the detection limit. Fifteen muscovite grains have high Rb, Ba, W, Co, As, Sb, and Th, and low of Sr, Zr and Hf (Figure 38). Three calc-silicate muscovite grains preserve 0.024-0.09 ppm Au.

Four grains preserve complex patterns. One grain shows enrichment ~100 times above average crustal abundance in Se and 10 times above average crustal abundance for Sb and W. A muscovite from metasediment (2066641) has high Bi, Cu, Pb, Ni and Sb at >10 times average crustal abundance

Muscovite REE patterns show REE content close to PAAS (Figure 39). LREE are depleted compared to HREE in granite samples. REEs show an overall depleted pattern relative to PAAS in granite. The muscovite REE patterns approximate PAAS in all but one calc-silicate sample (2066203) which shows extreme REE depletion.

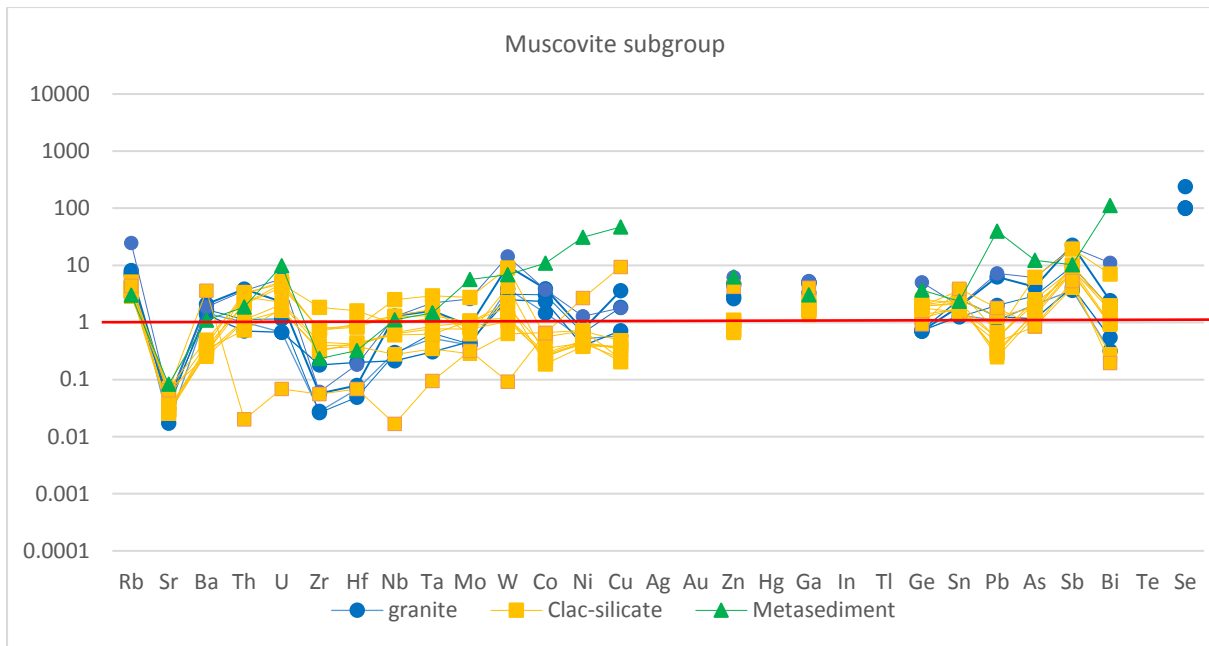


Figure 38. Multi-element plot for 15 muscovite grains (normalised to average upper crust) from granite (2066656 for 4 grains -2066174 for 1 grain), calc-silicate (2066199 for 8 grains and 2066203 for 1 grain) and metasediment (2066641 for 1 grain).

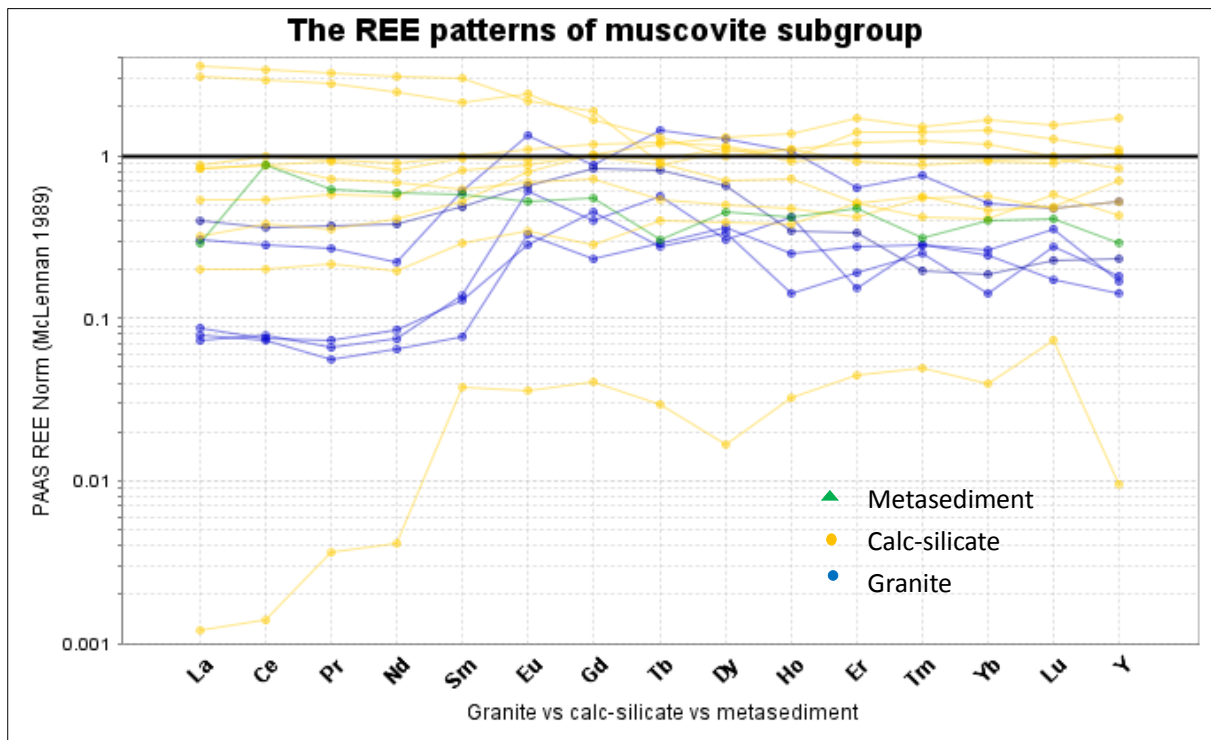


Figure 39. REE plot for muscovite grains from granite, calc-silicate and metasediment.

3.3.9 Carbonate

Electron microprobe analysis

Twenty-six carbonate grains were analysed by electron microprobe. Three grains are from a

granite with HSCC alteration (2066174, from drillhole PSC4-SASC2), five grains are from an amphibolite with MB alteration (2066177, from drillhole HL002), fifteen grains are from calc-silicate, eight grains are from a calc-silicate with CAM alteration (2066199, from drillhole WWDD1), and seven grains are from a calc-silicate with HSCC alteration (2066635, from drillhole IHAD 6). Three carbonate grains are from a metasediment with CAM alteration (2066655, from drillhole IHAD 5). The carbonate compositions varied from end-member calcite (CaCO_3) to dolomite $\text{CaMg}(\text{CO}_3)_2$ with a group of samples from calc-silicate rocks having significant Fe concentrations consistent with ankerite $((\text{Ca, Fe, Mg})_2(\text{CO}_3)_2)$ (Figure 40).

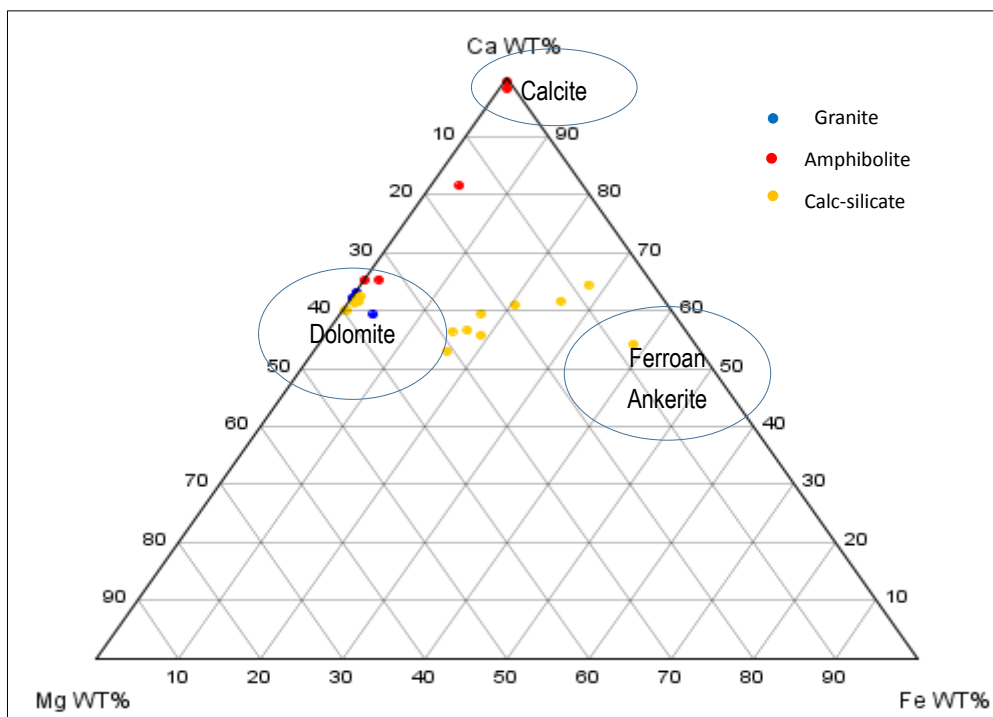


Figure 40. Ca-Mg-Fe ternary diagram for carbonate grains from granite, amphibolite and calc-silicate rocks. Dolomite is Fe- and Mg-rich. Calcite occurs in amphibolite.

Dolomite

LA-ICPMS analysis

Fourteen dolomite grains were analysed by LA-ICPMS with the beam focused on the location of previous electron probe analyses (granite sample 2066174, amphibolite sample 2066177, calc-silicate sample 2066635 and metasediment sample 2066655). Eleven of fourteen grains have stoichiometry consistent with carbonate minerals. Three of the fourteen analyses have elevated concentrations of Si or Al indicating significant inclusions of silicate minerals and are not presented below.

The trace element patterns are similar for all carbonate grains analysed. Concentrations of trace elements compared to average crustal abundance increase across the periodic table from alkali metal (left) to metalloids (right) on the multi-element diagram with most elements at or below average crustal abundance (Figure 41). The exceptions are Cu, Sb and Bi which range from below to ~ 1 order of magnitude greater than average crustal abundance.

REE patterns are also similar for all carbonates analysed, with a convex pattern showing relative enrichment in the middle REEs (Sm, Eu, Gd, Tb, Dy, Ho) and Y compared to the LREE and HREE (Figure 42). Two analyses from a metasedimentary sample and two from the amphibolite preserve a high positive Eu anomaly.

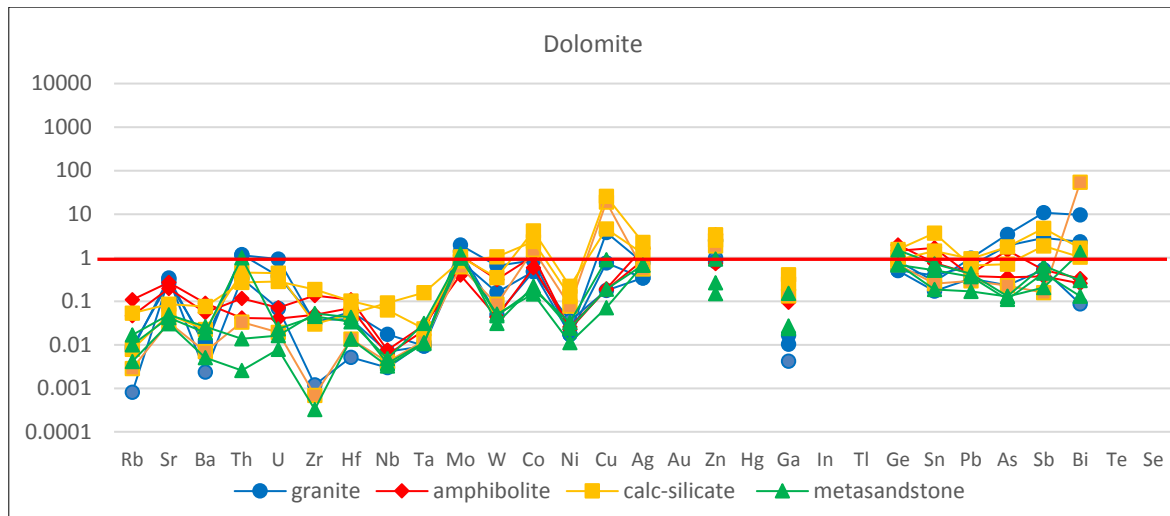


Figure 41. Multi-element diagram for 11 dolomite grains (normalised to average upper crust) within the four rock types. Se, Sb and Hg are below the detection limit. One grain preserves 0.12 ppm Ag, two grains preserve Ta (0.02 and 0.025 ppm) and Au (0.10 and 0.06 ppm). Dolomite shows enrichment of Co, Cu and Zn and depletion of Ba, Ni, Ga, Rb, Sr, Zr, Nb, Hf, W and U in the calc-silicate rock.

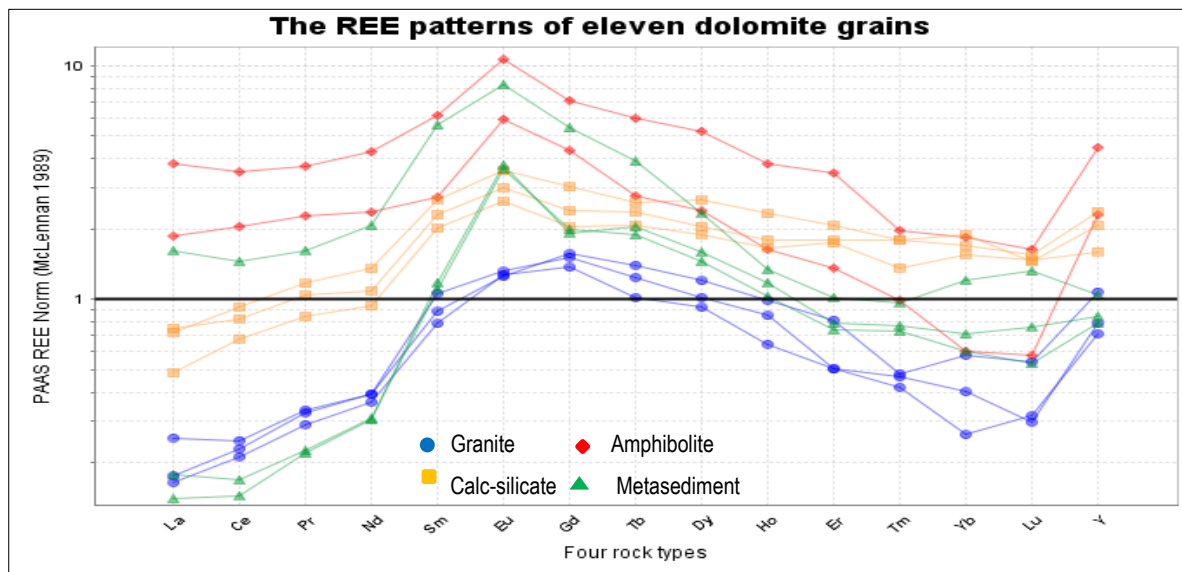


Figure 42. REE plot for dolomite grain analysis. HREE is enriched in dolomite from calc-silicate rock. LREEs are more variable relative to HREEs, and are enriched in amphibolite and depleted in granite.

3.3.10 Apatite and Nine other Minerals

Electron microprobe analysis

Eight apatite grains were analysed by electron microprobe. Four grains are from a granite with HSCC alteration (2066174, from drillhole PAS4_SASC2). Four grains are from calc-silicate, two grains are from a calc-silicate with CAM alteration (2066199, from drillhole WWDD1),

and two grains are from a calc-silicate with HSCC alteration (2066203, from drillhole GHDD4 and 2066635, from drillhole IHAD6).

The eight apatite grains average 38.7 wt % Ca, 17.2 wt % P and 36.6 wt % O and satisfy the standard chemical formula $\text{Ca}_5(\text{PO}_4)_3(\text{F},\text{Cl},\text{OH})$ (Appendix 3). The average apatite chemical formula is $\text{Ca}_{5.05}\text{P}_{2.90}\text{O}_{11.98}\text{F}_{1.06}$. The apatite is enriched in F (3.9 wt %), Mg, Mn and Zr (0.12-0.25 wt % average of for each element). Na, Si, Cl, K and Al range from 0.04-0.09 wt %. Zn, V, Ti, Cr and Ba are ≤ 0.01 wt % concentration. Apatite can be seen clearly to replace the monazite at electron microscope.

Additional analyses were done on garnet (2 spots), gypsum (2 spots), manganosite (4 spots), pyroxene (10 spots), ilmenite (3 spots), rutile (2 spots), monazite (2 spots), sphalerite (3 spots) and quartz (1 spot). Garnet is andradite with 17.0 wt % Si, 18.4 wt % Fe, 23.6 wt % Ca and 1.73 wt % Al with the chemical formula $\text{Ca}_3\text{Fe}_2\text{Si}_3\text{O}_{12}$. Pyroxene contains 24.7 wt % Si, 14.7 wt % Fe, 7.0 wt % Mg, 8.6 wt % Ca and 1 wt % Al, and is classified as augite with the chemical formula $\text{Ca}_{0.5}\text{Mg}_{0.7}\text{Fe}_{0.6}\text{Si}_2\text{O}_6$.

It is noted that all trace element and REE concentrations in the nine additional mineral phases were analysed using LA-ICPMS, but the data as not a statistically large enough population to assess (Appendix 4) and are therefore not presented here.

3.4 DISCUSSION

3.4.1 Significance of pyrite chemistry

Previous workers have attempted to use pyrite chemistry as an indicator of the conditions and geological setting at the time of pyrite growth (e.g. Bralía et al., 1979; Bajwah et al., 1987; Bettina 1989; Abraitis et al., 2004; Clark et al., 2004; Xiao-Wen et al., 2015). Fe deficient pyrite, as indicated by high S/Fe ratios, are typically interpreted as p-type semiconductors and tend to form in lower temperature conditions (Abraitis et al., 2004). The chemistry of these pyrite grains typically shows enrichment in As, Co, Ni, Sb and possibly Cu, Ag, Au and Sn up to percent level. S deficient pyrite grains, indicated by low S/Fe ratios, are typically interpreted as n-type semiconductors, form in higher temperature environments and are Co enriched (Abraitis et al., 2004). All of the pyrite grains observed in this study are Fe-deficient, p-type grains with S/Fe_{atom} ratios of 2.02-2.05, and are enriched in Se, Te and As, which have likely substituted for S. As has a mostly positive relationship with Au (Figure 25A).

Co/Ni ratios are also recognised to reflect the origin of pyrite grains (e.g. Bralía et al., 1979; Bajwah et al., 1987; Bettina 1989; Abraitis et al., 2004; Clark et al., 2004; Xiao-Wen et al., 2015). Bralía et al. (1979) suggested the Co/Ni ratio in pyrite proved a more reliable indicator in ore genesis than previously presumed. Based on work at the CSA Cu-Pb-Zn deposit, Bettina et al. (1989) suggested that Co/Ni ratios were on average 2.4 when formed in relation to hydrothermal processes, and that enrichment of Se is indicative of a metamorphic origin. Based on work at the Cadia Fe-Cu deposit, New South Wales, Bajwah et al. (1989) suggest that Co/Ni ratios >10 are indicative of a volcanic origin. Based on work at the Tianhu Fe deposit, NW China, Xiao-Wen et al. (2015) argued that pyrite with Co/Ni ratio 0.6-9.75 formed in a sedimentary type deposit originally but was later overprinted by a hydrothermal event. Co/Ni ratios (and Co and Ni concentrations) are also suggested to be sensitive to temperature of

formation; with lower temperature tending to have lower Co/Ni ratios; and higher temperatures leading to higher Co/Ni ratios (Abraitis et al., 2004).

The Co/Ni ratios for the samples used in this study cover a broad range of 0.24-9.75. The two calc-silicate samples, one metasediment and three granite samples have Co/Ni ratios <1, and are comparable with pyrite of a sedimentary origin (Figure 23). Four metasediment and three granite pyrite grains have a Co/Ni ratios between 1 and 10, suggesting a hydrothermal origin. It is noted though that two of the pyrite in metasediment samples have Co/Ni ratios close to 10 (9.42-9.75) and are therefore at the high end of being interpreted as hydrothermal in origin and border with values of pyrite with a volcanic origin (Figure 23 and Appendix 4). The large variations in Co/Ni contrast with the tight clustering of S/Fe ratios (Figure 22). Interesting that the petrogenetic context of the pyrite grains is similar in each sample (Figure 10A, 11B and 16C; see Chapter 2) but the Co/Ni chemistry was very different. The granite pyrites have Co/Ni ratios that fall within the magmatic field (Figure 23 and 16C) defined by Xiao-Wen et al. (2015). The protolith is suggested to have a strong control on the Co/Ni ratios and Co/Ni ratio may not be a great measure of the fluid chemistry.

As observed in pyrites from this study, Abraitis et al., (2004) have shown that As, Se, Co, Ni, Te and Au commonly occur at high concentrations in pyrite. In addition, Ag and Bi also have elevated concentrations in some or all of the pyrite grains analysed here (Figure 25). Concentrations of Ag, Au and Bi are significantly enriched in pyrites from metasedimentary protoliths compared to calc-silicate or granite protoliths, whereas Co, Ni, As, Se and Te are enriched in pyrite grains from all rock types. As-rich pyrite is considered by Abraitis et al. (2004) to be characteristic of pyrites formed at low temperature, consistent with the p-type S/Fe ratios of all pyrites analysed in this study. It is not clear to what extent differences in the trace element concentrations of pyrites in the three protolith types reflect protolith control or the variable effects of hydrothermal alteration.

3.4.2 Trace element deportment

The behavior of trace elements and REE may differ depending on the process by which they may enter the sulphide mineral lattice, their ability to substitute for major elements, and their availability within different protoliths and from alteration processes (Abraitis et al., 2004). In this study, sulphide minerals (pyrite, chalcopyrite and bornite) showed consistently elevated concentrations of trace elements (Table 5). Elements of elevated concentration include those commonly observed to substitute for sulphur in the mineral lattice of sulphide minerals (As, Se and Te) (Bettina 1989; David et al., 1995; Abraitis et al., 2004), those which substitute for Fe in the mineral lattice (Co and Ni) (David et al., 1995; Abraitis et al., 2004) and those that substitute for Cu in the mineral lattice (Ag, Sn, Bi and In) (Bettina 1989; Carew et al., 2006). In particular, pyrite was consistently rich in Co, Au, As, Se and Te, and to a lesser extent Ag, Ni and Bi. Chalcopyrite was consistently rich in Cu, Se and Te, and some grains showed elevated Ag, Au and Bi, while bornite was consistently rich in Cu, Ag, Bi, Se and Te, with lesser Au and Sb.

Additionally, this study found that hematite consistently contained elevated concentrations of Sb, Bi, Cu, Mo and W, and to a lesser extent Co, Zn, Sn and Pb. Other studies with similar findings include Andrei et al. (2008), who found hematite with significant concentrations of W and Bi at Canadian Creek, Yukon, Canada; Carew (2004) who showed hematite from IOCG deposits in the Cloncurry district are characterised by elevated As, Ga, Sb and W concentrations; and Satoshi et al. (2010) who found Sb can substitute for Fe in iron-oxide minerals, particularly under oxidising conditions. Therefore, this study and others show that hematite has the capacity to incorporate a number of elements as lattice substitutions, including important pathfinder elements in IOCG systems.

Magnetite analysed in this study did not show consistently elevated concentrations of trace elements. Ge, Sn, Sb and W showed variable concentrations, reaching ~10 times average crustal abundance in magnetite from one calc-silicate sample (Figure 27A). Sarah et al. (2014) showed that magnetite associated with magmatic-hydrothermal deposits including IOCGs and that forms at high temperatures (500°-700°C) typically preserves elevated concentrations of elements including Ni, V, Co, Zn, Mn and Sn. Conversely, magnetite forming at temperatures <500°C in hydrothermal (and other) environments will be notably depleted in these elements, likely due to their low solubility in low temperature fluids. The depletion of these elements within the magnetite analysed in this study is suggestive of formation associated with low temperatures (<500°C) in a hydrothermal environment. Carew (2004) showed that magnetite in IOCG systems in the Mt Isa district often preserve detectable concentrations of elements including Ti, Sc, Co, Ni, Cu, Zn, Ga, Sn, Pb, Mn, V, Cr and Mo. Similar patterns were observed in this study, although the concentrations of Mn, Ti, V and Cr are variable and Ga is consistently low (Figure 27A; Appendices 3 and 4).

In contrast to magnetite, hematite preserves elevated concentrations of trace elements. Hematite also often incorporates multiple inclusions of chlorite, quartz and sulphide minerals (Figures 10, 16 and 17) at a scale smaller than the ~30 micron laser ablation spot size used in analyses. Therefore, it is possible that elevated concentrations of trace elements resulted from inclusions (particularly, sulphide minerals), rather than from the hematite lattice. It is of note that apart from Co, the suite of elements enriched in hematite is different to the enriched elements in sulphide minerals.

Two feldspar types were identified: a sanidine-andesine-anorthite group and K-feldspar group (Figure 30). The former shows a higher concentration of Sr, lower concentrations of other trace elements and a narrower distribution range for trace elements normalised to upper crust values (Figure 30). Two K-feldspar samples (one from calc-silicate and another from amphibolite) contain Cu at ~100 times average crustal abundance. The trace elements including Th, U, Zr, Hf, Nb, Ta, W, Co, Ni and Cu are well below average crustal abundance in sanidine-andesine-anorthite and vary from 0.1-10 times average crustal abundance in K-feldspar. K-feldspar grains analysed in this study consistently contain Rb and Ga at a slightly greater concentration than average crustal abundance. K-feldspar from two locations was analysed - one from the centre of a hematite vein (sample 2066203) and the other from the within a carbonate vein (sample 2066199). The K-feldspar from within the hematite vein was found to be Ba-rich (~ 1.2 wt % Ba) and Fe-poor (~ 0.3 wt % Fe), and the calc-silicate K-feldspar is Fe-rich (~ 1.2 wt % Fe) and Ba-poor (~ 0.03 wt % Ba). These results are consistent with the findings of Kontonikas-Charos et al. (2017), who also report Ba-rich and Fe-rich K-feldspar in the eastern Gawler Craton IOCG system. Furthermore, Viladkar (2015) suggested that substitution of K by Ba in K-feldspar is reflective of very high temperatures during magma crystallisation. This suggests that the Ba-rich feldspar may have grown under higher temperature conditions relative to the Fe-rich feldspar identified in this study. David et al. (2000) and Henry et al. (2015) also suggested that growth of Ba-rich and Fe-rich K-feldspar is reflective of involvement of Ba-rich and Fe-rich fluids.

Chlorite from calc-silicate sample 2066635 showed higher trace element concentrations (with the exception of Rb, Ni, Zn and Ga) than chlorite samples from metasedimentary rock and granite protoliths. Chlorites from the calc-silicate sample had elevated concentrations of Sb and Bi and a slightly elevated concentrations of Cu, Ag and Co. In contrast, chlorites from the metasediment sample had elevated Cu and Ag and slightly elevated concentrations of Bi. Furthermore, chlorite from the calc-silicate sample had higher Σ REE and LREE enrichments compared to chlorite from other sample types, which showed depleted LREE compared to

HREE. Uvarova et al. (2018) identified late chlorite recrystallisation is recorded by compositional variation of chlorite proximal to chalcopyrite, these are consistent with the observation results for remobilisation and deposits of Cu.

Chlorites from the same geothermal field can have wide compositional variations related to protolith and thermodynamic conditions, particularly temperature, but also pressure and fluid composition (Dodge et al., 1973; Cathelineau and Nieva, 1985; Hillier et al., 1991; Árkai et al., 1997; Bertoldi et al., 2001). For instance, chlorite in this study contained elevated concentrations of Co, Cu, Zn, Ga, Ge, Ag, Sb and Bi. This suite of trace elements differed to trace elements identified by Wilkinson et al. (2015) - K, Li, Mg, Ca, Sr, Ba, Ti, V, Mn, Co, Ni, Zn and Pb - which can be incorporated in the chlorite lattice and display systematic spatial variations relative to centres of porphyry mineralisation. Three endmember chlorite sample types (Fe-rich, Mg-rich and Al-rich) are shown to be strongly influenced by composition of coexisting minerals (Dodge et al., 1973; Bernard et al., 1989; Patrice et al., 1993).

There have been various attempts to use major element chlorite chemistry as a geothermometer (Cathelineau and Nieva, 1985; De Caritat et al., 1993). Cathelineau and Nieva (1985) showed that Al content in hydrothermal chlorite was positively correlated to temperature and proposed that it could be used as a geothermometer. Application of the Cathelineau and Nieva (1985) geothermometer to chlorite from this study yielded formation temperature estimates between 250° and 290°C for a majority of samples (Figure 43). However, De Caritat et al. (1993) showed that no single geothermometer provides satisfactory temperature estimates over the range of conditions where chlorite might form. Thus, the temperature of formation estimates of 250°-290°C for chlorite in this study is equivocal.

Previous studies suggest that variations in trace element content within biotite associated with magmatic rocks is controlled by the anhydrous and volatile content of the melt (Nash and Crecraft, 1985) and can be used to correlate geographically disparate volcanic eruptions (Sliwinski et al., 2017). Biotite grains host within granite in this study contains consistently elevated concentrations of Rb, Nb, Co, Ni, Zn, Ga, Ge and Sn (Figure 36), and is consistent with the composition of magmatic biotite as described by Pearce et al. (1984). Two REE patterns were also observed in the biotite grains - one with relatively higher LREE content and a negative Eu anomaly, and the other with low LREE content and a positive Eu anomaly. The overall \sum REE for both groups is below average PAAS. Nash and Crecraft (1985) characterize biotite associated with silicic magmas as being enriched in LREE and having negative Eu anomalies. This suggests that the group of biotite grains with similar LREE and Eu anomaly patterns may also be related to a silicic magma. The Al content of biotite has also been suggested to be a useful vector towards potential IOCG mineralization (Porter 2010). However, our results identified a decrease in Al as a distal vector using biotite in unaltered granite (Figure 36).

Despite the common occurrence of white micas as an alteration product in hydrothermal mineral systems, there are few published studies on trace element chemistry of hydrothermal white mica. Zack et al. (2001) studied white mica from high pressure subduction zone settings and found that trace element behavior is complex and related to co-existing mineral assemblages, fluid-rock reactions, temperature and pressure, with significant trace element enrichment in Cs, Rb and Ba. Cohen (2011) showed that hydrothermal white mica associated with sericitic alteration from the Ann-Mason Cu porphyry deposit in Nevada is enriched in W, Sn and Tl. Yang et al. (2001) concluded that the composition of white mica does shows complex variation in major element chemistry from phengitic to muscovitic compositions in proximity to fluid channels and/or mineralization. Similarly, Tappert et al. (2013) showed that

variations in white mica major element chemistry is related to the degree of hydrothermal alteration, whereby phengite in heavily sericitized, ore-bearing rocks is Si- and Mg-poor, and Al-rich relative to phengite from weakly sericitized rocks. On the other hand, a number of studies have examined trace element chemistry of muscovite from granites and pegmatites associated with Sn, W, Li and rare metal mineral systems (Smeds, 1992; Neiva et al, 2002; Singh 2007; Wang, 2017). These studies highlight the potential for magmatic muscovite to incorporate elevated concentrations of Rb, Cs, Y, U, Nb, Ta, Pb, Sn, Bi, Be, W, Li, Ga, Ti and Mn, with the potential to be used as geochemical exploration tools. Magmatic muscovite associated with Li and Sn mineralisation typically show high concentrations of Sn, even in the absence of cassiterite (e.g. Smeds, 1992). Neiva et al. (2002) indicated that magmatic muscovite partitioned Sn, Sc, Sr and Ba compared to co-existing magmatic biotite in peraluminous granites from Portugal. Wang et al. (2017) analysed coexisting magmatic muscovite and biotite in granites from the Nanling Range (South China) and found that muscovite had typically flat REE profiles with prominent negative Eu anomalies and elevated incompatible trace elements including Rb, Cs, Y, U, Nb, Ta, W, Sn, Pb, Bi, Li, and Be compared to comagmatic biotite.

Muscovite analysed in this study preserves no negative Eu anomaly with most REE lower than PAAS and consistently elevated concentrations of Ga, Ge, Sn, As, Sb, Sn, Se, Rb, U and W (Figure 38), of which As, Sb, W, Bi, and Se are known key pathfinder elements for the eastern Gawler Craton IOCG alteration system (Fabris et al., 2013b). Trace elements in muscovite are generally incorporated by ionic substitution during magmatic crystallisation (Singh, 2007). Previous research suggests that Rb and Li are likely substitutes for K in muscovite structures, whereas W, Nb, Ga, Ti, Mn and Fe are likely substitutes for Al and Si in combinations that maintain charge balance (Graham and Morris, 1973). Of relevance to white micas from the eastern Gawler Craton, Sb⁵⁺ oxidation state has a similar ionic radius to W⁵⁺ and Ti⁴⁺ (Graham and Morris, 1973; Hans 1985) suggesting potential for ionic substitution in white mica. Thus, elevated concentrations of W and Sb in white micas of the eastern Gawler Craton require a coupled substitution tri- or divalent species (for example Fe or Mn) to maintain charge balance (see Appendix 6). Petrological results from this study show that muscovite in calc-silicate and metasediment was formed during hydrothermal alteration (Chapter 2) and may therefore show that hydrothermal white mica associated with IOCG deposits in the Gawler Craton is elevated in a variety of trace elements (Figure 38). Elevated W and Sn within the hydrothermal white mica is similar to the results of Cohen (2012).

Consistent with Land (1980), this study found dolomite is depleted of trace elements, particularly Ni and Ga (Figure 41). With no unique geochemical fingerprint, dolomite results from a variety of evolutionary trends (Chakhmouradian et al., 2016). Large-ion lithophile elements (LILE), such as Sr, Ba and Pb, within magmatic dolomite that is preserved in carbonatite rocks can be depleted by crystal fractionation of minerals such as fluorapatite and monazite. Dolomite alteration is an important upgrading process for Au and Ag (Pan and Dong, 1999). The highest trace element concentrations in dolomite identified in this study were 0.12 ppm for Ag and 0.06 ppm for Au, a finding consistent with CAM and HSCC alteration intensity of the pathfinder index, with the exception of MB. Further, dolomite contains Cu, Sb and Bi above average crustal abundance, but most trace elements were below average crustal abundance. Cu and Bi are present in concentrations 1-2 orders higher in altered calc-silicate samples.

Apatite in the study area contains U (up to 85 ppm), W (up to 38 ppm), As (up to 130 ppm) and Sb (up to 10 ppm)-rich and was responsible for REE enrichment linked to mineralogy (Appendix 4). Mao et al. (2016) suggested that apatite is characteristically enriched in Ca with

have lower concentrations of trace elements that partition into the Ca sites (REE, Y, Mn, Sr, Pb, Th, and U) from mineralized carbonates relative to apatite from un-mineralized carbonates. In particular, IOCG deposits in Canada, China, and Mexico were shown to typically preserve large negative Eu anomalies and low Mn contents. The positive Eu anomalies and high Σ REE in apatite in this study are inconsistent with Mao et al. (2016). Apatite is not the only mineral responsible for REE concentration but in the area apatite is one of major responsible for REE concentration.

High and low temperature mineral phases have been identified in this study from the mineral chemistry. These phases include magnetite, hematite and chlorite (Figs. 10, 12, 34). Magnetite and hematite in particular are useful phases because they are widespread and there is considerable empirical and thermodynamic evidence (Oreskes and Einaudi, 1990; Bastrakov et al., 2007; Skirrow, 2010; Chapter 4 of this thesis) to suggest that they are stable at contrasting temperature and redox conditions, magnetite being stable at hotter, more reduced conditions and hematite at cooler, more oxidized conditions. A general observation of this thesis is that low temperature mineral phases show higher concentrations of ore elements than high temperature phases. For instance, high temperature chlorite has less Cu, Au, U and REE elements, while low temperature chlorite has higher concentrations of these ore elements. The higher concentrations may be reflective of ore-element bearing micro-inclusions (Figure 10, 12, 16 and 17) or substitution of ore elements into the crystal lattice.

3.4.3 Relationship between trace elements and fluids

The high Cu concentrations from chalcopyrite, hematite and chlorite in metasediments and calc-silicate indicate at least two Cu sources: metasediment and calc-silicate (hydrothermal). These findings were consistent with magmatic heat driver and two Cu sources for IOCG mineralisation proposed by authors including Bastrakov et al. (2007), Porter (2010) and Daroch and Barton (2011).

Bonin et al. (1995) and Thomas et al. (2005) suggested that F enrichment in muscovite indicates a magmatic fluid source and input from the mantle. In this study, muscovite in granite and calc-silicate rocks were identified as either F-rich (0.3-0.5 wt % F) or F-poor (0 wt % F). F-rich muscovite may be consistent with Bonin et al. (1995) and Thomas et al. (2015). The elevated concentrations of F in chlorite, biotite and carbonate are also indicative of fluid circulation and these support Bonin et al. (1995) and Thomas et al. (2015). This can be used to infer that magmatic fluids were involved alteration which produced muscovite, chlorite, biotite and carbonate.

The presence of K-feldspar with elevated Ba, Na and Fe concentrations along with Ba-rich muscovite may indicate Ba-rich fluids in the study area. The high concentration of As and p-type S/Fe ratios of pyrite is consistent with pyrite formation at low temperature (200⁰-300⁰ C; Abraitis et al., 2004), which is in contrast to the interpretation of Bastrakov et al. (2007) who suggested ore fluid temperatures were 450⁰ -500⁰ C.

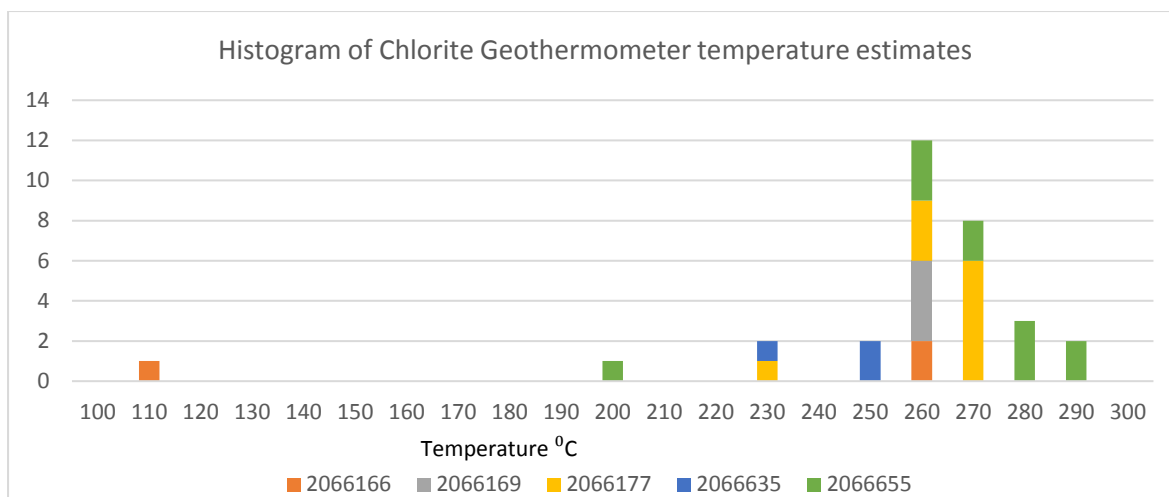


Figure 43. Calculated temperature estimates for chlorite using the method of Cathelineau and Nieva. (1985).

Table 5. The trace elements of minerals contribute to whole rock data

Minerals	Typical abundance range %	Average abundance of eleven samples approx.. %	Approx. enrichment factor required to influence whole rock chemistry	Elements in this range
Pyrite	0-5	1	100	Co Au As Se Te (Ag Ni Bi)
Chalcopyrite	0-3	0.5	200	Cu Se Te (Ag Au Bi)
Bornite	0-25	2.5	40	Cu Ag Bi Se Te (Au Sb)
Hematite	0-30	15	6	Sb Bi W Cu Mo (Co Zn Sn Pb)
Magnetite	0-20	2	50	No
K-feldspar	0-30	15	6	No
Chlorite	2-35	19	10	Sb Bi (Cu Ag Co As)
Biotite	0-25	3	30	No
Muscovite	0-40	4	25	(Se)
Dolomite	0-20	7	20	(Cu Bi)

3.4.4 Significance of trace element patterns

Trace element patterns in the minerals have the potential to be controlled by a number of factors, including similar physical properties of the elements (e.g. diameter, charge density, configuration of outer shell electrons). Here I consider factors related to protolith versus factors related to the IOCG mineralising system. As a general rule, the minerals that appear to have grown prior to mineralisation (biotite, anorthoclase) have tight trace element patterns, presumably representing protolith (or early alteration) controls. Conversely, minerals associated with alteration (e.g. hematite and chlorite) have a broader spread of trace element patterns with locally high values. Their trace element concentration might well be some measure of the mineralizing system.

Minerals associated with early high-T alteration (magnetite, sanidine and some calc-silicate minerals) preserve local trace element enrichments, but analysis suggests these minerals contributed less trace elements than HSCC alteration minerals (hematite, chlorite and

dolomite). It is interesting to note that most minerals associated with the HSCC alteration type (hematite, chlorite, muscovite and sulphides) had some form of localised enrichment in a subset of pathfinder minerals.

3.4.5 Mineral Contributions to Whole Rock Chemistry

The trace element patterns preserved within minerals have the potential to be controlled by a number of factors, including similar physical properties of the elements (e.g. diameter, charge density and configuration of outer shell electrons) and the availability of elements from fluids, host rocks or other sources. Here I consider factors related to the protolith versus factors related to the IOCG mineralising system. As a general rule, the minerals that appear to have grown prior to mineralisation (biotite, anorthoclase) have tight trace element patterns, presumably representing protolith (or early alteration) controls. Conversely, minerals associated with alteration (e.g. hematite and chlorite) have a broader spread of trace element patterns with locally high values. Their trace element concentration might well be some measure of the mineralizing system.

Initially, I wanted to examine trace element deportment in minerals within a series of rock sequences. Specifically, I sought to determine whether variations in the alteration index of Fabris (2013) reflect different types of alteration and/or deportment of elements in different phases. For example, at low alteration index, was there less alteration and were the elements in silicates or oxides rather than in sulphides? Using trace element analyses of multiple minerals from individual samples, I explored the whole rock geochemical signal by looking at elemental deportment in each mineral. I identified ten pathfinder elements as those present in concentrations above ten times average crustal abundance. Different rock samples contained different pathfinder elements. For example, granite samples had only 1-3 pathfinder elements and calc-silicate samples had 2-9 pathfinder elements. The association between more pathfinder elements being present in elevated concentrations in whole rock analysis and higher trace element content in the mineral analysis, including REE (see Appendix 5) is very clear. The control of each mineral on the observed whole rock trace element geochemical signature was assessed by multiplying the average LA-ICPMS results by the average abundance for analysed minerals and summing the results.

Metasedimentary rock with (CAM-HSCC alteration)

The first metasedimentary rock with HSCC alteration (sample 2066641) came from a depth of 799 m in drill hole IHAD3 outside Emmie Bluff. Assay for this whole rock sample showed high concentrations of the pathfinder elements As, Bi, Sb and Se (Table II in appendix 1). A second sample came from a depth of 1016 m in IHAD5 (2066655) with CAM alteration inside Emmie Bluff (Table II in appendix 1). Assay for this whole rock sample showed high concentrations of the pathfinder elements Cu, Mo, and Se. Analysed minerals in these samples include chlorite, dolomite, pyrite and chalcopyrite (Figure 44). Measured minerals contained S, Cu, Sb, Bi and Pb at average weight sums roughly equal to whole rock assay results. Other major constituents of these rock samples (quartz, feldspar and calcite) were not analysed. Sample 2066655 contained chalcopyrite with Cu, Ag and Bi trace element patterns, dolomite with Ce, and a combination of magnetite and hematite with Sb (Figure 44). No apatite was

measured in this sample which means that our findings may not reflect the complete whole rock geochemical signature for these samples.

For the above described metasedimentary rock sample 20066641, our results show that Ag and Pb was controlled by magnetite, but Cu, Sb, Bi, Ta, Ce, Th and U were controlled by a combination of hematite and biotite with no associated Cu minerals. Hematite in this sample contained Sb, Ta, Ce, Th and U at 57-92% of total weight average and was matched to 16-98% of the assay, with some uncertainty (see Appendix 5). For sample 2066655, results suggest hematite-pyrite contributed major concentrations of Sb, Ta, Th and U. Chalcopyrite contributed concentrations of Cu, Bi, Ag and Pb. Dolomite contributed major Ce to whole rock assay. Hematite contained Ta-Ce at 20-72% total weight average, matched to 1-26% for the assay, indicating some uncertainty. In general, it is also noted that element enrichment within hematite is not as high as in sulphide minerals, however, hematite still has the potential to influence whole rock chemistry because hematite is typically more abundant than the sulphides, with hematite commonly accounting for >10% of rock by mass.

Unaltered and Altered Granite

In this study, four granite samples were analysed, ranging from 2066178 (least altered), to 2066174 and 2066656 (moderate alteration), to the highest HSCC altered sample, 2066169. Sample 2066178 (least altered) came from a depth of 529 m as unaltered granite in drillhole HL002. Whole rock assay for this sample show high concentrations of Bi with little MB alteration. Sample 2066174 came from a depth of 539 m as HSCC altered granite in drillhole PSC4_SASC2. Whole rock assay for this sample indicated concentrations of As and Se. Sample 2066656 came from a depth of 819 m as CAM/HSC altered granite in drillhole IHAD2. Whole rock assay for this sample indicated high concentrations of Sb and Se. Sample 2066169 came from a depth of 1139 m in DRD drillhole with HSCC alterations. Whole rock assay for this sample indicated concentrations of Ag, S and W.

Trace element content was different among the four granite samples. Analysis of sample 2066178 (unaltered granite) showed that Sb, Th and U were controlled by hematite, Ag was controlled by K-feldspar and Cu, Ce and Pb were controlled by a combination of hematite and K-feldspar. For sample 2066656 (muscovite altered granite), Sb, Bi and Ta were controlled by hematite, Ce was controlled by K-feldspar and other elements (Cu, Ag, Pb, Th and U) were controlled by a combination of hematite, K-feldspar and muscovite (Figure 45). For dolomite altered granite (sample 2066174), Ce and U were controlled by apatite, Ta was controlled by biotite and Cu, Ag, Sb, Bi, Pb and Th were controlled by K-feldspar-biotite-dolomite-hematite. For sample 2066169, hematite altered granite, Cu, Ag, Ta and Bi were controlled by chalcopyrite and Sb, U and Pb were controlled by hematite (Figure 45).

Concentrations of ore elements within minerals hosted by granite was used to determine alteration processes. Compared to unaltered granite (sample 2066178), the hematite altered granite sample contained K-feldspar with 6-30 times Cu, chlorite with 8.2 times Cu and hematite with 7.7 times Cu. Again comparing unaltered granite with hematite-altered granite, the hematite-altered granite contained Ce, Th and U enrichment at 94-197 times, 696-1740 times and 80-823 times the level of unaltered granite, respectively, for K-feldspar (Appendix 5). The profile of granite ore enrichment was K-feldspar alteration with enrichments of Cu, Ce, Th and U, chlorite alteration with enrichment of Cu, S, Ag, Bi and U, and hematite alteration with enrichment of Cu, Sb and Pb in a progressive alteration processes. Progressive alteration processes were accompanied by Ag depletion (muscovite vs dolomite vs hematite alteration), S, Sb, Pb, Th and U (muscovite vs dolomite alteration) and Ce and Th depletion (dolomite vs hematite alteration) (Appendix 5). Alternatively, progressive alteration processes were

accompanied by Pb depletion (muscovite alteration), Ta and Ce depletion (muscovite to dolomite alteration and Ce, Th and U depletion (dolomite to hematite alteration) (Appendix 5). Overall, the association between elevated concentrations of ore elements and alteration minerals suggests that the hematite-altered granite (sample 2066169) became enriched in ore-elements during alteration.

Calc-silicate with CAM and HSCC alteration

In this study, four calc-silicate samples were analysed, and range from low (2066166), to moderate (2066199 and 2066635) to high (2066203) alteration intensity. The low alteration intensity sample (2066166) came from a depth of 970 m as chlorite altered calc-silicate in drillhole CSD1. Whole rock assay for this sample indicated high concentrations of Se and W with MB alteration. One moderate alteration intensity sample (2066199) came from a depth of 683 m as CAM altered calc-silicate in drillhole WWDD1. Whole rock assay for this sample shows high concentrations of Au, Bi, S, Sb, Se and W. The second moderate alteration intensity sample (2066635) came from a depth of 855 m as HSCC altered calc-silicate in drillhole IHAD6. Whole rock assay for this sample shows high concentrations of As, Bi, Cu, S, Sb and W. The high alteration intensity sample (2066203) came from a depth of 854 m in drillhole GHDD4 and preserves HSCC alteration. Whole rock assay shows elevated concentrations of Au, Ag, As, Bi, Cu, S, Sb, Se and W.

In all samples, Cu, Bi and Ag concentration in the whole rock chemistry is controlled by chalcopyrite, with the exception sample 2066199 that does not contain Cu-minerals. For CAM altered calc-silicate in 2066166, Sb and Pb were controlled by magnetite and chlorite, respectively, and Ta, Se, Th and U were controlled by garnet (Figure 46). For carbonate altered calc-silicate (2066199), all trace elements were controlled by a combination of K-feldspar and biotite. For HSCC chlorite altered calc-silicate (2066635), Sb, Ta, Se, Pb, Th and U were controlled by a combination of hematite and chlorite. In the highest alteration intensity sample (HSCC altered calc-silicate, 2066203), Ta was controlled by K-feldspar, Th and U were controlled by a K-feldspar-pyroxene combination and Sb and Pb were controlled by a pyroxene-Cu minerals-biotite \pm K-feldspar combination (Figure 46).

Our findings showed that the calc-silicate elemental profile was chalcopyrite-Cu, Ag and Bi enrichment, chlorite-Pb, magnetite-Sb, K-feldspar-Ce and Ta, chlorite-hematite-Ce, U and Pb, and hematite-Sb enrichment (Figure 46). Chlorite in moderate alteration intensity sample 2066635 contained high Cu, Sb, Bi, Ce, Th and U, while chlorite in low alteration intensity sample 2066166 contained low Cu, Sb, Bi, Ce, Th and U. Thus, I found that, for chlorite in calc-silicate samples, alteration intensity influenced the composition and key element concentration, where the high alteration intensity sample contained between 12-1680 times of Cu, Sb, Bi, Ce, Th and U as compared to the low alteration intensity sample (see Appendix 5).

Amphibolite

Amphibolite sample 2066177 came from a depth of 471 m in drillhole HL002. Whole rock assay for this sample indicated high concentrations of Bi with little MB alteration. In the CAM altered amphibolite, Cu and Se were controlled by chlorite and dolomite respectively, and Ag, Sb, Bi, Ta, Pb, Th and U were controlled by a combination of chlorite and dolomite (Figure 47). For this sample, whole rock analysis showed that 53% of Ce present was attributed to chlorite and dolomite (Figure 47). Further, our analysis showed that chlorite and dolomite contained 1-17% of S, Cu, Ag, Sb, Bi, Ta, Pb, Th and U, noting some uncertainty (Figure 47). Analysis of 11 hematite sites in this sample failed to show expected Fe content (at 47 wt %

content, rather than 69 wt % content), suggesting hematite in this sample was not pure. The presence of impure hematite influenced inclusion of other rock elements, including Si, Al and possibly Mg, K or Ca, and mineral inclusions such as quartz, chlorite, dolomite and biotite (1-5 μm inclusions).

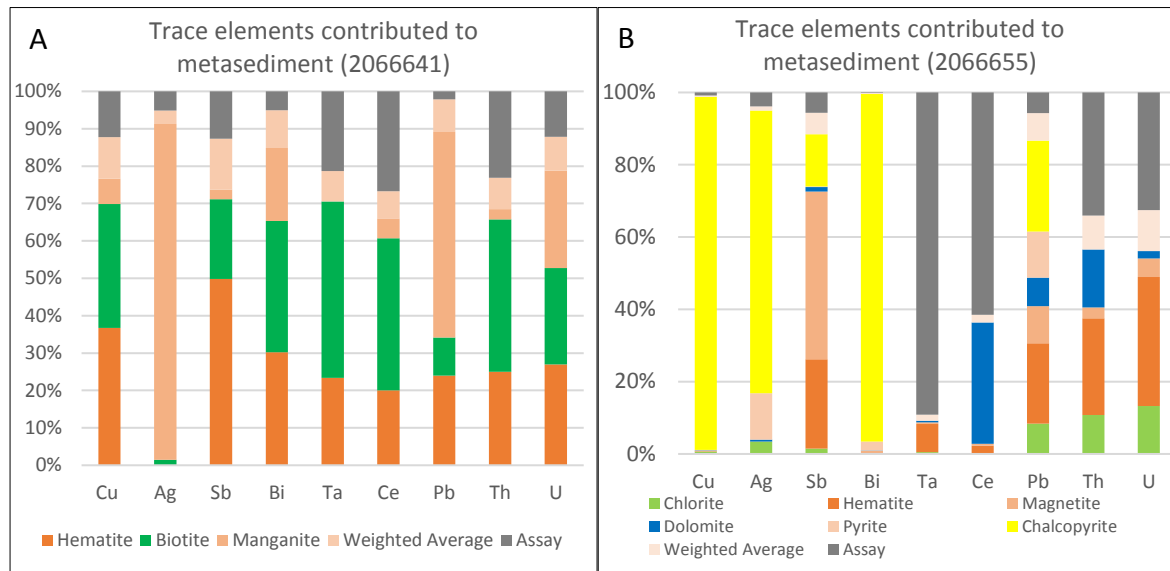


Figure 44. Calculated mineral contribution of trace elements to the whole rock data. In figures 44 to 47 the y-axis represents the percentage of the total whole rock concentration of each element that can be attributed to different minerals in the rock. 100% is effectively the whole rock concentration. Each mineral component is calculated by multiplying the estimated mineral abundance in the rock by the measured element concentration in that mineral. There is no requirement that the sum of mineral components should equal 100% (because not all minerals in the rock have been analysed and because the whole rock data are measured from 1m composites whereas mineral chemistry is measured from individual mineral grains). The component labelled “assay” in each plot represents the difference between the whole rock concentration and the summed mineral components. Where the sum of mineral components is close to 100% I consider it reasonable to interpret that the trace element concentration is controlled by the minerals that have been analysed. A) Metasediment sample 2066641 preserving HSCC alteration. There was no analysis of 35% quartz, 10% K-feldspar, 20% chlorite and 1% apatite. Cu, Sb, Bi and Ce are from hematite and biotite. B) Metasediment sample 2066655 preserving CAM alteration. There was no analysis of 25% quartz, 15% K-feldspar and 2% calcite in the sample. Cu and Bi are dominantly from chalcopyrite, Ce is dominantly within dolomite and Sb is within magnetite.

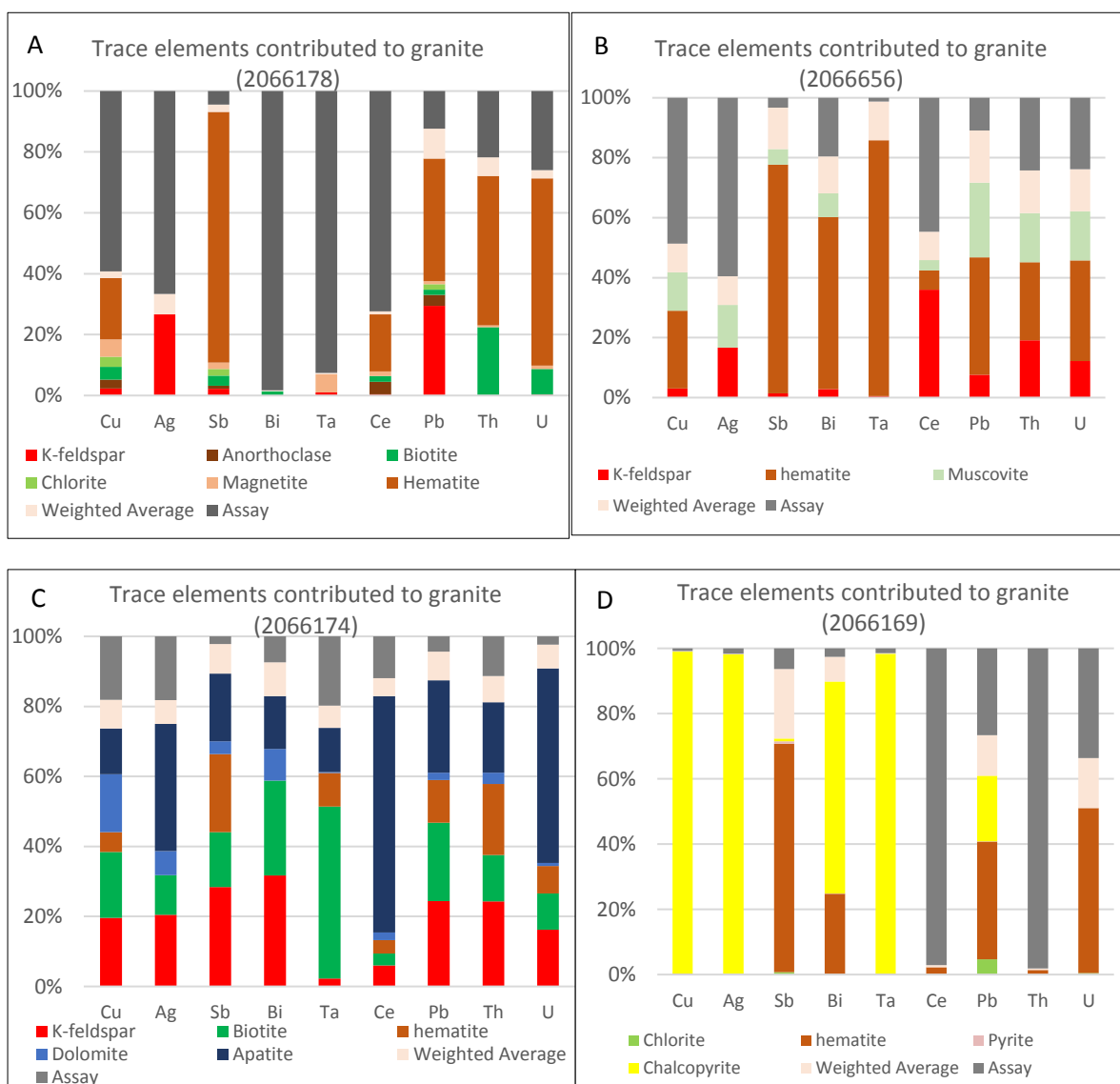


Figure 45. Calculated mineral contribution of trace elements to the whole rock data for granitic samples. A) Sample 2066178 (least altered) preserving minor MB alteration. There was no analysis of 35% quartz and 1% apatite in our sample. Cu, Sb and Ce are from chlorite. B) Sample 2066656 (moderate alteration) preserving CAM/HSCC alteration. There was no analysis of 10% quartz, 10% chlorite and 5% ilmenite in our sample. Cu, Sb, Bi and Ta are dominantly from hematite and Ce is from K-feldspar. C) Sample 2066174 (moderate alteration) preserving HSCC alteration. No analysis is available for 30% quartz and 20% chlorite in the sample. Ce is in apatite and Cu, Sb and Bi are in K-feldspar and biotite. D) Sample 2066169 (most altered) preserving HSCC alteration. No analysis of 20% quartz, 5% K-feldspar and 5% muscovite is available. Cu, Ag, Ta and possibly Bi are in chalcopyrite Sb and U are in hematite.

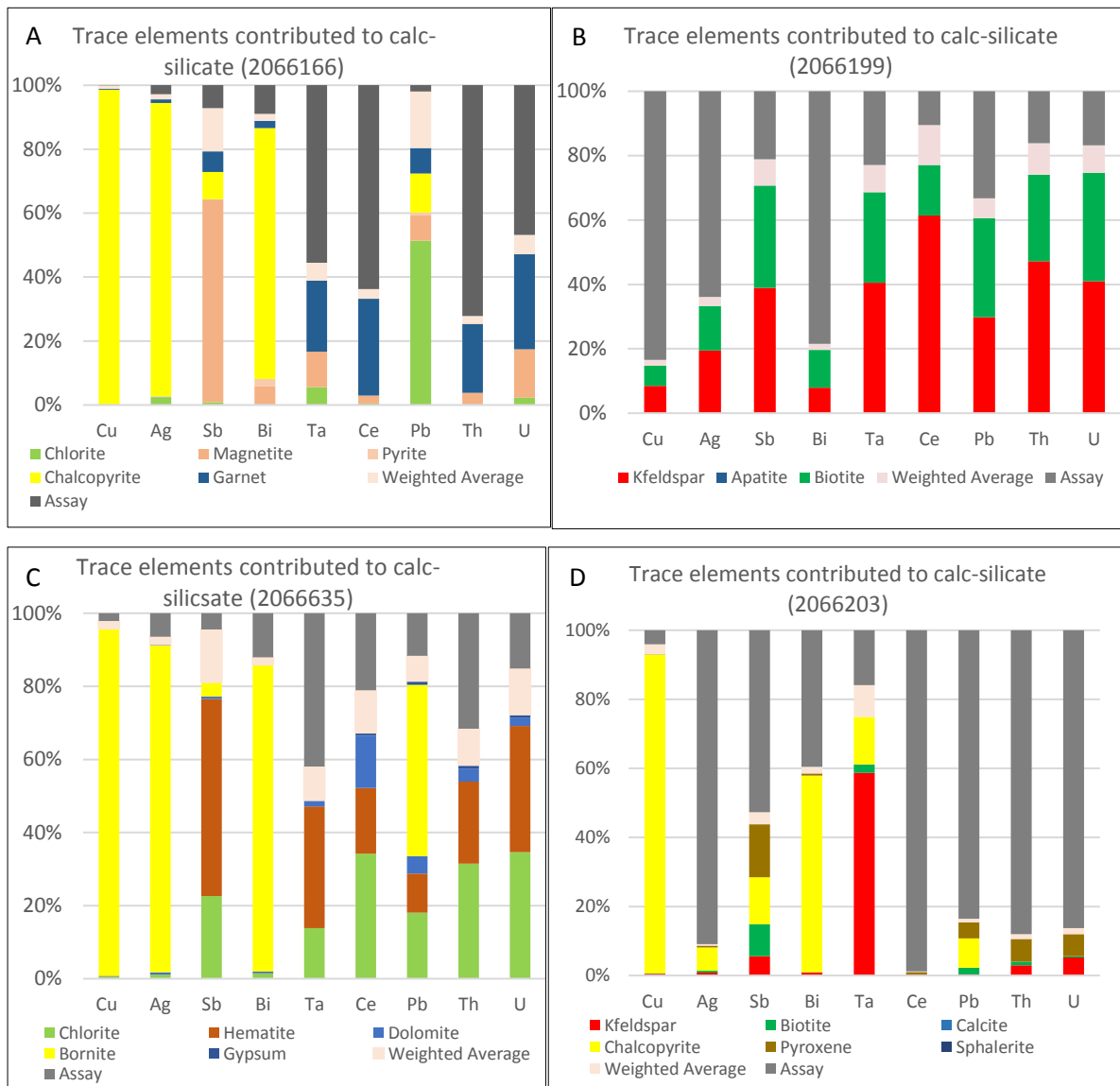


Figure 46. Calculated mineral contribution of trace elements to the whole rock data for calc-silicate rocks. A) Sample 2066166 (least altered) preserving minor MB alteration. There was no analysis of 30% quartz and chlorite in the sample. Cu, Ag and Bi are in chalcopyrite, Ce is in garnet and Sb is in magnetite. B) Sample 2066199 (moderately altered) preserving CAM alteration. There was only analysis of 20% K-feldspar and 1% biotite in the sample. Sb, Ce, Ta, Th and U are from K-feldspar. C) Sample 2066635 (moderately altered) preserving HSCC alteration. There was no analysis of 25% quartz and 10% K-feldspar and 3% apatite in the sample. Cu, Ag and Bi are in chalcopyrite and Sb, Ce, Ta, U and Th are in chlorite and hematite. D) Sample 2066203 (most altered) preserving HSCC alteration. There was only analysis of 15% K-feldspar, 3% chalcopyrite, 0.1% biotite and 15% pyroxene. Cu and Bi are in chalcopyrite.

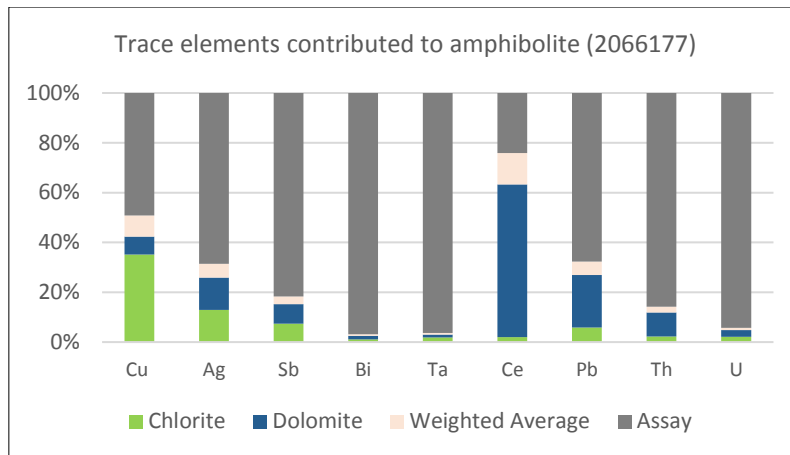


Figure 47. Calculated mineral contribution of trace elements to the whole rock data for amphibolite sample 2066177 that preserves CAM and minor MB alteration. There was only analysis of 20% chlorite and 20% dolomite in the sample. Cu is from chlorite and Ce is from dolomite.

3.4.6 Relationship between paragenesis and fluid/rock interactions

Overall, the genesis of IOCG deposits involves crustal and mantle contributions (Johnson and McCulloch 1995, Porter 2010) including for sources of Cu, Au and REE. The trace elements compositions of the minerals analysed in this study supports a system of complex fluid characteristics and multiple alteration phases as well as multiple fluid and metal sources, as has been interpreted by previous authors (e.g. Porter 2010). Pyrite interpreted to have a volcanic origin may be related to extrusion of the Gawler Range Volcanics and associated magmatic activity. The moderate temperature of fluids associated with pyrite mineralization may have been attained by mixing of high temperature fluids from magmatic sources with lower temperature fluids equilibrated with volcano-sedimentary rocks related to the Gawler Range Volcanics (Figure 23 and 24). The fluids migrated along fault systems that were active at the time of magmatism. Pyrite formed as S-rich, hydrothermal p-type pyrite and incorporated Cu that was derived from metasediment and granite sources.

The pathfinder elements have either been incorporated into the mineral lattice or are present as inclusions. For instance, chalcopyrite shows enrichment in Au, Ag, In, Bi, Se and Te, which display positive relationships with each other (Figure 25B) suggesting that these elements may be incorporated into the lattice of the chalcopyrite rather than within mineral inclusions. Where the pathfinder elements are present as inclusions, this is indicative of at least two phases of mineral growth. In this case, the ore elements entered the lattice of the mineral phase that was to become an inclusion at suitable temperatures (Figure 18, 19 and 20). The ore element-bearing mineral inclusions either pre-existed the host minerals and the host mineral grew around them, or the minerals grew at the same time and one was enveloped around the other.

The trace element content of K-feldspar indicates an early phase of mineral growth under hot conditions, resulting in leaching of Cu, Au, U and REE to fluids (Yang 2009). The same is interpreted for magnetite, chlorite and pyrite. These mineral phases later underwent alteration under cooler conditions resulting in further mineral growth characterized as having lots of 1-5 μm size mineral inclusions. The mineral inclusions are the host to the ore elements. The trace elements (Sb, Bi, W, Cu and Mo and lesser content Co, Zn, Sn and Pb) of magnetite-hematite support mineralisation in cool stage (Bastrakov et al., 2007). The host rocks for IOCG mineralization are mostly hematite breccia.

Fe alteration can result in an increase in the mineral Fe contents rather than new mineral growth. Fe metasomatism leading to higher Fe contents and replacement of Fe^{2+} by Fe^{3+} (e.g. hematite replacing magnetite) is linked to Au-Cu enrichments in minerals (such as pyrite with

high Co, Ni, Au, As, Bi, Se and Te) in metasediment, calc-silicate and granite, Cu and Ag in metasediment (Figure 25). These interpreted that CAM, MB and HSSC orebodies and nearby REE richest zones (Porter, 2010). Fe alteration is associated with leaching of REE from rock and to fluids.

Major ore formation is related to the S bearing fluids (p-type pyrite) and an oxidizing, hematite stable environment. Early phases of Cu-bearing minerals may have formed at high temperatures in a reducing environment and are associated with the K-feldspar-biotite-muscovite assemblage (Figure 19 and 20). This Cu mineralization is characteristically low grade. As the fluids migrated to higher crustal levels, they became more hypersaline, ore elements were leached and a chlorite-hematite alteration occurred. As temperatures decreased, conditions changed to a more oxidizing environment resulting in ore formation or upgrading and development of a chlorite-hematite-K-feldspar \pm pyrite+quartz assemblage. K-feldspar preserving ore mineral inclusions and pyrite-quartz veins (Figure 19 and 20) formed at this time. Later dolomite-impure hematite-manganosite-apatite veins formed without Cu-Au-U and with REE mineralisation (Figure 18 and 20).

3.5 CONCLUSION

This study assesses drill core from a number of locations across the Emmie Bluff IOCG deposit and surrounding region. Samples include a progression of alteration intensities within different rock types to assess the behavior of element deployment during mineral growth and how this is influenced by protolith. The trace elements had the footprints for alteration/mineralisation systems in the study area. Two footprints were the phase change inside mineral zones, and processes of mineral replacement by another, for example, hematite replacing magnetite, chlorite replacing biotite and monazite replacing apatite. The high temperature K-feldspar and magnetite were responsible for ore element removal to fluids. The low temperature hematite and chlorite were responsible for deportment of ore elements. This may be lack of ore elements in the cool fluid inclusions. Magnetite decomposition to hematite was one of the mineralisation processes but also other minerals (e.g. chlorite) were.

However, the magnetite was also stable at low temperature without decomposition, such as MB and CAM remaining magnetite. The findings indicated that the low temperature mineral phase II contained much more ore elements such as K-feldspar, chlorite, muscovite-biotite and magnetite-hematite. Furthermore, phase II of minerals had much more 1-5 μm size mineral inclusions. It was believed that the 1-5 μm size mineral inclusion made one of the major contributions to ore. The multiple mineralisations had derived from the mineral trace element markers.

Fe-alteration was responsible for Au-Cu-U mineralisation upgrading in mineral trace elements. The magnetite and hematite had similarity of REE patterns for REE removal. This could be interpreted that the REE high grade ore was always nearby the main IOCG Cu-Au orebodies.

Carbonate alteration was the major contribution for Th, U and REE upgrading. The garnet, pyroxene and manganite phase had 10-70 times enrichments of ore elements. The apatite was the REE-richest mineral. Future mineralogy studies (garnet, manganite, pyroxene and apatite) might reveal the details of carbonate effects in them. The HCh models will produce the details of the alteration/mineralisation processes.

4 HCh thermodynamic models of IOCG systems of the eastern Gawler Craton, South Australia

ABSTRACT

In this chapter I present results of thermodynamic modelling undertaken to further understand the temperature, pressure, fO_2 and fluid-rock ratio conditions responsible for a range of alteration types associated with iron-oxide copper gold (IOCG) mineralisation in the eastern Gawler Craton. Rather than demonstrating the conditions of ore formation - interested in effects in subeconomic and peripheral systems - e.g. where sulphide deposition is minimal. I modelled mixing of generic IOCG fluids (8-35 wt % NaCl equiv) with elemental concentrations consistent with measurements from fluid inclusion studies, and protolith compositions consistent with unaltered granite and calc-silicate sedimentary rocks. Modelling was conducted in a C-H-O-Cl-S-Na-K-Mg-Fe-Si-Al-Cu-Ca-Mn system at temperatures from 150^o to 500^oC, fO_2 of -34 to -26 and fluid-rock ratios from 10⁻³ to 10⁴. The modelling provides semi-quantitative constraints for mineral assemblages associated with IOCG mineral systems of the eastern Gawler Craton, namely:

- The transition from magnetite to hematite is predicted to be temperature and fO_2 sensitive. Magnetite is predicted to occur at higher temperature and under more reducing conditions than hematite.
- A progression from sanidine to microcline to muscovite with decreasing temperature is predicted. In low-K calc-silicate rocks this progression is predicted to occur at fluid-rock ratios >1. In high-K granite protoliths, sanidine and microcline are predicted to be stable at low fluid-rock ratios and temperatures of >350^oC and >250^oC, respectively; whereas muscovite is predicted to be stable at temperatures <350^oC and at fluid-rock ratios ≥1.
- Chlorite is an expected alteration phase in calc-silicate and granite protoliths and is predicted to be more abundant in calc-silicate protoliths.
- The Cu-sulphide minerals chalcocite, bornite and chalcopyrite are predicted to be temperature and fO_2 sensitive and to occur only at fluid-rock ratios >1 in all models.

Although Cu-sulphides are predicted to be stable over a range of temperature and fO_2 conditions, they are predicted to be most abundant between temperatures of ~300^o to 250^oC, fO_2 of -26 to -34 and at fluid-rock ratios >10. This corresponds to alteration assemblages at the magnetite and hematite boundary, with abundant chlorite and muscovite alteration. At 250^oC, fluid-rock ratio 1-10, fO_2 -26 to -34, the muscovite-hematite-chlorite-k-feldspar assemblage is very similar to the petrogenesis observation.

4.1 INTRODUCTION

The IOCG system in the eastern Gawler Craton is an important Cu-Au-U resource and has been extensively explored for valuable minerals. Alteration zones are key exploration areas in mineralisation systems (Pearce et al., 2015; Cleverley and Oliver, 2005). Alteration zones are the result of fluid-rock interactions as hydrothermal fluids migrate through the crust (Ord et al., 2012). Circulating hydrothermal fluids are significant agents of geological change. They advect heat and mass and are unlikely to be in equilibrium with the rocks through which they are passing. New minerals form as the combined fluid-rock system is driven toward a new equilibrium (although they may never reach equilibrium due to the transient nature of hydrothermal systems). Iron Oxide Copper Gold (IOCG) mineral systems, including the eastern Gawler Craton, are characterized by extensive alteration zones with abundant iron oxides, chlorite, muscovite and carbonate minerals (Hitzman et al., 1992; Gow et al., 1994; 1996; Haynes et al., 1995; Skirrow et al., 2002; 2007; Bastrakov et al., 2007; Porter, 2010; Wilkinson et al., 2015). Skirrow et al. (2002) identified three alteration types in the eastern Gawler Craton IOCG system: magnetite-biotite (MB), carbonate-alkaline minerals-magnetite (CAM) and hematite-sericite-carbonate-chlorite (HSCC). In our samples, MB is kept with major magmatic minerals (2066178) with the least alteration. CAM is in calc-silicate, with quartz-magnetite-hematite-chlorite-garnet assemblage (2066166) and with quartz-K-feldspar-chlorite-carbonate-hematite-apatite assemblage (2066199). HSCC is from granite with hematite alteration (2066169), dolomite alteration (2066174) and calc-silicate with chlorite alteration including hematite-calcite-pyroxene (2066203), with hematite alteration including dolomite-chlorite-gypsum (2066635). However, fluid-rock reactions during IOCG system formation remain unclear.

In this chapter I present a series of thermodynamic models aimed at better understanding the fluid-rock interactions responsible for the suite of alteration assemblages observed in the eastern Gawler Craton IOCG mineral system. HCh is a thermodynamic modelling software package specifically designed for modelling fluid-rock interactions (Oreskes and Einaudi, 1992; Haynes et al., 1995; Johnson and McCulloch, 1995; Oliver et al., 2004; Cleverley and Oliver, 2005; Bastrakov et al., 2007; Tooth et al., 2008; Schmidt et al., 2010; Tauson et al., 2013). In HCh modelling, the model is continually updated with a series of equilibrium states from a fully interactive database system (UNITHERM) (Cleverley and Oliver, 2005). Such models have been previously applied to Australian IOCG systems. Oliver et al. (2004) and Cleverley and Oliver (2005) used the HCh software to model fluid-rock reactions involved with sodic and potassic alteration in IOCG system of the eastern Mount Isa Block in northwest Queensland. In the eastern Gawler Craton, Haynes et al. (1995) used HCh modelling to describe fluid mixing relevant to Olympic Dam IOCG deposits and Bastrakov et al. (2007) applied HCh models to determine upgrading of the IOCG system involved in the alteration of magnetite to hematite. Building on the work of Haynes et al. (1995) and Bastrakov et al. (2007) I have constructed equilibrium thermodynamic models for granite and calc-silicate protoliths at a range of temperatures, pressures, fO_2 and fluid-rock ratios. This enables presentation of predicted mineral assemblages in T-P, fO_2 and fluid-rock diagrams as a means of visualizing the likely conditions of alteration and mineralization.

I conducted HCh modelling based on Donington suite granite and calc-silicate to predict

formation conditions in the eastern Gawler Craton. I applied the model granite represents the Donington suite granite and model calc-silicate represents Wallaroo Group calc-silicate rocks. Fluids covered the fluid inclusion data with representing a number of variables, namely fluids in eastern Gawler Craton IOCG system. HCh models will produce the multiple quantitative parameters to demonstrate geochemical processes and provide understanding of mineralisation (Andreas et al., 2009).

4.1.1 Background Geology

Geology of the eastern Gawler Craton IOCG system consists of basement rock including granite and calc-silicate rocks (Chapter 1.3 and Chapter 3.1.2). Donington Suite granite and Wallaroo Group calc-silicates were overprinted with three mineral assemblages (MB, CAM and HSCC) related to mineralisation (Figure 48). Bastrakov et al. (2007) identified Br/Cl ratios of the magnetite-forming fluids measured beyond the range of typical magmatic and/or mantle values, allowing for the possibility that the fluids originated as brines from a sedimentary basin or the crystalline basement in the eastern Gawler Craton IOCG system.

It has been suggested that the isothermal fluid–rock reaction may account for some alteration zonation of the Olympic Dam IOCG deposit (Cleverley et al., 2005). At least two sources of fluids, of contrasting temperature, composition, and oxygen isotope characteristics were involved in the formation of Olympic Dam (Oreskes and Einaudi, 1992).

Bastrakov et al. (2007) indicated a relatively oxidised fluid and a high temperature hypersaline with rich-Cu content. The S, O and H stable isotope have been done by previous authors indicating the fluid reequilibration with granite and Wallaroo Group with low fluid-rock ratios predate mineralisation (Oreskes and Einaudi, 1992; Bastrakov et al., 2007).

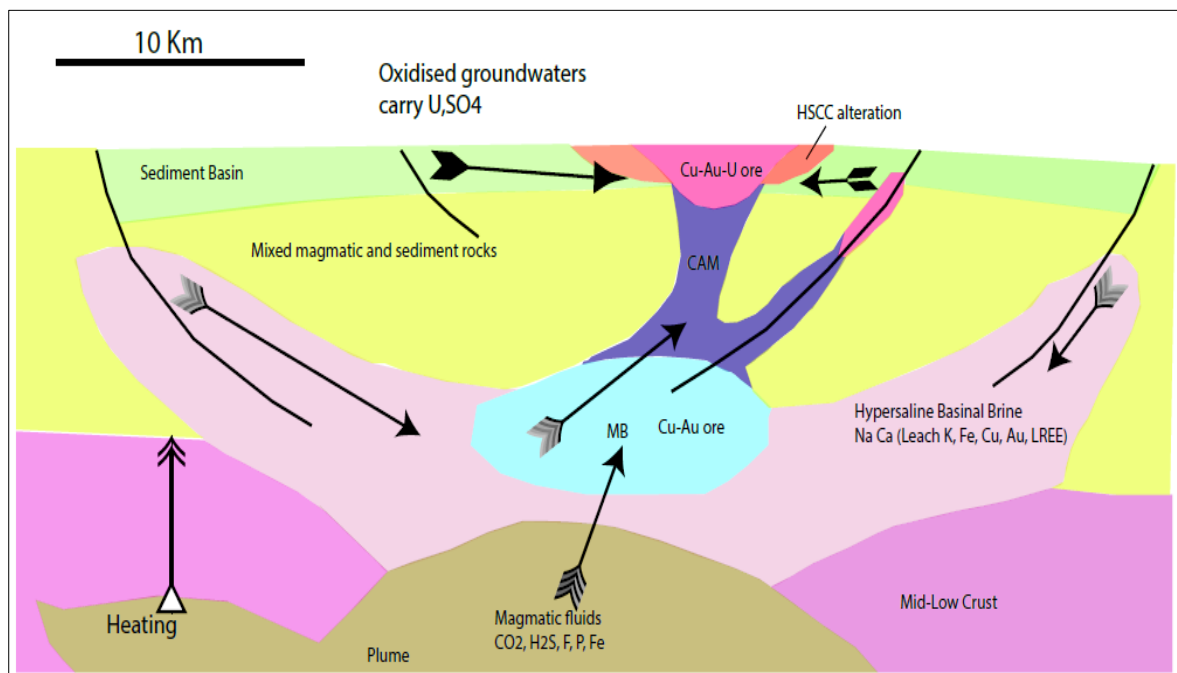


Figure 48. There is the simple alteration systems of the eastern Gawler Craton, modified from Giles. 2013. Commonwealth Agreement Milestone 3.2.1 Report-DET CRC September 2013 (unpublished report).

4.1.2 Models of ore formation for the Gawler Craton IOCG deposits

Previous authors have proposed four scenarios for the formation of IOCG mineralisation on the eastern Gawler Craton. Each scenario recognises the fundamental importance of redox reactions but places different emphasis on the nature of fluid/fluid or fluid/rock interactions and on the ultimate source and mechanism of precipitation of Cu and Au, namely (Table 6):

1. Early reduced, magnetite stable alteration phase was overprinted by an oxidised, hematite stable phase (Reeve et al., 1990; Oreskes and Einaudi, 1990 and 1992);
2. Oxidised Cu-Au-U fluids overprint a pre-existing magnetite-pyrite alteration assemblage (Gow et al., 1994);
3. Oxidised Cu-Au-U fluids mix with reduced fluids (Haynes et al., 1995);
4. Oxidised fluids interplay with reduced magnetite Cu-Au mineralisation (Oreskes and Einaudi, 1990; Gow et al., 1994; Gow, 1996; Bastrakov et al., 2007).

Skirrow (2010) suggested that two distinct processes in the formation of hematite bearing IOCG±U deposits: single-fluid-rock interaction, and two-fluid processes including mixing. The single fluid –rock reaction was the HCh models I had without consideration of two fluid processes.

Oreskes and Einaudi (1990) showed that hydrothermal processes associated with extensive hematite alteration and brecciation were a major contributor to REE mineralisation at Olympic Dam. The same authors (Oreskes and Einaudi, 1992) went on to present stable isotope and fluid inclusion evidence that at least two distinct hydrothermal events contributed to the formation of Olympic Dam - an early high-temperature magnetite stable event and a later lower temperature, oxidising event responsible for the formation of the hematite breccias. Gow et al. (1994) made similar conclusions based on their work at Emmie Bluff and inferred that Cu was introduced to the system by the later superimposed oxidising fluid and was deposited synchronous with magnetite alteration to hematite.

In contrast, Haynes et al. (1995) proposed that fluid mixing between deeply-derived, hot and reduced fluids and shallow oxidised and metal-rich fluids was the dominant process responsible for mineralisation at Olympic Dam. Haynes et al. (1995) conducted simple thermodynamic models involving different mixtures of three components, a cooler (150°C) H₂O-NaCl-Ca-HCO₃-SO₄ fluid, a hotter (250°C) H₂O-NaCl-HS-K-Ca-Fe-F fluid and a granite protolith. Haynes et al. (1995) models predict that mixing of the two fluids (resulting in voluminous hematite precipitation as seen in the Olympic Dam breccias) and alteration of granite by the mixed fluid would result in mineral assemblages and zoning almost identical to those observed in the Olympic Dam deposit. Haynes et al. (1995) argued that oxidisation of magnetite to hematite and coincident reduction of sulphate to sulphide would have resulted in a decrease in pH which would account for the extensive sericite-chlorite alteration associated with the deposit.

Over a decade later, Bastrakov et al. (2007) developed a fluid-rock reaction model in which oxidised fluids interact with pre-existing magnetite-Cu-Au mineralisation resulting in magnetite alteration to hematite, addition of Cu and Au to the system and upgrading pre-existing mineralisation. Bastrakov et al. (2007) described three types of fluid inclusions; type A high temperature vapor-rich inclusions; type B medium to low temperature, liquid-vapor inclusions, and type C high temperature, halite-saturated hypersaline multiphase fluid inclusions, with vapour, liquid and multiple solids, including chalcopyrite. Bastrakov et al. (2007) utilised thermodynamic modelling to test if alteration and ore phases in the Gawler Craton IOCG systems are consistent with alteration by the observed fluids. They specifically addressed the overprinting of pre-existing magnetite-bearing assemblages (formed by type C fluids) with lower temperature oxidised type B fluids. Their models were conducted using the HCh software package (see below) in a simplified chemical system H-O-Cl-S-Na-K-Mg-Fe-Si-Al-Cu-Au. Bastrakov et al. (2007) argued that type C fluids carried significant Cu but that there was no efficient mechanism to bring copper minerals to saturation during the early magnetite-stable alteration phase resulting in only subeconomic magnetite Cu-Au mineralisation. Overprinting of subeconomic magnetite-Cu-Au mineralisation by type B fluids resulted in oxidisation of pre-existing magnetite to hematite with two possible Cu mineralisation scenarios; 1) coincident reduction of sulphate from the type B fluid and deposition of Cu-sulphides (with Cu added from the type B fluid), and; 2) coincident dissolution and reprecipitation of sulphides at the magnetite-hematite alteration front resulting in local upgrading of pre-existing Cu-Au mineralisation.

Both the Haynes et al. (1995) and Bastrakov et al. (2007) models involve two fluids - a reduced, high temperature phase and an oxidised, low temperature phase - with the primary phase of sulphide mineralisation resulting from mixing of the two fluids or overprinting of the first by the second. Consensus is that ores tend to have high fluid-rock ratio, likely fluid mixing. But Bastrakov's data suggests the deep sourced hot and reduced fluid was primary carrier of Cu and Fe and that sub-economic mineralisation and/or iron oxide mineralisation occurs where Cu doesn't reach saturation. In contrast to Haynes et al. (1995) and Bastrakov et al. (2007) my modelling focuses on the interaction of a model metal-rich (type C) fluid with country rocks over a range of temperature, fluid/rock and redox conditions. My aim is to test if the range of observed alteration assemblages (both distal and proximal to mineralisation) are compatible with the passage of a single fluid or whether more complex, fluid mixing or overprinting relationships are required.

Table 6. Parameters of previous thermodynamic modelling of IOCG systems.

Deposit	Temperature (°C)	Fluid Inclusion types	Salinity (wt%)	Model system	Reactions	References
Olympic Dam	150-250	Estimated two fluids			Oxidised U-bearing fluid mixed with Reduced Cu-Au bearing fluid	Reeve et al., 1990
Olympic Dam	200-400	L+V+S, L+V	7-42	H ₂ O-NaCl-KCl-CaCl ₂ - CaF ₂ -BaCl ₂ -CO ₂ -FeCl ₂	Magmatic fluid mixing with cooler meteoric fluid	Oreskes and Einaudi, 1992
Olympic Dam	150-250	Estimated from mineral assemblages	14-16	H ₂ O-NaCl-KCl-CaCl ₂ - CaF ₂ -MgCl ₂ -MnCl ₂ -HCO ₃ -	Hotter saline water mixing with cooler meteoric water	Haynes et al., 1995
Olympic Dam	400-500, 250	L +V-rich +S, L+V, (L+V+nS)	13.9- 17.4	H ₂ O-NaCl-KCl-MgCl ₂ -FeCl ₂ -CaCl ₂ - FeS ₂ -CuFeS ₂ -Au	Oxide brine with sub economic Cu-Au mineralisation	Bastrakov et al., 2007
East Gawler Craton	250-300	(L+V+nS) L+ V	16.2-35	H ₂ O-NaCl-KCl-CaCl ₂ -FeCl ₂ -MgCl ₂ - CuCl-FeSO ₄ -FeS ₂ -HCO ₃	Variable fluid reacted granite and calc-silicate rock related fO ₂ and fluid-rock ratio and pH	This study

It is worth noting that the thermodynamic models of neither Bastrakov et al. (2007) nor Haynes et al. (1995) included CO₂ as a component of the chemical system, despite the occurrence of abundant carbonate phases (calcite, dolomite, ankerite and siderite) in the IOCG alteration systems.

4.2 METHODS

The fluid-rock interactions involved in the formation of ore deposits are dependent on many variables (e.g. temperature, pressure, rock composition and fluid composition, including pH, salinity and oxygen fugacity) and are inherently complex. There are a multitude of possible outcomes (in terms of alteration mineral assemblages) and conversely, there are potentially multiple combinations of input parameters that might achieve the same predicted outcome. The aim of thermodynamic modelling is not to identify the specific conditions under which observed alteration assemblages were formed but instead, after reducing the range of possible input parameters based on observations, to determine the key controls on alteration and the ‘family’ of conditions which are consistent with the observed alteration assemblages. The HCh software package is a useful thermodynamic modelling tool which has previously been applied to IOCG systems on the Gawler Craton (Haynes et al., 2005; Bastrakov et al., 2007). HCh was developed by Yuri Shvarov and Evgeniy Bastrakov at the Moscow State University (Shvarov and Bastrakov, 1999). It is based on the concept of minimising Gibbs free energy by using Debye-Huckel equations to calculate equilibria and reaction parameters for electrolytes. HCh utilises a continuously updated UNITERM database (Oliver et al., 2004; Cleverley et al., 2005). The modelling software facilitates use of 42 elements, 12 real gases, 107 basic species, 106 complexes and 198 pure phases. The program allows users to calculate chemical, dynamic equilibria at variable temperatures of between 0 and 1000°C and pressures of between 1 and 5 kbar (Cleverley and Oliver, 2005; Craig, 1996). The density and salinity of water are limited to above 0.35 g/cm³ and 3-5 mol/kg, respectively. A number of configurations of reaction

models are possible including closed system equilibrium models, titration models, fixed-fugacity and sliding-fugacity models, kinetic reaction models, local equilibrium models and continuum models (Craig, 1996).

I chose to use HCh in this study because it allowed rapid construction of numerous models for the eastern Gawler Craton IOCG system, over a range of conditions (particularly temperature, fO_2 and fluid/rock ratios) inferred from petrological observations, geochemistry (see chapter 1 and 2) and previous fluid inclusion and isotope studies (e.g. Oreskes and Einaudi, 1992; Bastrakov et al., 2007).

4.2.1 HCh modelling General Method

I used HCh to construct theoretical grids of the alteration products of model protolith rocks and starting fluids at a range of temperature (and pressure), fO_2 and fluid/rock ratios in five steps:

1. Select an appropriate geochemical system for the HCh models, including all elements sufficient to account for the chemistry of both solid and fluid phases;
2. Set the input composition of rocks and fluids;
3. Set variables, such as temperature, pressure, fluid-rock ratio and $\log fO_2$. Models can be set to calculate equilibria over a series of steps for one or more variables;
4. Run the chosen model fluid-rock reaction with outcomes produced in Excel files as a list of the predicted stable solid phases and composition of the predicted co-existing fluid, including pH;
5. Use these data to construct “grids” of predicted alteration assemblages over appropriate ranges of temperature (150° - 500° C) fluid-rock ratios (10^{-3} - 10^4) and $\log fO_2$ (-22 to -34).

4.2.2 Choice of System

Haynes et al. (1995) utilized a 23 element model system (H-O-C-S-Cl-Si-Al-Fe-Mg-Ca-Na-K-Mn-Zn-Cu-Co-Pb-Ag-Au-Sr-Ba-F-U) in an attempt to model a complex suite of ore minerals resulting from fluid mixing and fluid rock reactions at Olympic Dam. More recently, Bastrakov et al. (2007) applied a simplified chemical system of twelve elements (H-O-S-Cl-Si-Al-K-Na-Mg-Fe-Cu-Au) to their modelling of Gawler Craton IOCG alteration, intended as a reasonable approximation to a felsic rock type interacting with a saline, hydrothermal fluid and allowing for the presence of copper sulphide minerals and gold. Cleverley and Oliver (2005) took a similar approach and applied a simplified 13 element system (H-O-S-Cl-Si-Al-K-Na-Ca-Mg-Fe-Ti-Cu) in order to model K-alteration at the Ernest Henry IOCG deposit in northwest Queensland.

I chose a 14 element C-H-O-Cl-S-Na-K-Mg-Fe-Si-Al-Cu-Ca-Mn (see Table 7, 9 and appendix 7 for details). This system is similar to that used by Bastrakov et al. (2007) but includes C, Ca, Mn and excludes Au. This system allows for fluids with variable salinity and CO_2 content and solid phases (quartz, feldspars, micas, chlorite, calc-silicate, carbonate minerals, oxides and iron and copper sulphides) consistent with the protolith rocks and observed major alteration and ore phases.

4.2.3 Modelling conditions

I conducted a series of calculations using set rock and fluid compositions and varying temperature, pressure, fO_2 and fluid-rock ratios. The temperature range I applied in our models was 500°C to 150°C consistent with temperature estimates from fluid inclusion and thermodynamic studies in the eastern Gawler Craton (Oreskes and Einaudi, 1992; Bastrakov et al., 2007). I set pressure according to temperature using the formula:

$$P \text{ (bar)} = T * 8 - 1100 \text{ (Cleverley and Oliver, 2005),}$$

Resulting in a pressure range of 2900 bar to 100 bar. Using this relationship results a minimum temperature of 137.5°C, below this temperature the relationship produces negative pressure.

The near ubiquitous observation of hematite replacement of magnetite in association with sulphide mineralization suggests that alteration occurred close to the magnetite/ hematite redox buffer, which occurs in the range of $\log fO_2$ -20 to -40 at temperatures of 500° to 150°C. Redox conditions were varied from $\log fO_2$ -22 to -34, in increments of 2 log units. HCh does not accommodate $\log fO_2$ of less than -36. Fluid-rock ratios were varied from 10^{-3} to 10^4 . Sodium to potassium ratios were maintained at $Na/(Na+K) < 0.16$ because this is a requirement of K-feldspar precipitation in HCh modelling and K-feldspar is a common alteration mineral in both high and low temperature alteration assemblages in IOCG systems (Cleverley and Oliver, 2005; Chapter 2). Salinity was varied between 8 and 35 wt % consistent with the salt content of fluids observed in previous fluid inclusion studies (Bastrakov et al., 2007). Acid/base conditions are a calculated outcome of the equilibria computed by the HCh software. In the models conducted here pH was in the range of 2-13, and mostly between 6 and 7.

4.2.4 Rock and fluid composition

Rock composition

To model the full potential range of alteration it is desirable to enter rock compositions representing a protolith with little or no alteration. This is difficult to apply for rock compositions common to the eastern Gawler Craton because alteration is a near ubiquitous phenomenon. All samples examined in this study have been altered to a greater or lesser extent. As such I sought to define a model 'unaltered' protolith for two of the most common rock types in the study area: granite and carbonate bearing metasedimentary rocks.

Model granite

The eastern Gawler Craton database contains whole rock geochemical data for 504 granite samples from the study area, including granites of the Donington Suite and Hiltaba Suite. The least altered granites form a coherent geochemical group with SiO_2 (72-78 wt %), Al_2O_3 (12-20 wt %) and K_2O+Na_2O+CaO (8-12 wt %). Sixty five of the 504 granite samples have been identified as Donington Suite (Fabris et al., 2012; Chapter 2). The least altered group of Donington Suite granites typically have SiO_2 (60-74 wt %), Al_2O_3 (11-15 wt %), K_2O+Na_2O+CaO (7-10 wt %) and Fe_2O_3 (2-10 wt %) (See Chapter 2). These compositions are similar to the chemistry of unaltered Donington Suite granite from the Eyre Peninsula reported

by Mortimer et al., (1988). The granitoids reported by Mortimer et al. (1988) are pyroxene granitoids, ferro-hypersthene granites and alkali-feldspar granites with pyroxene and amphibole as the dominant mafic phases, rare biotite and a combination of potassium feldspars and plagioclase.

Table 7. Composition of granite used in HCh models

Described	Least Altered	Muscovite-hematite-altered	Dolomite-altered	Hematite-altered	Designed				
Namely	Granite I	Granite II	Granite III	Granite IV	Model granite				
Sample	2066178	2066656	2066174	2066169					
DH	HL002	IHAD2	PSC4-SASC2	DRD1					
From	529.13	819.61	539.46	1139.4					
To	529.27	819.76	539.53	1139.46					
Alteration	MB	CAM/HSCC	HSCC	HSCC					
Minerals	%								
Quartz	35	10	30	20	35				
Albite					9				
K-feldspar	30	20	15	5	30				
Anorthoclase	5				9				
Biotite	25		10						
phlogopite					13				
Chlorite	2	10	20	35	2				
Muscovite		40		5					
Magnetite	1				1				
Hematite	1	15	5	30	1				
Dolomite			15						
Apatite	1		5						
Pyrite				5					
Chalcopyrite				0.1					
Ilmenite		5							
Whole rock data from SARIG									
Samples	wt %								
	Al ₂ O ₃	CaO	Fe ₂ O ₃	K ₂ O	MgO	MnO	Na ₂ O	S	SiO ₂
504 samples	10.85	4.04	15.3	4.16	3.1	0.34	1.23	0.31	55.96
2066178	14.87	2.38	6.33	4.35	1.87	0.1	2.66	0.02	64.25
2066174	12.87	1.19	6.09	5.26	2.75	0.25	0.21	0.02	66.72
2066656	14.05	0.70	6.29	4.23	1.21	0.22	0.14	0.06	65.45
2066169	12.68	0.22	13.55	4.8	1.77	0.11	0.21	0.98	61.77

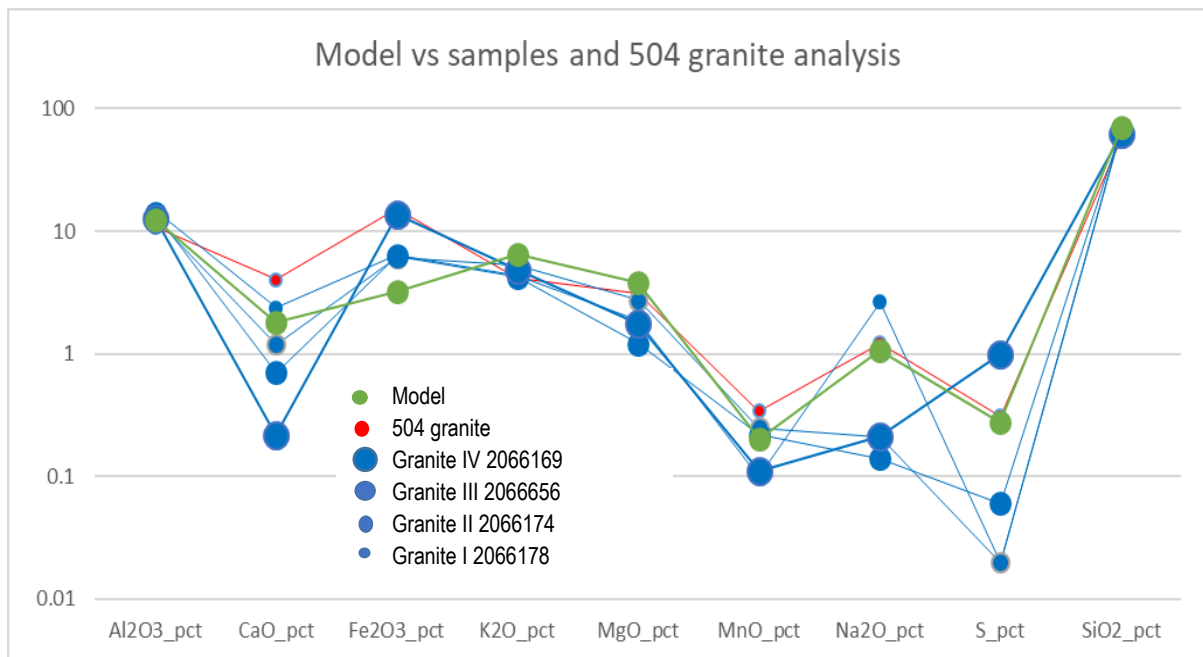


Figure 49. Granite I, II, III and IV samples have lower Ca-Mn-Mg content than the average for 504 granite samples (whole rock data). Model granite applied the average of S and Mn due to zero is not in the log unit.

The four altered granite samples described in chapter 2 (2066169, 2066174, 2066178 and 2066656) are all interpreted to have formed from Donington Suite protoliths. These samples have a range of compositions from SiO₂ (61-67 wt %), Al₂O₃ (12-15 wt %), K₂O+Na₂O+CaO (0.5-9.4 wt %) and Fe₂O₃ (6-14 wt %) (Figure 49). In contrast to the findings of Mortimer et al. (1988), the four samples of altered granite described in chapter 2 have no pyroxene and amphibole, very little plagioclase and significant components of alteration minerals (e.g. muscovite, chlorite, hematite and carbonate).

Without the benefit of an unaltered starting material I chose to create a model granite consistent with the average granite chemistry in the area (Figure 49) and modified from the least altered granite sample (2066178). Sample 2066178 has an estimated mineral composition of 35% quartz, 30% K-feldspar, 25% biotite, 5% anorthoclase, 2% chlorite, 1% magnetite, 1% hematite and 1% apatite. In contrast the model granite has a mineralogy of 35% quartz + 30% K-feldspar + 13% phlogopite + 9% albite + 9% anorthite and minor 2% chlorite + 1% magnetite + 1% hematite. The chemistry of model granite have been calculated by these minerals (Figure 49). This mineralogy is consistent with biotite monzogranite which occurs as fractionated end-member compositions in both the Donington Suite and Hiltaba Suite (see Creaser, 1996) and is thus a useful generic granite for the purposes of modelling.

Model calc-silicate

The eastern Gawler Craton database contains whole rock geochemical data for 205 calc-silicate samples from the study area, including 61 calc-silicate rocks assigned to the Wallaroo group

(Fabris et al., 2012; Chapter 2). The least altered calc-silicate rocks, including most of the Wallaroo Group, form a coherent geochemical group with increasing CaO+MgO on plots of Fe₂O₃-Al₂O₃-CaO+MgO (Chapter 2, Figure 7).

The four altered calc-silicate samples described in chapter 2 (2066166, 2066199, 2066203 and 2066635) are all interpreted to have formed from Wallaroo Group protoliths. They have a range of chemical composition; SiO₂ (35-52 wt %), Al₂O₃ (4.1-11.4 wt %), CaO+MgO (7.8-24 wt %) and Fe₂O₃ (8.8-50 wt %) (See Chapter 2 and Table 8). These samples all exhibit significant mineralogical and textural evidence of alteration, including abundant iron oxides, chlorite and K-feldspar (Chapter 2).

Table 8. The calc-silicate samples were used in the HCh models

Namely	Least altered	Carbonate	Hematite	Chlorite altered	Designed				
Sample	2066166	2066203	2066635	2066199	Unaltered				
DH	CSD1	GHDD4	IHAD6	WWDD1	Calc-silicate				
From	970.6	854	855.87	683.75					
To	970.7	854.15	855.99	683.86					
Alteration	CAM	HSCC	HSCC	CAM					
Rock type	Calc-silicate								
Quartz%	30	25	25	10	17				
K-feldspar%		15	10	20					
Chlorite%	30	20	15	20	21				
Hematite%	10	8	20	9					
Magnetite%	20								
Dolomite%			20	20	2				
Calcite%		10		10	33				
Pyrite%	1	2			3				
Chalcopyrite%	1	3	2						
Apatite%		1	3	5					
Mica%				Ms 1	Bt 24				
Rest %	Grt 8	Act 15							
Other%		Sp 1	Gp 5	Rut 5					
Whole rock data from SARIG									
Sample	wt %								
	Al ₂ O ₃	CaO	Fe ₂ O ₃	K ₂ O	MgO	MnO	Na ₂ O	S	SiO ₂
205 samples	6.93	12.63	20.91	2.80	5.65	0.93	0.31	0.39	42.00
CSD1	4.11	4.75	49.69	0.41	3.07	0.69	0.06	0.17	35.37
GHDD4	6.92	12.49	13.70	1.23	11.66	1.18	0.24	1.94	41.00
IHAD6	7.37	1.96	22.19	1.08	7.05	0.61	0.10	0.97	47.91
WWDD1	11.43	5.76	8.83	5.49	3.73	0.56	0.08	0.35	51.57

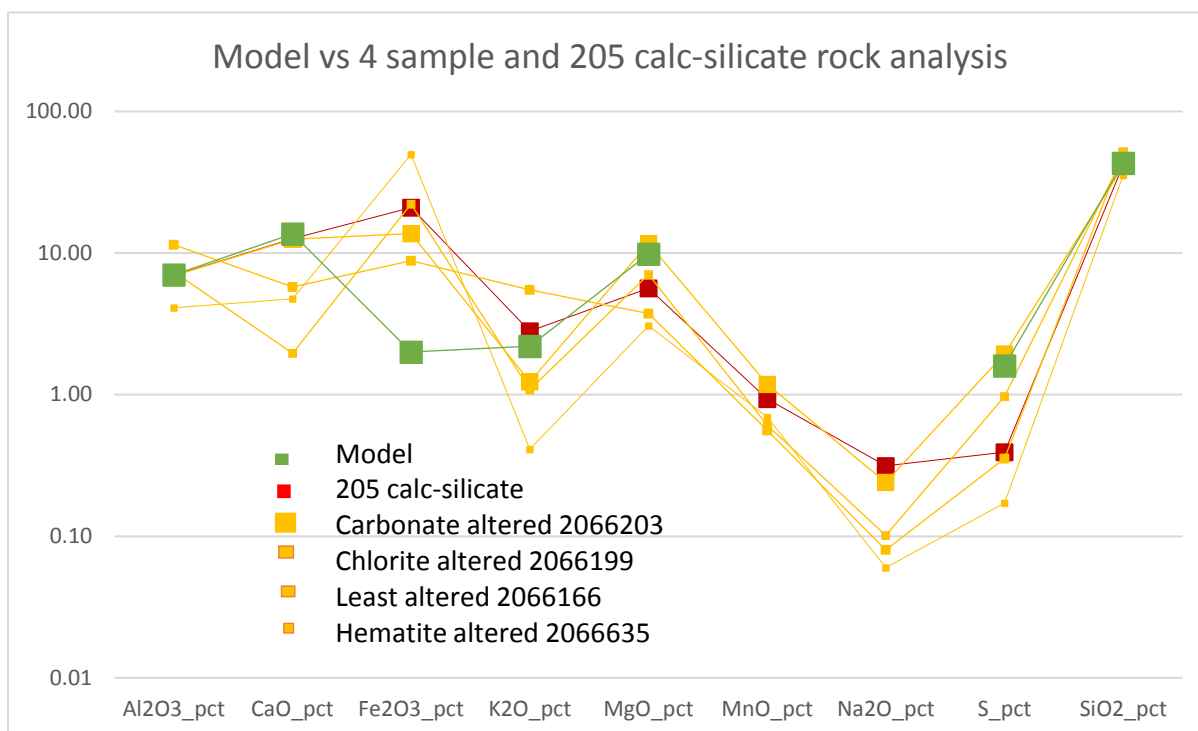


Figure 50. The calc-silicate samples have a little lower Ca-Na content than the average of 205 calc-silicate (whole rock data). Model calc-silicate contains lower Fe than the average of calc-silicate samples which is influenced by widespread Fe metasomatism. Our model calc-silicate does not contain Na or Mn.

Without the benefit of an unaltered starting material I chose to create a model calc-silicate with major element chemistry that is the average of the 205 calc-silicate samples from the study area (Figure 50). I added slightly more sulphur (1.6 wt % S) than the regional average because more Cu minerals will be produced. The S concentration is 1.94 wt % in ore sample 2066203 and the S concentration of average calc-silicate is 0.39 wt % so that the 1.6 wt % S is appropriate for providing the more Cu-S minerals. At temperatures of >350°C and low fluid rock ratios this produces a mineral assemblage of 17% quartz, 24% biotite, 21% chlorite, 33% calcite, 2% dolomite and 3% pyrite. This carbonate-rich mineralogy is comparable to the least altered parts of sample 2066635. I did not specify other high temperature calc-silicate phases (e.g. garnet, pyroxene, and amphibole) as observed in samples 2066166 and 2066203 because HCh models can produce all mineral assemblage in specified conditions.

Model Fluid Compositions

Our model fluid (Fluid A) is based on fluid inclusion data of type C (high temperature, hypersaline, metal-rich) fluids from the Emmie Bluff and Titan prospects presented in Bastrakov et al. (2007) see appendix 7. Type C fluid inclusions contain halite crystals as well as a number of other daughter crystals including silicates (ferropyrrosmalite), oxides (magnetite or hematite) and sulphides (chalcopyrite) (Bastrakov et al., 2007). Chemical analyses of the brines in Type C inclusions indicate high salinities (many in excess of 35 wt % NaCl equiv) and concentrations of Fe, Ca, K, Mn and Cu at percent levels (Table 9). Our model

Fluid A has concentrations of these elements in the range of Bastrakov et al's (2007) fluid inclusion data (including 1.5 wt % Cu) with NaCl added to sum to a total of 35 wt % NaCl equiv, the maximum salinity which is allowed in the HCh software. I added a small concentration of sulphur to the fluid in the form of 1.5 wt % FeSO₄ which corresponds to ~0.3% sulphur.

The choice of composition for our model Fluid B was informed by the results of the Fluid A calculations (see below) and was modified to have lower total salinity (16.2 wt %), still with concentrations of Fe, Ca, K and Mn at percent levels but with a lower concentrations of Cu and S and without Na. Model Fluid B1 has the same composition as Fluid B but without sulphur (see appendix 7).

Model Fluid C is the average of seven fluid inclusions presented by Bastrakov et al. (2007), with 80 g/L MgCl₂ added and with 30 wt % NaCl equiv (see Table 9).

Table 9. Representative results of PIXE analyses of elemental abundances for multiphase brine Inclusions (type C) from quartz in CAM alteration assemblages from Bastrakov et al. (2007).

Prospect Hole ID	ppm												Fluid wt %
	Cl	K	Ca	Ti	Mn	Fe	Cu	Zn	As	Br	Ba	Pb	
Emmie Bluff BD1	335110	37395	38414		6090	18710	499	2013	2182	910	7092	14619	46.3
	207346	23104	96396		20045	137667	679	4623	1378	1330	5624		49.8
	27768	15747	20888	162	8937	55468	288	1379	285	655	1705		13.3
Titan BD1	122429	69247	40015	1500	6532	277179	45934	1600	217	1716	3950	4229	57.5
		9177	11381	1477	2209	158890	19825	706			2163		20.6
	1960	1994	3427	536	2308	75171	344	490	63	201	719	1033	8.8
	15314	16397	3360	306	2395	86861	19045	352	50	383	1040	2223	14.8
Average (Fluid C)	118321	24723	30554	796	6931	115707	12373	1595	696	866	3185	5526	30

Notes: Blank is below the detection limit for a given fluid inclusion.

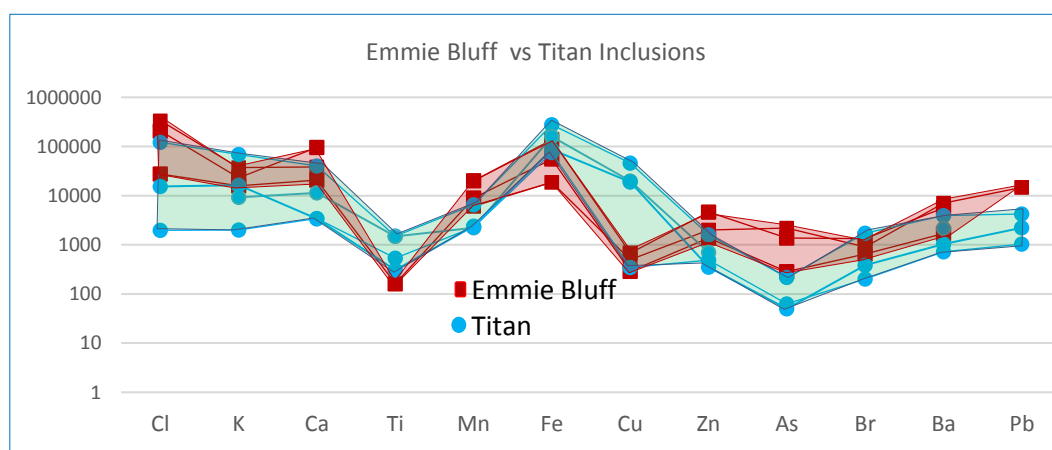


Figure 51. The seven fluid inclusions show the diagram in Olympic Dam (Emmie Bluff and Titan Data). The Emmie Bluff inclusions have the Cl-Ca-Mn-Zn-As-rich and the Titan inclusions have rich-Ti-Cu-Fe (Bastrakov et al., 2007). The element value is at ppm.

4.2.5 HCh Models

Specific experiments I conducted using HCh modelling were:

1. Model granite reacted with model Fluid A at a range of temperatures (from 150° to 500°C in 50°C increments), pressures (linked to temperature as above) and fluid-rock ratio (from 10^{-3} to 10^4 in units of *10) with $\log fO_2$ varying from -34 (~ the magnetite/hematite buffer at 250°C) to -22 (Figure 52). Designed to predict the alteration assemblages resulting from equilibrating a Cu-rich “Type C” fluid with granite over a range of conditions.
2. Model granite reacted with model Fluid B at a range of temperatures (from 150° to 500°C in 50°C increments), pressures (linked to temperature as above) and fluid-rock ratio (from 10^{-3} to 10^4 in units of *10) with $\log fO_2$ varying from -34 to -22 (Figure 53).
3. Model granite reacted with Fluid B1 (no sulphur) at a range of temperatures (from 150° to 500°C in 50°C increments), pressures (linked to temperature as above) and fluid-rock ratio (from 10^{-3} to 10^4 in units of *10) with $\log fO_2$ at -34 (Figure 54).
4. Granite I (based on sample 2066178) reacted with Fluid C at a range of temperatures (from 150° to 500°C in 50°C increments), pressures (linked to temperature as above) and fluid-rock ratio (from 10^{-3} to 10^4 in units of *10) with $\log fO_2$ varying from -34 to -22 (Figure 55). Designed to determine if magnesium-rich fluids are capable of stabilizing dolomite as a vein or alteration phase in granite protoliths.
5. Model calc-silicate reacted with model Fluid B at a range of temperatures (from 150° to 500°C in 50°C increments), pressures (linked to temperature as above) and fluid-rock ratio (from 10^{-3} to 10^4 in units of *10) with $\log fO_2$ varying from -34 to -22 (Figures 56 and 57).

4.3 RESULTS

Granite HCh models

4.3.1 Model Granite equilibrated with Cu-rich model fluid A (35 wt % NaCl equiv)

This set of calculations is represented in Figure 52. Notable observations from Figure 52A (Fluid-rock ratio vs temperature at $\log fO_2 = -34$) include:

- The “least altered” mineral assemblages (most like the starting Model Granite) occur in the lower left of the diagram at temperatures of $\geq 400^\circ\text{C}$ and fluid-rock ratio (F/R) of ≤ 0.1 . With co-existing magnetite, biotite and K-feldspar, this part of the diagram most closely represents the MB style of alteration.
- Starting in the lower left corner, at F/R of ≤ 0.1 and reducing temperatures, sanidine K-feldspar is predicted to be replaced by microcline (between 400 and 350°C), biotite and plagioclase are replaced by chlorite and calcite (between 350 and 300°C) and magnetite is replaced by hematite (between 300 and 250°C).

- The boundary between hematite (lower temperature) and magnetite (higher temperature) is defined by the magnetite-hematite redox buffer and is vertical (between 250°C and 300°C). This boundary is consistent for all of the models presented.
- Chlorite is an important alteration mineral at $F/R \leq 1$, particularly at temperatures of $\leq 300^\circ\text{C}$. Microcline K-feldspar (potassium-rich) is an important alteration mineral at $F/R \leq 10$, and temperatures of $\leq 350^\circ\text{C}$. The presence of chlorite and microcline along with magnetite defines the CAM alteration field.
- Muscovite is an important alteration phase at $F/R \geq 1$ and temperatures of $\leq 350^\circ\text{C}$. Assemblages with co-existing hematite, muscovite and chlorite (HSCC) occur at temperatures of $\leq 250^\circ\text{C}$ and moderate F/R of ~ 1 . At higher F/R (≥ 10 , ≤ 100) hematite and muscovite occur together without chlorite.
- Copper bearing phases (including native copper, bornite, chalcocite and Cu-chloride) occur at $F/R \geq 10$ at all temperatures. Native copper and bornite are the predominant Cu phases at temperatures of $\geq 400^\circ\text{C}$, bornite and chalcocite predominant at temperatures $\leq 350^\circ\text{C}$ and $\geq 250^\circ\text{C}$ and CuCl(s) predominant at temperatures of $\leq 200^\circ\text{C}$.

Notable observations from Figure 52B (F/R vs $\log f\text{O}_2$ at temperature = 300°C) include:

- The lower left corner (low F/R and low $\log f\text{O}_2$) is characterised by chlorite, microcline and magnetite bearing assemblages corresponding to the CAM style of alteration.
- Magnetite is predicted to be replaced by hematite at $\log f\text{O}_2$ of approximately -30.
- Chlorite is predicted to be stable at $F/R \leq 1$ across the range of modelled $\log f\text{O}_2$, and replaced by muscovite at $F/R \geq 1$.
- Hematite and muscovite bearing assemblages are predicted to occur at $F/R \geq 1$ and $\log f\text{O}_2 \geq -30$. Whereas hematite, muscovite and chlorite bearing assemblages, most characteristic of HSCC, alteration are restricted to a narrower range ($10 \geq F/R \geq 1$).
- Copper bearing phases (including bornite, chalcocite and Cu-chloride) occur at $F/R \geq 10$ at all $\log f\text{O}_2$. Bornite and chalcocite are the predominant Cu phases at $\log f\text{O}_2 \leq -28$ and CuCl(s) predominant at $\log f\text{O}_2 \geq -26$.

Notably absent from the assemblages shown in Figure 52 are pyrite (the most abundant sulphide observed in the eastern Gawler Craton samples presented in this thesis) and chalcopyrite (the most abundant Cu-bearing sulphide).

In general terms, the equilibration of a model granite protolith with the high-salinity model fluid A predicts a progression from MB, to CAM to HSCC styles of alteration with decreasing temperature, increasing F/R and increasing $\log f\text{O}_2$.

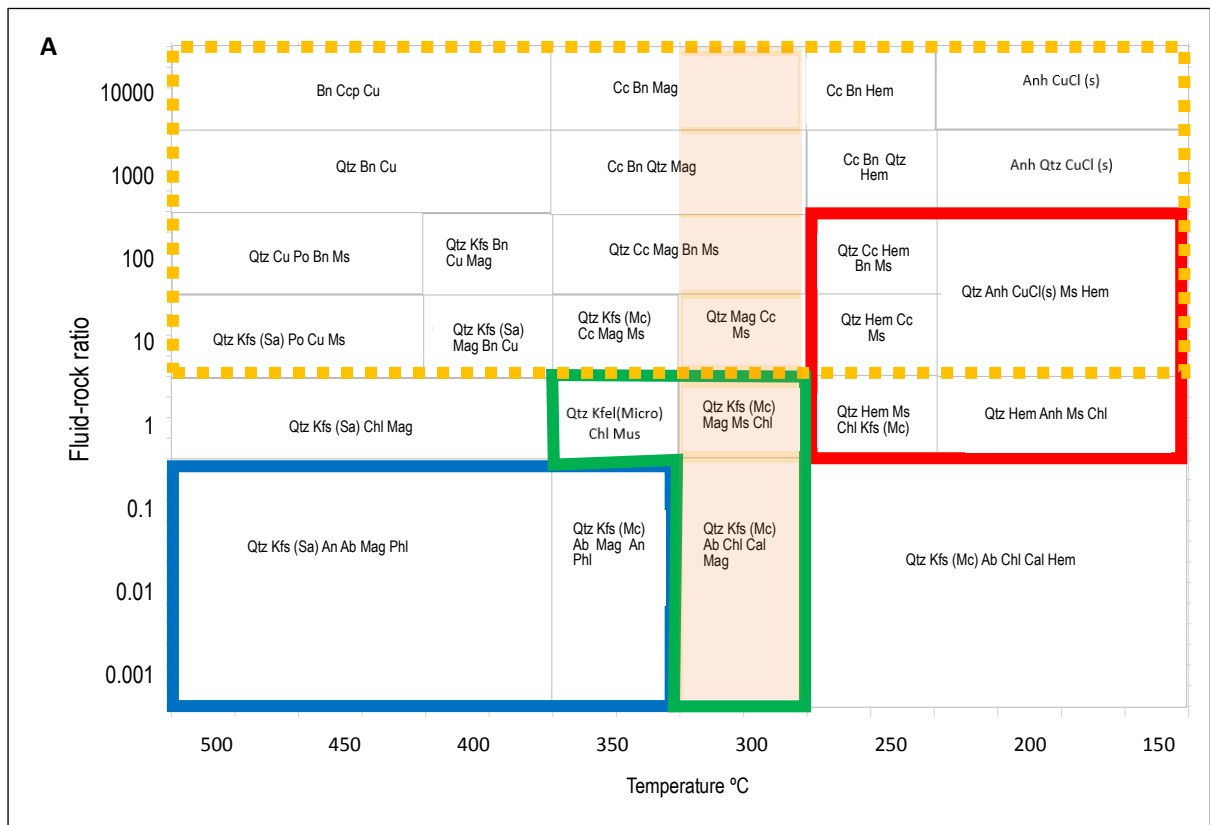


Figure 52. (Previous page). Simplified plots of calculated equilibrium mineral assemblages for the model granite + model fluid A (35 wt % NaCl equivalent, 0.96 wt % Cu, 0.54 wt % Sulphur) for; **A.** Fluid-rock ratio vs Temperature with $\log fO_2$ fixed at -34, and **B.** Fluid-rock ratio vs $\log fO_2$ with temperature fixed at 300°C. Vertical shaded yellow areas are identical in the two plots. The calculated pH varies between 6.1 and 6.7. Fields for the commonly observed alteration assemblages in the eastern Gawler Craton are superimposed; Blue = Magnetite-Biotite±K-feldspar (MB); Green = Chlorite-Alkali Feldspar-Magnetite (CAM); Red = Hematite-Muscovite-Chlorite±Carbonate (HSCC); Dashed Orange = copper minerals. Mineral abbreviations: Anh = anhydrite, An = Anorthite, Ab = albite, Bn = bornite, Cal = calcite, Cc = Chalcocite, Chl = chlorite, Hem = hematite, Kfs = K-feldspar, Mag = magnetite, Mc = microcline, Ms = muscovite, Phl = phlogopite, Po = pyrrhotite, Qtz = quartz, Sa = sanidine, Cu=copper, CuCl(s) = solid CuCl.

4.3.2 Model Granite equilibrated with model fluid B (16.2 wt % NaCl equiv)

The equilibration of a model granite protolith with the model fluid B predicts a similar progression as the previous model; from MB, to CAM to HSCC styles of alteration with decreasing temperature, increasing F/R and increasing $\log fO_2$. This set of calculations is represented in Figure 53. Notable observations from Figure 53A:

- The “least altered” mineral assemblages (most like the starting Model Granite) occurs in the lower left of the diagram at a temperature of 500°C and F/R of ≤ 0.1 .
- Co-existing magnetite, biotite and K-feldspar occur at F/R ≤ 0.1 and temperatures of $\leq 450^\circ\text{C}$ and $\geq 350^\circ\text{C}$. This part of the diagram most closely represents the MB style of alteration. Noting that the K-feldspar transitions from sanidine to microcline with decreasing temperature.
- Starting in the lower left corner, at F/R of ≤ 0.1 and reducing temperatures, sanidine K-feldspar is predicted to be replaced by microcline (between 400 and 350°C), biotite and plagioclase are replaced by chlorite and calcite (between 350 and 300°C) and magnetite is replaced by hematite (between 300 and 250°C). These changes mimic those in Figure 52.
- The boundary between hematite (lower temp) and magnetite (higher temp) is defined by the magnetite-hematite redox buffer and is vertical (between 250°C and 300°C). This boundary is consistent for all of the models presented.
- At temperatures $\geq 350^\circ\text{C}$ chlorite is an important alteration mineral at F/R ≥ 1 and ≤ 10 . At temperatures of $\leq 300^\circ\text{C}$ chlorite is an important alteration mineral at F/R ≤ 10 . The presence of chlorite and microcline along with magnetite defines the CAM alteration field.
- Muscovite is an important alteration phase at F/R of ≥ 1 and temperatures of $\leq 300^\circ\text{C}$. Assemblages with co-existing hematite, muscovite and chlorite (HSCC) occur at temperatures of $\leq 250^\circ\text{C}$ and F/R ≥ 1 and ≤ 10 . At higher F/R (≥ 100 , ≤ 1000) hematite and muscovite occur together without chlorite.
- Pyrrhotite is a common alteration phase at F/R ≥ 10 and temperatures of $\geq 300^\circ\text{C}$ whereas pyrite is a common phase at F/R ≥ 10 and temperatures of $\leq 250^\circ\text{C}$.
- Copper bearing phases (including chalcocite, bornite and chalcopyrite) occur at F/R ≥ 10 across a wide range of temperature. Chalcocite is the predominant Cu phase at the temperatures at the extremes of the model ($\geq 450^\circ\text{C}$ and $\leq 200^\circ\text{C}$), bornite is predominant

at temperatures $\leq 400^{\circ}\text{C}$ and $\geq 350^{\circ}\text{C}$ and chalcopyrite is predominant at temperatures of $\leq 300^{\circ}\text{C}$ and $\geq 250^{\circ}\text{C}$.

Notable observations from Figure 53B (F/R vs $\log f\text{O}_2$ at temperature = 300°C) include:

- The lower left corner (low F/R and low $\log f\text{O}_2$) is characterised by chlorite, microcline and magnetite bearing assemblages corresponding to the CAM style of alteration.
- Magnetite is predicted to be replaced by hematite at $\log f\text{O}_2 \geq -30$.
- Chlorite is predicted to be stable at $F/R \leq 100$ at $\log f\text{O}_2$ of -34 and then at lower F/R as $\log f\text{O}_2$ increases, such that chlorite is only stable at $F/R \leq 1$ at $\log f\text{O}_2 \geq -26$.
- Hematite and muscovite bearing assemblages are predicted to occur at $F/R \geq 1$ and ≤ 1000 and $\log f\text{O}_2 \geq -30$. Whereas hematite, muscovite and chlorite bearing assemblages, most characteristic of HSCC, alteration are restricted to a narrower range ($10 \geq F/R \geq 1$).
- Pyrite occurs at $F/R \geq 10$ and $\log f\text{O}_2 \geq -32$ and ≤ -28 .
- Copper bearing phases (including chalcocite and chalcopyrite) occur at $F/R \geq 10$ at $\log f\text{O}_2 \leq -26$. Chalcopyrite is the predominant Cu phase at $\log f\text{O}_2 \leq -28$ and chalcocite is predominant at $\log f\text{O}_2 \sim -26$.

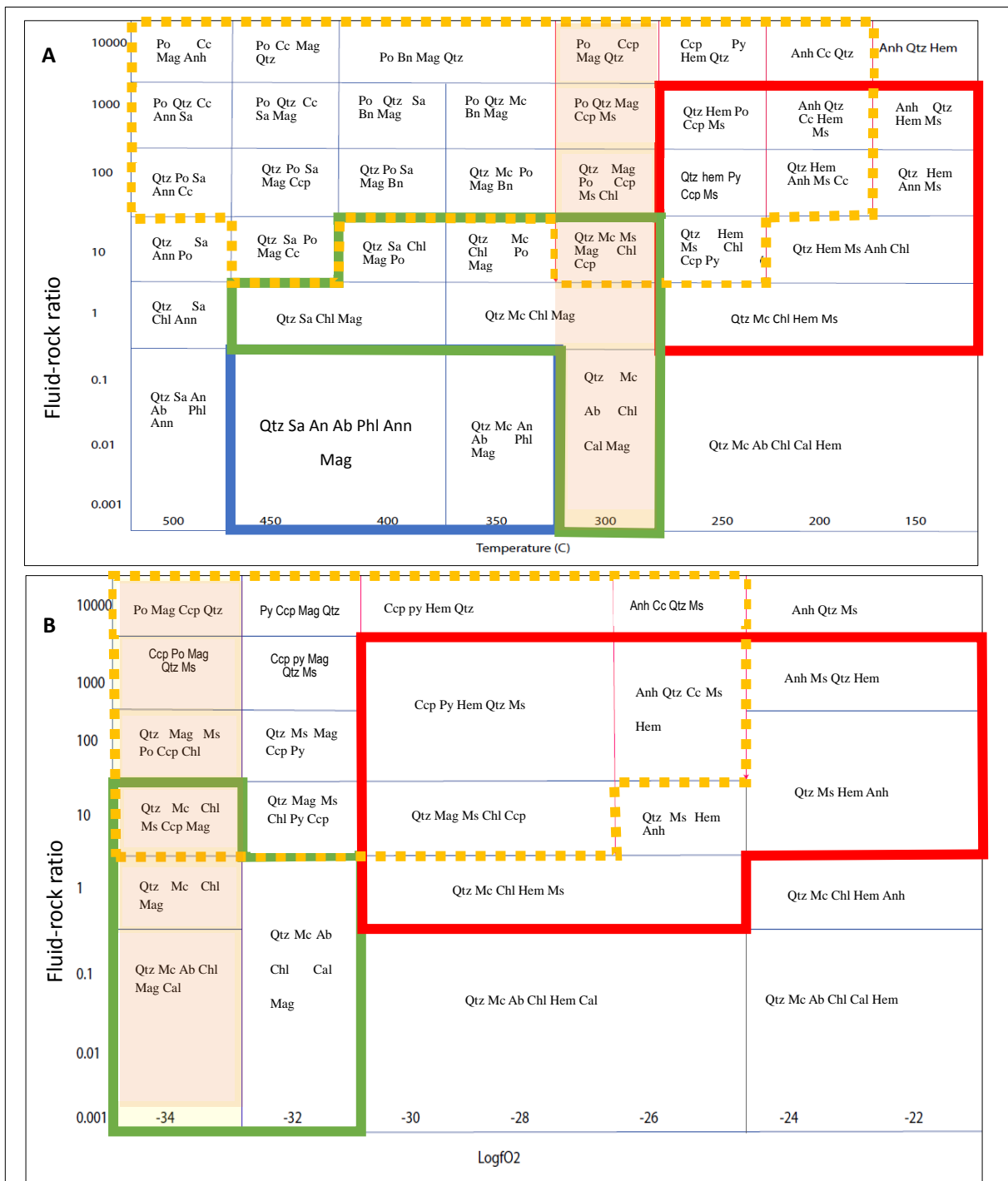


Figure 53. Simplified plots of calculated equilibrium mineral assemblages for the model granite + model fluid B (16.2 wt % NaCl equivalent, 0.64 wt % Cu, 0.36 wt % S) for; **A.** Fluid-rock ratio vs Temperature with logfO₂ fixed at -34, and **B.** Fluid-rock ratio vs logfO₂ with temperature fixed at 300°C. Vertical shaded yellow areas are identical in the two plots. The calculated pH varies between 6.1 and 6.7. Fields for the commonly observed alteration assemblages in the eastern Gawler Craton are superimposed; Blue = Magnetite-Biotite±K-feldspar (MB); Green = Chlorite-Alkali Feldspar-Magnetite (CAM); Red = Hematite-Muscovite-Chlorite±Carbonate (HSCC); Dashed Orange = copper minerals. Mineral abbreviations as Figure 52, Ann = Annite, Ccp = chalcopyrite.

4.3.3 Model Granite equilibrated with model fluid B1 (16.2 wt % NaCl equiv. no sulphur)

These calculations were designed to determine the importance of sulphur on the stability of Cu minerals. Two Figures are shown: an F/R vs temperature plot (Figure 54A) comparable to Figure 53A but lacking sulphide and sulphate phases, and a mineral abundance vs F/R plot at a temperature of 250°C and logfO₂ of -34. The F/R vs temperature plot shows a similar progression as the previous model; from MB, to CAM to HSCC styles of alteration with decreasing temperature and increasing F/R. The magnetite to hematite transition occurs at between 250° and 300°C (Figure 54A). Above 450°C magnetite is replaced by biotite. K-feldspar is predicted to be a stable phase in all areas but the top right of Figure 54A, at F/R ≥10 and temperatures of ≤300°C. Sanidine K-feldspars are favoured at higher temperatures and lower fluid-rock ratios than microcline K-feldspars. Muscovite is stable at temperatures ≤300°C. Chlorite is stable across the modelled temperature range, at F/R ≤1 for temperatures ≥400°C, F/R ≤10 for temperatures ≤350°C and ≥300°C and at F/R ≤100 at temperatures of ≤250°C.

Figure 54B illustrates a typical vertical profile through the F/R vs temperature plot. The minerals stable at low F/R are incrementally replaced by iron-oxide (in this case hematite but the same is true for magnetite at higher temperatures) and muscovite with chlorite being an important alteration phase at low to moderate F/R.

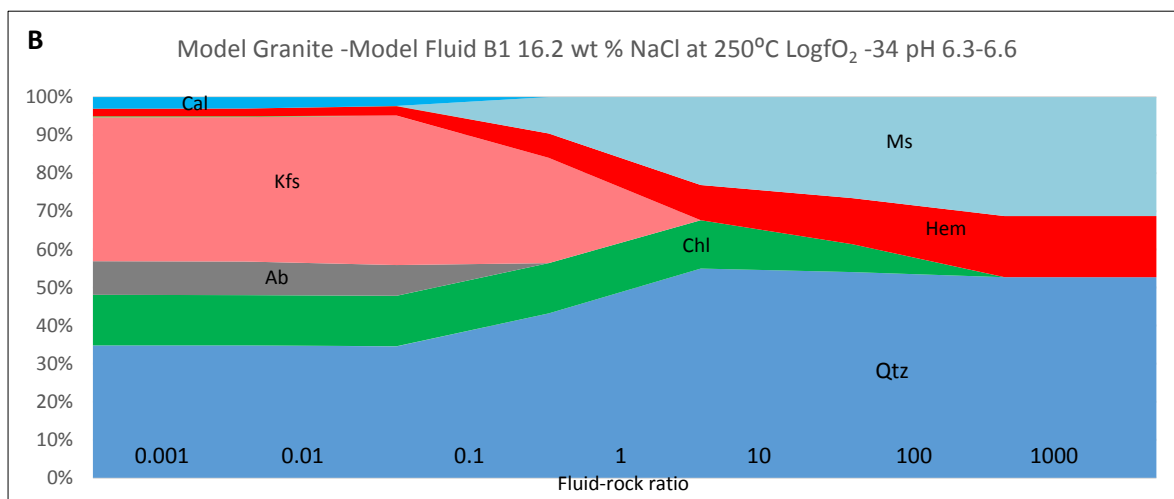
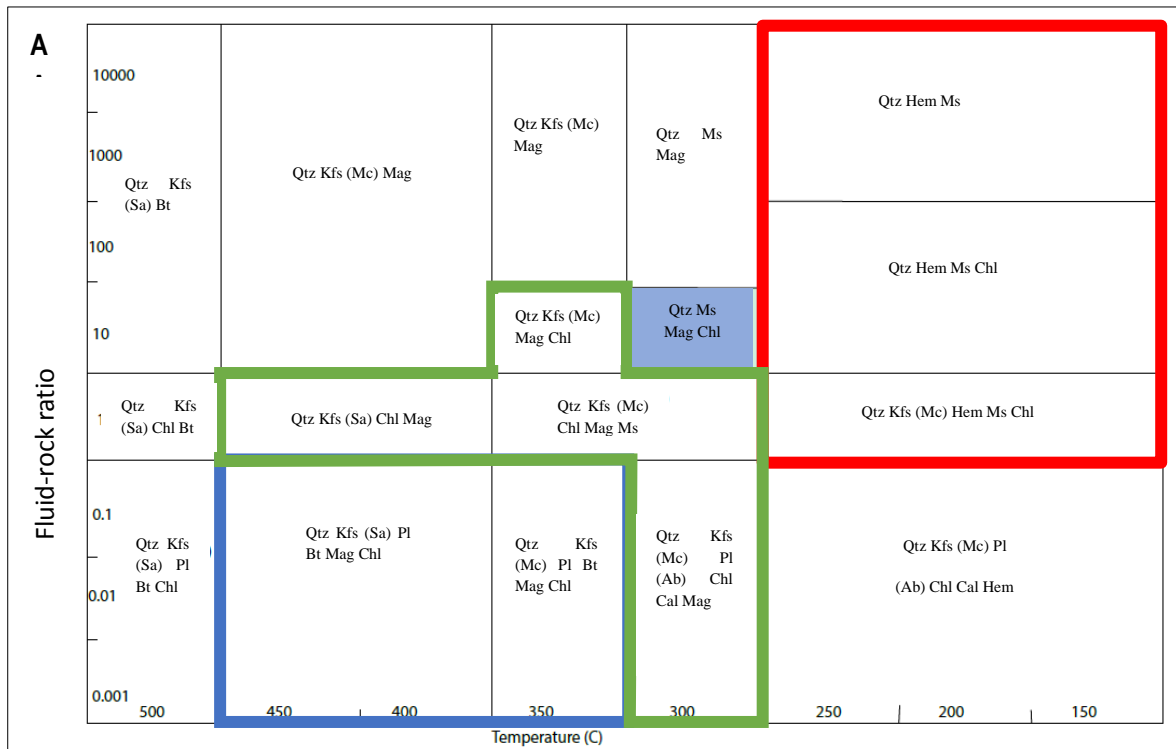


Figure 54: A. Predicted mineral assemblages for the model granite mixed with model fluid B1 for fluid-rock ratios of 10^{-3} to 10^4 and temperatures of 150° to 500°C . Figure 54B occupies a vertical section at 250°C . Predicted mineral assemblages and relative mineral abundances for the model granite mixed with model fluid A at 250°C at fluid-rock ratios of 10^{-3} to 10^4 . Main alteration fields and mineral abbreviations are as for Figures 52 and 53.

4.3.5 Model Granite equilibrated with model fluid C (Mg-rich, 30 wt % NaCl equiv)

Granite I reacted with fluid C with models simulating calcite-hematite-quartz-microcline assemblage similar to dolomite alteration granite III. Calcite-hematite-quartz-microcline±phlogopite-chlorite assemblage formed at fluid-rock ratio >1 at 250°C . HCh modelling produced K-feldspar-chlorite-quartz-hematite assemblage which changed to calcite-hematite at fluid-rock ratio >10 with minor apatite and phlogopite.

HCh modelling of granite I-fluid C (30 wt % NaCl equiv) interactions was conducted for a range of temperatures 150°-500°C and fluid-rock ratios 10^{-3} - 10^4 at $\log fO_2$ -34 (Figure 55). I found that hematite assemblage was replaced by magnetite assemblage at $>275^\circ\text{C}$, quartz–hematite-anhydrite-manganosite \pm phlogopite formed at $<225^\circ\text{C}$ with fluid-rock ratio <10 and K-feldspar (sanidine) was replaced by microcline at 375°C with fluid-rock ratio >0.1 .

To understand the mechanism of dolomite replacing calcite in granite I, I altered 30 wt % NaCl equiv fluid composition in HCh modelling by reducing CaCl_2 to 4.6 g and adding 5 g MgCl_2 (Figure 55). Results predict that hematite-dolomite–anhydrite-manganosite assemblage occurred at fluid-rock ratio >10 at $<275^\circ\text{C}$, and magnetite–dolomite assemblage occurred at $>275^\circ\text{C}$ with fluid-rock ratio >10 . Bornite occurred at 350°C - 400°C and chalcocopyrite occurred at 250°C - 300°C with fluid-rock ratio <1 .

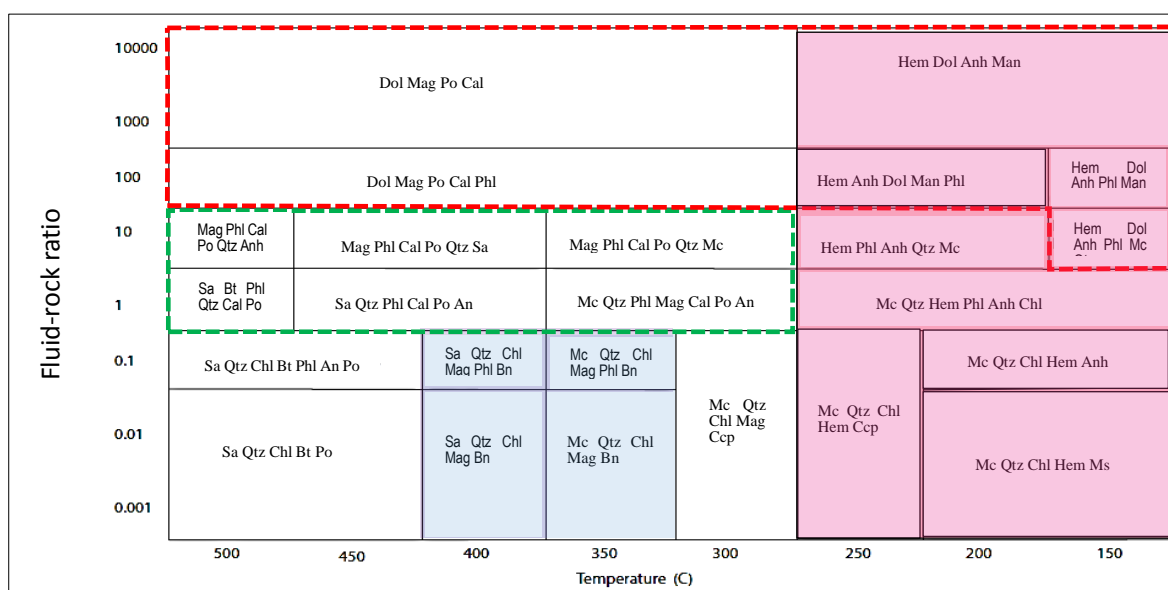


Figure 55. The models added MgCl_2 for making the dolomite alteration. The model has the pH 6-6.3, 500° - 150° C with T-P grid with $\log fO_2$ -34. It supports the dolomite alteration surround the apatite cut through the sanidine veins in the petrogenesis. The dolomite area has the fluid–rock ratio >10 , and the hematite-dolomite-anhydrite occurs at ratio 10 with low temperature 150° C. The sanidine changes to microcline at 375° C. Blue area = bornite assemblage, Red area = hematite assemblage, Red dashed line = Dolomite assemblage, Green dashed line = calcite assemblage. Mineral abbreviations: Bn=bornite, Dol=dolomite, Man=manganite.

Our modelling predicted that dolomite formation is dependent on fluid components and oxide environments. With rich-Fe fluids, HCh modelling predicted that dolomite–hematite–manganosite-anhydrite assemblage resulted. When $\log fO_2$ was altered from -29 to -34, formation of magnetite-hematite-chalcopyrite-dolomite changed to chalcopyrite-bornite, where bornite was associated with magnetite and chalcocite was associated with hematite. Magnetite had a 275°C temperature boundary with hematite and sanidine replacing microcline above 400°C (Figure 55).

Results of HCh modelling showed that calcite formation was restricted to $>220^\circ\text{C}$ and fluid-rock ratio of >0.1 under reduced conditions of fO_2 -34. Modelling predicted that calcite

and hematite formed together at 225⁰-275⁰C and fluid-rock ratio >1 (Figure 55). Calcite was replaced by dolomite at <275⁰C where fluids contained MgCl₂ (Figure 55). Dolomite and calcite had a temperature boundary of ~250⁰C at fluid-rock ratio 10, while sanidine changed to microcline at 370⁰C at fluid-rock ratio <10 (Figure 55). Chlorite-hematite-quartz-K-feldspar assemblage occurred at fluid-rock ratio <1 and hematite-dolomite-anhydrite-manganosite with phlogopite and sanidine occurred at fluid-rock ratio >10. Results of our modelling describe the hematite-dolomite assemblage area similar to granite III.

Results presented here suggest that magnetite and hematite in Emmie Bluff were formed from different fluids with contrasting oxygen isotope ratios (Oreskes and Einaudi, 1992). Hematite had the same <275⁰C boundary with magnetite when fluids changed from 16.2 to 35 wt % in reduction environments. Hematite forms in reduction environments with ore minerals at <275⁰C.

Calc-silicate HCh models

4.3.6 Model calc-silicate -fluid B

This set of calculations is represented in Figure 56 and 57 with calculated pH 6.2-6.7. Notable observations from Figure 56 and 57 (Fluid-rock ratio vs temperature at logfO₂ = -34) include:

- The “least altered” mineral assemblages (most like the starting Model calc-silicate) occur in the lower left of the diagram at temperatures $\geq 300^{\circ}\text{C}$ and $F/R \leq 0.1$. With co-existing magnetite, biotite and K-feldspar, this part of the diagram most closely represents the MB style of alteration in Figure 57.
- Starting in the lower left corner, at F/R of ≥ 10 and reducing temperatures, sanidine K-feldspar is predicted to be replaced by microcline (between 400° and 350°), plagioclase are replaced by chlorite (between 350° and 300°) and magnetite is replaced by hematite (between 300° and 250°).
- The boundary between hematite (lower temperature) and magnetite (higher temperature) is defined by the magnetite-hematite redox buffer and is vertical (between 250° and 300°). This boundary is consistent for all of the models presented.
- Chlorite is an important alteration mineral at $1 \leq F/R \leq 100$, particularly at temperatures of ~300° but minor chlorite up to 450° at F/R 10. Microcline K-feldspar (potassium-rich) is an important alteration mineral at $F/R \geq 100$, and temperatures of ~350°. The presence of chlorite and microcline along with magnetite defines the CAM alteration field.
- Muscovite is an important alteration phase at F/R of ≥ 100 and temperatures of 250 to 350°. Assemblages with co-existing hematite, muscovite and chlorite (HSCC) occur at temperatures of $\leq 250^{\circ}\text{C}$ and moderate F/R of ≥ 100 . At higher F/R (≥ 1000) hematite and muscovite occur together without chlorite.
- Copper bearing phases (including chalcopyrite and chalcocite) occur at $F/R \geq 10$. Chalcocite occur at almost temperatures but chalcopyrite occur at 300 and $F/R \sim 10$ without native copper and bornite.

Notable observations from Figure 57B (F/R vs $\log fO_2$ at temperature = 300°C) include:

- The lower left corner (low F/R and low $\log fO_2$) is characterised by calcite, chlorite, and phlogopite bearing assemblages corresponding to the CAM style of alteration.
- Magnetite is predicted to be replaced by hematite at $\log fO_2$ of approximately -30 from F/R 1 to 10 and up to -34 at F/R ≥ 100 .
- Chlorite is predicted to be stable at F/R ≤ 1 across the range of modelled $\log fO_2$, F/R ≤ 10 and $\log fO_2 \leq -26$ and replaced by muscovite at F/R ≥ 10 and $\log fO_2$ from -26 to -32, and F/R ≥ 1 from -22 to -26.
- Hematite and muscovite bearing assemblages are predicted to occur at F/R ≥ 10 and $\log fO_2$ from -22 to -26 and F/R ≥ 100 and $\log fO_2 \leq -28$. Whereas hematite, muscovite and chlorite bearing assemblages, most characteristic of HSCC, alteration are restricted to a narrower range (F/R ~ 10 and $\log fO_2 \sim -26$).
- Copper bearing phases (including chalcopyrite and chalcocite) occur at F/R ≥ 10 at $\log fO_2 \leq -26$, Chalcopyrite are the predominant Cu phases at $\log fO_2 \leq -28$ and F/R ~ 10 and chalcocite occur at F/R ≥ 100 and $\log fO_2 \leq -26$.

Notably pyrite assemblages shown in Figure 57 occur at F/R ≤ 0.1 and temperature $\geq 300^\circ\text{C}$ which is consistent in the MB (the most abundant sulphide observed in the eastern Gawler Craton samples presented in this thesis) in Figure 57A and pyrite-chalcopyrite assemblages occur at F/R ~ 10 and $\log fO_2$ -28 to -32 (the most abundant Cu-bearing sulphide).

At 300°C our models produced 35 wt % chlorite very similar to sample 2066203 (Figure 56). Specifically, models predict chlorite at 15 wt % to a peak of 35 wt % at fluid-rock ratio 1 to 10 at 300°C. Thirteen minerals resulted from modelling at 300°C, with chalcopyrite-chalcocite assemblage formation at fluid-rock ratio 1-100 and temperature 250°-300°C (Figure 57).

In HCh modelling, chlorite formed across a large fluid-rock ratio range of 1 to 100 at 200°C. Dolomite formed at 200°C and fluid-rock ratio 1 with very less chalcocite without chalcopyrite. However, at 200°C mineral formation was simpler (10 minerals) as compared to 300°C (13 minerals). Notably, anhydrite, a major S mineral formed at 200°C, but not at 300°C and chalcocite, a Cu mineral, occurred at both 200°C and 300°C. Pyrrhotite and chalcopyrite did not form at low temperature (200°C). At high temperature (300°C) magnetite replaced hematite which formed at low temperature (200°-250°C).

In HCh modelling, I changed $\log fO_2$ to -36 to increase reduction. Results of the 300°C model did not change, but the 200°C model resulted in no bornite and less chalcocite. Results of the 400°C model predicted a small chlorite formation fluid-rock ratio range with chalcopyrite-chalcocite-bornite assemblage. The 500°C model predicted chalcopyrite-chalcocite assemblage at fluid-rock ratio 0.1 to 1, but chlorite did not form.

HCh modelling predicted that low temperature (150°C) resulted in less minerals being formed, with eight minerals forming at pH 6.1 (acid), and no ore mineral formation, but an increase in anhydrite (S mineral) formation. Chlorite formed at 200°C with a fluid-rock ratio 1 to 100 at pH 6.2. Less chalcocite (ore mineral) formed at 200°C, as compared to formation at higher temperatures. Anhydrite formed at 200°C and no chalcopyrite or bornite formed at this

temperature. Temperature increase to 300°C resulted in chlorite becoming unstable as pH increased, but more minerals formed (13 minerals). Formation of bornite may occur at high temperature >300°C. Under reduction conditions of $\log fO_2$ -34, results of HCh modelling for calc-silicate predict that the best simulation was at 250°C with formation of 12 minerals, including hematite-pyrite-chalcopyrite-chalcocite-anhydrite assemblage as I seen most in chapter 2 exclude chalcocite.

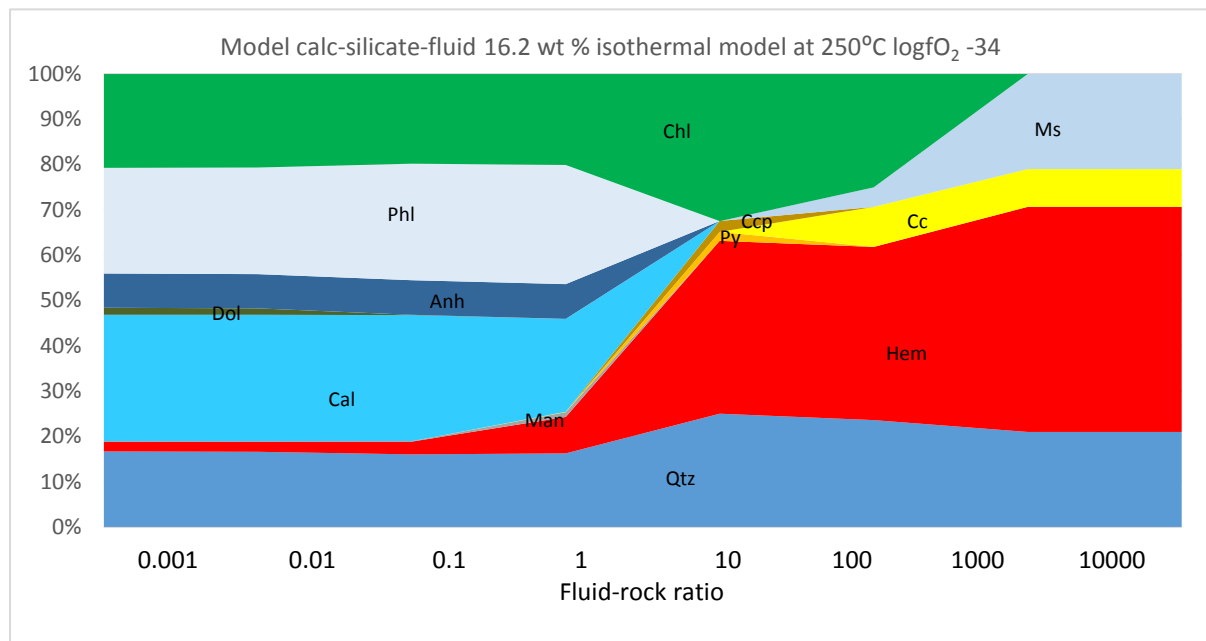


Figure 56. 12 minerals are simulated at 250°C with 35 wt % chlorite at fluid-rock ratio 10. The chlorite up to 40 wt % are simulated with the hematite-chalcopyrite-chlorite- anhydrite as the observation in sample 2066203.

In HCh modelling, I added 30 g pyrite to unaltered calc-silicate-fluid B reactions to consider S content of resultant mineral assemblages (Figure 57). I found that chalcocite occurred at $\log fO_2 < -24$ and chalcopyrite-chalcocite occurred at $-32 < \log fO_2 < -26$. Magnetite-muscovite-chalcocite assemblage occurred at $\log fO_2 < -34$. Thus, fO_2 had a major effect on formation of ore minerals, where S content of rock or fluids resulted in ore mineral formation.

HCh modelling with addition of pyrite predicted that Cu minerals formed at 300°C with fO_2 between -28 to -30 and fluid-rock ratio >1. Chalcopyrite was a major ore mineral under these modelling conditions, with chalcopyrite being replaced by bornite in more reductive environments and by chalcocite in more oxide environments. At higher temperatures, hematite was replaced by magnetite (at temperature >275°C and $fO_2 < -30$). Specifically, hematite was replaced by magnetite at $fO_2 < -32$ with fluid-rock ratio >1 in fluid-calc-silicate modelling reactions (Figure 57).

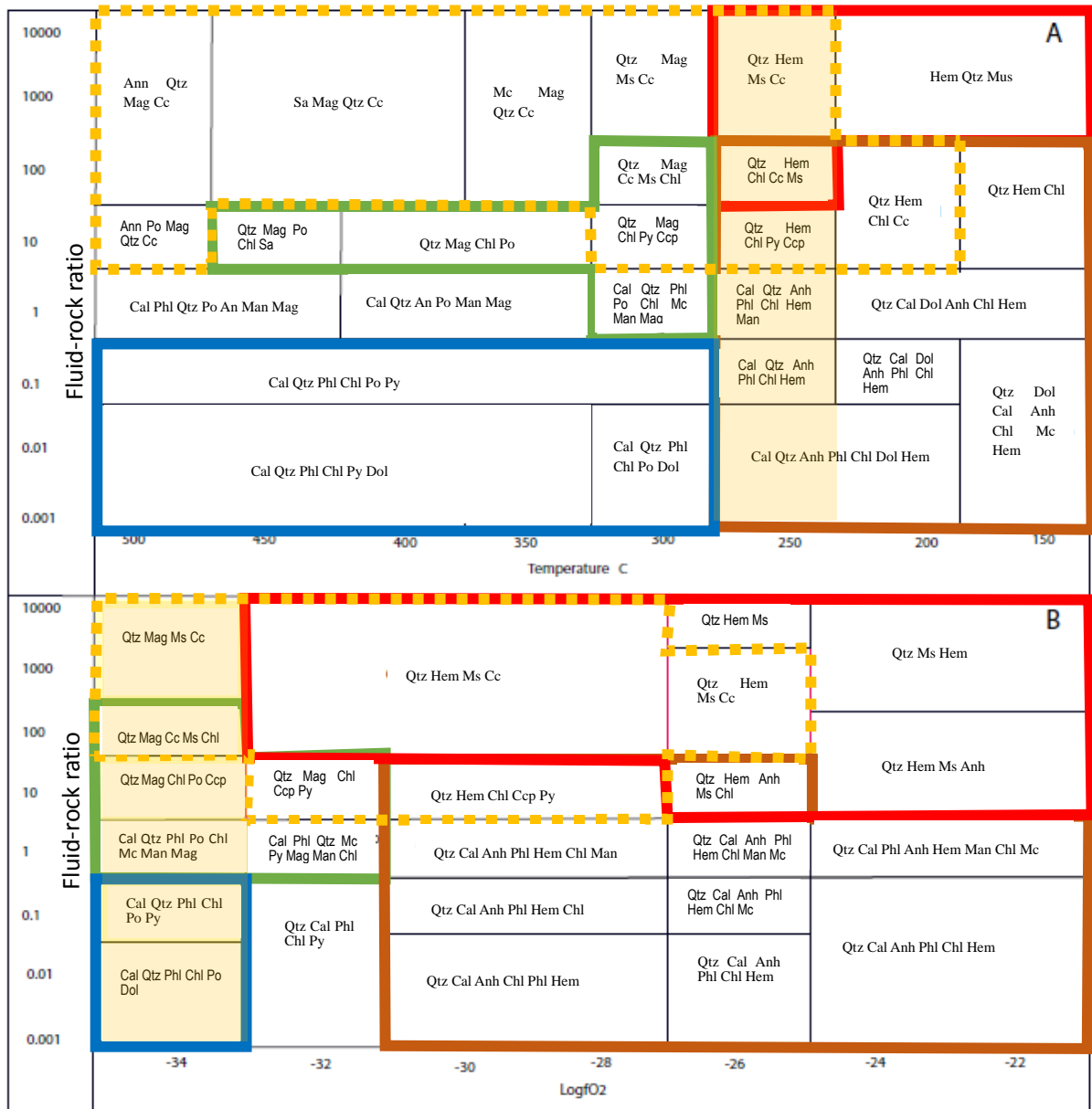


Figure 57. The temperature affects the ore minerals (A) match with the fO_2 affects the ore minerals at 3 wt % pyrite in calc-silicate rock at 300°C (B). The magnetite has the 275°C boundary with hematite in ~275°C in A. There is no Cu minerals formed at $fO_2 > -24$ in B, the Cu minerals is formed above ratio 1. The 3D models have the same mineral assemblage as yellow areas.

4.4 DISCUSSION

Although the equilibrium models presented here are simplified representations of a complex system, involving numerous assumptions and approximations they share a number of common features and predict alteration assemblages and paragenetic sequences that occur in the eastern Gawler Craton. The following discussion highlights some of the consistent modelling outcomes, as influenced by the important variables fluid composition, rock composition, F/R, temperature (and pressure) and $\log fO_2$.

The effect of fluid-rock ratio (F/R)

Fluid–rock ratio affects mineral assemblages. Major minerals changed at fluid–rock ratio >10 , depending on rock and fluid compositions. Ore minerals changed at fluid–rock ratio in the range of 10^{-3} to 1, as ore mineral contents are far less than that of alteration minerals in samples. Fluid–rock ratio in the range 1 to 10 may be resulted in formation areas of mineralisation/alteration. Chlorite existed at fluid–rock ratio in range 10–100 with temperature 275° – 350° C as minor phases, and chlorite existed at fluid–rock ratio range 10–100 with temperature 200° – 275° C and 440° – 500° C as two major phases. In the temperature range 150° – 275° C, microcline–albite–chlorite–calcite–hematite changed to microcline–hematite–muscovite–chlorite in fluid–rock ratios from 0.01–0.1 to 1–10. Increasing fluid–rock ratio to >10 , mineral assemblage changed to hematite–muscovite–chlorite and then at fluid–rock ratio > 1000 final hematite–muscovite formed. The hematite–muscovite–chlorite assemblages depend on Fe-rich–Ca–Mg–K–Mn fluids at 16.2 wt % NaCl equiv. Fluid–rock ratios have been argued with theoretical fluid infiltration through a saturated rock column, models using equilibrium steps should converge on reactive transport models only when the equilibrium steps are infinitesimally small and kinetic effects are ignored (Cleverley and Oliver, 2005). I applied HCh models to fix the fluid–rock ratio which was important in all reactions.

The effect of protolith composition

Protolith composition is a significant influence on mineral assemblages at $F/R < 10$ and is the dominant influence at $F/R < 1$. There is relatively little change in mineral assemblages present between $F/R = 0.001$ and 1.

The effect of fluid composition

The effect of fluid composition are dominant at $F/R > 1$. The major mineral assemblage changed as fluid composition at $F/R > 10$. S-bearing fluids form the sulphur minerals including chalcopyrite, bornite and chalcocite when fluids contained Cu in fluids. Specifically, Cu-bearing fluids mixed with S-rich rock units, they formed the Cu sulphides in redox situations. In without sulphur situations, the rich-Cu hypsyaline formed in flow processes.

The effect of temperature (and pressure)

Hematite transferred to magnetite at above 275° C. Muscovite formed below 350° C. Chlorite existed at all temperature ranges at fluid–rock ratio ≤ 1 . Microcline transferred to sanidine above 400° C. Biotite existed at $\geq 500^{\circ}$ C for all fluid–rock ratios and at temperature range 350° – 500° C at fluid–rock ratio < 1 . Our models predict Cu sulphide minerals are consistent with an orebody at temperatures of 250° – 300° C (Cleverley and Oliver, 2005), rather than low temperature 150° C (Oreskes and Einaudi, 1992; Haynes et al. 1995). As pressure decreases, hematite may increase, consistent with fault system formation at lower pressure.

Chalcocite formed between 150° and 200° C and chalcopyrite formed at 250° – 350° C, then bornite formed at 350° – 400° C. Secondary chalcocite and chalcopyrite formed at $>400^{\circ}$ C. Our model supports multiple processes with Cu–S minerals (chalcocite and bornite) precipitating at the coolest end of the model in response to unbuffered changes in pH and fluid redox (Cleverley and Oliver, 2005).

The effect of $\text{Log}f\text{O}_2$

In oxide conditions ($\log fO_2$ -24 to 1) ore minerals do not form, but ore element-rich fluids do form. The ore minerals involved in reduction environment and the fluid must be changed from oxide to reduction (redox) or say the redox controlled the formation of ore minerals. At fluid-rock ratio >10 , chalcocite formed at fO_2 -26, but when $fO_2 >-26$ no Cu minerals formed. At fluid-rock ratio >1 , chalcopyrite formed at fO_2 -28 to -30. When fO_2 decreased to -32, pyrite occurred with chalcopyrite. Then, at fO_2 -34 pyrrhotite-chalcopyrite-magnetite-muscovite assemblage formed. The fO_2 -26 to -34 in our models is consistent with reduction environments of Bastrakov et al. (2007). Redox conditions are important for reduction Cu mineral formation and oxide conditions result in leaching processes.

pH

HCh models involved three parameters (fluid-rock ratio, temperature-pressure and fO_2) associated with pH. In HCh modelling, pH is automatically calculated. pH of 2.1 to 4.1 in leaching fluids (18.7 wt % NaCl equiv) resulted in pyrite-muscovite-anhydrite assemblage formation and K-feldspar, albite, magnetite and chalcopyrite-chalcocite dissolved into fluids and the fluids are leaching most ore minerals and formed pyrite-muscovite-anhydrite assemblage. This situation is similar to the Emmie Bluff having the muscovite in hang wall and foot wall and the leaching processes may be the earlier stage fluid-rock reaction. Late stage fluid-rock reaction may not have pH 2.1 to 4.1. The idea of pH changes is that fluid-rock reaction will be leading to pH 7 neutral rather than go acid or alkaline. In contrast, alkaline fluids are leaching fluids carrying ore elements as described by Bastrakov et al. (2007). Haynes et al. (1995) applied pH 5.4 in hot water (250⁰C) with high Cl-Na-S content. In the study area, Na content is lower than that possible in HCh models. Cooler water (150⁰-200⁰C) is calculated at pH 4.5-6.9 with resulting hematite-calcite-manganosite assemblage. In calc-silicate models, pH is stable at 6.2-6.7 and forms rich chalcopyrite-chalcocite assemblage with 13 minerals at most. Calc-silicate models also show that pH leading to neutral accompanied with temperature increasing from 150⁰ to 300⁰C with the rich ore minerals. For dolomite alteration (17.4 wt %) with very alkaline fluid (pH 12.7), more muscovite-chlorite formed at 200⁰C than at 300⁰C. Pearce et al., (2015) suggested pH 7-9.8 of gold deposit related to carbonate of biotite and Bastrakov et al., (2007) did not mention pH but applied the NaCl fluids. Our models with pH 6-7.4 predicted Cu sulphide formation period not consistent with the ore form at pH 5.4 (Haynes et al. 1995) and pH 2.9 Cleverley and Oliver (2005) and pH 4.8-5.2 Oliver et al., (2004).

Limitations of HCh models

Hypersaline fluids of > 35 wt % saline, present in fluid inclusion data for the eastern Gawler Craton IOCG deposit, are beyond the limitations of HCh modelling requirements. Interesting is that the average 7 fluid inclusion data is 30 wt % NaCl equiv and these are good for HCh model requirements. The CO₂ may exist at fluids mostly and the hematite veins may be the impure hematite. There are lots of ore metal related to carbonate and change the impure-hematite with ore metal although far away to mineralisation. LA-ICPMS and EM (19 analysis) fail at 46-59 wt % Fe with lots of quartz-chlorite inclusions in the hematite of dolomite and these indicated the impure hematite.

IMPLICATIONS FOR PATHFINDER METALS

Fabris et al. (2012) identified that ten pathfinder element index (Au, Ag, As, Bi, Cu, Mo, S, Sb, Se and W) empirically-spatially related to IOCG mineral deposits. This thesis present evidence that these elements hosted by different minerals in different rocks (Figure 58). The fluid controlled the minerals assemblage at fluid-rock ratio >10 . The mineral assemblages are controlled by both protolith rocks and fluids when fluid-rock ratio between 0.1 and 10. The mineral assemblages are controlled by protolith rocks at fluid-rock ratio <1 .

Cu, Ag, Au, As, Bi, Se and S are dominantly hosted by sulphide minerals, with As being most strongly enriched in pyrite (but not the copper sulphides) and Cu and Bi being most strongly enriched in the copper sulphides. Sulphides occur over a range of temperature, fluid-rock and redox conditions however pyrite and chalcopyrite are most abundant at relatively high fluid-rock ratios, at temperatures of 250-300° C and $\log fO_2 \sim -32$ to -30 , corresponding to the magnetite-hematite redox buffer. Elevated concentrations of As and other chalcophile elements in pyrite are consistent with p-type pyrite formed from relatively low temperature hydrothermal alteration (Abratis et al., 2004). However pyrite is observed in a wider range of alteration types, inferred to occur over a range of conditions. Thus the elements commonly enriched in pyrite (including As) are likely to have wider geographic distribution than the elements enriched in the copper sulphides. The conditions for elevated concentrations of 6 of the 10 pathfinder elements (enriched in the copper sulphides) are high fluid rock ratios (for example within faults or shear zones), presence of sulphur (either introduced by the fluid or pre-existing in the rock) and fluid-rock interactions (specifically redox reactions) resulting in sulphide precipitation. These correspond to the likely conditions of ore formation.

Sb, and to a lesser extent Mo and W, are not strongly enriched in sulphide minerals and are dominantly hosted by Fe-oxide minerals in particular hematite. Sb and W also have elevated concentrations in muscovite are possibly linked to muscovite formation at temperatures $<350^\circ\text{C}$ and at fluid-rock ratios ≥ 1 . Hemattite is an abundant and widespread alteration mineral on the central eastern Gawler Craton. The presence of hydrothermal hematite indicates temperatures and $\log fO_2$ below the magnetite-hematite buffer ($<300^\circ\text{C}$ and $>\log fO_2 -30$ in the models presented here). Although IOCG mineralisation is intimately linked to hematite, there is abundant hematite that is not enriched in sulphides. This means that Sb (Mo and W) will likely have a much broader geographic distribution, with elevated concentrations more distal to mineralisation than Cu, Ag, Au, Bi, Se and Te.

In combination the observations and modelling suggest that the pathfinder elements are likely to be spatially distributed as follows:

- Cu, Ag, Au, Bi, Se and Te associated with intense hematite alteration and sulphide mineralisation proximal to ore bodies.
- As associated with pyrite, which might be present in both magnetite and hematite stable alteration assemblages and thus with a ptentially broad geographic footprint.

- Sb (Mo, W) associated with widespread hematite alteration (not necessarily with sulphide) with a broad geographic footprint and potentially providing a distal indicator of the mineral system.

The broader geographic footprint of Sb, W and As than other pathfinder elements is consistent with the observations of Fabris et al. (2012) and Fabris (2013a and b) who found enrichments of these elements of greater than 50 times crustal abundance at distances of greater than 20 km from known ore deposits. In contrast the elements most enriched in copper sulphides (Cu, Ag and Au) are largely restricted to within kilometres of known deposits.

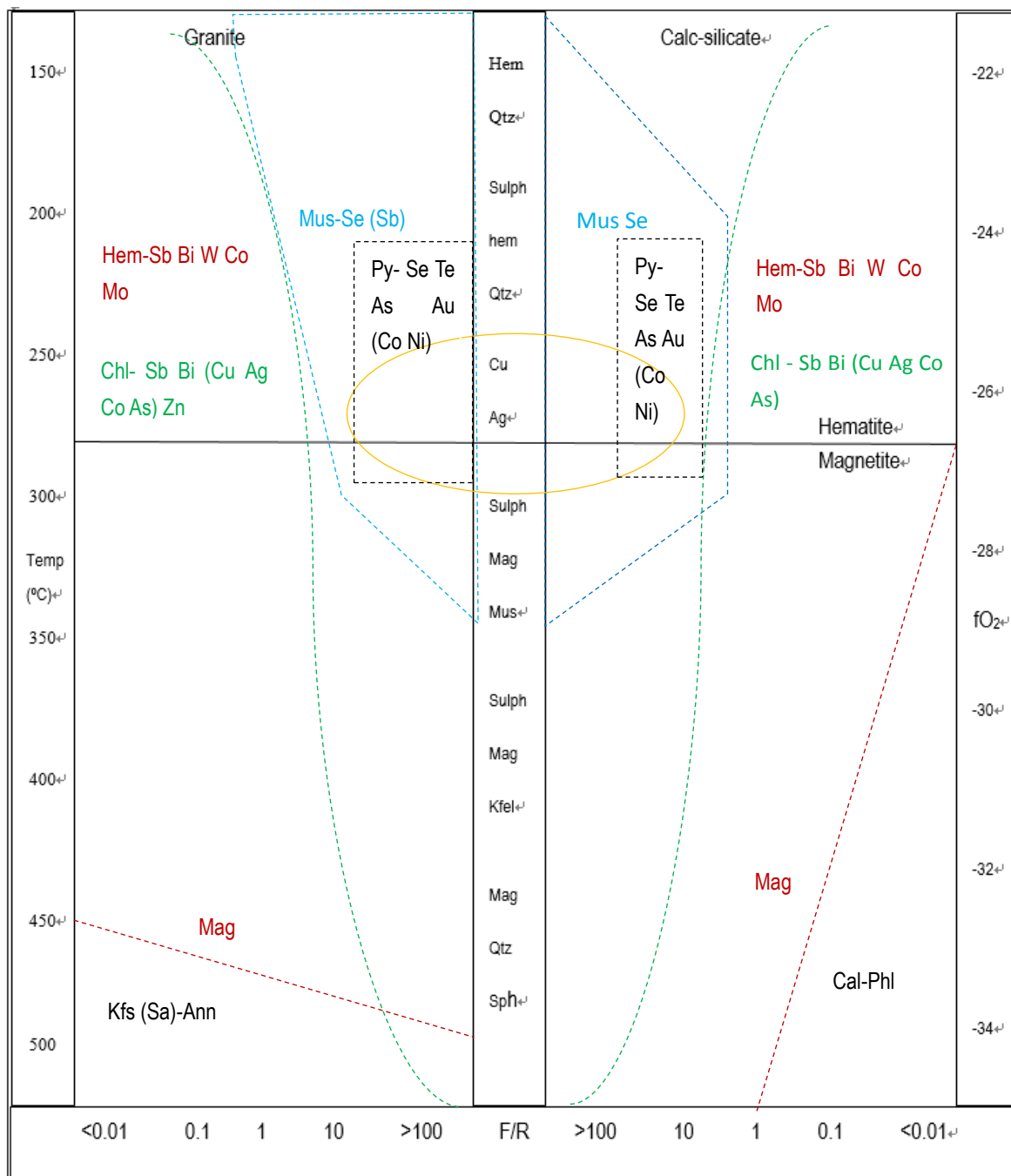


Figure 58. The HCh models of model granite and model calc-silicate rock reacted with 16.2 wt % fluids with temperature decrease and fO_2 increase vs fluid-rock ratio decrease.

4.5 CONCLUSIONS

HCh models simulated all alteration intensities. However, ore elements in fluids are the important component for ore formation. A single fluid without ore elements does not result in ore formation (e.g. sample 2066178).

HCh models simulated second minerals, K-feldspar, chlorite, hematite and muscovite, as observed in Donington Suite granite. Chlorite-carbonate-hematite assemblage did not produce ore bodies in HCh models as the fluid did not contain ore elements. Hypersaline fluids are important for mineralisation as these fluids carry metal elements and form magnetite assemblage. Fluid-granite reactions at ratio >10 predict primary mineral change. Major mineral assemblage was not changed at fluid-rock ratio <1 , but did change at fluid-rock ratio >10 . Ore forms in reaction with reduction fluids, but oxide fluids remove all trace elements. Second generation K-feldspar, chlorite and muscovite have considerable ore mineral inclusion as seen in petrogenesis (see Figures 10, 12 and 13). Second generation minerals may be important for ore formation as HCh models simulated second generation chlorite, K-feldspar, dolomite and muscovite.

Log fO_2 and temperature are important to formation of chalcopyrite-bornite-chalcocite. Ore minerals do not form under highly oxide environments against the oxide fluids (Bastrakov et al., 2007). S content is important, whether present in fluids or rock. S may be present in fluids as unaltered granite has no S content. The protoliths having pre-existing sulphides are potential hosts of mineralisation (eg. Bastrakov et al., 2007). From acid to weak alkaline and from high- to low-pressure hematite increased consistent with ore formation of fault systems.

Main conclusions are presented in Figure 58. Ore formed at temperature 250° - 300° C and pyrite formed at 200° - 300° C at F/R ratio ≤ 10 and contains Se, Te, As, Au, (Co and Ni). Hematite formed at $\sim 275^{\circ}$ C containing Sb, Bi, W, Co and Mo. Chlorite formed at larger range containing Sb, Bi, Zn (Cu, Ag, Co, As). Muscovite formed at F/R ≤ 1 containing Se (Sb). The granite HCh models are similar to calc-silicate HCh models in Figure 58. In general terms, the equilibration of a model granite protolith with the high-salinity model fluid A predicts a progression from MB, to CAM to HSCC styles of alteration with decreasing temperature, increasing F/R and increasing $\log fO_2$. The progression from MB via CAM to HSCC is F/R increasing and temperature-pressure decreasing in all our models. The minerals stable at low F/R are incrementally replaced by iron-oxide (in this case hematite but the same is true for magnetite at higher temperatures) and muscovite with chlorite being an important alteration phase at low to moderate F/R.

5 Thesis conclusions

The research focused on the IOCGs has provided the following:

Chapter 2

- Multiple, overprinting paragenetic relationships can be interpreted within the framework of five paragenetic stages.
- The paragenesis is consistent with successive periods of Fe-K-metasomatism, with early higher temperature, more reduced (magnetite stable) alteration being consistently overprinted by lower temperature, more oxidized (hematite stable) alteration and with the bulk of Cu-sulphide mineralization occurring at close to the transition from magnetite to hematite.
- It is possible that variable overprinting (e.g. Bastrakov et al., 2007) and/or mixing (e.g. Haynes et al., 1995) of two discrete fluids was responsible for the observed paragenesis. However it is also possible that an initially highly-saline, hot and reduced fluid evolved toward a cooler, lower-salinity and more oxidized fluid as it migrated through the crust.
- In all rock types, alteration intensity was greatest in samples with breccia textures, intermediate in samples with veining and micro-fractures and least in samples with little evidence of deformation. These observations are consistent with a link between alteration intensity and increased fluid-rock ratios due to transient structurally controlled permeability.

Chapter 3

- Minerals that pre-date the main sulphide phase typically have major and trace element concentrations within expected ranges for comparable rock types outside the eastern Gawler Craton mineral province. Abundant hydrothermal hematite, overprinting all previous mineral assemblages, is a characteristic feature of the sulphide stage of petrogenesis.
- Where hematite and magnetite occur in the same rock, hematite consistently overprints magnetite in the paragenesis and has higher average concentrations than magnetite (between 1 and 2 orders of magnitude higher) of Ba, Cu, Mo, Nb, Pb, Th, Ta, U and \sum REE (Rare Earth Elements). Hydrothermal hematite contains elevated concentrations of Cu, U, Sb and Bi compared to the average upper crustal abundance.
- Petrologic overprinting provides evidence for two stages of hydrothermal chlorite growth; prior to and subsequent to chalcopyrite deposition.
- Hydrothermal chlorite contains elevated concentrations of Cu, S and a range of chalcophile “pathfinder” elements including As, Bi, Mo and Sb. The first stage of chlorite has relatively lower concentrations of Cu (up to ~80 ppm) and S (~ 500 ppm) than the second stage of chlorite (up to ~7500 ppm Cu and ~1000 ppm S). Second stage chlorite may contain Cu mineral inclusions.
- Where sulphide minerals are present chalcophile pathfinder elements (e.g. Ag, As, Bi, Cu, Sb and Se) are dominantly deported in the sulphides, even at low concentrations, far from mineralisation. Pyrite is the most common sulphide, with chalcopyrite increasing in abundance closer to mineralisation. The pyrites are p-type, with S/Fe_{atom}

ratios of > 2 and Co/Ni ratios ranging between 0.4 and 10, but mostly above 1. This is consistent with a moderate -temperature hydrothermal origin for the pyrite. There is considerable chalcophile trace element enrichment within pyrite.

- Concentrations of Co, As, Bi, Se, Te and Au reach 2 to 3 orders of magnitude above the upper crustal abundance. Cu, Bi, Te, Au, Ag and Pb display large variations in concentration (up to 4 orders of magnitude for Bi) and are most abundant in hydrothermally altered rocks of metasedimentary protoliths.
- The chalcopyrite grains show variable enrichment in pathfinder elements and are most enriched in Bi, Se, Te and Ag, with values ranging between 1 and 4 orders of magnitude above crustal abundance.
- At elevated whole rock concentrations, within altered rocks, the REE are deposited in hydrothermal apatite. This is consistent with the extreme capacity of the hydrothermal system to mobilise, and locally accumulate, even the most refractory elements. REE enrichment (up to 2604 ppm) is a good proximity indicator to ore, since it only occurs around the mineral system.
- Semi quantitative mass balance calculations show that Cu, Sb, Bi, Ce are contributed by their different stages or phases of hematite, biotite, chlorite, K-feldspar, chalcopyrite (Ce is not contributed by chalcopyrite but instead of dolomite).

Chapter 4

- Thermodynamic modelling using the HCh software provides semi-quantitative constraints for mineral assemblages associated with IOCG mineral systems of the eastern Gawler Craton.
- The transition from protolith assemblages to magnetite-K-feldspar assemblages to chlorite-magnetite-K-feldspar assemblages to hematite-chlorite-muscovite assemblages with decreasing temperature, increasing fluid-rock ratio and increasing $\log f_{O_2}$. This is consistent with the petrologic observations presented in this thesis, namely the consistent overprinting of stage 1, magnetite-K-feldspar alteration by stage 2, hematite-chlorite and muscovite alteration.
- Although Cu-sulphides are predicted to be stable over a range of temperature and f_{O_2} conditions, they are predicted to be most abundant between temperatures of $\sim 300^\circ$ to 250°C , f_{O_2} of -26 to -34 and at fluid-rock ratios >10 . This corresponds to alteration assemblages at the magnetite and hematite boundary, with abundant chlorite and muscovite alteration.
- The distribution of pathfinder elements (measured in whole rock chemistry) within the central eastern Gawler Craton IOCG province can be predicted by combining petrological observations with mineral chemistry and thermodynamic modelling and are consistent with the observations of Fabris (2012, 2013).
- Elements associated with hematite alteration (notably Sb and W) are expected to have a wide geographic footprint.
- Elements enriched in pyrite (notably As, but also S and Se) are likely to have a broad geographic distribution in line with the presence of pyrite in both magnetite and

hematite stable alteration assemblages.

- Elements most enriched in copper sulphides (Cu, Ag and Au) are largely restricted to within <5 km of known deposits.

6 References

- Abraitis P. K., Patrick R. A. D and Vaughan D. J. 2004 Variations in the compositional, textural and electrical properties of natural pyrite: a review, *International Journal of Mineral Processing*, vol. 74, no. 1–4, pp. 41-59.
- Alderton D. H.M., 1980 Rare earth element mobility during granite alteration: Evidence from southwest England. *Earth and Planetary Science Letters*, Volume 49, Issue 1, August 1980, Pages 149-165.
- Andrei Y. B., Robert F. M., Lang S., William L., Yana F. 2008 Oscillatory zoning in stanniferous hematite and associated W and Bi-rich minerals from Canadian Creek, Yukon, Canada, *The Canadian Mineralogist*, Volume 55, Number 3.
- Andrea Agangi, Kamenetsky, V.S., McPhie, J., 2010. The role of fluorine in the concentration and transport of lithophile trace elements in felsic magmas: Insight from the Gawler Range Volcanics, South Australia: *Chemical Geology* 273, 314-325.
- Ares J. R., León M., Arozamena N. M., Sánchez-Páramo J., Celis P., Ferrer I. J., Sánchez C. 1998 Evolution of the seebeck coefficient during the formation and crystallisation of pyrite thin films, *Journal of physics: Condensed matter*, Vol. 10, No.19, P.4281.
- Bajwah Z. U., Seccombe P. K. and Offler R. 1987 Trace element distribution, Co:Ni ratios and genesis of the big Cadia Iron-Copper deposit, New South Wales, Australia, *Mineralium Deposita*, Vol. 22. No.4, pp. 292-300.
- Barton M. D., Kreiner D and Girardi J. 2010 Regionally extensive brine-dominated hydrothermal alteration and IOCG systems, northern Chile, *SGA Abstracts with Program*, vol. 42, no. 5.
- Bastrakov E. N., Skirrow R. G and Davidson G. J. 2007 Fluid Evolution and Origins of Iron Oxide Cu-Au Prospects in the Olympic Dam District, Gawler Craton, South Australia, *Economic Geology*, vol. 102, no. 8, pp. 1415-1440.
- Baumgartner L. P and Olsen S. N. 1995 A least-squares approach to mass transport calculations using the isocon method. *Economic Geology* 90, 1261–1270.
- Belperio A., Flint R and Freeman H. 2007 Prominent Hill: A Hematite-Dominated, Iron Oxide Copper-Gold System, *Economic Geology*, vol. 102, no. 8, pp. 1499-1510.
- Benavides J., Kyser T. K., Clark A. H., Oates C. J., Zamora R., Tarnovschi R., Castillo B. 2007 The Mantoverde Iron Oxide-Copper-Gold District, III Región, Chile: The Role of Regionally Derived, Nonmagmatic Fluids in Chalcopyrite Mineralization, *Economic Geology*, vol. 102, no. 3, pp. 415-440.
- Bernard M., Jean P. F., Philippe M., Francis V. 1989 Comparative mineralogy, geochemistry, and conditions of formation of two metasomatic talc and chlorite deposits; Trimouns (Pyrenees, France) and Rabenwald (Eastern Alps, Austria). *Economic Geology* (1989) 84 (5): 1398-1416.
- Bertelli M and Baker T. 2010 A fluid inclusion study of the Suicide Ridge Breccia Pipe, Cloncurry district, Australia: Implication for Breccia Genesis and IOCG mineralization, *Precambrian Research*, vol. 179, no. 1–4, pp. 69-87.
- Bettina A. B. 1989 Trace-element Contents and partitioning of elements in ore minerals from the CSA Cu-Pb-Zn

- deposit, Australia. *Canadian Mineralogist*, Vol, 27, pp 263-274 (1989).
- Billstrom K., Eilu P., Martinsson O., Niiranen T., Broman C., Weihed p., Wnag hainen C., Ojala J. 2010 IOCG and Related Mineral Deposits of the Northern Fennoscandian Shield in - Porter, T.M. (ed.), 2010 - Hydrothermal Iron Oxide Copper-Gold and Related Deposits: A Global Perspective, volume 4, Advances in the Understanding of IOCG Deposits; PGC Publishing, Adelaide. pp. 381-414.
- Bonin B., Azzouni-Sekkal A., Bussy F., Ferrag S. 1998 Alkali-calcic and alkaline post-orogenic PO/ granite magmatism: petrologic constraints and geodynamic settings. *Lithos* 45, 1998. 45–70.
- Blissett, A.H., 1975 Rock Units in the Gawler Range Volcanics, South Australia., Geological Survey of South Australia, Quarterly Geological Notes, 55, p2-14.
- Bralia A., Sabatini G and Troja F. 1979 A revaluation of the Co/Ni ratio in pyrite as geochemical tool in ore genesis problems, *Mineralium Deposita*, vol. 14, no. 3, pp. 353-374.
- Carew M. J., Mark G., Oliver N. H. S., Pearson N. 2006 Trace element geochemistry of magnetite and pyrite in Fe oxide (\pm Cu–Au) mineralised systems: Insights into the geochemistry of ore-forming fluids, *Geochimica et Cosmochimica Acta*, vol. 70, no. 18, Supplement, p. A83.
- Carlson C. J. 2002. Iron Oxide Systems and Base Metal Mineralisation in Northern Sweden. In: Porter T. M. ed. Hydrothermal Iron oxide Copper- Gold and Related Deposits: A Global perspective, Vol 1, PGC Publishing, Adelaide, 283-296.
- Cathelineau and Nieva. 1985 A chlorite solid solution geothermometer, the Los Azufres (Mexico) geothermal system. *Contrib Mineral Petrol* (1985) 91:235-244.
- Chakhmouradian A. R., Reguir E. P., Coueslan C., Yang P. 2016 Calcite and dolomite in intrusive carbonatites. II. Trace-element variations. *Miner Petrol* (2016) 110:361–377.
- Chen H. Y., 2010 Mesozoic IOCG Mineralisation in the central Andes: an updated review; in Porter. T.M., (ed.), Hydrothermal Iron Oxide Copper-Gold & Related deposits: A global perspective, v.3 – advances in the Understanding of IOCG deposits; PGC Publishing, Adelaide, pp. 259-272.
- Clark C., Grguric B and Mumm A. S. 2004 Genetic implications of pyrite chemistry from the Palaeoproterozoic Olary Domain and overlying Neoproterozoic Adelaidean sequences, northeastern South Australia, *Ore Geology Reviews*, vol. 25, no. 3–4, pp. 237-257.
- Clark C., Schmidt Mumm A and Faure K. 2005. Timing and nature of fluid flow and alteration during Mesoproterozoic shear zone formation, Olary Domain, South Australia. *Journal of Metamorphic Geology* 23, 147-164.
- Cleverley J. S and Oliver N. H. S. 2005 Comparing closed system, flow-through and fluid infiltration geochemical modelling: examples from K-alteration in the Ernest Henry Fe-oxide–Cu–Au system, *Geofluids*, vol. 5, no. 4, pp. 289-307.
- Cohen, J. F. 2011. Compositional variations in hydrothermal white mica and chlorite from wall-rock alteration at the Ann-Mason porphyry copper deposit, Nevada. MSc. Thesis, Oregon State University (unpub.).
- Conor C. H. H. 2006 Geology of the Olary Domain, Curnamona Province, South Australia. South Australia Department of Primary Industries and Resources. Report Book, August 2006/13.

- Cook N. J., Ciobanu, C. L., Meria, D., Silcock D., Wade, B. 2013a Arsenopyrite-Pyrite Association in an Orogenic Gold Ore: Tracing Mineralization History from Textures and Trace Elements, *Economic Geology*, vol. 108, no. 6, pp. 1273-1283.
- Cook N. J., Cristiana L. C., Daniel O., Robin W., Kevin D., Benjamin W. 2013b Mineral chemistry of Rare Earth Element (REE) mineralization, Browns Ranges, Western Australia, *Lithos*, vol. 172–173, no. 0, pp. 192-213.
- Cook N. J., Ciobanu, C. L., Pring, A., Skinner, W., Shimizu, M., Danyushevsky, L., Saini-Eidukat, B., Melcher, F. 2009 Trace and minor elements in sphalerite: A LA-ICPMS study, *Geochimica et Cosmochimica Acta*, vol. 73, pp. 4761-4791.
- Cooke D. R., Hollings P., Wilkinson J J., Tosdal R. M. 2014 13.14 - Geochemistry of Porphyry Deposits A2 - Turekian, Heinrich D. Holland Karl K. *Treatise on Geochemistry (Second Edition)*. pp. 357-381. Oxford: Elsevier.
- Corriveau L. 2006. Iron oxide copper-gold (\pm Ag \pm Nb \pm P \pm REE \pm U) deposits: A Canadian perspective. Natural Resources Canada, Geological Survey of Canada, 490 de la Couronne, Quebec, GIK 9A9.
- Corriveau L., Mumin H and Setterfield T. 2010 IOCG Environments in Canada: Characteristics and Geological Vectors to Ore in - Porter, T.M. (ed.), 2010 - Hydrothermal Iron Oxide Copper-Gold and Related Deposits: A Global Perspective, volume 4, *Advances in the Understanding of IOCG Deposits*; PGC Publishing, Adelaide. pp. 311-344.
- Craig M. B. 1996 Geochemical reaction modeling. Oxford University. Book 303-307.
- Creaser R. A., 1996 Petrogenesis of a Mesoproterozoic quartz latite-granitoid suite from the Roxby Downs area, South Australia. *Precambrian Research* 79 (1996) 371-394.
- David L. H., Soey H. S., Gary F. S. David R. C., Ross A. B. 1995 Trace elements in sulfide minerals from eastern Australian volcanic-hosted massive sulfide deposits; Part I, Proton microprobe analyses of pyrite, chalcopyrite, and sphalerite, and Part II, Selenium levels in pyrite; comparison with delta 34 S values and implications for the source of sulfur in volcanogenic hydrothermal systems. *Economic Geology*, Vol. 1 (1905).
- David S., Bruce E. N., Karlis M. 2000 Hydrothermal Alteration and Fluid Chemistry of the Endako Porphyry Molybdenum Deposit, British Columbia. *Economic Geology*, Vol. 95, 2000, pp. 183–202.
- Davidson G.J., Paterson H., Meffre S., and Berry R.F., 2007 Characteristics and origin of the Oak Dam East breccia-hosted, iron oxide-Cu-U-(Au) deposit: Olympic Dam region, Gawler craton, South Australia: *ECONOMIC GEOLOGY*, v. 102, p. 1471–1498.
- Daly S.J., Fanning C.M and Fairclough M. C. 1998 Tectonic evolution and exploration potential of the Gawler craton, South Australia: *AGSO Journal of Australian Geology and Geophysics*, v. 17, p. 145–168.
- Daly S and Rowett A. 2007 *Industry news, MESA*, vol. 47, pp. 32-34.
- Dawson J. B., Hinton R. W 2003 Trace-element content and partitioning in calcite, dolomite and apatite in carbonatite, Phalaborwa, South Africa. *Mineralogical Magazine, Journal of Mineral Science*, Volume 67. Issue 5 (Oct 2003).
- De Carritat P., Hutcheon I., Walshe J. L. 1993 Chlorite geothermometry: a Review. *Clays and Clay Minerals*, Vol.

41, No. 2, 219-239, 1993.

- Deditius A. P., Reich M., Kesler S. E., Utsunomiya S., Chryssoulis S. L., Walshe J., Ewing R. C. 2014 The coupled geochemistry of Au and As in pyrite from hydrothermal ore deposits, *Geochimica et Cosmochimica Acta*, vol. 140, pp. 644-670.
- Daroch G. A., Barton M D. 2011 Hydrothermal alteration and mineralization in Santo, Domingo Sur Iron Oxide (-Cu-Au) (IOCG) deposit, Atacama Region, Chile. 11 th SGA Biennial Meeting, Let's Talk Ore Deposits, 26-29th September 2011 Antofagasta, Chile.
- Direen N. G and Lyons P. 2007 Regional Crustal Setting of Iron Oxide Cu-Au Mineral Systems of the Olympic Dam Region, South Australia: Insights from Potential-Field Modeling, *Economic Geology*, vol. 102, no. 8, pp. 1397-1414.
- Domanik K. J and Holloway J. R. 1996 The stability and composition of phengitic muscovite and associated phases from 5.5 to 11 GPa: Implications for deeply subducted sediments. *Geochimica et Cosmochimica Acta*, Vol. 60, No. 21, pp. 4133-4150, 1996.
- Drexel, J.F., Preiss, W. V and Parker, A.J., 1993 *The geology of South Australia: Volume 1, The Precambrian, South Australia: South Australia Geological Survey, Bulletin 54, p. 242.*
- Dupuis C., Beaudoin G. 2011 Discriminant diagrams for iron oxide trace element fingerprinting of mineral deposit types. *Miner Deposita* (2011) 46:319–335.
- Espinoza J. I. 2002 Fe Oxide-Cu-Au Deposits in Peru, an Integrated View in - Porter, T.M. (Ed), 2002 - Hydrothermal Iron Oxide Copper-Gold and Related Deposits: A Global Perspective, PGC Publishing, Adelaide, v.2, pp 97-113.
- Eldridge C. S and Danti, K. 1994 Low sulfur isotope ratios: High gold values—a closer look at the Olympic Dam deposit via SHRIMP [abs]: *Geologica Society of America Abstracts with Programs*, p. A-498–A-499.
- Fabris A., van der Wielen, S. E., Mauger, A., Halley, S., Keeping, T., and Keeling, J. 2012 Geochemical trends in IOCG alteration—new data from the Gawler Craton. In *Unlocking SA's mineral wealth, technical forum* (Vol. 2, pp. 7-8).
- Fabris A., Halley S, van der Wielen S, Keeping T, Gordon G. 2013a. IOCG-style mineralisation in the central eastern Gawler Craton, SA; characterisation of alteration, geochemical associations and exploration vectors, Report Book 2013/00014. Department of Innovation, Manufacturing, Trade, Resources and Energy, South Australia, Adelaide.
- Fabris A. 2013b P3.4 – Maps of Basement and Cover Geochemistry, Eastern Gawler Craton, SA.
- Fairclough M. 2005 Geological and metallogenic setting of the Carrapateena FeO–Cu–Au prospect — a PACE success story, *MESA*, vol. 38, pp. 4-7.
- Ferris G. M., Schwarz M. P. and Heithersay P. 2002 The Geological Framework, Distribution and Controls of Fe-Oxide Cu-Au Mineralisation in the Gawler Craton, South Australia. Part I - Geological and Tectonic Framework. in - Porter, T.M. (Ed). *Hydrothermal Iron Oxide Copper-Gold and Related Deposits: A Global Perspective*, PGC Publishing, Adelaide,. pp. 9-13.
- Gandhi S. S. 2003 An overview of the Fe oxide-Cu-Au deposits and related deposit types: CIM Montreal 2003

Mining Industry Conference and Exhibition, Canadian Institute of Mining, Technical Paper, CD-ROM.

- Gandhi S. S. 2004 Magmatic-hydrothermal Fe oxide±Cu±Au deposits: classification for a digital database and an overview of selected districts: IAVCEI General Assembly 2004, Pucón, Chile, CD-ROM, Abstracts01a_pt_169.
- Gomes A., Ares J. R., Ferrer I. J., da Silva Pereira M. I., Sánchez C. 2003 Formation of n-type pyrite films from electrodeposited iron sulphides: effect of annealing temperature, *Materials Research Bulletin*, vol. 38, no. 7, pp. 1123-1133.
- Gow P. A., Wall V. J., Oliver, N. H. S., Valenta, R. K. 1994 Proterozoic iron oxide (Cu-U-Au-REE) deposits: Further evidence of hydrothermal origins, *Geology*, vol. 22, no. 7, pp. 633-636.
- Gow P. A. 1996 Geological Evolution of the Stuart Shelf and Proterozoic Iron Oxide-associated Mineralization: Insights from Regional Geophysical Data. Monash University.
- Grant J. A. 1986 The isocon diagram; a simple solution to Gresens' equation for metasomatic alteration, *Economic Geology*, vol. 81, no. 8, pp. 1976-1982.
- Graham J., Morris R.C., 1973. Tungsten- and antimony-substituted rutile. *Min. Mag.* 39, 470– 473.
- Groves D. I., Bierlein F. P., Meinert L. D., Hitzman, M. W. 2010 Iron Oxide Copper-Gold (IOCG) Deposits through Earth History: Implications for Origin, Lithospheric Setting, and Distinction from Other Epigenetic Iron Oxide Deposits, *Economic Geology*, vol. 105, no. 3, pp. 641-654.
- Hand M., Reid A and Jagodzinski L. 2007 Tectonic Framework and Evolution of the Gawler Craton, Southern Australia, *Economic Geology*, vol. 102, no. 8, pp. 1377-1395.
- Hans P. E. 1985 Granites and hydrothermal ore deposit: a geochemical framework. *Mineralogical magazine*, March 1985, Vol.49 pp.7-23.
- Haynes D. W., Cross K. C., Bills R. T., Reed M. H. 1995 Olympic Dam ore genesis; a fluid-mixing model, *Economic Geology*, vol. 90, no. 2, pp. 281-307.
- Henry D. J., Will C. N., Mueller P. A. 2015 Ba-rich K-feldspar from mafic xenoliths within mesoarchean granitic rocks, beartooth Mountains, Montana, USA: Indicators for barium metasomatism. *Canadian Mineralogist* 53(2), pp. 185-198.
- Helgeson H. C., Kirkham D. H. Flowers G. C. 1981 Theoretical prediction of the thermodynamic behaviour of aqueous electrolytes at high pressures and temperatures: calculation of activity coefficients, osmotic coefficients, and apparent molal and standard and relative partial molal properties to 600°C and 5 kb. *American Journal of Science*, 281, 1249–516.
- Hitzman M. W., Oreskes N and Einaudi M. T. 1992, Geological characteristics and tectonic setting of Proterozoic iron oxide (Cu-U-Au-REE) deposits: *Precambrian Research*, v. 58, p. 241–287.
- Hou T., Charlier B., Namur O., Schütte P., Schwarz-Schampera U., Zhang Z., Holtz F. 2017 Experimental study of liquid immiscibility in the Kiruna-type Vergenoeg iron–fluorine deposit, South Africa, *Geochimica et Cosmochimica Acta*, vol. 203, pp. 303-322.
- Huntington J. F., Mauger, A. J., Skirrow R. G., Bastrakov E. N., Connor P., Keeling J. L., Coward D. A., Berman M., Phillips, R., Whitbourn L. B., Heithersay P. S. 2006 Automated mineralogical core logging at the Emmie

- Bluff iron oxide – copper–gold prospect, MESA, vol. 41, pp. 38-44.
- Ismail R., Ciobanu C. L., Cook N. J., Teale G. S., Giles, D., Mumm, A. S., Wade, B. 2014 Rare earths and other trace elements in minerals from skarn assemblages, Hillside iron oxide–copper–gold deposit, Yorke Peninsula, South Australia, *Lithos*, vol. 184–187, no. 0, pp. 456-477.
- Jagodzinski E. A. 2005 Compilation of SHRIMP U-Pb geochronological data, Olympic Domain, Gawler craton, South Australia, 2001-2003: *Geoscience Australia, Record 2005/20*, p. 211.
- Johnson J. P and McCulloch M. T. 1995 Sources of mineralising fluids for the Olympic Dam deposit (South Australia) : Sm/Nd isotopic constraints, *Chemical Geology*, vol. 121, no. 1–4, pp. 177-199.
- Julian A. P., Nigel B. W. H., Andrew G. T. 1984 Element Discrimination Diagrams for the Tectonic Interpretation of Granitic Rocks. *Journal of Petrology* (1984) 25 (4): 956-983.
- Kathleen M. J., Jane M. H., Michael L. Z and Connie L. D. 2014. USGS Mineral Resources Program Web site, <http://minerals.usgs.gov/global/>.
- Kathy Ehrig, Jocelyn Mcphie, Vadim Kamenetsky, 2012. *Geology and Mineralogical Zonation of the Olympic Dam Iron Oxide Cu-U-Au-Ag Deposit, South Australia. Society of Economic Geologists, Special Publication 16*, pp. 237–267.
- Klemme S., Marschall H R., Jacob D. E., Prowatke S., Ludwig T. 2011 Trace-element partitioning and boron isotope fractionation between white mica and tourmaline. *Mineralogical Association of Canada, Volume 55, Number 4*.
- Knutson J., Donnelly T. H., Eadington P. J and Tonkin D. G. 1992 Hydrothermal alteration of middle Proterozoic basalts, Stuart Shelf, South Australia: A possible source for Cu mineralization: *ECONOMIC GEOLOGY*, v. 87, p. 1054–1077.
- Kontonikas-Charos A., Ciobanu C. L and Cook N. J. 2014 Albitization and redistribution of REE and Y in IOCG systems: Insights from Moonta-Wallaroo, Yorke Peninsula, South Australia, *Lithos*, vol. 208, pp. 178-201.
- Kontonikas-Charos A., Ciobanu, C. L., Cook N. J., Ehrig K., Krneta S., Kamenetsky V. S. 2017 Feldspar evolution in the Roxby Downs Granite, host to Fe-oxide Cu-Au-(U) mineralisation at Olympic Dam, South Australia, *Ore Geology Reviews*, vol. 80, pp. 838-859.
- Land L. S. 1980 The isotopic and trace element geochemistry of dolomite: the state of the art: *SEPM special publication No 28 P 87 110 November 1980*.
- Large R. R., Danyushevsky L., Hollit C., Maslennikov V., Meffre S., Gilbert S., Bull S., Scott R., Emsbo P., Thomas H., Singh B., Foster J. 2009 Gold and Trace Element Zonation in Pyrite Using a Laser Imaging Technique: Implications for the Timing of Gold in Orogenic and Carlin-Style Sediment-Hosted Deposits, *Economic Geology*, v. 104, pp. 635–668.
- Large R. R., Halpin Jacqueline A., Danyushevsky, Leonid V., Maslennikov, Valeriy V., Bull, Stuart W., Long John A., Gregory Daniel D., Lounejeva E., Lyons T. W., Sack P. J., McGoldrick, P. J. Calver C. R. 2014 Trace element content of sedimentary pyrite as a new proxy for deep-time ocean–atmosphere evolution, *Earth and Planetary Science Letters*, vol. 389, no. 0, pp. 209-220.
- Mao M, Alexei S. R, Stephen M. R, Jody S, Laurence A. C. 2016 Apatite Trace Element Compositions: A Robust

New Tool for Mineral Exploration. *Economic Geology*, v. 111, i. 5, p. 1187-1222.

- Mark G., Foster D. R. W., Pollard P. J., Williams P. J., Tolman J., Darvall M and Blake K. L. 2004. Stable isotope evidence for magmatic fluid input during large-scale Na-Ca alteration in the Cloncurry Fe oxide Cu-Au district, NW Queensland, Australia. *Terra Nova* 16, 54-61.
- Manickavasagam S., Saltiel C. and Giesche H. 2004 Characterization of colloidal hematite particle shape and dispersion behaviour, *Journal of Colloid and Interface Science*, vol. 280, no. 2, pp. 417-430.
- McDonough W. F and Sun S. S. 1995 The composition of the Earth, *Chemical Geology*, vol. 120, no. 3-4, pp. 223-253.
- McPhie J., Kamenetsky V., Allen S., Ehrig K., Agangi A., Bath A. 2011 The fluorine link between a supergiant ore deposit and a silicic large igneous province. *Geological Society of America, Geology*, Nov 2011; V. 39.
- McIntire W. L. 1963 Trace element partition coefficients—a review of theory and applications to geology, *Geochimica et Cosmochimica Acta*, vol. 27, no. 12, pp. 1209-1264.
- McLellan J., Blenkinsop T., Oliver N., Mustard R., McKeagney C. 2010 Critical Ingredients of IOCG Mineralisation in the Eastern Fold Belt of the Mount Isa Inlier: Insights from Combining Spatial Analysis with Mechanical Numerical Modelling. in - Porter, T.M. (ed.), 2010 - Hydrothermal Iron Oxide Copper-Gold and Related Deposits: A Global Perspective, volume 3, Advances in the Understanding of IOCG Deposits; PGC Publishing, Adelaide. pp. 233-256.
- Monteiro L. V. S., Xavier R. P., Hitzman M. W., Julian, C., de Souza Filho C. R., Carvalho E. R. 2008 Mineral chemistry of ore and hydrothermal alteration at the Sossego iron oxide-copper-gold deposit, Carajás Mineral Province, Brazil, *Ore Geology Reviews*, vol. 34, no. 3, pp. 317-336.
- Mortimer G. E., Cooper J. A., Oliver R. L. 1988 The geochemical evolution of Proterozoic granitoids near Port Lincoln in the Gawler orogenic domain of South Australia. *Precambrian Research*, Elsevier.
- Nadoll P., Angerer T., Mauk J. L., French D., Walshe J. 2014 The chemistry of hydrothermal magnetite: A review. *Ore Geology Reviews*. Volume 61, September 2014, Pages 1-32.
- Nakamura N. 1974 Determination of REE, Ba, Fe, Mg, Na and K in carbonaceous and ordinary chondrites, *Geochimica et Cosmochimica Acta*, vol. 38, no. 5, pp. 757-775.
- Nash W. P and Crecraft H. R. 1985 Partition coefficients for trace elements in silicic magmas. *Geochimica et Cosmochimica Acta* Vol. 49. pp. 2309-2322.
- Naslund H. R., Henríquez F., Nyström J. O., Vivallo W., Michael D. F. 2002 Magmatic Iron Ores and Associated Mineralisation: Examples from the Chilean High Andes and Coastal Cordillera. in - Porter, T.M. (Ed), 2002 - Hydrothermal Iron Oxide Copper-Gold and Related Deposits: A Global Perspective, PGC Publishing, Adelaide, v.2, pp 207-226.
- Neiva A M. R., Silva M M. V. G., Gomes M E. P., Campos T F. C. 2002 Geochemistry of Coexisting Biotite and Muscovite of Portuguese Peraluminous Granitic Differentiation Series. *Chemie der Erde – Geochemistry*, Volume 62, Issue 3, 2002, Pages 197-215.
- Oliver N. H. S., Cleverley, J. S., Mark, G., Pollard, P. J., Fu, B., Marshall, L. J., Rubenach, M. J., Williams, P. J., Baker, T. 2004 Modeling the Role of Sodid Alteration in the Genesis of Iron Oxide-Copper-Gold Deposits,

- Eastern Mount Isa Block, Australia, *Economic Geology*, vol. 99, no. 6, pp. 1145-1176.
- Ord A., Hobbs E. B., Lester R.D. 2012. The mechanics of hydrothermal systems: I. Ore systems as chemical reactors. *Ore Geology Reviews* 49 (2012) 1–44.
- Oreskes N and Einaudi M. T. 1990 Origin of rare earth element-enriched hematite breccias at the Olympic Dam Cu-U-Au-Ag deposit, Roxby Downs, South Australia, *Economic Geology*, vol. 85, no. 1, pp. 1-28.
- Oreskes N and Einaudi M. T. 1992 Origin of hydrothermal fluids at Olympic Dam; preliminary results from fluid inclusions and stable isotopes, *Economic Geology*, vol. 87, no. 1, pp. 64-90.
- Pan Y and Dong P. 1999 The Lower Changjiang (Yangzi/Yangtze River) metallogenic belt, east central China: intrusion- and wall rock-hosted Cu–Fe–Au, Mo, Zn, Pb, Ag deposits. *Ore Geology Reviews*. Volume 15, Issue 4, December 1999, Pages 177-242.
- Parce M. A., White A. J. R., Fisher L. A., Hough R. M., Cleverley J. S. 2015 Gold deposition caused by carbonation of biotite during late-stage fluid flow, *Lithos*, vol. 239, pp. 114-127.
- Porter T. M. 2010 Current Understanding of Iron Oxide Associated-Alkali Altered Mineralised Systems; Part 1 - An Overview; Part 2 - A Review. in - Porter, T.M. (ed.), 2010 - Hydrothermal Iron Oxide Copper-Gold and Related Deposits: A Global Perspective, volume 3, *Advances in the Understanding of IOCG Deposits*; PGC Publishing, Adelaide. pp. 5-106.
- Qiuyue Huang, Vadim S. Kamenetsky, Kathy Ehrig, Jocelyn McPhie, Maya Kamenetsky, Ken Cross, Sebastien Meffre, Andrea Agangi, Isabelle Chambefort, Nicholas G. Direen, Roland Maas, Olga Apukhtina, 2016. Olivine-phyric basalt in the Mesoproterozoic Gawler silicic large igneous province, South Australia: Examples at the Olympic Dam Iron Oxide Cu–U–Au–Ag deposit and other localities, *Precambrian Research* 281, 185–199.
- Qiuyue Huang, Vadim S. Kamenetsky, Kathy Ehrig, Jocelyn McPhie, Maya Kamenetsky, Olga Apukhtina, Isabelle Chambefort, 2017. Effects of hydrothermal alteration on mafic lithologies at the Olympic Dam Cu-U-Au-Ag deposit, *Precambrian Research* 292, 305–322.
- Reeve J.S., Cross K.C., Smith R.N and Oreskes, N. 1990 Olympic Dam copper-uranium-gold-silver deposit, in Hughes, F. E., ed., *Geology of the mineral deposits of Australia and Papua New Guinea*: Melbourne, Australasian Institute of Mining and Metallurgy, p. 1009–1035.
- Reich M., Kesler S. E., Utsunomiya S., Palenik C. s., Chryssoulis S. L., Ewing R. 2005 Solubility of gold in arsenian pyrite. *Geochimica et Cosmochimica Acta*, Vol. 69, No. 11, pp. 2781–2796.
- Reid A. J. H and M.P. 2008 Aspects of Palaeoproterozoic orogenesis in the Gawler Craton; the c.1850 Ma Cornian Orogeny *MESA Journal* vol. 50 pp. 26-31.
- Reid A. J., Swain G., Mason D., Maas R. 2011 Nature and timing of Cu–Au–Zn–Pb mineralisation at Punt Hill, eastern Gawler Craton. *MESA Journal* vol.60 pp. 1-11. Department of Primary Industries and Resources South Australia, Adelaide.
- Robert M., Richard A. L and Walter M. 2002. La Candelaria and the Punta del Cobre District: Early Cretaceous Iron- oxide Cu-Au (-Zn-Ag) mineralisation. In: Porter T. M. ed. *Hydrothermal Iron oxide Copper- Gold and Related Deposits: A Global perspective*, Vol 1, PGC Publishing, Adelaide, 163-175.

- Rusk B., Oliver, N., Blenkinsop, T., Zhang, D., Williams, P., Cleverley, J., Habermann, P. 2010 Physical and Chemical Characteristics of the Ernest Henry Iron Oxide Copper Gold Deposit, Cloncurry, Queensland, Australia; Implications for IOCG Genesis in - Porter, T.M. (ed.), 2010 - Hydrothermal Iron Oxide Copper-Gold and Related Deposits: A Global Perspective, volume 3, Advances in the Understanding of IOCG Deposits; PGC Publishing, Adelaide. pp. 201-218. . pp. 201-218.
- Sarah A. S. D., Sarah-Jane B., Georges B., Julien M., Emilie B., Christophe P. D. 2014 Trace elements in magnetite as petrogenetic indicators. *Miner Deposita* (2014) 49:785–796.
- Satoshi M., Yoshio T., Yasuko T and Masahiro S. 2010 Antimony (V) Incorporation into Synthetic Ferrihydrite, Goethite, and Natural Iron Oxyhydroxides. *Environ. Sci. Technol.*, 2010, 44 (10), pp 3712–3718.
- Schlegel T. U., Heinrich C. A., 2015 Lithology and Hydrothermal Alteration Control the Distribution of Copper Grade in the Prominent Hill Iron Oxide-Copper-Gold Deposit (Gawler Craton, South Australia). *Society of Economic Geologists, Inc. Economic Geology*, v. 110, pp. 1953–1994.
- Schmidt Mumm A., Brugger J., Zhao C. Schacht U. 2010 Fluids in geological processes — The present state and future outlook, *Journal of Geochemical Exploration*, vol. 106, no. 1–3, pp. 1-7.
- Schmidt Mumm A., Clark C and Skirrow R. 2006 Mineral exploration under cover: Characterizing mineralizing fluid systems, *Journal of Geochemical Exploration*, vol. 89, no. 1–3, pp. 359-362.
- Shannon R. D. 1976 "Revised Effective Ionic Radii and Systematic Studies of Interatomic Distances in Halides and Chalcogenides", *Acta Cryst.* A32 751-767 (1976). Database of Ionic Radii.
- Shao Jilian, Chen Shengping, Zhao Aixing., 1979. Teaching materials for colleges and universities. *Journal of Crystallography and Mineralogy - Department of Mineral Resources, Wuhan University of Geosciences*, 1979.
- Shvarov Y and Bastrakov E. 1999 HCh: a software package for geochemical equilibrium modelling. User's Guide. Australian Geological survey Organisation, Record 1999125.
- Shvarov Y. 2016 For those who is interested in thermodynamic modeling: http://www.geol.msu.ru/deps/geochems/soft/index_e.html.
- Sliwinski J. T., Ellis B. S., Dávila-Harris P., Wolff J. A., Olin P. H., Bachmann O. 2017 The use of biotite trace element compositions for fingerprinting magma batches at Las Cañadas volcano, Tenerife.
- Singh Y. 2007 Trace Element Chemistry of Muscovite from Rare Metal Pegmatites of Kawadgaon, Bastar District, Chhattisgarh. *Journal of Geological Society of India*, Volume 69, Issue 4, April 2007.
- Smeds S. A. 1992 Trace elements in potassium-feldspar and muscovite as a guide in the prospecting for lithium- and tin-bearing pegmatites in Sweden. *Journal of Geochemical Exploration*, Volume 42, Issues 2–3, February 1992, Pages 351-369.
- Smith M and Wu C. Y. 2002. The geology and genesis of the Bayan Obo Fe-REE-Nb deposit: A review. In: Porter T. M. ed. *Hydrothermal Iron oxide Copper- Gold and Related Deposits: A Global perspective*, Vol 1, PGC Publishing, Adelaide, 271-281.
- Skirrow R. G., Bastrakov E., Davidson G., Raymond O L., Heithersay, P. 2002 The geological framework, distribution and controls of Fe-oxide and related mineralisation in the Gawler Craton, South Australia. , Part 1:

- alteration and mineralisation. In: Porter, T.M. (Ed.), Hydrothermal iron oxide copper–gold and related deposits; a global perspective. vol. PGC Publishing, Adelaide, Vol. 2, pp. pp.33-4.
- Skirrow R. G., Bastrakov E. N., Barovich K., Fraser G. L., Creaser R. A., Fanning C. M., Raymond O. L., Davidson G. J. 2007 Timing of Iron Oxide Cu-Au-(U) Hydrothermal Activity and Nd Isotope Constraints on Metal Sources in the Gawler Craton, South Australia, *Economic Geology*, vol. 102, no. 8, pp. 1441-1470.
- Skirrow, R. G. 2010. Hematite-group. IOCG+ U ore systems: Tectonic settings, hydrothermal characteristics, and Cu-Au and U mineralizing processes: Geological Association of Canada Short Course Notes, 20, 39-59.
- Senior A. B. 2016. Australian Resources Review: Gold. Geoscience Australia, Canberra, Australia.
- Stewart J. I. 2008 Annual report for EL 3084 Intercept hill. Period 8th May 2007 to 8th May 2008.
- Tan K. P., Ceritat P. DE., Scott K.M., Eggleton R. A., Skidmore C and Lawie D. 2004. Portia and north Portia Cu-Au-Mo prospects, South Australia. CRC LEME 2004.
- Tappert, M. C., Riard, B., Giles, D., Tappert, R. and Mauger, A. 2013. The mineral chemistry, near-infrared, and mid-infrared reflectance spectroscopy of phengite from the Olympic Dam IOCG deposit, South Australia. *Ore Geology Reviews* 53, 26-38.
- Tauson V. L., Babkin, D. N., Akimov, V. V., Lipko, S. V., Smagunov, N. V., Parkhomenko, I. Y. 2013 Trace elements as indicators of the physicochemical conditions of mineral formation in hydrothermal sulfide systems, *Russian Geology and Geophysics*, vol. 54, no. 5, pp. 526-543.
- Taylor S.R., McLennan. S. M., 1985 *The continental crust: Its composition and evolution*, Blackwell Sci. Publ., Oxford, 330 pp. *The continental crust: Its composition and evolution*, Blackwell Sci. Publ., Oxford, 330 pp. (1985). In *Earth bulk continental crust and upper continental crust* (edit)-https://en.wikipedia.org/wiki/Abundances_of_the_elements.
- Teale G. S. and Fanning C. M. 2002. The Portia–North Portia Cu-Au (-Mo) Prospect, South Australia; Timing of Mineralisation, Albitisation and Origin of Ore Fluid. In: Porter T. M. ed. *Hydrothermal Iron oxide Copper-Gold and Related Deposits: A Global perspective*, Vol 1, PGC Publishing, Adelaide, 137-147.
- Thomas R., Förster H. J., Rickers K., Webster J. D. 2005 Formation of extremely F-rich hydrous melt fractions and hydrothermal fluids during differentiation of highly evolved tin-granite magmas: a melt/fluid-inclusion study. *Contributions to Mineralogy and Petrology*, January 2005, Volume 148, Issue 5, pp 582–601.
- Tooth B., Brugger, J., Ciobanu, C., Liu, W. H. 2008 Modeling of gold scavenging by bismuth melts coexisting with hydrothermal fluids, *Geology*, vol. 36, no. 10, pp. 815-818.
- Uvarova Y. A., Pearce M. A., Liu W., Cleverley J. S., Hough R. M. 2018 Geochemical signatures of copper redistribution in IOCG-type mineralisation, Gawler Craton, South Australia. *Miner Deposita* (2018) 53: 477–492.
- Verdugo-Ihl, M.R., Ciobanu, C.L., Cook, N.J., Ehrig, K.J., Courtney-Davies, L., and Gilbert, S. (2017). Textures and U-W-Sn-Mo signatures in hematite from the Olympic Dam Cu-U-Au-Ag deposit, South Australia: Defining the archetype for IOCG deposits. *Ore Geology Reviews*, 91: 173-195.
- Viladkar S. G. 2015 Preliminary investigation of Ba-rich sanidine in phonolites of Badmer, Rajasthan. *Journal of the Geological Society of India*, 86(3), pp. 300-304.

- Wang X., Ren M., Chen J. 2017 The muscovite granites: Parental rocks to the Nanling Range tungsten mineralization in South China. *Ore geology Reviews*, Volume 88, August 2017, Pages 702-717.
- Warren J. K. 1997. Evaporites, brines and base metals: Fluids, flow and 'the evaporite that was'. *Australian Journal of Earth Sciences* 44, 149-183.
- Wilkinson J. J., Chang Z., Cooke D. R., Baker M. J., Wilkinson C. C., Inglis S., Chen H., Gemell J. B. 2015 The chlorite proximator: a new tool for detecting porphyry ore deposits, *Journal of Geochemical Exploration*, 152 pp. 10-26. ISSN 0375-6742.
- Williams P. J. and Skirrow R. G. 2002. Overview of Iron Oxide-Copper-Gold Deposits in the Curnamona province and Cloncurry District (Eastern Mount Isa Block), Australia. In: Porter T. M. ed. *Hydrothermal Iron oxide Copper- Gold and Related Deposits: A Global perspective*, Vol 1, PGC Publishing, Adelaide, 105-122.
- Williams P. J., Kendrick M. A and Xavier R P. 2010 Sources of Ore Fluid components in IOCG Deposits. In: Porter T. M. ed. *Hydrothermal Iron oxide Copper- Gold and Related Deposits: A Global perspective*, V.3- Advance in the understanding of IOCG deposits; PGC Publishing, Adelaide, 107-116.
- Xavier R. B., Monteiro, L. V. S., Filho, C. R. S., Torresi, I., Emerson de Resende Carvalho, E. R., Pestilho, A. L. S., Moreto C. P. N. 2010 The Iron Oxide Copper-Gold Deposits of the Carajás Mineral Province, Brazil: An Updated and Critical Review in - Porter, T.M. (ed.), 2010 - *Hydrothermal Iron Oxide Copper-Gold and Related Deposits: A Global Perspective*, volume 3, Advances in the Understanding of IOCG Deposits; PGC Publishing, Adelaide. pp. 285-306.
- Xiao-Wen H., Jian-Feng G., Liang Q., Mei-Fu Z. 2015 In-situ LA-ICP-MS trace elemental analyses of magnetite and Re-Os dating of pyrite: The Tianhu hydrothermally remobilized sedimentary Fe deposit, NW China. *Ore Geology Reviews*, Volume 65, Part 4, March 2015, Pages 900-916.
- Yang C. L. 2009 Progressive albitisation in the " Migmatite Creek" region, Weekeroo Inlier, Curnamona. *Earth and Environmental*. ebooks.adelaide.edu.au: The University of Adelaide.
- Yang, K., Huntington, J. F., Cudahy, T. J., Mason, P. and Scott, K. M. 2001. Spectrally mapping the compositional variation of white micas in hydrothermal systems and the application in mineral exploration. *International Geoscience and Remote Sensing Symposium, IGARSS '01*. IEEE 2001 International, Sydney, NSW, Australia, pp. 3294-3296.
- YE L., Cook N. J., Ciobanu, C. L., Liu, Y. P., Zhang Q., Liu, T., Gao W., Yang Y. L., Danyushevskiy, L. 2011 Trace and minor elements in sphalerite from base metal deposits in South China: A LA-ICPMS study, *Ore Geology Reviews*, vol. 39, no. 4, pp. 188-217.
- Zack T., Rivers T., Foley S. 2001 Cs-Rb-Ba systematics in phengite and amphibole: an assessment of fluid mobility at 2.0 GPa in eclogites from Trescolmen, Central Alps. *Contributions to Mineralogy and Petrology*, March 2001, Volume 140, Issue 6, pp 651-669.
- Zhang D. X., Rusk B. G., Oliver, Nicholas H. S. C 2009. Trace elements in sulfides and magnetite from the Ernest Henry iron oxide-copper-gold deposit, Australia. *Central South University, School of Geosciences and Environmental Engineering*. *Geological Society of America*, 2009 annual meeting, Vol 41(7), pp.85.
- Zhao H. X., Frimmel H. E., Jiang S. Y., Dai B. Z. 2011 LA-ICP-MS trace element analysis of pyrite from the Xiaoqinling gold district, China: Implications for ore genesis, *Ore Geology Reviews*, vol. 43, no. 1, pp. 142-153.

SARIG:http://minerals.statedevelopment.sa.gov.au/online_tools/free_data_delivery_and_publication_dow

Mindat.org URL: <https://www.mindat.org/min-967.html>.

7 Appendixes

Appendix 1: The summary of work

Table I. The summary work has been done

Methods	Petrology	PXRF	SEM	Electron Microprobe	LA-ICPMS	Calculated whole rock form mineral chemistry
Analysis	44 samples	90 points	Element mappings and mineral identified in 11 samples	234 points with 22 minerals	133 of 139 silicate, 47 of 101 FeOx and 51 of 51 sulphide points	√
Chapter	2	2	2	3 and 4	3	3

Table II. All analysis and observation and calculation

Sample ID	Drillhole	From	To	Protolith	Alt Type	Pathfinder> 10 *Crust abundance	Petrology	PXRF	SEM maps and mineral identified	EMP	LA-ICPMS	Calc-whole rock
2066163	CSD1	865	866	Metasandstone	CAM	As Sb	Yes	BG	No	No	No	No
2066164	CSD1	880.35	881.35	Metasandstone	CAM	As Bi Sb	Yes	Hem	No	No	No	No
2066165	CSD1	880.35	881.35	Metasandstone	CAM	As Bi Sb	Yes	Kfel, BG	No	No	No	No
2066166	CSD1	969.9	970.9	Calc-silicate	CAM	Se W	Yes	Mag, Hem	166B, 166E, Mon	3 Chlorite, 2 magnetite and 2 garnet, 1 Fe.	5 chlorite, 2 garnet, 4 magnetite, 3 chalcopyrite and 2 pyrite.	Yes
2066167	CSD1	976.8	977.8	Metasiltstone	CAM	Se	Yes	Hem, Mag	No	No	No	No
2066168	DRD1	1080	1081	Granite	HSCC	Ag As Bi S Sb W	Yes	Py Hem, BG	No	No	No	No
2066169	DRD1	1138.5	1139.5	Granite	HSCC	Ag S W	Yes	BG, ,Py	169A, Ap, Chal, Py	8 Hematite, 4 Chlorite, 6 pyrite and 1 chalcopyrite.	5 chlorite, 9 hematite, 6 pyrite and 3 chalcopyrite.	Yes
2066170	DRD1	1180.7	1181.75	Granite	HSCC/CAM	Au Ag As Bi Cu S Sb Se W	Yes	Py, ,Bre	No	No	No	No
2066171	DRD1	1120.2	1121.2	Granite	HSCC	0	Yes	Kfel, Chl	No	No	No	No
2066172	PSC4_SASC2	520	521	Granodiorite	HSCC	0	Yes	BG	No	No	No	No

2066173	PSC4_SASC2	529.6	530.6	Granodiorite	HSCC	Se	Yes	BG	No	No	No	No
2066174	PSC4_SASC_2	539	539.9	Granodiorite	HSCC	As Se	Yes	Mal, Bre, BG	Ap, Gnt	6 K-feldspar, 1 feldspar, 2 Biotite, 3 apatite, 3 calcite, 6 Hematite	3 K-feldspar, 1 biotite, 3 calcite and 2 apatite, 1hematite,	Yes
2066175	PSC4_SASC2	548.8	549.5	Granodiorite	HSCC	Se	Yes	BG, Kfel	No	No	No	No
2066176	HL002	429	429.5	Granite	MB	Se	Yes	BG, Kfel	No	No	No	No
2066177	HL002	471	471.45	Amphibolite	MB	Bi	Yes	Carb, BG	177B, 177C, Ap	1 K-feldspar, 1 feldspar, 2 biotite, 10 chlorite, 3 calcite, 2 dolomite, 2 magnetite, 10 hematite, 1 apatite.	1 K-feldspar, 15 chlorite, 2 dolomite and 2 diopside	Yes
2066178	HL002	528.9	529.65	Granodiorite	MB	Bi	Yes	Kfel, Dup, BG	178B, Mag	1 K-feldspar, 5 feldspar, 11 biotite, 5 hematite, 1 ilmenite, 1 unknow.	3 K-feldspar, 4 feldspar, 6 biotite, 1 chlorite and 1 Qtz+Bio, 5 hematite, 3 magnetite.	Yes
2066179	HL002	539.45	540	Granodiorite	MB	W	Yes	Kfel, BG	No	No	No	No
2066196	HL002	651	651.5	Granite	HSCC	Se	Yes	BG, Kfel	No	No	No	No
2066197	WWDD1	624.35	625.2	Sandstone-siltstone	CAM	Ag As Bi Cu Mo S Se	Yes	BG	No	No	No	No
2066198	WWDD1	614.95	615.85	Sandstone-siltstone	CAM	Bi Cu S Se	Yes	Kfel	No	No	No	No
2066199	WWDD1	683.4	684.3	Calc-silicate	CAM	Au Bi S Sb Se W	Yes	Kfel, BG	199E, Gy	8 K-feldspar, 5 biotite, 4 carbonate, 4 dolomite, 1 monazite, 1 Ti mineral, 2 apatite.	5 K-feldspar, 9 biotite, 1 chlorite and 1 Qtz+Bio.	Yes
2066200	WWDD1	804.7	805.55	Sandstone-siltstone	CAM	Bi Se	Yes	BG, Bre	No	No	No	No
2066201	WWDD1	845.55	846.3	Sandstone-siltstone	CAM	Se	Yes	Mus, BG	No	No	No	No
2066202	GHDD4	846	847	Skarn	HSCC	Au Ag As Bi Cu S Sb Se W	Yes	BG, Py	No	No	No	No

2066203	GHDD4	854	855	Skarn	HSCC	Au Ag As Bi Cu S Sb Se W	Yes	Chl, BG, Py	203A,203B, 203C, Ap, Chal	1 K-feldspar, 4 feldspar, 1 biotite, 1 chlorite, 10 pyroxene, 3 hematite, 1 apatite	2 K-feldspar, 1 feldspar, 1 biotite, 3 pyroxene, 2 chlorite, 1 apatite, 1 K-fel+Qtz and 6 chalcopryrite.	Yes
2066204	GHDD4	905	906	Calc-silicate	HSCC	Au Ag As Bi Cu Mo S Se W	Yes	Kfel, Py	No	No	No	No
2066205	GHDD4	915	916	Skarn	HSCC	Au Ag As Bi Cu S Sb Se W	Yes	Hem, BG	No	No	No	No
2066206	GHDD4	934	935	Skarn	HSCC	Au Ag As Cu Mo S Sb Se W	Yes	Py, BG, Chl	No	No	No	No
2066634	IHAD6	827	828	Carbonate	HSCC	As Bi Sb W	Yes	Hem, Kfel, Bre	No	No	No	No
2066635	IHAD6	855	856	Calc-silicate	HSCC	As Bi Cu S Sb W	Yes	Hem, Kfel, Chl	635F, 635J. Apa	3 chlorite, 6 dolomite, 1 calcite, 1 hematite, 2 apatite and 1 gypsum, 2 pyrite, 7 bornite, 1 chalcopryrite and 1 sphalerite.	7 chlorite, 3dolomite, 2 apatite, 1 gypsum, 1 quartz, 1 Dol+Qtz, 1hematite, 10 chalcopryrite, 6 bornite and 2 sphalerite.	Yes
2066636	IHAD6	859	860	Carbonate	HSCC	Bi Cu Sb Se	Yes	Mus, BG, Vein	No	No	No	No
2066637	IHAD6	1000	1001	Metasandstone	HSCC	Sb Se	Yes	Mat, Clast	No	No	No	No
2066639	IHAD3	761.13	762.17	Metasediment	HSCC	As Bi Cu Sb	Yes	Hem, Bre, Chl	No	No	No	No
2066640	IHAD3	789	790	Metasediment	HSCC	Ag As Bi Cu Sb Se	Yes	Hem, Bre	No	No	No	No
2066641	IHAD3	799	800	Metasediment	HSCC	AS Bi Sb Se	Yes	Hem, Kfel	641C, Man	1 feldspar, 2 biotite, 6 hematite, 4 manganite.	1 biotite, 2 manganite and 1 Qtz+Chl, 5 hematite.	Yes
2066642	IHAD5	850.5	851.3	Granite	HSCC	As Cu Sb Se	Yes	BG, Hem	No	No	No	No
2066643	IHAD5	919	920	Granite	HSCC	Ag Bi Cu S Se	Yes	BG, Kfel	No	No	No	No
2066644	IHAD5	926	927	Granite	HSCC	Ag As Bi Cu S Sb Se W	Yes	Hem, Kfel	No	No	No	No
2066645	IHAD5	1092	1093	Metasandstone	HSCC	As Bi	Yes	Chl, BG	No	No	No	No

2066646	IHAD5	1097	1098	Metasandstone	HSCC	0	Yes	Kfel, BG	No	No	No	No
2066655	IHAD5	1016	1017	Metasandstone	CAM	Cu Mo Se	Yes	Mag, Bre	655A,655B.Py	11 chlorite, 3 calcite, 6 hematite, 3 pyrite and 2 chalcopyrite.	20 chlorite, 3 dolomite, 11 hematite, 2 magnetite, 5 pyrite and 7 chalcopyrite.	Yes
2066656	IHAD2	819	820	Granite	CAM/HSCC	Sb S	Yes	Mus, Hem	656A,656B, Ti minerals	1 feldspar, 1 chlorite, 3 muscovite, 3 hematite, 2 ilmenite, 1 monazite and 1 rutile.	1K-feldspar, 4 muscovite, 5 hematite	Yes
2066657	IHAD2	879	880	Granite	HSCC	As Se W	Yes	BG	No	No	No	No
2066658	IHAD2	969	970	Metasediment	HSCC	0	Yes	Bre, BG, Hem	No	No	No	No

Notes: The failed analysis are not in the tables, for example, 17 hematite spots in 2066177 due to Fe 41-58 wt % in LA-ICPMS analysis.

Appendix 2: The Handheld X-ray Data

Sample ID	Mineral	Al	Si	S	K	Ca	Ti	V	Cr	Mn	Fe	Co	Ni	Cu	Zn	As	Zr	Bi
2066163	BG	4.04	13.25		1.28	1.33	0.24	0.02	0.03	1.15	45.96		0.06	0.02	0.10	0.01	0.04	0.00
2066164	Hem	1.40	34.24		1.24	1.07	0.08	0.00	0.01	0.50	21.06		0.02	0.01	0.06	0.00	0.04	0.01
2066165-1	Vein	4.92	50.73	0.13	3.68		0.22	0.02	0.01	0.30	5.91		0.01	0.09	0.04	0.00	0.01	0.01
2066165-2	BG	4.74	55.66		3.93		0.26	0.02	0.01	0.19	0.69		0.00	0.01	0.03	0.00	0.01	0.02
2066166-1	Mag		30.72		1.25	5.31	0.07	0.01		0.50	41.09		0.03		0.02	0.00	0.00	0.01
2066166-2	Hem	1.93	27.48	1.11	1.23	8.65	0.05	0.01		0.60	33.94		0.02	0.05	0.02			0.01
2066167-1	Hem		44.53		1.24	0.28	0.05	0.01	0.01	0.25	14.78		0.01		0.03	0.00		0.01
2066167-2	BG		37.90		1.37	2.36	0.07	0.00	0.01	0.54	24.64		0.02		0.03	0.00	0.01	0.01
2066168-1	Pyrite		0.70	17.44	1.26	18.29	0.06	0.01	0.01	2.58	18.49		0.01					0.01
2066168-2	Hem		17.33		1.42	2.03	0.10	0.02	0.02	1.55	43.24		0.05		0.04	0.01	0.00	0.01
2066168-3	BG		1.27		1.29	16.60	0.12	0.01	0.01	0.99	1.06			0.00				0.02
2066169-1	BG		45.09	0.17	1.24		0.05	0.01		0.05	22.35		0.06	0.01	0.06			0.01
2066169-2	Pyrite		5.07	30.34	1.25			0.01		0.03	58.40		0.11	0.37	0.20			0.00
2066170-1	Pyrite	5.44	29.03	10.20	3.97	0.38	0.16	0.02	0.01	0.08	20.92		0.01	0.10	0.00		0.01	0.01
2066170-2	Breccia	11.24	37.48		5.13		0.28	0.04	0.03	0.07	10.17		0.00	0.01	0.01		0.01	0.01
2066171-1	Kfel	8.08	44.10		4.68		0.25	0.02	0.01	0.07	4.46		0.00	0.01	0.01		0.02	0.02
2066171-2	Chl	7.37	42.27		3.88		0.29	0.01	0.01	0.06	5.80		0.01		0.01		0.02	0.02
2066172	GRT	13.17	44.67	0.30	4.37	0.18	0.40	0.02	0.01	0.09	6.75		0.00	0.02	0.02		0.02	0.01
2066173	Grt	13.69	43.26		4.82	0.56	0.52	0.02	0.01	0.06	4.41		0.00		0.01		0.01	0.01
2066174-1	Mala	7.02	53.83		3.34	0.54	0.25	0.02	0.01	0.11	1.73		0.00	0.01	0.01	0.01	0.01	0.02
2066174-2	Breccia	5.09	50.73		3.02	1.93	0.20	0.02	0.01	0.23	1.85			0.00	0.01	0.00	0.01	0.02
2066175-1	Grt	16.33	45.23		7.07		0.29	0.02	0.02	0.08	-0.03		0.00	0.01	0.00		0.01	0.02
2066175-2	Kfel	9.13	49.74		4.17		0.33	0.02	0.01	0.09	1.51		0.00	0.00	0.01		0.01	0.02
2066176-1	BG	7.90	25.65		2.50	0.40	0.51	0.01	0.01	0.11	8.14		0.01		0.01		0.02	0.01
2066176-2	Kfel	14.40	37.62	0.09	7.34		0.29	0.03	0.01	0.06	-0.33		0.00	0.00	0.00		0.00	0.02
2066177-1	Vein	2.11	26.63	0.12	1.31	4.75	0.53	0.01	0.00	0.44	13.34		0.01	0.01	0.02		0.01	0.01
2066177-2	BG	3.51	24.80		1.84	1.32	1.20	0.02	0.00	0.19	18.34		0.01		0.02		0.02	0.01
2066178-1	Kfel	6.85	57.35	0.13	4.51	0.70	0.18	0.02	0.01	0.03	-1.36			0.00	0.00		0.00	0.02
2066178-2	Dup	7.02	57.35	0.11	4.51	0.70	0.20	0.02	0.01	0.02	-1.38			0.00	0.00		0.00	0.02
2066178-3	BG	9.30	49.88		2.54	1.22	0.26	0.01	0.01	0.05	1.71		0.00		0.01		0.01	0.02
2066179-1	Kfel	15.27	44.95		8.36	0.20	0.31	0.04	0.02	0.02	-1.52		0.00	0.00			0.00	0.02
2066179-2	BG	13.69	41.71		3.90	1.49	0.29	0.02	0.01	0.04	2.51		0.00		0.00		0.01	0.02
2066196-1	BG	7.02	37.76		2.97	1.94	0.56	0.01	0.01	0.08	7.53		0.01	0.00	0.02		0.02	0.01
2066196-2	Fel	14.75	43.54		6.68	1.00	0.32	0.03	0.02	0.04	-0.16		0.00	0.01	0.00		0.01	0.02
2066197	Kfel	4.04	41.00		2.84	5.91	0.19	0.01	0.01	0.43	1.87		0.00		0.01		0.02	0.02
2066198	Kfel	11.41	34.80		3.71	5.71	0.29	0.01	0.01	0.34	3.12		0.00		0.01		0.02	0.02
2066199-1	Kfel	12.29	31.14		4.17	7.21	0.38	0.03	0.02	0.63	3.65		0.01	0.00	0.00		0.01	0.02
2066199-2	BG	8.25	16.91	0.34	2.40	12.26	0.57	0.07	0.02	0.95	6.98		0.01	0.03	0.01		0.01	0.01

To be continued

Sample ID	Mineral	Al	Si	S	K	Ca	Ti	V	Cr	Mn	Fe	Co	Ni	Cu	Zn	As	Zr	Bi
2066200-1	BG	7.55	49.32		4.77	0.69	0.17	0.02	0.01	0.14	2.30		0.00		0.01		0.01	0.02
2066200-2	Breccia	8.25	45.79		4.21	1.63	0.24	0.02	0.01	0.19	4.36		0.00		0.01		0.01	0.02
2066201-1	Vein	4.74	25.65	5.43	2.01	7.02	5.92	0.96	0.11	0.78	3.33		0.02	0.02	0.01		0.01	0.01
2066201-2	BG	10.71	47.06	0.08	4.97	1.48	0.29	0.03	0.02	0.17	0.60		0.00	0.00	0.01		0.01	0.02
2066202	BG	4.74	20.15	0.28	1.24	19.49	0.18	0.02	0.01	0.69	10.33		0.01	0.02	0.04		0.01	0.01
2066202	Pyrite		18.32	10.00	1.25	7.43	0.06	0.00		0.30	14.15		0.02	2.89	9.59		0.00	0.01
2066203-1	Chl	3.51	21.84	1.38	1.27	17.73	0.12	0.01	0.01	0.41	16.05		0.00	0.11	2.80	0.01	0.00	0.01
2066203-2	BG	6.14	29.03		2.76	4.72	0.18	0.02	0.01	0.89	10.19		0.02	0.04	0.07		0.01	0.01
2066203-3	Pyrite	5.97	31.70	5.01	3.11	3.77	0.17	0.01	0.01	0.57	10.90		0.02	1.78	2.03		0.01	0.01
2066204-1	Kfel	13.69	36.92	0.47	5.64	2.61	0.36	0.04	0.02	1.62	3.22		0.01	0.08	0.50		0.01	0.01
2066204-2	Pyrite	6.85	31.14		3.12	6.50	0.28	0.02	0.02	2.14	5.91		0.01	0.06	0.07		0.01	0.01
2066205-1	Hem		15.08	1.56	1.24	14.03	0.07	0.01	0.01	0.38	26.21		0.04	0.99	0.10	0.01	0.00	0.01
2066205-2	BG	3.69	14.23	0.94	1.24	21.42	0.15	0.01	0.01	0.46	12.91		0.01	0.58	0.06	0.00	0.00	0.01
2066206-1	Pyrite	10.18	37.90	0.93	5.31	3.22	0.28	0.03	0.01	0.27	5.32		0.00	0.41	0.19		0.01	0.01
2066206-2	BG	12.11	40.72	0.65	6.48	2.46	0.34	0.03	0.02	0.18	2.03		0.00	0.14	0.34		0.01	0.02
2066206-3	Chl	3.69	29.87		2.54	10.42	0.26	0.02	0.01	0.88	5.17		0.01	0.01	0.08		0.01	0.01
2066634-1	Hem		13.25		1.34	0.40	0.07			0.51	66.27		0.02	0.01	0.02	0.01	0.01	0.00
2066634-2	Kfel		57.63		1.40		0.09	0.01	0.01	0.11	9.73	0.05		0.01	0.01	0.02	0.00	0.01
2066634-3	Breccia	3.34	46.22		2.05	1.67	0.22	0.01	0.01	0.55	9.02		0.01	0.01	0.02	0.00	0.02	0.01
2066635-1	Hem		3.38		1.24	0.30	0.04	0.00		0.12	81.87		0.01		0.01	0.01	0.01	0.00
2066635-2	Kfel	2.98	9.72	0.94		12.91	0.12	0.01	0.01	1.99	5.22		0.00	1.66	0.37		0.00	0.01
2066635-3	Chl	3.69	7.75	6.10	1.24	12.26	0.14	0.01	0.01	1.82	6.14		0.00	2.98	0.18		0.02	0.01
2066636-1	Vein		1.27			9.44	0.04	0.00		0.72	38.95			0.02		0.00	0.00	0.01
2066636-2	BG		3.24		1.23	16.44	0.17	0.01	0.01	1.38	2.38		0.00	0.02	0.00		0.01	0.02
2066636-3	Vein		16.20	2.18	1.24	13.04	0.10	0.01	0.01	1.16	9.41		0.00	0.00	0.02	0.00	0.01	0.01
2066637-1	Fine	5.44	58.19		3.63		0.44	0.01	0.01	0.01	2.70						0.03	0.02
2066637-2	Coarse	6.32	52.42		3.53		0.74	0.02	0.01	0.01	6.81	0.03					0.07	0.01
2066639-1	Hem		18.18		1.54	0.09	0.03			2.74	59.40		0.08	0.06	0.03	0.01		0.00
2066639-2	Breccia		31.99		1.38	2.29	0.07	0.01		0.83	19.34		0.01	0.05	0.01	0.00	0.00	0.01
2066639-3	Chl		52.98	0.08	1.51	1.33	0.13	0.01	0.01	0.07	-0.81		0.00	0.02	0.00	0.00	0.00	0.02
2066640-1	Hem		29.59		1.82	0.44	0.05	0.00		1.47	53.25		0.07	0.24	0.04	0.02	0.00	0.00
2066640-2	BG	3.51	60.17	0.10	2.64	0.40	0.26	0.02	0.01	0.20	-1.47		0.00	0.06	0.01	0.01	0.01	0.02
2066641-1	Hem		29.87		1.84		0.07	0.01		1.43	50.82		0.06	0.11	0.03	0.01	0.01	0.00
2066641-2	Kfel	12.82	43.40		3.91		0.48	0.05	0.01	1.62	5.56		0.00	0.04	0.02		0.01	0.01
2066642-1	BG	13.52	40.72		5.91		0.25	0.02	0.01	0.14	4.20		0.00	0.15	0.01		0.01	0.01
2066642-2	Hem	2.81	17.05		1.60		0.10	0.01	0.01	0.21	53.39		0.02	0.20	0.04	0.02	0.01	0.00
2066643-1	BG	8.25	53.26	0.14	5.60		0.29	0.02	0.01	0.04	1.11			0.01	0.00		0.01	0.02
2066643-2	Kfel	11.94	41.99	1.91	7.34	0.62	0.39	0.06	0.01	0.04	-1.00		0.00	0.03	0.00		0.00	0.02

To be continued

Sample ID	Mineral	Al	Si	S	K	Ca	Ti	V	Cr	Mn	Fe	Co	Ni	Cu	Zn	As	Zr	Bi
2066644-1	Hem		6.20	1.80	1.26	0.08					79.29			5.99				0.00
2066644-2	Kfel	4.04	2.11	8.23	1.29	0.28	4.12	0.66	0.05	0.23	44.52		0.03	4.58		0.01	0.01	0.00
2066645-1	Chl		39.45	4.75	1.24	7.25	0.12	0.01	0.01	0.82	2.89			0.02	0.01		0.00	0.01
2066645-2	BG		58.76		1.29		0.12	0.01	0.01	0.09	5.86				0.01		0.01	0.01
2066646-1	Vein		22.26	0.27	1.52	14.67	0.12	0.01	0.01	1.58	1.57				0.00		0.00	0.02
2066646-2	BG		60.87	0.08	2.35		0.14	0.01	0.01	0.03	-1.33						0.00	0.02
2066655-1	Mag		13.67		1.26	0.59	0.04			0.10	77.86			0.04	0.01		0.00	0.00
2066655-2	Breccia	4.21	35.79		1.25		0.10	0.01	0.00	0.08	27.93		0.00	0.01	0.01	0.00	0.01	0.01
2066656-1	Mica	17.55	46.78		4.59		0.24	0.02	0.01	0.07	1.38		0.00	0.03	0.02		0.00	0.02
2066656-2	Hem	12.29	45.94		3.79		0.25	0.01	0.01	0.17	8.85		0.00	0.01	0.01		0.01	0.01
2066657	BG	7.02	34.52	6.10	3.01	2.75	0.44	0.02	0.01	0.08	7.99	0.04	0.00	0.00	0.01		0.01	0.01
2066658-1	Breccia	1.40	42.69		1.25		0.10	0.01	0.01	0.10	21.20		0.01	0.01	0.01		0.00	0.01
2066658-2	BG	3.51	44.10		1.70		0.12	0.01	0.00	0.07	18.63	0.03	0.00		0.03		0.00	0.01
2066658-3	Hem		31.14		1.25		0.02	0.00	0.00	0.04	46.96		0.01		0.01	0.00		0.00

Notes: Total of 90 spots has been analyzed with four standards controlled (901, 903, 163 and 165)

1. Rb, Sr, Sb, W, Au, Ag, Se, Mo is under the detected limitation as zero value. 17 elements have the values and empty is zero.
2. Four times of Standard have been applied by every twenty measuring spots.
3. The soil mode data have to give up and the mining Plus mode has been used due to factors.
4. The mining mode standard can be match to the references.
5. Eleven highlight samples have been further analysis by SEM, EM and LA-ICPMS.

Appendix 3: The Electron Microprobe Data

Table III. The pyrite (11 grains) contains element Co and As, and ratios of Fe/S atom

SAMPLE	Fe wt %	Co wt %	Cu wt %	S wt %	As wt %	Bi wt %	Fe atom	S atom	Fe/Satom			
2066169A1	48.00	0.13	0.01	55.20	0.00	0.00	0.86	1.73	0.50			
2066169A2	47.03	0.18	0.00	55.25	0.00	0.00	0.84	1.73	0.49			
2066169A3	47.35	0.22	0.02	55.25	0.04	0.00	0.85	1.73	0.49			
2066169B1	41.51	0.00	0.10	33.32	0.00	0.17	0.74	1.04	0.71			
2066169B2	41.32	0.00	0.11	33.22	0.00	0.17	0.74	1.04	0.71			
2066169B3	41.54	0.00	0.11	33.48	0.00	0.21	0.74	1.05	0.71			
2066655A1	41.44	0.22	0.12	33.49	0.00	0.00	0.74	1.05	0.71			
2066655A2	41.87	0.06	0.02	34.11	0.07	0.00	0.75	1.07	0.70			
2066655A3	41.91	0.14	0.07	34.46	0.00	0.00	0.75	1.08	0.69			
2066635B1	43.04	0.05	0.64	43.84	0.02	0.00	0.77	1.37	0.56			
2066635B2	42.33	0.06	0.35	43.34	0.05	0.00	0.76	1.35	0.56			
Re analysed data												
Sample	S	Fe	Co	Total	Co/Ni	S	As	Fe	Cu	Bi	Co	Total
169A	53.82	46.20	0.41	100.51	0.4	66.77	0.03	32.91	0.01	0.00	0.27	100.00
169A	53.63	46.31	0.57	100.51	0.4	66.59	0.00	33.02	0.00	0.00	0.38	100.00
169A	53.89	46.47	0.43	100.84	0.4	66.68	0.01	33.01	0.00	0.01	0.29	100.00
169B	53.98	46.01	0.62	100.63	0.4	66.85	0.01	32.72	0.01	0.00	0.42	100.00
169B	53.82	45.91	0.57	100.30	0.4	66.87	0.00	32.75	0.00	0.00	0.38	100.00
169B	53.73	46.25	0.57	100.56	0.4	66.66	0.00	32.94	0.01	0.00	0.38	100.00
635B	53.61	46.55	0.10	100.58	0.4	66.56	0.02	33.19	0.16	0.01	0.07	100.00
635B	53.54	46.62	0.05	100.37	0.5	66.58	0.00	33.29	0.10	0.00	0.04	100.00

635B	53.51	46.37	0.14	100.57	0.4	66.48	0.01	33.08	0.33	0.00	0.09	100.00
655A	53.98	46.47	0.11	100.59	0.4	66.86	0.00	33.05	0.01	0.00	0.08	100.00
655A	53.92	46.41	0.07	100.46	0.4	66.87	0.04	33.05	0.00	0.00	0.04	100.00
655A	53.77	46.16	0.23	100.18	0.4	66.88	0.00	32.96	0.01	0.00	0.16	100.00

Silicate and Oxide Electron Microprobe Data: 1-8 grains (2066166) and 9-20 grains (2066199)

Rock	Calc-silicate - 2066166																			
Sample ID	Si WT %	Zr WT %	Ti WT %	Zn WT %	Al WT %	V WT %	Cr WT %	Fe WT %	Mn WT %	Mg WT %	Ca WT %	Ba WT %	Na WT %	K WT %	P WT %	Cl WT %	F WT %	O WT %	H WT %	TOTAL
166B Mag1	0.06	0.00	0.00	0.00	0.02	0.00	0.00	71.28	0.08	0.01	0.01	0.01	0.03	0.01	0.01	0.02	0.43	30.59	0.00	102.5
166B Mag2	0.11	0.06	0.02	0.05	0.03	0.00	0.00	71.34	0.14	0.07	0.08	0.04	0.01	0.01	0.01	0.00	0.46	30.80	0.00	103.2
166B Gt	17.04	0.00	0.01	0.00	1.73	0.01	0.00	18.40	0.76	0.08	23.59	0.00	0.00	0.00	0.00	0.00	0.14	35.87	0.00	97.63
166B Chl	11.52	0.00	0.00	0.00	8.37	0.02	0.00	26.27	2.76	4.42	0.03	0.00	0.02	0.00	0.02	0.00	0.16	31.79	0.00	85.37
166E Fe	0.00	0.01	0.00	0.05	0.00	0.00	0.01	46.40	0.00	0.00	0.00	0.02	0.00	0.00	0.00	53.45	0.00	0.41	0.00	100.3
166E Chl1	11.56	0.00	0.00	0.00	8.57	0.00	0.00	26.51	2.89	4.11	0.09	0.00	0.04	0.00	0.02	0.00	0.16	31.94	0.00	85.90
166E Gt	16.94	0.00	0.07	0.00	1.58	0.01	0.00	19.49	1.16	0.01	22.53	0.00	0.00	0.00	0.01	0.00	0.13	35.63	0.00	97.54
166E Chl2	15.57	0.00	0.00	0.04	5.74	0.00	0.02	8.13	0.65	15.03	0.32	0.00	0.05	0.02	0.05	0.02	0.23	35.38	0.00	81.24
Rock	Granite -2066169																			
169A Hem4	0.80	0.00	0.01	0.04	0.33	0.02	0.01	65.14	0.04	0.03	0.03	0.00	0.52	0.01	0.01	0.04	0.40	29.30	0.00	96.75
169A Hem5	0.12	0.01	0.07	0.05	0.04	0.04	0.00	67.32	0.06	0.01	0.06	0.00	0.05	0.00	0.02	0.01	0.43	29.08	0.00	97.35
169A Hem6	0.19	0.00	0.01	0.03	0.05	0.01	0.00	66.01	0.04	0.02	0.04	0.00	0.04	0.01	0.01	0.01	0.39	28.55	0.00	95.41
169A Chl1	12.85	0.00	0.00	0.00	10.72	0.00	0.00	15.14	0.04	11.53	0.02	0.00	0.00	0.00	0.00	0.04	0.35	35.97	0.00	86.66
169A Chl2	12.66	0.00	0.01	0.01	10.47	0.00	0.00	15.44	0.04	10.99	0.04	0.00	0.00	0.00	0.02	0.05	0.34	35.29	0.00	85.35
169A Hem1	0.80	0.00	1.20	0.00	0.14	0.06	0.01	63.72	0.02	0.06	0.05	0.03	0.05	0.02	0.00	0.02	0.38	29.18	0.00	95.73
169A Hem2	0.01	0.00	0.07	0.00	0.02	0.00	0.01	68.35	0.00	0.00	0.01	0.00	0.00	0.00	0.00	0.00	0.43	29.28	0.00	98.18
169B Hem2	0.18	0.01	0.00	0.00	0.05	0.00	0.01	67.24	0.00	0.02	0.02	0.00	0.07	0.03	0.02	0.03	0.46	29.02	0.00	97.13
169B Hem3	0.02	0.01	0.00	0.03	0.02	0.00	0.01	67.70	0.02	0.00	0.01	0.00	0.06	0.01	0.01	0.01	0.45	29.01	0.00	97.35
169B Hem4	0.12	0.01	0.11	0.00	0.14	0.03	0.00	67.20	0.00	0.04	0.00	0.02	0.09	0.02	0.00	0.03	0.43	29.11	0.00	97.35
169B Chl1	12.39	0.00	0.00	0.01	10.41	0.00	0.00	15.48	0.10	10.41	0.05	0.00	0.04	0.03	0.00	0.06	0.35	34.57	0.00	83.90
169B Chl2	12.82	0.00	0.00	0.01	10.74	0.00	0.00	15.20	0.04	11.30	0.02	0.00	0.02	0.01	0.00	0.05	0.33	35.83	0.00	86.36

Silicate and Oxide Electron Microprobe Data – 21-41 grains (2066174)

Rock	Granite-2066174																			
Sample ID	Si WT %	Zr WT %	Ti WT %	Zn WT %	Al WT %	V WT %	Cr WT %	Fe WT %	Mn WT %	Mg WT %	Ca WT %	Ba WT %	Na WT %	K WT %	P WT %	Cl WT %	F WT %	O WT %	H WT %	TOTAL
174A Cal1	0	0	0	0	0	0	0	0	3.85	13.39	22.98	0	0	0	0	0.01	0.08	12.29	51.83	104.44
174A Cal2	0.03	0.02	0	0	0.01	0.01	0	1.35	3.51	12.13	19.59	0	0.01	0	0	0.02	0.18	12.53	50.59	99.98
174A Cal3	0	0	0	0.04	0	0	0.01	0.01	4.57	12.61	20.74	0	0	0	0	0	0.05	12.46	51.11	101.59
174A Hem1	0	0.13	0	0	0	0.02	0	0.09	0.01	0	41.12	0	0.02	0.01	18.66	0	4.66	38.65	0	103.36
174A Bt1	21.22	0	0.06	0	12.31	0	0	8.89	0.04	1.27	0.06	0.05	0.22	6.12	0	0.05	0.18	39.83	0	90.3
174A Bt2	22.06	0.01	0.05	0	17.76	0.04	0	2.5	0	0.66	0.04	0.23	0.15	7.03	0	0	0.11	43.62	0	94.26
174A Ksp1	30.18	0	0.01	0	9.74	0	0	0.02	0	0.01	0.09	0.23	0.92	12.23	0	0	0	45.96	0	99.4
174A Ksp2	30.35	0	0	0	9.87	0	0	0.02	0	0	0.01	0.47	0.39	11.94	0	0.14	0	45.96	0	99.15
174B Ksp1	30.19	0.01	0.01	0	9.66	0	0	0	0	0	0.02	0.18	0.82	12.61	0	0.02	0	45.89	0	99.42
174B Ap1	0.06	0.11	0.01	0	0.01	0	0	1.71	0.01	0.02	38.38	0	0.05	0	17.46	0.01	4.01	36.84	0	98.7
74B Kfs2	29.15	0	0.01	0	9.21	0	0	1.15	0	0	0.03	0.21	0.24	12.94	0.01	0.03	0	44.52	0	97.51
174B Ap2	0.06	0.13	0	0.01	0	0.01	0	0.08	0	0.01	39.67	0	0.58	0.13	18.1	0.33	5.58	37.17	0	101.85
174B Fe1	1.1	0.01	0.46	0	0.6	0.02	0.03	59.97	0.05	0.04	0.48	0	0.13	0.18	0.03	0.11	0.44	28.03	0	91.68
174B Fe2	0.75	0	0.28	0	0.39	0.03	0.02	60.3	0.06	0.01	0.42	0	0.2	0.08	0.02	0.13	0.29	27.48	0	90.46
174C Kfs1	30.47	0	0	0	9.81	0	0	0.43	0.01	0.01	0.02	0.03	0.22	13.6	0	0.01	0	46.44	0	101.05
174C Hem1	0.56	0	0.16	0.01	0.44	0.09	0.02	63.5	0.05	0.01	0.05	0	0.06	0.16	0.01	0.05	0.46	28.38	0	94.01
174C Hem2	0.84	0.01	0.13	0.02	0.6	0.06	0.02	63.5	0.04	0.02	0.04	0	0.09	0.37	0	0.05	0.31	28.92	0	95.01
174C Kfs2	24.12	0.03	0.02	0	14.46	0	0	2.76	0.03	0.65	0.07	0.08	0.1	7.36	0	0.02	0.28	43.05	0	93.03
174D Ap1	0	0.08	0	0	0	0.02	0	0.17	0	0	40.23	0	0.03	0.01	17.94	0.01	4.82	37.29	0	100.6
174D Fe1	23.57	0	0.02	0	14.49	0.01	0	2.97	0.01	1.11	0.18	0.1	0.07	6.79	0	0.14	0.16	42.74	0	92.36
174D Fe1	1.22	0	0.8	0.02	0.62	0.05	0.04	61.9	0.4	0.09	0.46	0.06	0.02	0.26	0.01	0.05	0.38	29.39	0	95.76

Silicate and Oxide Electron Microprobe Data – 42-73 grains (2066177)

Rock	Amphibolite - 2066177																			
Sample ID	Si WT %	Zr WT %	Ti WT %	Zn WT %	Al WT %	V WT %	Cr WT %	Fe WT %	Mn WT %	Mg WT %	Ca WT %	Ba WT %	Na WT %	K WT %	P WT %	Cl WT %	F WT %	O WT %	H WT %	TOTA L
177A Cal2	0	0	0	0.04	0	0	0	0.12	3.84	0.12	42.73	0	0.01	0.01	0	0	0.12	11.21	48.13	106.32
177A Dol1	0	0.02	0	0	0.01	0	0	0.6	6.3	11.44	22.7	0	0	0	0	0.01	0.09	12.09	50.79	104.04
177A Dol2	0	0.02	0	0	0	0	0	1.42	3.46	6.14	33.22	0	0.03	0.01	0	0.02	0.12	11.64	49.69	105.76
177A Cal1	0	0	0	0.02	0	0	0	0	2.39	13.48	25.26	0	0	0	0	0	0.11	12.23	52.21	105.71
177A Chl1	12.2	0	0	0	10.2	0.01	0	21.68	0.36	8.04	0.02	0	0.03	0.01	0	0.05	0.09	34.56	0	87.26
177A Chl2	11.74	0.03	0.01	0.03	10.14	0.02	0	21.23	0.34	7.43	0.05	0	0.01	0.05	0	0.08	0.18	33.45	0	84.8
177A Hem1	0.83	0.01	0.2	0	0.63	0.45	0.02	57.71	0.09	0.39	0.2	0	0.07	0	0	0.07	0.27	26.93	0	87.88
177A Fe1	22.45	0	0	0	11.33	0.05	0	3.3	0.04	1.86	0.11	0	0.05	4.55	0	0.15	0.26	38.71	0	82.86
177B Hem1	1.95	0	0.09	0	1.11	0.15	0	45.74	0	0.21	0.15	0	0.09	0.61	0.01	0.21	0.17	23.24	0	73.74
177B Mag1	2.63	0	0.03	0	1.42	0.14	0	41.23	0	0.24	0.06	0	0.1	0.81	0	0.24	0.21	22.3	0	69.41
177B Hem2	7.38	0	0.04	0	4.23	0.15	0	48.03	0	0.7	0.04	0	0.13	2.12	0	0.11	0.38	33.69	0	97.01
177B Mag2	3.73	0	0.07	0	1.93	0.22	0	49.5	0.02	0.36	0.06	0	0.08	0.75	0	0.15	0.2	27.72	0	84.78
177B Bt1	16.91	0	0.01	0	8.9	0.13	0	22.82	0.02	1.52	0.1	0	0	4.95	0	0.04	0.31	35.7	0	91.4
177B Hem3	2.56	0.01	0.04	0	1.46	0.18	0.01	44.43	0.01	0.26	3.08	0	0	0.71	1.45	0.12	0.39	26.66	0	81.36
177B Chl1	12.02	0	0.01	0.04	9.92	0.05	0	21.34	0.47	7.41	0.06	0	0.07	0.13	0	0.08	0.15	33.69	0	85.43
177B Chl2	12.06	0	0	0	9.9	0.01	0	22.98	0.34	7.29	0.01	0	0.02	0.04	0.01	0.06	0.13	33.99	0	86.84
177B Hem4	0.54	0	0.04	0	0.3	0.17	0	60.92	0.04	0.04	0.18	0	0.09	0.13	0.01	0.07	0.34	27.19	0	90.07
177B Hem5	4.85	0	0.06	0	2.59	0.17	0	45.69	0	0.49	0.19	0	0.05	1.36	0.01	0.01	0.22	28.18	0	83.86
177B Chl3	12.31	0.01	0	0.02	10.16	0.03	0	20.98	0.41	8.04	0.04	0	0.07	0.09	0	0.07	0.18	34.48	0	86.9
177B Bt	16.2	0	0	0.09	9.28	0.03	0	13.84	0.51	7.02	0.1	0	0.09	1.99	0	0.07	0.26	35.84	0	85.33
177B Hem5	1	0	0.03	0	0.58	0.16	0	51.91	0.03	0.14	0.07	0	0.14	0.26	0	0.08	0.28	24.17	0	78.85

To be continued

Rock	Amphibolite - 2066177																			
Sample ID	Si WT %	Zr WT %	Ti WT %	Zn WT %	Al WT %	V WT %	Cr WT %	Fe WT %	Mn WT %	Mg WT %	Ca WT %	Ba WT %	Na WT %	K WT %	P WT %	Cl WT %	F WT %	O WT %	H WT %	TOTAL
177C Hem1	0.646	0	0.212	0	0.508	0.444	0.004	58.678	0.079	0.149	0.201	0	0.035	0.011	0.008	0.07	0.326	26.83	0	88.2
177C Chl1	12.27	0	0.009	0.007	9.893	0.017	0	21.229	0.291	8.279	0	0	0.021	0.024	0	0.056	0.109	34.365	0	86.57
177C Kfs1	30.272	0	0.006	0	9.742	0	0.007	0.155	0	0	0.015	0.231	0.163	13.669	0.003	0	0	46.097	0	100.36
177C Chl2	12.005	0	0.016	0	9.997	0.01	0	21.325	0.388	7.579	0.039	0	0.112	0.099	0.004	0.08	0.148	33.797	0	85.598
177C Chl3	11.936	0	0.005	0	10.235	0.003	0.002	21.318	0.341	7.581	0.008	0.002	0.083	0.08	0.013	0.083	0.133	33.897	0	85.722
177C Ap1	23.648	0.069	0.012	0.026	0.054	0	0.008	0.338	0.018	0.034	18.893	0	0.037	0.013	9.861	0.108	2.22	46.491	0	101.83
177C Chl4	10.652	0	0	0	9.097	0.015	0	14.993	0.244	6.541	0.066	0	0.41	0.13	0.016	0.294	0.14	28.998	0	71.596
177C Hem2	8.658	0.048	0.033	0.037	6.905	0.057	0	24.307	0.372	5.569	0.833	0	0.294	0.095	0.016	0.179	0.142	30.677	0	78.221
177C Cal1	0	0	0	0	0	0	0.013	0.363	5.09	0.349	39.882	0.004	0.066	0.007	0	0.047	0.114	11.265	47.723	104.92
177C Hem3	2.361	0	0.07	0	1.861	0.101	0	29.91	0.346	2.477	3.113	0	0.423	0.057	0	0.174	0.087	20.35	0	61.329
177C Chl5	12.097	0	0.019	0	9.968	0	0	21.052	0.363	7.779	0.023	0	0.183	0.04	0	0.145	0.12	33.918	0	85.706

Silicate and Oxide Electron Microprobe Data - 74 to 97 grains (2066178)

Rock	Granite- 2066178																			
Sample ID	Si	Zr	Ti	Zn	Al	V	Cr	Fe	Mn	Mg	Ca	Ba	Na	K	P	Cl	F	O	H	TOTAL
178AHem1	0.11	0.00	0.12	0.00	0.07	0.08	0.03	66.84	0.03	0.00	0.04	0.00	0.23	0.02	0.02	0.10	0.46	28.96	0.00	97.11
178A Kfs1	26.5	0.00	0.00	0.00	14.95	0.01	0.00	0.11	0.17	0.05	1.11	0.02	3.60	3.82	0.00	0.01	0.01	46.09	0.00	96.45
178A Bt3	15.9	0.04	1.24	0.05	8.24	0.02	0.00	17.50	0.28	4.89	0.18	0.16	0.09	7.10	0.02	0.02	1.04	35.82	0.00	92.61
178A Fsp2	29.7	0.00	0.00	0.01	13.10	0.00	0.00	0.12	0.00	0.02	2.92	0.02	6.34	0.59	0.00	0.05	0.00	49.06	0.00	101.94
178A Fsp3	29.3	0.03	0.01	0.00	13.10	0.00	0.00	0.47	0.00	0.07	2.76	0.00	6.44	1.45	0.00	0.02	0.01	48.91	0.00	102.61
178A Bt1	16.6	0.00	1.44	0.03	8.53	0.03	0.01	16.99	0.25	5.04	0.00	0.10	0.09	7.92	0.01	0.03	1.04	37.03	0.00	95.18
178A Bt2	16.4	0.00	1.27	0.02	8.62	0.03	0.01	17.56	0.26	5.40	0.04	0.04	0.07	7.46	0.01	0.03	0.97	37.07	0.00	95.26
178A Bt4	17.2	0.01	1.01	0.00	8.81	0.03	0.00	16.79	0.21	5.64	0.03	0.07	0.08	7.95	0.01	0.03	0.96	38.01	0.00	96.87
178B Bt1	16.5	0.02	1.67	0.04	8.33	0.03	0.00	17.29	0.25	5.00	0.10	0.10	0.15	7.72	0.01	0.05	1.28	36.82	0.00	95.35
178B Fel1	27.1	0.00	0.01	0.00	14.86	0.00	0.00	0.22	0.01	0.04	0.65	0.03	4.11	3.60	0.00	0.03	0.00	46.69	0.00	97.42
178B Bt2	16.6	0.01	1.25	0.03	8.22	0.07	0.00	16.60	0.22	5.32	0.04	0.13	0.08	7.85	0.00	0.05	1.01	36.70	0.00	94.22
178B Bt1	16.8	0.00	0.95	0.00	8.79	0.02	0.00	16.66	0.27	5.32	0.02	0.02	0.04	7.93	0.00	0.03	1.40	37.05	0.00	95.32
178B ilm1	0.07	0.02	28.96	0.08	0.02	0.19	0.02	30.64	5.48	0.01	0.19	0.37	0.05	0.03	0.00	0.01	0.26	34.37	0.00	100.76
178B Fsp2	21.8	0.00	0.94	0.00	16.36	0.11	0.03	2.65	0.00	0.84	0.02	0.35	0.14	6.00	0.00	0.00	0.50	42.50	0.00	92.23
178B unk1	15.7	0.13	1.58	0.09	7.78	0.13	0.06	10.00	0.25	0.21	11.32	0.11	0.26	0.18	0.01	0.13	0.44	33.60	0.00	82.01
178B Bt3	16.6	0.00	0.66	0.02	8.72	0.03	0.00	16.61	0.22	6.44	0.06	0.05	0.06	6.90	0.00	0.03	1.16	37.22	0.00	94.82
178B Fsp3	30.5	0.00	0.00	0.00	9.88	0.00	0.00	0.01	0.00	0.00	0.02	0.48	0.54	12.52	0.00	0.00	0.00	46.37	0.00	100.33
178BHem1	0.10	0.00	0.01	0.00	0.05	0.03	0.08	66.00	0.05	0.01	0.03	0.01	0.02	0.01	0.00	0.00	0.23	28.52	0.00	95.14
178BHem2	0.00	0.01	0.01	0.04	0.00	0.04	0.01	71.11	0.02	0.00	0.02	0.01	0.11	0.01	0.01	0.03	0.44	30.49	0.00	102.37
178FHem1	0.04	0.01	0.00	0.01	0.09	0.14	0.15	68.68	0.04	0.02	0.00	0.00	0.06	0.00	0.00	0.00	0.10	29.78	0.00	99.10
178FHem2	0.01	0.00	0.02	0.00	0.03	0.12	0.14	70.32	0.02	0.00	0.00	0.02	0.03	0.02	0.00	0.00	0.48	30.21	0.00	101.43
178F bt1	16.6	0.01	1.61	0.03	8.50	0.05	0.02	17.30	0.25	4.72	0.02	0.06	0.08	7.93	0.00	0.02	1.20	36.91	0.00	95.34
178F bt2	16.2	0.00	0.95	0.01	8.16	0.02	0.00	15.39	0.23	5.18	0.18	0.07	0.09	7.51	0.01	0.04	0.68	35.67	0.00	90.41
178F bt3	17.1	0.00	1.21	0.05	8.89	0.04	0.01	16.50	0.21	5.30	0.15	0.11	0.09	7.71	0.02	0.02	1.22	37.77	0.00	96.43

Silicate and Oxide Electron Microprobe Data - 98 to122 grains (2066199)

Rock	Calc-silicate -2066199																			
Sample ID	Si WT %	Zr WT %	Ti WT %	Zn WT %	Al WT %	V WT %	Cr WT %	Fe WT %	Mn WT %	Mg WT %	Ca WT %	Ba WT %	Na WT %	K WT %	P WT %	Cl WT %	F WT %	O WT %	H WT %	TOTAL
199A Kfs1	24.47	0.00	0.14	0.02	11.54	0.00	0.01	6.78	0.03	1.30	0.11	0.04	0.05	6.50	0.01	0.03	0.20	42.37	0.00	93.58
199A Kfs2	30.44	0.00	0.00	0.03	9.96	0.01	0.01	0.22	0.01	0.00	0.03	0.11	0.66	12.26	0.03	0.01	0.00	46.43	0.00	100.21
199A Kfs3	25.12	0.02	0.08	0.01	13.35	0.01	0.03	3.59	0.01	1.65	0.11	0	0.16	5.26	0	0.03	0.31	43.73	0	93.47
199A Bt4	25.44	0	0.11	0	13.73	0.02	0.01	3.67	0.01	1.68	0.18	0.03	0.04	4.9	0.03	0.03	0.33	44.43	0	94.63
199A Car1	0	0	0	0.01	0.01	0	0	7.12	4.23	6.45	21.15	0	0.01	0.03	0	0.03	0.12	11.97	47.81	98.94
199A Car2	0	0	0	0	0	0	0	6.59	1.13	10.32	22.07	0	0.01	0.01	0	0	0.12	12.1	50.02	102.37
199A Bt5	30.17	0.02	0.03	0	11.84	0	0	1.25	0.02	0.51	0.07	0.08	0.1	8.11	0.01	0.02	0.04	47.36	0	99.64
199A Kfs4	24.37	0.02	0.65	0	13.9	0.01	0.01	3.3	0.01	1.41	0.11	0.09	0.08	5.88	0	0.03	0.38	43.57	0	93.81
199A bt1	25.72	0.00	0.11	0.03	12.74	0.01	0.02	3.44	0.02	1.58	0.10	0.06	0.06	5.81	0.02	0.04	0.34	43.88	0.00	93.96
199A bt2	23.88	0.02	0.22	0.00	12.72	0.03	0.02	6.35	0.03	1.58	0.11	0.03	0.04	5.77	0.02	0.02	0.43	42.64	0.00	93.90
199A bt3	26.28	0.02	0.10	0.02	11.40	0.01	0.00	4.05	0.01	0.91	0.07	0.05	0.06	7.48	0.01	0.02	0.19	43.43	0.00	94.08
199A Kfs1	24.47	0.00	0.14	0.02	11.54	0.00	0.01	6.78	0.03	1.30	0.11	0.04	0.05	6.50	0.01	0.03	0.20	42.37	0.00	93.58
199A Kfs2	30.44	0.00	0.00	0.03	9.96	0.01	0.01	0.22	0.01	0.00	0.03	0.11	0.66	12.26	0.03	0.01	0.00	46.43	0.00	100.21
199A Ap1	0.50	0.07	0.00	0.00	0.33	0.00	0.00	2.27	1.54	1.92	33.25	0.00	0.00	0.16	12.07	0.07	3.34	30.71	0.00	86.23
199ACaMg	0.04	0.00	0.00	0.00	0.01	0.00	0.00	3.79	0.70	7.20	12.40	0.00	0.03	0.02	0.00	0.00	0.11	11.01	0.00	35.32
199ACaFe1	0.00	0.00	0.00	0.00	0.00	0.00	0.00	7.13	1.28	9.56	21.06	0.00	0.06	0.01	0.00	0.06	0.00	17.12	0.00	56.27
199D Ti	0.03	0.04	57.53	0.00	0.00	0.33	0.00	0.54	0.00	0.00	0.02	0.75	0.01	0.14	0.01	0.02	0.05	38.91	0.00	98.37
199D Ap	0.01	0.17	0.00	0.00	0.00	0.01	0.00	0.21	0.00	0.01	40.41	0.01	0.01	0.07	18.79	0.01	4.35	38.72	0.00	102.77
199DHem1	0	0	0	0.03	0	0	0	31.93	9.12	1.99	0.21	0	0.03	0	0	0	0.2	17.71	0	61.22
199D Dol	0	0	0	0.01	0	0	0	13.65	6.33	2.66	19.27	0	0.04	0.01	0	0.01	0.22	11.36	45.39	98.96
199D Dol1	0.02	0	0	0	0	0	0	6.51	4.77	8.84	22.49	0	0.03	0.03	0	0	0.14	11.76	49.37	103.96
199D Dol2	0	0	0	0.03	0.15	0	0	6.12	0.97	11.52	22.87	0	0.05	0.03	0	0	0.07	12.04	50.97	104.84
199D Dol3	0	0.02	0	0	0	0	0	8.38	9.77	4.12	20.13	0	0.02	0.01	0	0.1	0.17	11.42	46.35	100.5
199DHem2	0.1	0	1.33	0	0.02	0.01	0	66.06	0	0.02	0.04	0	0.03	0.09	0	0.01	0.49	29.27	0	97.47
199D Kfs1	30.95	0.00	0.01	0.00	10.06	0.00	0.00	0.32	0.02	0.04	0.04	0.03	0.10	12.67	0.00	0.02	0.00	46.98	0.00	101.25
199D Kfs2	30.44	0.00	0.00	0.00	9.69	0.01	0.00	0.20	0.00	0.01	0.10	0.18	0.29	13.28	0.00	0.02	0.02	46.25	0.00	100.52
199D Mon	24.47	0.01	0.26	0.00	11.79	0.03	0.01	6.92	0.01	1.46	0.12	0.02	0.08	5.85	0.04	0.02	0.28	42.70	0.00	94.06

Silicate and Oxide Electron Microprobe Data - 123 to143 grains (2066203)

Rock	Calc-silicate - 2066203																			
	Sample ID	Si WT %	Zr WT %	Ti WT %	Zn WT %	Al WT %	V WT %	Cr WT %	Fe WT %	Mn WT %	Mg WT %	Ca WT %	Ba WT %	Na WT %	K WT %	P WT %	Cl WT %	F WT %	O WT %	H WT %
203A Hem1	1.48	0	0.45	0.01	0.13	0.02	0.01	64.35	0.15	0.76	0.44	0.02	0.09	0.02	0	0.02	0	30.52	0	98.46
203A Pyro1	24.65	0	0.01	0.2	1	0	0	14.67	0.3	6.95	8.63	0	0.23	0.32	0	0.16	0	41.45	0	98.58
203A Pyro2	24.83	0.04	0.01	0.15	1.99	0	0	13.96	0.55	8.34	8	0	0.65	0.46	0	0.3	0	43.22	0	102.5
203A Bt1	29.96	0	0	0.02	9.78	0	0	0.29	0.01	0	0.03	0.81	0.13	13.47	0	0	0	45.84	0	100.35
203A Fel1	30.49	0	0.01	0.11	9.85	0	0	0.32	0.01	0	0.02	0.64	0.16	12.44	0	0.06	0	46.3	0	100.41
203A Pyro3	23.67	0.01	0.02	0.04	1.86	0	0.02	14.86	1.8	5.7	8.61	0	0.16	0.81	0	0.8	0	40.68	0	99.05
203A Hem2	0.53	0	0.31	0.06	0.16	0.02	0.02	65.18	0.09	0.26	0.09	0	0.12	0.02	0.01	0.01	0	29.29	0	96.17
203A Pyro4	22.49	0.02	0	0.06	2.03	0	0.01	11.73	2.7	7.76	7.14	0	0.25	0.29	0	0.33	0	39.64	0	94.46
203A Kfs2	29.77	0	0.01	0	9.93	0	0.02	0.09	0	0.01	0.15	1.21	0.63	12.77	0.01	0.04	0	45.84	0	100.48
203A Pyro5	22.85	0	0.04	0.02	2.49	0	0	14.71	0.59	6.76	7.85	0	0.48	0.72	0	0.46	0	40.47	0	97.44
203A Hem3	0.17	0.02	0.37	0	0.08	0.02	0	66.26	0.04	0.1	0.02	0	0.07	0.01	0	0.02	0	29.12	0	96.32
203D Fel1	30.25	0	0	0	9.83	0	0	0.09	0	0	0.02	1.06	0.37	12.94	0	0	0	46.15	0	100.72
203D Pyro1	21.3	0.02	0.04	0.01	3.82	0	0	15.42	0.31	6.05	8.59	0	0.72	0.97	0	0.5	0	39.96	0	97.7
203D Pyro2	20.6	0.02	0.04	0	3.99	0.01	0	14.78	0.23	5.8	8.5	0	1.4	0.96	0	1.15	0	39.01	0	96.49
203D Ap1	0.09	0.14	0	0.02	0.01	0	0.01	0.16	0.04	0.01	39.46	0	0.05	0.01	18.22	0.06	0	39.52	0	97.81
203D Fel2	29.99	0	0	0	9.69	0.01	0	0.49	0.01	0.13	0.15	0.72	0.26	12.99	0	0.03	0	45.91	0	100.39
203D Fel3	30.93	0.01	0	0	9.5	0	0	0.16	0	0.01	0.02	0.51	0.24	13.11	0	0	0	46.58	0	101.07
203D Pyro3	23.31	0	0.03	0.01	2.43	0	0	11.86	0.28	7.78	8.61	0	0.65	0.59	0	0.2	0	41.08	0	96.84
203D Pyro4	21.05	0	0	0	2.96	0.01	0	17.39	0.31	4.97	8.52	0	0.48	1.15	0	1.19	0	38.5	0	96.54
203D Chl1	29.95	0.01	0	0.01	9.59	0	0	0.06	0	0.01	0.09	0.3	0.2	13.25	0	0.03	0	45.53	0	99.02
203D Pyro5	21.49	0.01	0.04	0	3.7	0.01	0	15.25	0.27	6.04	8.55	0.02	0.69	0.97	0	0.49	0	39.98	0	97.51

Silicate and Oxide Electron Microprobe Data - 144 to157 grains (2066635)

Rock	Calc-silicate - 2066635																				
	Sample ID	Si WT %	Zr WT %	Ti WT %	Zn WT %	Al WT %	V WT %	Cr WT %	Fe WT %	Mn WT %	Mg WT %	Ca WT %	Ba WT %	Na WT %	K WT %	P WT %	Cl WT %	F WT %	O WT %	H WT %	TOTAL
635B hem1	0.47	0.00	0.24	0.01	0.23	0.00	0.00	64.24	0.10	0.18	0.02	0.03	0.01	0.01	0.01	0.01	0.01	0.43	28.50	0.00	94.48
635B chl1	12.29	0.00	0.01	0.04	8.60	0.01	0.00	14.40	0.73	11.40	0.04	0.00	0.02	0.00	0.01	0.02	0.02	0.20	33.47	0.00	81.26
635F chl1	12.83	0.01	0.00	0.06	7.92	0.00	0.00	12.23	0.81	12.60	0.14	0.00	0.02	0.01	0.01	0.03	0.45	33.59	0.00	80.70	
635F chl2	12.20	0.00	0.00	0.01	8.75	0.00	0.00	13.60	1.51	11.04	0.08	0.00	0.03	0.00	0.01	0.03	0.29	33.21	0.00	80.77	
635F Ap1	0.00	0.11	0.00	0.07	0.00	0.00	0.00	0.08	0.04	0.00	36.68	0.00	0.01	0.00	16.12	0.16	4.08	33.79	0.00	91.14	
635B dol1	0.00	0.00	0.00	0.03	0.01	0.00	0.00	0.24	3.31	12.86	20.72	0.00	0.03	0.03	0.00	0.04	0.03	12.56	51.23	101.06	
635F cal1	2.56	0.02	0.10	0.04	1.46	0.01	0.00	9.86	4.33	2.80	22.99	0.00	0.05	0.01	0.01	0.01	0.27	11.73	50.57	106.81	
635F dol1	0.00	0.00	0.00	0.04	0.00	0.00	0.00	0.25	3.32	12.80	21.42	0.00	0.00	0.00	0.00	0.03	0.04	12.50	51.29	101.68	
635F dol2	0.17	0.00	0.00	0.09	0.03	0.01	0.00	0.41	2.89	12.89	21.28	0.00	0.00	0.00	0.00	0.03	0.01	12.53	51.56	101.91	
635G dol1	0.17	0.00	0.00	0.03	0.03	0.02	0.00	0.29	3.28	11.29	19.17	0.00	0.10	0.02	0.00	0.13	0.30	12.71	50.11	97.62	
635G dol2	0.00	0.02	0.00	0.00	0.00	0.00	0.00	0.20	3.12	13.41	20.36	0.00	0.02	0.01	0.00	0.03	0.06	12.58	51.43	101.24	
635G gy1	0.00	0.00	0.00	0.00	0.00	0.00	0.00	0.00	0.00	0.00	25.74	0.00	0.01	0.00	0.00	0.00	0.06	10.25	0.00	36.06	
635G dol3	0.00	0.04	0.00	0.05	0.00	0.00	0.00	0.09	2.30	13.43	20.40	0.00	0.01	0.01	0.00	0.02	0.04	12.68	51.48	100.54	
635J apa1	0.012	0.151	0.024	0.126	0.000	0.016	0.037	0.057	0.050	0.000	4.587	0.038	0.013	0.019	15.615	0.023	2.795	0.000	0.025	23.59	

Silicate and Oxide Electron Microprobe Data - 158 to171 grains (2066641)

Rock	Metasediment - 2066641																			
Sample ID	Si WT %	Zr WT %	Ti WT %	Zn WT %	Al WT %	V WT %	Cr WT %	Fe WT %	Mn WT %	Mg WT %	Ca WT %	Ba WT %	Na WT %	K WT %	P WT %	Cl WT %	F WT %	O WT %	H WT %	TOTAL
641A Bt1	10.74	0	0.26	0	6.33	0.03	0	30.14	0.67	0.7	0.13	0.02	0.08	3.12	0.01	0.01	0.2	28	0	80.44
641A Hem1	28.72	0.01	0.09	0	1.8	0.02	0	14.12	0.35	0.17	0.02	0.02	0	0.72	0	0.01	0.05	40.8	0	86.89
641A Hem2	0.51	0.02	0.11	0.02	0.37	0	0.01	59.57	2.68	0.03	0.06	0.04	0.04	0.04	0.02	0.02	0.36	27.32	0	91.22
641B Hem1	0.22	0	0.07	0.01	0.23	0.02	0	55.56	2.57	0	0.02	0	0.32	0.04	0.02	0.1	0.38	25.11	0	84.68
641B Hem2	0.41	0	0.06	0.01	0.3	0	0	55.72	2.17	0.01	0.06	0.01	0.06	0.04	0.04	0.05	0.34	25.32	0	84.61
641B Hem3	0	0	0.01	0	0.1	0.02	0.01	65.1	0	0	0.01	0	0.02	0	0	0	0.39	27.93	0	93.59
641B Fe1	37.05	0	0.02	0	2.97	0	0	0.81	0	0.06	0.02	0	0.05	1.21	0	0.02	0	45.42	0	87.63
641C Bt1	20.67	0.01	0.07	0	12.35	0	0	5.35	0.13	1.5	0.04	0.04	0.04	5.21	0.01	0.02	0.32	38.11	0	83.87
641C Hem1	1.49	0	0.31	0	0.54	0.01	0	57.29	2.17	0.05	0.11	0.02	0.06	0.12	0.04	0.02	0.3	27.68	0	90.22
641C Mn1	0	0	0.03	0.01	0.13	0	0	0.17	49.63	0	0.09	6.94	0.27	1.96	0.02	0.05	0.52	15.77	0	75.59
641C Mn2	0.01	0	0.02	0	0.22	0	0	0	50.4	0	0.07	7.26	0.24	2.02	0.02	0.02	0.45	16.1	0	76.83
641C Mn3	0.05	0	2.64	0	0.51	0.03	0	4.21	38.95	0	0	12.39	0.03	0.02	0	0	0.5	16.09	0	75.41
641C Mn4	0	0	0.03	0	0.13	0	0	0	49.32	0	0.07	7.99	0.18	1.56	0	0.05	0.53	15.61	0	75.48
641C Hem2	0.58	0	0.06	0.05	0.4	0	0	59.18	2.66	0.03	0.07	0.03	0.02	0.02	0.01	0.01	0.41	27.19	0	90.75

Silicate and Oxide Electron Microprobe Data – 171-191 grains (2066655)

Rock	Metasediment - 2066655																			
Sample ID	Si	Zr	Ti	Zn	Al	V	Cr	Fe	Mn	Mg	Ca	Ba	Na	K	P	Cl	F	O	H	TOTAL
	WT %	WT %	WT %	WT %	WT %	WT %	WT %	WT %	WT %	WT %	WT %	WT %	WT %	WT %	WT %	WT %	WT %	WT %	WT %	
655A cal1	0.00	0.00	0.00	0.00	0.00	0.00	0.00	3.71	6.47	9.60	21.03	0.00	0.03	0.02	0.00	0.07	0.00	17.66	58.60	117.19
655A chl1	11.57	0.00	0.00	0.03	10.38	0.00	0.00	26.57	0.28	5.47	0.01	0.00	0.02	0.00	0.00	0.00	0.08	33.69		88.11
655A chl2	11.62	0.00	0.00	0.01	9.70	0.01	0.00	24.45	0.17	6.51	0.03	0.00	0.03	0.02	0.01	0.03	0.19	33.16		85.93
655A chl3	11.77	0.00	0.00	0.01	9.26	0.01	0.00	25.09	0.52	5.81	0.03	0.00	0.04	0.01	0.01	0.01	0.19	32.78		85.54
655A cal2	0.03	0.00	0.00	0.00	0.00	0.00	0.00	4.31	5.36	9.28	21.03	0.00	0.00	0.00	0.00	0.13	0.00	17.31	57.45	114.90
655A cal3	0.00	0.00	0.00	0.00	0.00	0.00	0.00	6.23	4.70	8.18	19.94	0.00	0.00	0.00	0.00	0.07	0.00	16.48	55.60	111.21
655A hem1	0.02	0.00	0.08	0.00	0.02	0.03	0.00	67.94	0.01	0.00	0.00	0.00	0.00	0.00	0.00	0.01	0.26	19.47		87.85
655A hem2	0.73	0.02	0.01	0.00	0.25	0.00	0.00	68.87	0.00	0.11	0.10	0.00	0.02	0.14	0.00	0.02	0.29	20.83		91.39
655B chl1	12.18	0.00	0.00	0.00	9.18	0.00	0.00	22.60	0.06	7.75	0.06	0.00	0.10	0.04	0.04	0.04	0.10	33.71		85.86
655B hem1	0.31	0.00	0.05	0.00	0.10	0.00	0.01	69.28	0.02	0.00	0.06	0.00	0.03	0.02	0.00	0.02	0.27	20.27		90.45
655B chl2	11.49	0.00	0.01	0.00	10.01	0.01	0.00	23.73	0.11	6.60	0.01	0.00	0.03	0.01	0.01	0.03	0.26	33.10		85.41
655B hem2	0.32	0.00	0.55	0.00	0.15	0.00	0.01	66.94	0.02	0.00	0.05	0.00	0.08	0.07	0.00	0.02	0.21	20.02		88.43
655B chl3	12.14	0.00	0.01	0.00	9.55	0.00	0.01	23.32	0.06	7.59	0.00	0.00	0.04	0.02	0.00	0.06	0.07	34.02		86.89
655B chl4	12.20	0.02	0.00	0.00	8.99	0.01	0.01	22.87	0.06	7.76	0.01	0.00	0.33	0.03	0.00	0.16	0.13	33.61		86.17
655B chl5	11.57	0.00	0.01	0.00	9.74	0.00	0.00	23.93	0.22	6.38	0.05	0.00	0.07	0.05	0.03	0.09	0.15	32.99		85.27
655B hem3	0.02	0.00	0.06	0.00	0.17	0.01	0.00	67.81	0.00	0.02	0.01	0.00	0.00	0.00	0.00	0.00	0.20	19.59		87.90
655C hem1	0.52	0.00	0.00	0.00	0.04	0.01	0.00	69.52	0.01	0.02	0.04	0.00	0.03	0.03	0.00	0.01	0.21	20.50		90.94
655C chl1	13.17	0.00	0.01	0.07	9.07	0.00	0.00	23.36	0.69	5.96	0.02	0.00	0.08	0.04	0.02	0.01	0.18	33.91		86.57
655C chl2	11.85	0.00	0.00	0.00	9.12	0.00	0.00	22.75	0.11	7.51	0.01	0.00	0.04	0.01	0.00	0.03	0.18	33.06		84.68
655C chl3	11.10	0.00	0.00	0.01	9.92	0.00	0.00	26.06	0.38	5.15	0.06	0.00	0.61	0.08	0.00	0.02	0.07	32.67		86.12

Silicate and Oxide Electron Microprobe Data – 192-203grains (2066656)

Rock	Granite - 2066656																			
Sample ID	Si WT %	Zr WT %	Ti WT %	Zn WT %	Al WT %	V WT %	Cr WT %	Fe WT %	Mn WT %	Mg WT %	Ca WT %	Ba WT %	Na WT %	K WT %	P WT %	Cl WT %	F WT %	O WT %	H WT %	TOTAL
656A Mus1	21.55	0	0.05	0	14.98	0	0	4.46	0.13	0.9	0.04	0.08	0.07	7.86	0	0.02	0	41.48	0	91.64
656A Mus2	20.36	0	0.15	0.02	13.9	0	0	7.52	0.24	0.9	0.05	0.06	0.06	7.3	0	0.03	0	40.02	0	90.63
656AMus3	22.94	0.02	0.02	0.03	16.43	0.01	0	2.06	0.11	0.7	0.11	0.06	0.1	7.74	0	0.01	0	43.54	0	93.88
656A Chl1	8.35	0	0.38	0	7.18	0	0	32.21	1.35	6.34	0.13	0	0.03	0.19	0.02	0	0	30.06	0	86.22
656A Ilm1	0.01	0.02	32.31	0.01	0	0.28	0	29.41	0.08	0	0.02	0.47	0.33	0.01	0	0.19	0	30.32	0	93.48
656B Hem1	0.09	0	0.36	0	0.29	0.07	0	66.43	0	0.02	0.01	0.02	0.02	0.02	0	0.01	0	29.21	0	96.54
656BRut1	0.05	0.01	42.41	0	0	0.24	0	17.77	0.06	0	0.06	0.56	0.02	0.01	0.01	0.04	0	33.71	0	94.95
656B Fel1	22.51	0	0.01	0	16.05	0	0	2.41	0.15	0.81	0.16	0.15	0.07	7.81	0	0	0	42.9	0	93.02
656B Hem2	0.52	0	0.08	0	0.36	0.13	0.12	64.76	0.03	0.04	0.06	0.01	0.12	0.12	0.01	0.05	0	29.04	0	95.45
656B Ilm2	0.03	0	31.63	0	0.01	0.16	0	31.33	0.12	0	0.02	0.42	0.02	0.02	0	0.02	0	34.8	0	98.57
656B Hem3	0.51	0	0.14	0	0.41	0.09	0.09	64.65	0.04	0.03	0.05	0	0.17	0.16	0	0.09	0	29.03	0	95.47
656B Mon1	13.78	0.11	0.15	0.45	0.7	0.09	0.13	2.74	0.16	0.08	0.33	0.34	0.08	0.44	8.06	0.09	0	28.24	0	55.98

Electron Microprobe Data (continued) - S minerals - 204 to 234grains (2066635 to 2066203)

Sample ID	Mineral	Fe WT %	Co WT %	Cu WT %	S WT %	As WT %	Bi WT %	TOTAL
2066166 B1	Chalcopyrite	29.929	0.018	34.76	36.668	0.0207	0	101.40
2066169A1	Pyrite	47.999	0.134	0.01	55.204	0	0	103.347
2066169A2	Pyrite	47.028	0.18	0	55.248	0	0	102.456
2066169A3	Pyrite	47.349	0.223	0.018	55.247	0.039	0	102.877
2066169B1	Pyrite	41.512	0.1743	0.102	33.321	0.001	0	75.11
2066169B1	Chalcopyrite	29.431	0.015	33.945	36.412	0	0	99.804
2066169B2	Pyrite	41.321	0.167	0.105	33.215	0.001	0	74.81
2066169B3	Pyrite	41.541	0.211	0.106	33.481	0.001	0	75.34
2066203A1	Chalcopyrite	24.284	0.045	25.787	26.018	0	0	76.135
2066203A1	Sphalerite	1.263	0.002	0.058	24.188	0	0	25.51
2066203A2	Chalcopyrite	28.405	0.028	30.978	31.384	0.003	0	90.796
2066203A2	Sphalerite	3.295	0	0.204	24.233	0	0	27.731
2066203D1	Chalcopyrite	29.266	0.023	33.751	36.411	0.003	0	99.455
2066203D2	Chalcopyrite	29.42	0.011	34.073	36.534	0.009	0	100.046
2066203D3	Chalcopyrite	29.507	0.034	33.997	36.652	0.063	0	100.252
2066635B1	Pyrite	43.044	0.049	0.643	43.836	0.018	0	87.59
2066635B1	Bornite	11.007	0.021	52.073	23.634	0	0	86.735
2066635B2	Pyrite	42.326	0.057	0.347	43.345	0.049	0	86.125
2066635B2	Bornite	13.11	0.008	49.296	21.627	0.045	0.011	84.096
2066635F1	Bornite	11.781	0.032	52.418	23.884	0.007	0	88.121
2066635F1	Sphalerite	0.787	0	3.838	20.911	0.005	0	25.541
2066635F2	Bornite	10.736	0.021	55.702	21.495	0	0	87.953
2066635G1	Bornite	10.3	0.017	57.65	20.279	0	0.014	88.259
2066635G2	Bornite	10.054	0.016	57.502	19.632	0.017	0	87.22
2066635G3	Bornite	10.318	0.009	57.583	19.933	0	0	87.843
2066635J 1	Chalcopyrite	2.238	0.025	11.57	13.574	0	0	27.406
2066655A1	Pyrite	41.444	0.22	0.121	33.492	0.001	0	75.279
2066655A1	Chalcopyrite	26.937	0.036	30.893	23.341	0.022	0	81.228
2066655A2	Pyrite	41.872	0.055	0.017	34.112	0.065	0	76.122
2066655A3	Pyrite	41.907	0.14	0.067	34.458	0	0	76.572
2066655B1	Chalcopyrite	4.747	0.077	4.7	17.453	0.027	0	27.004

Appendix 4: The LA-ICPMS Analysed Data

Table IV. The Co/Ni ratio of pyrite in the rocks

Rock	Element	Na23	S33	S34	Fe57	Co59	Ni60	Co/Ni
Calc-silicate	166E-1	12.81	460493.3	498067	463899	271	674	0.40
Calc-silicate	166E-2	483.79	488143.8	497556	463899	85	351	0.24
Granite	169A-01	1.15	485784.9	490959	474937	1053	2586	0.41
Granite	169A-02	1.2	485375.6	478992	474937	1228	2716	0.45
Granite	169A-03	1.37	461690.2	473135	474937	533	3006	0.18
Granite	169B-08	0.94	437807	429420	414929	5785	1323	4.37
Granite	169B-09	0.93	416091.6	418973	414929	5581	927	6.02
Granite	169B-10	0.96	435447.5	447938	414929	3674	1700	2.16
Metasediment	655A-02	6.56	431613	429052	414401	769	82	9.42
Metasediment	655A-03	3.86	434667.9	419427	418701	381	39	9.75
Metasediment	655A-04	40.01	450154.5	425459	418701	208	57	3.63
Metasediment	655A-05	6.27	426577.1	429019	419061	380	266	1.43
Metasediment	655A-06	3.74	418135.4	427685	419061	397	624	0.64

Table V. Trace elements of 24 hematite grains of calc-silicate, granite and metasediments.

Rock	N	Na23	Ca43	Ti49	Cr53	Mn55	Fe57	Co59	Ni60	Cu65	Zn66
Calc-silicate	1	169	315	5176	18	2252	642401	58	13	85	225
Granite	10	177	468	48062	237	831	661775	25	135	116	226
Metasediment	13	1788	2045	2038	27	56977	635586	157	21	581	356
Rock		Ga69	Sr88	Zr90	Nb93	Ba137	Ta181	W182	Pb208	Bi209	U238
Calc-silicate	1	6	4	24	18	25	1.4	28	24	0.1	10
Granite	10	12	5	5	328	46	42.5	46	79	5.5	6
Metasediment	13	518	42	23	9	13104	0.6	12	624	6.5	13

Notes: The element value is at ppm in the average. N=10 (ten hematite grains).

Silicate analyzed data (133) – 1 to 12 grains (2066166 to 1066169)

Rock	Calc-silicate-2066166							Granite-2066169				
Sample ID	166B-9	166B-10	166B-11	166B-12	166E-1	166E-2	166E-3	169A-7	169A-8	169B-5	169B-6	169B-7
Mineral	Garnet			Chlorite				Chlorite				
Na23	89.82	222.05	168.18	137.94	96.77	121.66	57.68	28.56	28.82	53.58	89.37	48.1
Mg25	7780.9	3608.1	9131	21639.	47245.9	23430.1	1266.67	121581	125119	118903	116401	117199
Al27	10112.0	24118.1	20044.2	32794.8	89557.9	38155.2	5566.48	112051	111734	115175	105473	106667
Si29	170008	170008	119992	119992	119992	119992	119992	127985	127985	127985	127985	127985
P31	25.77	68.54	20.44	15.41	31.14	23.08	11.93	27.68	36.42	35.57	26.66	37.37
S34	154.87	438.91	118.39	151.78	290.74	265.91	186.53	248.84	306.76	282.75	272.09	284.2
K39	47.72	28.04	84.48	62.11	64.92	74.38	23.49	41.18	42.73	133.97	178.12	124.68
Ca43	647.11	231850	787.85	1398.79	525.22	100017	74708.7	449.18	319.99	290.55	377.08	333.07
Ti49	50.88	1131.4	313.26	45.56	9.42	347.57	218.6	157.98	190.54	133.34	98.15	169.73
V51	11.43	189.08	26.21	26.65	54.58	70.51	32.56	44.8	38.64	49.84	34.18	40.06
Cr53	1.66	6.21	<1.17	<1.37	4.15	3.92	<1.36	<2.65	<2.99	<3.04	<2.64	3.37
Mn55	3205.6	10329	5367.53	10309.3	27735.2	14643.7	3720.61	997.33	894.54	2019.52	1100.11	1042.44
Fe57	13797	74078	20139	36378.2	80661.7	70480.1	22915.5	51190	49740.6	53421.0	48830.6	48106
Co59	13.31	1.84	25.97	40.86	116	49.49	1.98	174.82	113.58	206.31	160.56	125.33
Ni60	7.05	1.68	11.31	23.11	55.77	24.84	1.32	1124.76	1456.59	1689.25	1603.59	1301.27
Cu65	437.41	641.65	112.87	256.5	180.28	163.26	8.51	11.73	7.52	21.93	19.29	9.49
Zn66	169.64	25.04	301.23	497.21	913.18	516.36	21.9	619.98	457.33	796.14	685.28	391.95
Ga69	4.43	10.65	8.52	14.42	33.69	20.69	5.42	61.36	59.92	62.07	60.25	57.63
Ge73	1.24	2.34	0.86	<0.62	1.3	2.18	2.29	4.36	5.95	3.97	6.31	6.26
As75	5.91	38.03	1.66	9.94	3.94	15.25	5.11	<0.78	1.1	1.38	2.1	1.28
Se82	<3.89	<10.22	<4.15	<5.14	<10.09	<9.08	<5.02	<10.74	<10.50	<10.34	<9.82	<9.50
Rb85	0.186	0.155	0.377	0.269	0.263	0.236	0.394	0.73	0.8	0.63	0.87	1.13
Sr88	1.88	2.37	5.98	1.26	0.86	0.76	0.396	0.336	0.503	0.439	0.51	0.185
Y89	2.64	234.89	2.2	3.08	1.08	20.13	29.25	0.138	0.091	0.124	0.182	0.055
Zr90	0.55	29.19	2.29	0.48	0.45	5.42	2.72	<0.127	<0.146	<0.137	<0.080	<0.110
Nb93	0.182	3.36	0.47	0.286	<0.068	2.01	1.26	<0.077	<0.040	<0.064	<0.068	<0.00
Mo95	<0.16	0.96	<0.14	0.42	0.33	<0.26	0.15	0.17	0.17	<0.47	<0.19	<0.26
Ag107	0.018	<0.104	0.055	<0.043	0.089	0.232	<0.022	<0.116	<0.106	<0.071	0.078	<0.090
Sn118	3.49	32.28	16.68	5.2	4.79	26.29	8.75	2.32	2.24	2.25	2.42	2.1
Sb121	0.437	1.53	0.53	0.6	<0.127	0.47	0.377	0.134	0.175	0.111	0.129	<0.084
Te125	<0.00	<0.00	<0.00	<0.00	<0.00	<0.00	<0.00	<0.00	<0.00	<0.00	<0.00	<0.00
Ba137	1.61	5.83	6.59	4.45	1.77	2.32	1.31	0.97	5.9	4.88	5.11	1.39
La139	0.536	22.36	0.08	0.95	0.206	1.86	0.543	0.093	0.076	0.057	<0.037	0.033
Ce140	1.63	76.21	0.99	2.74	0.659	13.73	6.36	0.202	0.081	0.063	0.058	0.04
Pr141	0.225	9.45	0.053	0.373	0.145	5.04	2.69	<0.0132	0.021	<0.025	0.032	<0.023
Nd146	1.34	46.17	0.063	2.03	0.46	34.76	22.42	<0.106	<0.134	3.7	0.102	<0.092
Sm147	0.38	12.77	0.082	0.43	0.109	7.88	7.47	<0.151	0.069	<0.187	<0.109	<0.106
Eu153	0.072	2.61	0.032	0.126	0.059	2.61	1.44	<0.021	<0.022	0.016	<0.019	<0.018
Gd157	0.39	20.65	0.26	0.66	0.22	4.33	5.65	<0.00	<0.126	0.032	0.118	<0.150
Tb159	0.051	4.56	0.061	0.058	0.025	0.663	0.869	0.0095	<0.025	<0.0168	<0.0109	<0.0151
Dy163	0.35	35.36	0.76	0.55	0.16	3.71	5.35	0.093	<0.050	<0.047	0.086	<0.073
Ho165	0.09	7.71	0.12	0.085	0.053	0.634	1.12	<0.021	<0.0177	<0.0166	<0.0108	<0.00
Er166	0.162	25.7	0.228	0.236	<0.055	2.68	3.24	<0.072	0.014	<0.049	<0.063	0.052
Tm169	0.058	3.68	0.057	0.045	<0.0169	0.282	0.474	<0.0156	0.0131	<0.0150	<0.020	<0.0191
Yb172	0.28	24.88	0.222	0.285	<0.043	1.64	3.8	<0.070	<0.113	<0.082	0.034	<0.043
Lu175	0.042	3.51	0.082	0.046	0.032	0.272	0.541	<0.0161	<0.00	0.0084	<0.0101	0.0076
Hf178	<0.018	0.398	0.111	<0.00	0.085	0.094	0.047	<0.072	<0.042	<0.040	<0.052	<0.050
Ta181	0.028	0.141	0.031	<0.0100	0.022	0.149	0.101	<0.0144	0.024	0.027	<0.022	<0.0176
W182	0.73	24.9	0.096	1.4	<0.113	5.56	0.417	<0.126	<0.065	<0.121	<0.111	0.088
Au197	<0.0160	<0.037	<0.031	<0.025	<0.073	<0.00	<0.016	<0.037	<0.066	<0.051	0.041	<0.056
Hg202	<0.00	<0.00	<0.00	<0.00	<0.00	<0.00	<0.00	<0.00	<0.00	<0.00	<0.00	<0.00
Pb208	12.47	8.3	12.4	46.34	67.46	66.05	4.32	12.07	8.47	12.59	12.05	4.68
Bi209	0.213	0.176	0.0098	0.032	0.021	0.067	<0.0125	<0.0293	<0.0213	<0.0244	0.036	<0.0200
Th232	0.097	3.37	0.0149	0.139	<0.0144	0.724	0.329	<0.0162	0.0045	<0.0191	0.0125	<0.0140
U238	0.724	7.93	0.309	1.174	0.326	5.26	1.98	0.046	0.0115	0.096	0.074	0.04

Silicate analyzed data (133) – 13 to 21 grains (2066174)

Rock	Granite -2066174								
Sample ID	174A-01	174A-02	174A-03	174A-05	174A-07	174B-02	174B-04	174C-03	174C-04
Mineral	Calcite			White Mica	Kfeldspar	Apatite		Kfeldspar	
Na23	127.25	3123.07	2505.21	1481.71	1579.85	781.89	562.43	6135.18	4286.1
Mg25	143894.8	139908.3	140645.2	36336.18	35295.82	23034.91	263854.7	3812.39	2595.43
Al27	10.74	186.36	263.17	114177.2	165024.2	55745.07	120.61	34436.3	27696.85
Si29	918.66	11793.94	10099.96	219999.8	301999.4	93030.56	2890.4	119999.6	119999.6
P31	26.28	27.82	34.04	23.37	214.71	62792.02	78.88	17.24	14.23
S34	232.37	258.19	221.1	<140.88	586.33	397.37	470.46	125.12	136.87
K39	12.56	119.77	109.69	66017.78	92055.23	25977.55	42.13	19534.7	15207.06
Ca43	209979.1	209979.1	209979.1	1420.7	2860.55	383800.8	383800.8	4153.05	2795.21
Ti49	4.65	27.78	28.08	6734.87	5917.88	3214.41	9.41	91.69	72.35
V51	5.2	26.26	49.21	246.44	455.23	133.07	38.71	25.72	15.39
Cr53	<2.00	<1.93	<2.07	52.29	78.55	14.35	<3.62	9.73	3.21
Mn55	34953.98	33424.99	41052.05	2002.66	2321.62	1399.49	69070.36	42.11	32.76
Fe57	278.78	1787.35	4354.93	170824.4	215617.6	98781.02	9186.59	2154.74	1586.88
Co59	8.33	8.36	15.14	64.41	54.79	15.27	13.96	2.11	1.307
Ni60	1.66	0.82	0.81	60.26	59.56	12.69	<0.67	3.92	1.43
Cu65	4.96	21.28	105.88	50.26	52.37	34.63	11.61	8.91	3.58
Zn66	66.83	54.64	165.02	413.3	348.04	205.38	145.31	54.11	9.75
Ga69	<0.073	0.287	0.18	93.19	134.02	47.89	0.157	13.2	15.89
Ge73	0.71	<0.72	<1.17	7.06	11.29	23.14	1.71	1.41	0.86
As75	1.11	9.12	16.4	29.4	43.15	129.5	18.22	3.28	1.38
Se82	<7.08	<7.76	<7.91	<20.99	<22.56	20.97	<13.76	<6.02	<5.11
Rb85	0.068	0.76	0.65	2071.5	1716.65	351.53	<0.140	171.04	110.86
Sr88	102.74	85.58	108.6	15.22	30.65	230.26	177.97	5.79	5.19
Y89	19.2	21.27	29.1	6.27	7.75	370.36	65.85	0.721	0.263
Zr90	0.232	7.13	6.12	11.76	16.44	15.39	3.11	8.76	5.31
Nb93	<0.036	0.083	0.209	15.16	21.53	13.64	<0.066	0.383	0.886
Mo95	1.54	0.92	2.17	2.82	1.32	3.81	3.89	<0.120	0.092
Ag107	<0.035	<0.035	<0.082	<0.089	<0.183	0.163	<0.128	<0.041	<0.041
Sn118	<0.36	0.82	0.6	4.1	7.94	1.47	<0.70	3.47	1.84
Sb121	0.211	1.14	4.32	8.24	15.63	10.2	1.42	0.637	0.627
Te125	<0.00	<0.00	<0.00	<0.00	<0.00	<0.00	<0.00	<0.00	<0.00
Ba137	1.47	7.27	5.65	1176.02	1747.62	672.41	2.28	154.27	276.72
La139	6.26	6.7	9.74	15.1	24.44	307.56	13	12.18	0.415
Ce140	16.86	18.24	19.79	28.86	51.32	572.72	30.08	27.82	0.842
Pr141	2.57	2.88	2.96	3.3	5.83	129.43	4.84	2.69	0.09
Nd146	12.29	13.32	13.29	12.78	18.4	668.45	26.7	10.28	0.342
Sm147	4.36	5.9	4.91	2.66	4.27	189.33	11.44	1.52	0.082
Eu153	1.38	1.42	1.35	0.71	1.2	29.23	3.32	0.22	0.027
Gd157	6.38	7.06	7.29	3.87	5.54	176.2	17.45	0.82	<0.058
Tb159	0.786	0.958	1.084	0.633	0.734	19.67	2.79	0.079	0.0149
Dy163	4.31	4.76	5.61	3.07	3.08	92.07	14.52	0.16	0.042
Ho165	0.637	0.843	0.979	0.342	0.295	12.85	2.48	0.0252	<0.0110
Er166	1.43	1.43	2.32	0.96	0.96	24.34	5.81	0.07	<0.026
Tm169	0.17	0.188	0.194	0.08	0.116	2.25	0.618	0.0123	0.0126
Yb172	0.74	1.13	1.62	0.53	0.73	8.9	4.08	0.088	0.057
Lu175	0.137	0.129	0.234	0.099	0.079	0.92	0.557	<0.0105	<0.0108
Hf178	<0.027	0.203	0.302	0.97	1.81	0.82	0.186	0.386	0.166
Ta181	<0.0191	<0.0166	<0.017	1.99	2.63	0.509	<0.030	0.074	0.159
W182	<0.093	0.305	1.23	27.25	45.74	37.54	0.9	0.125	0.4
Au197	<0.035	<0.035	<0.037	0.024	<0.076	<0.083	<0.046	<0.056	<0.041
Hg202	<0.00	<0.00	<0.00	<0.00	<0.00	<0.00	<0.00	<0.00	<0.00
Pb208	5.63	11	16.61	122.76	133.47	143.7	10.47	2.43	1.37
Bi209	<0.0138	0.369	1.53	1.76	2.11	1.02	3.07	0.071	0.042
Th232	3.47	12.29	11.87	37.99	69.58	57.73	18.33	2.28	0.41
U238	0.185	1.025	2.51	15.7	24.7	84.62	1.2	0.159	0.079

Silicate analyzed data (133) – 22 to 41 grains (2066177)

Rock	Amphibolite-2066177									
Sample ID	177B-06	177B-07	177B-08	177B-11	177B-16	177C-02	177C-05	177C-07	177C-08	177C-12
Mineral	Chlorite			Diopside		Chlorite				
Na23	155.45	231.86	111.71	45190.76	6733.97	1231.92	124.86	52.4	48.44	48.17
Mg25	84370.05	90160.91	86673.22	188026.3	220919.2	86922.77	84087.08	91811.28	90952.48	82022.74
Al27	108620.4	109096	110644	10327.24	1456.22	106676	100147	109345.1	108398.6	99571.53
Si29	120199.7	120199.7	120199.7	169999.7	24231.84	122999.6	122999.7	119999.6	119999.6	106500
P31	35.11	21.24	34.09	142.04	47.88	30.29	28.81	25.05	24.93	24.59
S34	300.09	219.54	215.62	574.8	204.13	322.05	185.8	279.28	251.52	279.32
K39	672	350.75	506.91	6686.97	641.55	671.84	512.28	312.28	267.42	229.77
Ca43	307.34	522.97	337.41	441422.3	383800.8	1293.16	873.88	384.25	350.9	311.79
Ti49	199.71	165.25	242.04	210.92	7.89	228.6	2869.85	253.49	290.71	192.75
V51	309.45	301.82	290.36	313.9	8.72	294.34	289.51	280.15	268.86	261.23
Cr53	<3.38	4.99	<3.22	4.73	<4.31	28.31	27.14	14.22	19.34	5.2
Mn55	4062.74	4139.12	3977.59	38426.39	40119.17	3885.31	4069.9	3744.37	3650.7	3312.01
Fe57	72176.55	68886.72	71275.16	59352.4	1426.1	67827.76	66162.62	68681.71	67370.45	61909.62
Co59	65.63	86.68	69.78	12.21	18.83	48.76	55.29	53.76	51.21	49.34
Ni60	101.12	83.8	92.91	1.52	1.05	110.81	98.07	86.92	81.99	89.37
Cu65	36.38	59.62	28.37	14.61	5.43	10.67	9.86	5.46	4.62	6.97
Zn66	552.41	609.51	526.77	45.3	48.78	409.72	580.31	402.62	364.09	338.43
Ga69	50.39	54.37	53.78	8.41	1.64	50.58	46.98	52.91	50.21	48.11
Ge73	1.44	1.77	2.36	13.79	2.76	<1.19	<1.01	1.99	<1.14	<0.80
As75	<0.76	1.3	<0.67	21.68	7.01	<0.79	0.93	<0.75	0.69	<0.67
Se82	<10.21	<10.37	<10.91	<19.54	<13.93	<10.72	<10.06	<11.25	<9.88	<9.93
Rb85	9.64	3.96	5.29	107.72	9.04	10.96	5.19	3.26	2.6	3.13
Sr88	1.08	1.53	0.93	245.64	85.86	1.35	1.03	0.521	0.38	0.463
Y89	0.434	0.169	0.28	334.02	120.81	0.259	0.66	0.074	<0.047	0.065
Zr90	0.188	<0.098	0.159	47.31	9.39	2.32	7.96	<0.104	<0.082	<0.077
Nb93	<0.078	<0.067	<0.00	0.55	<0.071	<0.033	2.1	0.076	<0.059	<0.032
Mo95	0.34	<0.32	<0.39	10.67	1.23	0.45	<0.31	0.09	<0.189	<0.176
Ag107	<0.048	<0.066	<0.109	1.14	<0.172	<0.047	<0.079	<0.099	<0.048	<0.045
Sn118	<0.52	0.61	<0.49	7.63	1.58	1.17	<0.43	<0.48	0.47	<0.47
Sb121	0.225	<0.075	0.181	5.4	0.21	0.132	0.111	0.049	0.1	<0.083
Te125	<0.00	<0.00	<0.00	<0.00	<0.00	<0.00	<0.00	<0.00	<0.00	<0.00
Ba137	3.81	4.23	3.64	72.74	56.48	5.1	4.26	1.58	2.37	1.7
La139	0.14	0.14	0.074	281.63	145.62	0.189	0.085	0.061	<0.029	0.062
Ce140	0.351	0.172	0.142	615.74	278.9	0.408	0.334	0.122	0.056	0.79
Pr141	0.037	<0.026	0.037	76.79	32.93	0.029	0.067	<0.0122	0.014	0.0161
Nd146	0.141	0.094	0.142	336.85	145.06	0.207	0.25	<0.099	0.083	<0.109
Sm147	<0.080	<0.108	<0.114	88.99	34.02	<0.108	0.17	0.075	<0.078	<0.126
Eu153	<0.033	0.021	0.049	34.6	11.47	<0.0181	<0.040	<0.019	<0.0185	<0.030
Gd157	<0.111	0.17	0.122	102.79	33.13	0.087	0.17	0.135	0.079	<0.072
Tb159	<0.019	0.0124	<0.016	14.98	4.6	<0.0215	<0.018	<0.0114	<0.0155	<0.0205
Dy163	<0.077	0.025	<0.090	74.81	24.62	0.085	<0.059	0.042	0.067	<0.058
Ho165	0.014	0.036	0.0115	11.07	3.75	<0.0151	<0.018	<0.0196	<0.0155	0.0109
Er166	0.067	<0.044	0.041	22.61	9.89	<0.044	0.141	<0.066	<0.055	<0.042
Tm169	<0.0142	<0.0167	<0.0143	2.43	0.801	<0.0166	<0.013	<0.0177	<0.0139	0.0033
Yb172	<0.064	0.025	<0.064	12.41	5.18	<0.075	<0.059	<0.079	<0.062	<0.071
Lu175	<0.0104	<0.0172	0.0128	1.57	0.708	<0.0242	<0.0167	<0.0105	<0.0175	<0.0164
Hf178	0.046	0.062	<0.053	1.69	0.37	<0.086	0.34	<0.00	<0.051	<0.00
Ta181	0.016	<0.025	<0.00	0.067	<0.037	0.025	0.088	0.014	0.019	<0.0167
W182	0.51	<0.093	<0.137	9.18	0.6	0.162	0.238	<0.056	<0.093	0.16
Au197	<0.035	<0.047	<0.061	<0.00	<0.100	<0.033	<0.033	0.016	<0.048	0.045
Hg202	<0.00	<0.00	<0.00	<0.00	<0.00	<0.00	<0.00	<0.00	<0.00	<0.00
Pb208	2.44	2.16	1.75	15.14	7.22	4.11	1.34	1.18	0.267	0.9
Bi209	0.036	0.031	<0.027	0.693	0.053	<0.0128	0.044	0.0104	<0.021	<0.0194
Th232	0.162	0.06	0.062	3.03	0.43	0.031	0.14	0.0113	<0.00	0.0143
U238	0.255	0.101	0.121	2	0.108	0.055	0.145	0.028	<0.0136	0.0264

To be continued

Rock	Amphibolite										
Sample ID	177C-13	177C-14	177C-15	177A-01	177A-02	177A-03	177A-04	177A-05	177A-06	177A-07	
Mineral	Chl			Dol	Chl					Kfel	Dol
Na23	32.75	36.96	28.34	25383.76	329.03	64.17	83.98	2014.58	10422.03	82236.52	
Mg25	80105.07	42937.24	41872.25	145939	91375.19	88606.09	88560.34	84068.02	64170.89	1663971	
Al27	97011.78	51375.9	52565	717.16	110936.8	110846	115708.1	89683.4	166566.5	14796.1	
Si29	106500	56092.72	56092.72	84858.68	119999.6	119999.6	119999.6	119999.6	299999.8	299999.8	
P31	20.62	16.23	15.45	40.74	27.76	27.4	27.47	19.08	39.54	311.76	
S34	298.05	124.53	137.15	295.46	296.49	271.09	334.1	332.35	514.14	4459.09	
K39	215.48	122.35	287.48	867.15	960.04	683.82	331.47	618.34	78203.82	35120.11	
Ca43	282.21	353.37	185.59	252600.3	852.21	9583.06	330.25	22691.09	11228.05	3331921	
Ti49	152.07	96.3	93.64	40.56	321.45	194.13	162.89	184.68	222.72	145.45	
V51	254.98	148.56	148.69	1.37	288.31	288.79	273.46	262.86	799.43	108.19	
Cr53	2.57	<1.33	<1.30	<2.35	<3.21	<3.33	<2.65	<2.99	23.28	<32.14	
Mn55	3216.8	1793.18	1849.41	22924.73	3840.49	4609.91	4121.15	5735.6	2832.67	363721.8	
Fe57	62470.19	32292.92	34454.27	1248.63	69143.86	69923.29	74383.01	58341.66	40363.09	84263.66	
Co59	44.26	32.79	28.8	10.17	75.02	79.25	58.74	55.84	57.69	29.91	
Ni60	90.89	43.95	47.07	1.21	81	97.87	104.55	86.84	52.01	15.88	
Cu65	7.5	11.63	2.47	5.1	16.45	13.77	27.72	24.32	60.39	41.03	
Zn66	299.96	232.3	185.84	226.5	447.42	612.48	416.19	439.9	617.54	235.61	
Ga69	49.05	24.21	25.04	1.82	53.03	52.4	53.61	42.76	66.63	14.98	
Ge73	<0.96	<0.77	<0.58	2.03	<1.54	<1.30	<1.54	1.75	<2.05	88.27	
As75	0.82	<0.34	<0.42	1.69	<0.78	1.04	<0.63	<0.69	<1.04	22.06	
Se82	<10.48	<5.24	5.77	<11.42	<11.58	<11.02	<11.59	<10.27	<16.98	<124.14	
Rb85	3.87	1.69	4.59	3.91	10.16	9.85	5.61	9.99	1503.91	164.08	
Sr88	0.303	0.343	0.371	62.86	1.48	2.03	0.66	18.88	10.58	2015.81	
Y89	0.063	0.122	0.067	62.12	0.109	0.8	0.093	26.14	4.76	3340.56	
Zr90	<0.053	<0.041	0.054	26.19	1.27	<0.059	0.127	2.84	17.9	77.03	
Nb93	<0.044	0.0098	0.046	0.091	<0.070	<0.096	<0.052	0.067	<0.102	0.82	
Mo95	<0.24	<0.094	0.18	0.44	<0.33	0.33	<0.20	<0.37	<0.63	5.54	
Ag107	0.018	<0.042	<0.032	<0.092	0.019	0.075	<0.052	<0.068	<0.15	<0.83	
Sn118	<0.41	0.24	<0.20	3.52	0.81	<0.48	<0.46	1	15.63	12.58	
Sb121	0.106	0.057	0.077	0.15	0.198	0.101	0.028	0.41	1.53	1.58	
Te125	<0.00	<0.00	<0.00	<0.00	<0.00	<0.00	<0.00	<0.00	<0.00	<0.00	
Ba137	0.66	0.84	1.53	34.7	8.24	5.14	2.4	6.31	80.91	138.21	
La139	<0.034	0.014	0.142	71.17	0.151	1.13	0.071	21.98	3.55	2153.19	
Ce140	0.101	0.051	0.255	163.64	0.558	2.49	0.113	47.1	7.03	4649.87	
Pr141	<0.019	<0.0083	0.037	20.14	0.064	0.334	<0.013	5.79	0.88	631.2	
Nd146	0.051	<0.058	0.054	79.75	0.118	1.06	<0.103	27.11	4.1	2842.67	
Sm147	0.097	0.045	<0.052	15.12	<0.161	0.35	<0.119	6.33	1.41	789.48	
Eu153	0.021	<0.016	0.015	6.4	0.031	0.14	<0.00	2.9	0.48	333.14	
Gd157	0.192	0.099	0.092	20.14	<0.112	0.39	<0.083	8.7	1.45	1064.65	
Tb159	<0.0141	<0.0095	0.0118	2.14	0.027	0.019	0.0068	1.17	0.142	148.7	
Dy163	<0.069	0.013	<0.036	11.17	<0.064	0.212	0.189	5.42	1.12	744.18	
Ho165	0.0136	<0.0094	0.0073	1.62	<0.0160	0.019	0.0136	0.87	0.181	111.52	
Er166	<0.0292	0.0092	<0.026	3.88	<0.033	0.056	0.049	1.68	0.251	226.38	
Tm169	<0.0127	<0.0085	<0.0046	0.4	<0.0203	0.022	0.0061	0.147	0.041	21.83	
Yb172	<0.070	<0.0220	<0.0295	1.68	<0.046	0.086	<0.067	1.19	0.27	122.29	
Lu175	<0.0130	0.0072	<0.0068	0.248	<0.0104	<0.0143	0.0126	0.138	0.051	15.08	
Hf178	<0.00	<0.0310	<0.038	0.57	<0.037	<0.036	<0.00	0.117	1.68	3.84	
Ta181	<0.0163	<0.0126	<0.0060	0.025	0.01	<0.0178	0.016	0.021	0.093	<0.152	
W182	0.067	<0.060	0.304	<0.082	0.084	0.027	0.081	0.158	0.8	<1.27	
Au197	<0.062	<0.0296	<0.032	0.104	<0.036	0.018	<0.037	<0.034	<0.052	<0.59	
Hg202	<0.00	<0.00	<0.00	<0.00	<0.00	<0.00	<0.00	<0.00	<0.00	<0.00	
Pb208	0.575	0.519	1.68	6.48	2.06	1.84	1.66	3.02	12.35	32.46	
Bi209	<0.0190	<0.0080	0.049	0.041	0.03	0.047	<0.025	0.07	0.095	<0.25	
Th232	0.0137	0.0246	0.121	1.22	0.027	0.098	0.031	0.86	1.37	13.66	
U238	0.036	0.0314	0.163	0.191	0.048	0.0136	0.048	0.155	0.515	0.81	

Silicate analyzed data (133) – 42 to 57 grains (2066178)

Rock	Granite-2066178							
Sample ID	178A-01	178A-02	178A-05	178A-06	178A-07	178A-08	178A-09	178B-01
Mineral	Biotite		Feldspar	Chlorite	Feldspar		Biotite	
Na23	455.45	357.79	61765.18	384.94	57171.73	53435.62	436.43	517.98
Mg25	54123.57	56170.78	1610.94	54265.14	1666.04	1806.45	60535.42	55465.46
Al27	86300.52	87936.27	124263.7	87821.5	128373.6	134134.4	85992.7	88773.59
Si29	159999.9	159999.9	289999.4	159999.9	289999.4	289999.4	159999.9	164999.6
P31	33.49	33.54	39.62	23.07	41.05	43.36	40.4	31.61
S34	261.76	511	554.32	455.99	348.48	404.57	427.79	504.57
K39	78882.88	80468.46	19666.21	78432.48	26641.37	38222.64	75202.98	79860.5
Ca43	295.14	<178.55	14977.56	<226.69	13572.31	6799.15	1129.48	<240.79
Ti49	15085.56	14298.57	<7.97	14015.7	9.95	79.87	10418.17	18831.68
V51	294.62	271.94	<0.203	237.14	<0.173	6.7	164.56	327.58
Cr53	108.38	120.45	4.5	64.39	<3.91	<3.32	<2.84	110.26
Mn55	2485.45	2194.02	61.6	2173.92	86.14	107.94	2124.55	2499.17
Fe57	46975.97	46289.47	1175.62	45247.8	819.06	1929.36	44167.85	48391.34
Co59	65.04	61.31	0.41	61.24	0.44	0.95	65.68	66.26
Ni60	85.62	84.98	<0.83	84.59	<0.53	<0.69	78.67	82.4
Cu65	<0.85	1.02	2.29	2.39	1.68	1.94	3.48	5
Zn66	671.86	558.61	27.68	564.94	32.62	27.86	626.04	619.65
Ga69	92.28	81.9	32.52	95.19	39.41	37.96	66.28	206.05
Ge73	2.54	2.7	<2.44	6.79	2.19	<1.82	5.25	6.98
As75	<0.80	<1.07	2.05	<0.95	<0.96	<1.22	<0.78	<1.00
Se82	<19.44	<17.69	<24.92	<18.84	<21.71	<22.75	<18.14	<20.62
Rb85	2287.87	2092.2	185.93	2050.68	207.88	585.81	1963.79	1294.47
Sr88	0.354	0.32	333.95	0.313	365.69	151.02	0.88	0.597
Y89	<0.054	<0.066	0.204	0.047	0.529	1.96	2.71	<0.073
Zr90	0.143	<0.138	<0.205	0.103	<0.120	<0.140	1.46	<0.125
Nb93	74.91	64.92	<0.063	72.63	<0.070	<0.114	54.58	71.49
Mo95	<0.36	<0.41	<0.61	<0.26	<0.50	<0.60	<0.27	<0.49
Ag107	<0.104	<0.104	<0.124	<0.121	<0.112	<0.172	<0.144	<0.101
Sn118	30.68	32.75	1.36	28.54	<0.69	1.36	32.9	28.56
Sb121	0.38	0.42	<0.147	0.29	<0.175	0.133	0.52	0.311
Te125	<0.00	<0.00	<0.00	<0.00	<0.00	<0.00	<0.00	<0.00
Ba137	989	816.31	201.87	1137.4	357.19	202.1	357.29	3760.1
La139	<0.051	<0.044	0.317	0.033	1.77	10.73	0.72	0.041
Ce140	0.019	<0.043	0.489	<0.041	3.06	16.45	2.93	0.087
Pr141	<0.030	<0.033	<0.026	<0.028	0.273	1.44	0.375	<0.026
Nd146	<0.156	0.216	0.28	<0.081	0.66	5.69	2.28	<0.21
Sm147	<0.163	<0.27	<0.224	<0.137	<0.16	0.73	1	<0.31
Eu153	0.145	0.142	0.227	0.15	0.469	0.92	0.166	0.316
Gd157	<0.22	<0.270	0.19	<0.186	<0.27	0.38	1.23	<0.25
Tb159	<0.0136	0.017	<0.032	<0.049	<0.033	0.035	0.144	0.024
Dy163	0.087	<0.120	<0.165	<0.096	0.112	0.31	0.55	<0.084
Ho165	<0.024	<0.0240	<0.027	<0.025	0.046	0.057	0.112	<0.043
Er166	<0.110	<0.042	<0.13	<0.086	<0.135	<0.126	0.249	<0.080
Tm169	<0.032	<0.034	0.026	<0.0231	0.028	<0.036	<0.027	0.0055
Yb172	<0.059	<0.178	<0.141	<0.136	<0.192	0.17	<0.106	0.111
Lu175	<0.019	<0.033	<0.045	0.023	<0.033	<0.0166	<0.020	<0.033
Hf178	<0.132	0.303	<0.137	0.311	<0.122	<0.137	<0.126	0.47
Ta181	12.16	9.89	0.06	38.02	0.098	0.113	24.57	7.11
W182	2.76	2.75	<0.162	2.7	<0.118	0.22	1.12	2.66
Au197	0.075	<0.094	<0.111	<0.084	<0.115	<0.130	<0.119	<0.128
Hg202	<-NaN	<-NaN	<-NaN	<-NaN	<-NaN	<-NaN	<-NaN	<-NaN
Pb208	3.38	2.94	8.57	3.16	4.1	1.22	3.29	4.36
Bi209	<0.028	<0.040	<0.051	<0.029	<0.049	<0.055	<0.036	<0.041
Th232	<0.036	0.267	<0.053	<0.037	<0.0254	0.067	42.82	<0.023
U238	<0.021	<0.027	<0.028	<0.03	<0.033	0.053	2.88	0.02

To be continued

Rock	Granite-2066178							
Sample ID	178B-02	178B-07	178B-08	178B-09	178B-10	178F-04	178F-05	178F-06
Mineral	Feldspar	Kfeldspar	Biotite	Kfeldspar		Biotite	Quartz+Biotite	Biotite
Na23	45924.22	61692.04	277.35	3277.89	5236.44	494.52	76.16	414.48
Mg25	575.63	513.23	68459.21	21.04	193.38	52269.2	20841.58	54087.84
Al27	151697.2	124430.9	92037.77	90567.13	88564.51	89560.79	25097.61	88333.85
Si29	289999.4	289999.4	164999.6	289999.4	289999.4	164999.6	164999.6	164999.6
P31	35.96	32.82	33.99	43.34	34.69	41.78	19.08	40.32
S34	399.6	380.96	260.37	191.23	275.64	337.03	169.68	469.51
K39	46411.72	12884.6	70499.25	137884.8	130383.4	82670.11	18423.84	81997.26
Ca43	4721.44	23497.64	3255.29	1827.83	913.24	430.67	467.64	<264.24
Ti49	33.13	<9.75	11995.75	82.66	31.41	17486.7	2443.57	14534.47
V51	<0.23	<0.259	190.22	<0.206	<0.161	364.94	78.22	313.65
Cr53	<3.54	<2.91	<3.58	<2.92	<3.14	194.88	21.24	176.12
Mn55	1237.13	64.34	2257.47	3.95	1.75	2461.39	577.67	2149.77
Fe57	227.67	635.29	47969.59	40.88	24.09	47274.32	12971.16	46546.7
Co59	<0.26	<0.25	70.75	0.117	<0.186	65.18	20.83	64.56
Ni60	1.25	1.06	87.93	0.92	<0.57	76.6	24.96	77.12
Cu65	3.54	<0.97	2.71	1.33	2.2	1.96	3.43	1.85
Zn66	24.09	12.95	608.05	<4.47	<3.51	607.04	181.85	530.46
Ga69	39.54	25.09	69.58	177.64	124.5	76.5	18.99	76.12
Ge73	3.04	<2.42	3.41	<2.07	<1.61	4.27	<1.38	3.37
As75	1.31	<1.12	<0.91	<1.05	<0.94	<1.36	<0.62	<0.88
Se82	<25.56	<23.66	<21.65	<22.15	<18.48	<19.93	<10.80	<20.79
Rb85	160	85.29	1879.51	596.44	618.75	2052.62	455.96	1758.17
Sr88	327.15	249.16	1.54	65.43	18.33	0.353	0.168	0.388
Y89	2.18	0.245	7.51	0.23	0.059	<0.073	0.051	<0.054
Zr90	<0.134	<0.168	0.196	<0.184	1.21	<0.137	<0.091	<0.131
Nb93	<0.090	<0.087	45.58	<0.099	<0.065	64.32	11.6	63.21
Mo95	<0.70	<0.54	0.36	<0.59	<0.36	<0.44	<0.25	<0.42
Ag107	<0.191	<0.070	<0.136	<0.092	0.04	<0.157	<0.056	<0.106
Sn118	<0.81	<0.76	31.78	<0.64	0.76	27.81	6	28.15
Sb121	<0.18	<0.123	0.35	<0.23	0.39	0.3	0.126	0.46
Te125	<0.00	<0.00	<0.00	<0.00	<0.00	<0.00	<0.00	<0.00
Ba137	169.43	132.01	362.08	4345.7	3049.25	760.01	120.86	739.55
La139	3.24	1.43	1.3	1.4	0.813	<0.043	0.016	<0.036
Ce140	7.78	2.72	2.5	0.739	0.332	<0.020	0.14	<0.027
Pr141	0.892	0.369	0.424	0.056	<0.030	<0.028	<0.022	<0.031
Nd146	3.87	0.53	1.58	<0.192	<0.135	<0.094	0.104	<0.254
Sm147	1.6	0.25	0.84	<0.200	<0.162	<0.34	<0.128	<0.188
Eu153	2.35	0.88	<0.082	0.392	0.384	<0.070	<0.032	0.09
Gd157	0.53	<0.21	0.96	<0.25	<0.180	<0.219	0.121	<0.209
Tb159	0.124	0.034	0.175	0.026	<0.033	<0.023	0.021	<0.035
Dy163	0.28	<0.142	1.3	<0.147	<0.107	0.214	<0.080	<0.138
Ho165	0.108	<0.048	0.177	<0.029	<0.024	0.027	0.028	<0.047
Er166	0.14	<0.135	0.73	<0.114	<0.058	<0.112	<0.035	<0.095
Tm169	<0.050	<0.034	0.122	<0.0224	<0.026	<0.035	0.015	<0.015
Yb172	<0.181	<0.191	0.68	<0.144	<0.101	<0.123	<0.062	<0.165
Lu175	<0.032	<0.047	0.069	<0.043	<0.019	<0.032	<0.0162	<0.038
Hf178	<0.117	<0.131	0.1	0.38	0.35	<0.118	<0.059	0.159
Ta181	0.088	<0.037	15.51	1.18	1.15	5.33	0.791	5.05
W182	<0.245	0.16	2.72	<0.117	<0.189	2.41	<0.081	2.64
Au197	0.074	<0.125	<0.108	0.067	<0.094	<0.151	<0.057	<0.154
Hg202	<-NaN	<-NaN	<-NaN	<-NaN	<-NaN	<-NaN	<-NaN	<-NaN
Pb208	1.65	16.39	2.99	77.09	28.03	3.8	0.64	2.78
Bi209	<0.043	<0.052	0.053	<0.038	<0.028	<0.041	<0.017	<0.032
Th232	0.025	0.043	0.06	<0.040	0.037	<0.017	<0.017	<0.033
U238	<0.040	<0.0221	0.336	0.034	<0.031	<0.037	<0.017	<0.030

Silicate analyzed data (133) – 58 to 73 grains (2066199)

Rock	Calc-silicate-2066199							
Sample ID	199A-01	199A-02	199A-05	199A-06	199A-07	199A-08	199A-09	199A-10
Mineral	Kfeldspar			White Mica		Chlorite	White Mica	
Na23	152.82	188.51	182.17	431.23	659.43	383.56	546.53	321.03
Mg25	6553.44	6485.46	6201.15	18762.8	31424.83	116882.6	18982.49	9358.88
Al27	53787.69	53888.93	55004.37	118558.2	90309.95	50717.72	136253.6	82837.3
Si29	119999.7	119999.7	119999.7	299999.8	299999.8	106847.5	299999.8	199999.6
P31	81.34	51.32	121.67	399.64	193.8	79.6	185.24	295.68
S34	182.58	139.93	167.37	547.71	462.59	460.37	331.23	351.66
K39	38819.08	39272.15	39015.62	83938.15	74317.7	38528.32	94934.17	59047.34
Ca43	1382.42	2112.84	942.61	16480.55	51965.77	332500.4	11298.55	4695.13
Ti49	1149.06	2031.9	1922.46	9410.6	2592.8	1380.67	4988.15	4627.19
V51	55.37	56.66	58.05	185.32	92.16	58.15	140.78	97.73
Cr53	41.3	44.89	42.8	142.29	72.6	35.93	114.48	73.25
Mn55	138.6	267.54	55.22	2078.9	4935.71	74507.88	1096.45	436.85
Fe57	6314.94	6546.41	7112.16	65444.41	19253.65	40371.07	14209	19192.13
Co59	4.21	2.52	2.63	9.69	6.09	11.34	7.34	4.52
Ni60	15.91	12.62	11.16	33.08	20.31	16.02	40.81	19.47
Cu65	5.62	3.36	7.31	13.44	6.61	7.19	12.48	10.06
Zn66	37.78	30.37	27.2	73.32	56.75	50.36	77.52	61.04
Ga69	19.78	19	19.78	41.47	34.03	25.54	49.09	27.47
Ge73	1.28	1.85	1.97	2.72	<1.92	2.4	4.61	3.47
As75	4.19	4.03	4.49	29.83	10.25	3.39	7.96	12.19
Se82	<8.71	<7.64	<8.52	<24.13	<21.16	<23.42	<19.76	<12.78
Rb85	185.71	175.87	190.97	427.32	312.41	168	454.28	290.79
Sr88	4.56	6.59	4.98	16.38	22.39	19.48	16.94	10.35
Y89	8.09	11.06	12.37	28.21	19	29.93	27.24	29.73
Zr90	48.33	65.64	70.43	144.4	87.41	117.96	134.32	138.68
Nb93	4.09	6.88	8	30.06	7.96	3.69	18.8	15.84
Mo95	0.28	0.5	0.57	3	1.11	1.99	0.61	0.68
Ag107	<0.063	<0.043	<0.051	<0.170	<0.091	<0.18	<0.149	<0.086
Sn118	2.87	2.84	2.65	7.53	3.68	2.25	6.07	4.62
Sb121	1.94	1.96	2.13	7.72	2.86	1.28	3.74	3.4
Te125	<0.00	<0.00	<0.00	<0.00	<0.00	<0.00	<0.00	<0.00
Ba137	116.73	114.42	132.09	251.35	312.34	272.78	299.41	180.34
La139	6.2	17.51	14.29	115.76	136.66	6.82	56.31	33.64
Ce140	13.82	43.94	32.25	230.33	266.83	17.69	123.55	79.58
Pr141	2.13	4.56	3.65	24.25	28.42	2.25	13.04	8.36
Nd146	5.88	16.8	12.92	83.58	103.6	8.88	44.5	30.6
Sm147	1.32	2.87	2.25	11.87	16.65	2.36	7.72	5.53
Eu153	0.255	0.531	0.518	2.6	2.33	0.88	1.21	1.18
Gd157	0.93	2.01	2.28	7.71	8.82	3.87	5.46	5.45
Tb159	0.27	0.291	0.326	1	0.689	0.57	0.701	0.937
Dy163	1.57	1.69	2.05	4.64	3.26	4.63	4.52	5.32
Ho165	0.318	0.365	0.546	1.09	0.72	0.97	0.92	0.967
Er166	1.03	1.13	1.64	2.59	1.45	2.93	2.22	3.98
Tm169	0.161	0.14	0.235	0.356	0.226	0.51	0.402	0.564
Yb172	1.21	1.22	1.36	2.62	1.3	2.82	2.4	4.06
Lu175	0.157	0.203	0.181	0.39	0.209	0.389	0.424	0.547
Hf178	1.59	1.98	2.26	4.36	2.21	2.84	4.91	4.99
Ta181	0.454	0.734	0.713	2.65	0.774	0.272	1.56	1.51
W182	1.04	1.82	1.63	17.05	3.49	1.85	2.77	7.95
Au197	<0.032	<0.063	<0.039	<0.116	<0.099	<0.170	<0.102	<0.066
Hg202	<-NaN	<-NaN	<-NaN	<-NaN	<-NaN	<-NaN	<-NaN	<-NaN
Pb208	2.54	4.73	4.09	11.47	9.22	3.13	6.49	9.01
Bi209	0.049	0.095	0.089	1.12	0.151	0.092	0.122	0.257
Th232	6.48	10.08	11.58	34.96	29.19	8.58	22.31	32.24
U238	3.49	4.66	5.45	12.67	6.11	5.03	9.1	14.12

To be continued

Rock	Calc-silicate-199							
Sample ID	199A-11	199A-12	199A-13	199D-04	199D-05	199D-07	199D-09	199D-10
Mineral	White Mica	Kfeldspar		White Mica				Qtz +Bio
Na23	239.24	332.59	344.08	297.01	295.51	337.06	310.72	9430.08
Mg25	26788.69	10793.56	10656.66	10120.58	11593.67	13322.54	10411.23	26996.98
Al27	65608.65	94243.48	88683.88	85874.73	89360.84	84899.21	91542.11	28144.93
Si29	199999.6	199970.6	199970.6	199999.6	199999.6	214999.7	214999.7	214999.7
P31	112.08	394.36	236.67	127.87	121.53	94.57	93.49	54.45
S34	277.48	282.25	225.89	308.05	256.63	352.38	326.9	232.56
K39	49380.36	66614.62	62827.39	61685.27	64222.43	64610.15	60606.9	19451.21
Ca43	54210.87	3900.71	2567.6	2686.31	4536.56	9913.29	1894.73	53897.66
Ti49	904.78	2918.02	2928.88	2816.33	2232.52	2361.46	4363.82	840.54
V51	68.33	89.21	88.97	94.44	92.63	90.71	103.02	44.32
Cr53	53.1	65.01	69.11	70.8	58.5	61.11	71.76	18.35
Mn55	7546.8	281.33	267.1	261.93	549.48	943.25	154.05	5124.7
Fe57	12359.87	7448.61	7566.52	13224.21	12616.52	14200.54	15014.98	9688.87
Co59	11.46	4.46	3.98	4.31	4.68	5.01	3.25	4.8
Ni60	33.97	21.8	20.24	20.94	20.79	22.49	17.92	11.97
Cu65	6.48	7.47	5.83	9.52	10.14	5.73	10.82	5.94
Zn66	58.25	53.7	51.76	47.72	43.86	49.99	71.13	39.78
Ga69	23.62	31.85	31.01	28.27	29.82	29.64	33.45	10.76
Ge73	2.5	1.71	10.15	2.79	2.65	<1.68	2.83	<1.66
As75	4.09	5.81	6.36	7.45	6.32	7	8.72	2.9
Se82	<13.47	<12.90	<12.59	<13.54	<12.51	<14.67	<15.47	<14.74
Rb85	235.14	315.62	306.25	287.59	312.37	299.74	310.34	104.8
Sr88	21.09	10.97	23.14	8.19	9.18	9.72	9.42	15.73
Y89	22.53	20.43	23.22	46.01	13.94	11.5	27.3	11.01
Zr90	66.38	143.39	99.18	354.27	75.45	60.59	152.53	46.63
Nb93	3.3	10.06	11.05	11.34	7.57	7.24	15.11	2.91
Mo95	<0.31	<0.34	0.51	0.91	0.84	1.17	1.12	0.71
Ag107	<0.111	<0.098	<0.127	<0.089	<0.076	<0.110	<0.111	<0.135
Sn118	3.19	3.55	4.8	4.33	4.66	3.73	5.29	2.78
Sb121	1.63	2.84	2.59	4.04	3.04	3.22	3.45	1.14
Te125	<0.00	<0.00	<0.00	<0.00	<0.00	<0.00	<0.00	<0.00
Ba137	158.68	172.58	175.92	187.57	179.71	213.55	235.55	64.51
La139	20.22	52.75	514.3	12.15	31.51	7.59	31.59	20.68
Ce140	42.54	114.4	1223.73	30.45	69.88	16.01	70.17	46.68
Pr141	5.12	12.99	101.43	3.12	6.33	1.89	8.12	5.21
Nd146	19.24	44.97	318.93	13.77	22.92	6.61	27.34	18.22
Sm147	4.5	7.62	42.67	2.89	3.42	1.61	5.3	3.25
Eu153	0.94	1.43	6.32	0.856	0.738	0.367	1.02	0.607
Gd157	4.67	5.74	21.96	4.68	3.36	1.33	4.57	2.12
Tb159	0.732	0.781	1.87	0.918	0.419	0.312	0.68	0.341
Dy163	5.27	4.31	6.58	6.12	2.34	1.82	5.04	2.13
Ho165	0.915	0.761	0.912	1.36	0.47	0.373	1.07	0.353
Er166	2.82	2.49	2.52	4.85	1.2	1.44	3.39	1.16
Tm169	0.391	0.391	0.285	0.607	0.224	0.17	0.494	0.199
Yb172	2.66	2.51	2.12	4.63	1.6	1.16	3.3	1.29
Lu175	0.422	0.284	0.333	0.667	0.207	0.252	0.433	0.226
Hf178	2.02	4.66	3.22	8.48	2.14	2.33	4.56	1.83
Ta181	0.311	1.1	1.06	1.08	0.694	0.556	1.19	0.372
W182	1.2	1.31	2.27	2.23	1.99	2.27	4.26	6.6
Au197	0.064	<0.078	<0.065	<0.103	0.09	<0.062	<0.076	<0.090
Hg202	<-NaN	<-NaN	<-NaN	<-NaN	<-NaN	<-NaN	<-NaN	<-NaN
Pb208	7.72	4.22	8.37	4.9	4.19	5.46	21.91	15.31
Bi209	0.044	0.038	0.056	0.281	0.146	0.315	0.156	0.069
Th232	10.88	22	66.27	22.41	11.73	7.77	22.09	9.71
U238	4.32	7.43	7.49	12.69	5.58	4.67	11.23	3.07

Silicate analyzed data (133) – 86 to 100 grains

Rock	Calc-silicate-2066635							
Sample ID	635B-01	635B-02	635B-09	635B-13	635G-04	635G-05	635J-01	635J-04
Mineral	Chlorite				Dolomite	Quartz	Gypsum	Apatite
Na23	5582.37	675.28	13067.8	12916.67	286.06	415539.3	62336.96	68813.92
Mg25	101634.1	114393.8	358590.2	76444.02	117878.7	115311.2	16317.61	19083.81
Al27	76038.7	86904.57	189086.4	58042.45	8925.93	12397.96	1798.99	2064.49
Si29	122999.7	122999.7	318626.1	122999.7	13014.72	1441118	210402.7	247186.3
P31	50.98	64.05	222.06	326.58	48.19	262.89	39.19	35.48
S34	319.37	469.33	872.74	376.22	216.36	2377.51	261.38	338.04
K39	294.6	269.07	1042.48	706.29	192.99	13039.9	2005.9	2289.01
Ca43	3961.25	1212.39	215000.6	9800.56	203600.5	257400.3	36399.72	45900.25
Ti49	2439.76	3940.56	4589.96	3615.88	10.44	665.56	101.97	112.28
V51	102.54	170.68	227.54	123.26	6.09	9.15	0.83	0.98
Cr53	17.02	21.09	31.67	20.65	<1.84	13.1	1.87	<1.77
Mn55	9702.35	10782.44	58156.79	7436.39	32914.61	235.45	31.19	34.76
Fe57	109321.2	182302.1	240675	154390	4998.2	949.35	134.08	170.83
Co59	430.28	448.33	734.33	267.35	26.13	3.19	0.206	0.223
Ni60	56.24	64	98.02	35.23	3.63	6.27	1.1	1.35
Cu65	346.03	6494.53	10730.57	321.48	528.43	33.23	3.53	74.77
Zn66	920.41	1061.04	1894.48	703.61	124.03	<17.32	<2.67	262.07
Ga69	19.34	20.87	47.71	14.33	2.31	10.27	1.79	2.04
Ge73	4.56	4.32	<5.81	7.01	<0.98	<6.35	<1.00	<1.23
As75	53.25	107.39	116.6	89.94	1.09	<3.06	<0.60	<0.70
Se82	<13.02	<17.85	<41.39	<13.95	<8.79	<59.27	<8.15	<10.27
Rb85	1.81	1.91	5.1	2.97	0.239	44.09	6.9	7.64
Sr88	9.39	9.95	31.53	20.22	10.47	124.07	16.89	18.81
Y89	13.62	23.49	100.41	21.65	43.22	12.86	2.16	2.38
Zr90	18.24	16.81	127.94	30.33	0.133	359.27	55.68	62.92
Nb93	5.54	9.84	10.38	7.93	<0.049	2.33	0.3	0.526
Mo95	6.74	14.89	14.1	10.25	0.68	<1.55	<0.30	<0.36
Ag107	<0.128	<0.192	<0.31	<0.104	<0.057	<0.46	<0.089	0.073
Sn118	13.82	20.09	33.4	21.4	0.53	44.9	6.82	8.43
Sb121	35.07	68.93	66.22	52.79	<0.063	0.75	<0.078	<0.111
Te125	<0.00	<0.00	<0.00	<0.00	<0.00	<0.00	<0.00	<0.00
Ba137	24.43	29.4	75.76	46	4.4	411.2	61.59	68.4
La139	33.84	40.14	62.12	253.47	18.42	15.25	1.99	2.42
Ce140	70.29	85.4	143.73	499.13	53.76	22.1	3.61	4.14
Pr141	7.02	9.01	17.07	50.36	7.45	3.29	0.444	0.466
Nd146	27.68	32.91	68.98	232.95	31.74	10.07	1.45	1.83
Sm147	5.25	6.31	18.35	28.23	11.16	2.16	0.45	0.33
Eu153	0.92	1.69	4.85	5	2.83	0.6	0.071	0.058
Gd157	4.02	7.16	17.21	15.95	9.51	2.05	0.58	0.4
Tb159	0.577	0.98	3.35	1.42	1.61	0.171	<0.021	0.086
Dy163	3.42	6.47	22.36	6.85	8.87	1.21	0.268	0.307
Ho165	0.722	1.1	4.4	1.15	1.65	0.37	0.074	0.06
Er166	2.08	3.62	13.09	3.35	4.95	1.09	0.08	0.282
Tm169	0.295	0.471	2.43	0.447	0.552	<0.130	0.022	0.05
Yb172	2.14	3.26	14.17	3.28	4.39	1.05	0.248	0.171
Lu175	0.249	0.454	2.16	0.581	0.633	<0.135	0.026	0.03
Hf178	0.45	0.58	3.03	1.02	<0.072	10.8	1.3	1.43
Ta181	0.631	0.93	1.06	0.86	<0.022	<0.18	<0.022	<0.024
W182	15.58	38.33	35.76	22.22	0.162	<0.46	<0.102	0.078
Au197	<0.079	<0.097	<0.27	0.066	<0.040	<0.28	<0.070	<0.074
Hg202	<-NaN	<-NaN	<-NaN	<-NaN	<-NaN	<-NaN	<-NaN	<-NaN
Pb208	40.16	78.38	90.86	65.86	5.01	14.64	2.55	2.9
Bi209	9.04	18.05	13.85	17.03	8.58	<0.22	0.028	0.295
Th232	20.87	35.79	47.07	40.22	0.35	4.99	0.71	0.84
U238	9.82	18.83	25.42	14.25	0.052	1.62	0.226	0.249

To be continued

Rock	Calc-silicate-2066635						
Sample ID	635J-05	635F-01	635F-02	635F-03	635F-04	635F-05	635F-06
Mineral	Apatite	Chlorite		Dol +Qtz	Dolomite	Chlorite	Dolomite
Na23	73211.68	6247.9	2414.06	63471.8	4071.77	44882.53	31635.07
Mg25	19617.91	96017.91	89494.52	319267.2	132517.2	145409	222496.2
Al27	2191.57	68467.26	64635.45	152802.9	15061.48	50017.97	24301.68
Si29	255582.2	124999.8	124999.9	694263.2	33073.33	229337.1	155253.3
P31	31.06	128.64	80.82	181.81	41.17	125.56	81.61
S34	329.63	241.4	298.07	1459.51	325.43	3919.82	809.02
K39	2260.95	295.02	170.82	2387.93	195.96	1559.34	1212.91
Ca43	45900.25	4569.3	2455.94	215000.6	215000.6	215000.6	366800.3
Ti49	122.93	792.67	59.27	243.79	539.88	491.39	314.97
V51	1.14	53.54	43.16	102.01	22.93	41.63	18.37
Cr53	<2.40	33.78	30.44	82.66	8.19	10.06	5.84
Mn55	36.47	6675.92	7369.49	42612.76	36076.39	41133.09	55798.07
Fe57	158.14	41819.38	28065.31	67676.97	15533.95	26772.48	14864.85
Co59	0.34	153.12	263.19	396	40.83	106.59	71.91
Ni60	1.34	26.73	40.31	68.5	6.03	16.89	10.34
Cu65	3.71	2052.32	1942.65	9350.12	713.2	453.61	128.64
Zn66	<3.31	789.23	727.66	1550.77	167.7	529.77	224.08
Ga69	2.54	19.11	16.01	40.75	4.39	13.75	7.12
Ge73	<1.55	3.52	1.62	9.22	<1.26	<1.89	2.15
As75	<0.68	10.73	1.27	7.95	8.5	6.24	3.41
Se82	<12.66	<9.52	<9.20	<38.53	<10.04	<18.94	<20.47
Rb85	7.29	1.15	0.81	8.53	0.66	5.35	4.46
Sr88	19.74	6.23	3.81	34.98	15.52	324.83	27.47
Y89	2.7	23.44	2.79	44.04	55.92	51.15	64.21
Zr90	69.82	150.18	5.31	86.58	5.74	47.76	35.68
Nb93	0.422	1.54	<0.056	0.4	1.1	0.95	0.75
Mo95	<0.30	1.13	0.22	1.37	0.93	1.83	1.15
Ag107	<0.140	<0.095	<0.101	3.8	0.119	0.095	<0.122
Sn118	7.23	5.01	1.85	19.8	2.96	12.18	7.66
Sb121	<0.085	2.77	0.294	1.03	1.89	0.62	0.74
Te125	<0.00	<0.00	<0.00	<0.00	<0.00	<0.00	<0.00
Ba137	74.93	65.09	27.6	158.05	14.08	68.37	47.59
La139	2.9	25.93	25.18	48.96	28.68	31.68	27.56
Ce140	4.18	55.48	58.42	110.69	65.67	77.58	73.76
Pr141	0.544	5.47	5.88	13.05	9.19	9.32	10.31
Nd146	1.86	19.17	19.25	48.2	36.85	39.3	45.79
Sm147	0.4	3.83	2.59	11.32	12.77	9.1	14.86
Eu153	0.055	0.743	<0.206	2.64	3.24	2.67	3.83
Gd157	0.28	3.32	1.44	9.71	11.16	8.98	14.1
Tb159	0.058	0.567	0.162	1.44	1.83	1.48	2.01
Dy163	0.45	4.62	0.66	7.57	9.6	8.97	12.45
Ho165	0.105	1.24	0.128	1.42	1.78	1.75	2.3
Er166	0.17	3.89	0.273	4.27	5.1	4.65	5.9
Tm169	0.029	0.735	0.037	0.71	0.73	0.69	0.73
Yb172	0.246	6.14	0.525	4.85	5.32	4.18	4.77
Lu175	0.052	1.06	0.051	0.73	0.63	0.63	0.67
Hf178	1.56	5.81	0.149	2.07	0.27	1.31	0.54
Ta181	0.052	0.314	0.045	0.126	0.142	0.228	<0.041
W182	0.149	9.79	<0.115	<0.33	2	1.27	0.66
Au197	<0.066	<0.083	<0.066	<0.25	<0.069	<0.150	<0.11
Hg202	<-NaN	<-NaN	<-NaN	<-NaN	<-NaN	<-NaN	<-NaN
Pb208	2.64	13.41	4.26	17.17	16	22.44	11.31
Bi209	0.154	0.275	0.025	16.8	0.263	<0.052	0.164
Th232	0.82	18.02	2.75	9.22	4.79	3.33	2.84
U238	0.317	5.98	0.346	2.44	1.2	0.97	0.77

Silicate Analyzed Data (133) 101 to 109 grains (2066641-2066656)

Rock	Ironstone breccia-2066641				Granite-2066656				
Sample ID	641C-04	641C-07	641B-05	641C-01	656B-04	656A-01	656A-02	656A-03	656A-04
Mineral	Manganite		Qtz+Chl	Biotite	K-feldspar	Muscovite			
Na23	1895.64	1410.37	77.75	838.43	546.89	666.5	656.03	928.19	20932.65
Mg25	43.08	47.12	931.47	5528.31	7593.32	8371.47	15476.64	8322.42	12110.02
Al27	2210.98	1019.6	11887.38	62678.65	167426.6	168981	171059.4	169806.1	112768.3
Si29	2106.9	1671.7	299999.8	199999.5	224999.6	229999.8	229999.8	229999.8	229999.8
P31	17.92	10.46	39.64	70.67	92.24	31.64	57.83	18.31	<14.77
S34	152.86	124.28	252.95	269.44	311.33	276.85	<140.82	463.02	312.35
K39	19970.96	13082.72	6700.24	33994.09	78670.2	87253.09	82911.14	85370.44	54969.81
Ca43	799.75	799.75	145.39	1198.87	1132.76	961.39	1274.83	1263.97	14546.09
Ti49	566.24	347.65	718.7	3309.58	137.23	1337.29	4959.25	1468.24	1056.21
V51	30.23	31.23	15.86	171.34	56.36	146.41	119.42	85.1	49.43
Cr53	4.84	<0.85	16.51	43.29	46.96	79.59	93.81	56.92	36.91
Mn55	392256.5	323442.2	1364.34	13226.33	1155.96	890.25	3521.39	1744.78	964.49
Fe57	45303.63	2776.14	15605.78	136528.9	4501.28	12224.44	51805.89	17306.34	8207.12
Co59	419.96	374.35	35.71	189.62	52.08	25.3	66.86	52.75	40.2
Ni60	25.34	7.7	6.37	31.1	24.22	24.5	35.21	30.65	18.28
Cu65	344.12	196.2	221.6	1307.89	8.51	16.37	100.39	51.32	20.07
Zn66	824.81	1023.14	152.95	421.5	285.48	174.48	323.09	298.81	192.02
Ga69	4328.77	4349.14	8.77	53.51	81.27	87.53	89.73	83.76	57.65
Ge73	0.56	<0.52	1.39	5.14	3.01	<1.95	<1.98	<2.05	<2.05
As75	19.78	19.42	3.6	58.54	4.36	9.97	20.16	14	5.53
Se82	<6.88	<4.58	<9.01	<12.07	<13.37	21.57	<17.84	<18.05	<18.31
Rb85	23.3	16.14	52.81	251.41	535.54	679.3	612.62	571.52	416.59
Sr88	251.07	210.33	1.36	26.41	10.13	5.49	13.91	9.9	12.22
Y89	2.82	3.73	1.43	7.91	0.91	3.87	14.11	4.54	4.93
Zr90	2.29	1.42	17.91	44.84	3.15	5.33	11.05	5.06	34.55
Nb93	3.21	0.694	2.22	13.4	<0.064	3.58	15.63	3.35	2.56
Mo95	11.34	9.64	0.49	6.2	<0.34	<0.44	0.97	<0.46	<0.51
Ag107	2.8	4.6	0.192	<0.110	<0.144	<0.158	<0.144	<0.14	<0.176
Sn118	<0.32	0.213	<0.44	4.92	2.41	2.83	4.02	2.63	5.35
Sb121	0.87	0.124	0.99	4.12	0.83	1.45	8.99	3.87	1.65
Te125	<0.00	<0.00	<0.00	<0.00	<0.00	<0.00	<0.00	<0.00	<0.00
Ba137	89947.1	90447.23	133.46	687.14	1263.39	908.88	1313.8	1055.41	857.28
La139	2.73	3.28	0.412	11.04	48.54	3	11.6	2.77	3.35
Ce140	10.35	7.83	3.28	69.9	82.53	5.81	22.24	6.2	5.96
Pr141	1.07	1.41	0.157	5.44	9.61	0.492	2.37	0.58	0.653
Nd146	3.74	5.53	0.47	19.93	108.43	2.18	7.56	2.51	2.9
Sm147	0.9	1.11	0.141	3.22	6.19	0.43	3.33	0.76	0.72
Eu153	1.18	1.09	0.028	0.566	1.35	0.355	1.45	0.66	0.306
Gd157	1.45	5.47	0.118	2.55	2.08	1.07	4.12	1.86	2.1
Tb159	0.056	0.113	0.024	0.234	0.186	0.222	1.11	0.439	0.214
Dy163	0.4	0.593	0.154	2.09	0.41	1.68	5.92	1.42	1.57
Ho165	0.097	0.11	0.041	0.41	0.064	0.248	1.05	0.417	0.141
Er166	0.169	0.259	0.161	1.36	0.1	0.78	1.79	0.44	0.54
Tm169	0.0241	0.0318	0.027	0.125	<0.019	0.114	0.308	0.115	0.102
Yb172	0.19	0.187	0.156	1.13	0.184	0.68	1.44	0.74	0.4
Lu175	0.0233	0.0404	<0.021	0.177	<0.033	0.074	0.206	0.154	0.119
Hf178	0.148	0.049	0.478	1.7	0.219	0.36	0.42	0.26	1.06
Ta181	0.065	0.0186	0.299	1.33	0.451	0.473	1.43	0.58	0.274
W182	11.05	4.74	0.85	13.1	0.26	7.37	18.48	5.94	4.79
Au197	<0.051	<0.032	<0.048	<0.086	<0.073	<0.095	<0.15	<0.100	<0.121
Hg202	<0.00	<0.00	<0.00	<0.00	<0.00	<0.00	<0.00	<0.00	<0.00
Pb208	3556.52	3717.09	20.35	674.96	10.69	18.37	106.77	33.92	21.53
Bi209	8.01	11.88	0.229	17.93	0.057	<0.051	0.387	0.293	0.087
Th232	1.68	0.965	2.23	19.58	15.93	10.61	40.1	11.85	7.41
U238	38.46	14.88	1.22	26.44	1.87	1.82	6.21	3.11	1.82

Silicate Analyzed Data - 110 to 132 grains (2066655)

Rock	Metasandstone-2066655											
SampleID	655A-07	655A-08	655A-09	655A-13	655A-14	655A-15	655A-16	655A-17	655B-04	655B-05	655B-08	
Mineral	Dolomite			Chlorite			Dolomite			Chlorite		
Na23	790.19	29.85	44.88	111.49	113.91	594.23	8304.05	6573.64	69.48	61.91	176.24	
Mg25	96648.3	53337	56559.2	65288.08	60250.58	60846.69	90270.06	108756	75832.49	75739.16	41797.64	
Al27	1416.9	108702	101833.	103365.5	97559.09	92452.51	277.91	267.23	100449.8	101699.8	64397.09	
Si29	2984.88	115999	115999.	115999.7	115999.7	115999.7	25788.91	21750.81	119999.6	119999.6	119999.6	
P31	24.05	32.12	32.67	29.62	32.06	28.68	22.4	21.37	37.95	24.38	19.97	
S34	202.54	365.28	469.27	233.83	213.39	268.65	215.76	315.64	1050.18	317.52	223.26	
K39	162.56	44.97	30.61	144.1	113.71	117.46	445.03	326.2	54.07	66.43	175.45	
Ca43	210300	296.58	352.44	336.29	349.63	635.66	210300	210300	205.78	184.58	189.76	
Ti49	3.77	85.31	236.75	258.11	196.36	149.15	17.89	15.33	163.15	200.33	124.81	
V51	0.44	33.06	40.49	56.76	67.06	69.62	0.48	0.69	53.6	50.22	31.85	
Cr53	<1.38	12.37	16.41	37.77	25.72	8.19	<1.58	<1.93	12.31	7.25	24.99	
Mn55	51827.9	2811.5	3427.96	2284.8	3044.54	3846.3	52161.46	53686.71	931.96	1246.49	884.37	
Fe57	12827.9	80756.	76682.2	71285.78	71178.26	68544.86	11129.73	32226.35	79593.61	76723.04	45401.15	
Co59	3.78	63.74	59.46	22.26	25.78	33.47	2.55	3.21	9.37	10.71	8.97	
Ni60	1.13	31	32.21	27.94	28.49	25.28	0.53	1.54	25.64	26.08	15.61	
Cu65	5.26	11.79	38.29	128.02	79.42	74.64	1.97	25.06	7513.56	263.06	450.87	
Zn66	17.71	780.49	660.93	382.87	588.78	780	61.9	9.92	122.05	163.35	152.88	
Ga69	2.64	141.05	137.65	88.44	70.17	53.52	0.469	0.411	114.99	104.11	61.14	
Ge73	<1.00	4.64	5.77	2.26	2.84	2.62	0.96	2.08	2.84	2.13	2.63	
As75	<0.62	1.65	2.21	1.71	0.84	2.7	<0.53	<0.63	6.81	4.11	2.38	
Se82	<8.95	<10.30	15.15	<10.94	<10.31	<9.56	<8.39	<10.21	15.56	<12.77	<7.83	
Rb85	0.348	0.213	0.187	1.47	0.98	0.536	1.42	0.84	0.454	0.475	1.72	
Sr88	9.64	0.579	1	2.1	2.1	2.41	15.68	13.4	0.344	0.265	0.99	
Y89	22.95	0.085	0.138	4.95	1.74	1.09	21.42	28.32	0.826	0.51	3.35	
Zr90	<0.063	<0.070	0.16	18.04	10.06	5.23	10.01	8.62	4.12	2.04	12.81	
Nb93	0.039	<0.041	0.39	0.198	<0.056	<0.057	<0.045	<0.058	0.232	0.097	0.066	
Mo95	1.34	<0.31	1.16	0.83	<0.34	<0.33	1.07	1.18	0.28	<0.36	0.23	
Ag107	<0.071	<0.107	0.131	<0.077	<0.103	<0.105	<0.073	<0.058	1.73	<0.101	<0.071	
Sn118	<0.39	<0.46	<0.47	1.6	3.26	4.28	1.07	1.52	1.95	1.49	0.78	
Sb121	<0.082	<0.130	0.385	0.194	0.223	0.199	0.175	0.26	0.63	0.298	0.428	
Te125	<0.00	<0.00	<0.00	<0.00	<0.00	<0.00	<0.00	<0.00	<0.00	<0.00	<0.00	
Ba137	3.16	0.68	0.86	3.34	2.54	4.51	16.5	11.81	1.57	1.67	3.41	
La139	5.35	<0.031	0.06	0.071	0.027	0.052	6.77	61.79	0.047	<0.036	0.162	
Ce140	11.51	0.0171	0.146	0.289	0.153	0.19	13.4	115.65	0.141	0.049	0.319	
Pr141	1.93	<0.021	0.025	<0.025	<0.027	0.0161	1.99	14.31	0.023	<0.026	<0.0184	
Nd146	10.33	<0.143	<0.149	0.35	<0.19	0.226	10.46	69.91	<0.079	0.129	0.15	
Sm147	6.56	<0.127	0.114	0.28	<0.137	<0.168	6.14	30.98	0.171	<0.128	0.15	
Eu153	4.07	<0.043	<0.030	0.057	<0.035	<0.034	3.89	8.99	<0.034	<0.049	0.041	
Gd157	8.98	<0.161	0.138	0.21	0.27	0.184	9.29	25.25	<0.189	<0.140	0.311	
Tb159	1.58	<0.021	0.025	0.083	0.051	0.027	1.46	3.01	0.023	0.029	0.096	
Dy163	7.48	0.104	<0.067	0.71	0.44	0.167	6.82	10.99	0.149	0.14	0.85	
Ho165	1.17	0.02	0.027	0.217	0.106	0.047	1.02	1.33	0.06	0.046	0.167	
Er166	2.25	<0.074	<0.063	0.66	0.232	<0.063	2.11	2.91	0.137	<0.079	0.387	
Tm169	0.313	<0.020	<0.023	0.092	0.082	<0.027	0.295	0.392	<0.018	<0.025	0.092	
Yb172	2	<0.090	0.121	0.52	0.235	0.155	1.69	3.4	0.178	<0.104	0.569	
Lu175	0.331	<0.018	<0.023	0.123	0.042	0.023	0.23	0.57	<0.027	<0.026	0.08	
Hf178	<0.072	<0.080	<0.091	0.324	0.265	0.158	0.227	0.179	<0.068	0.105	0.542	
Ta181	<0.0191	<0.030	0.045	0.035	<0.025	<0.020	<0.020	0.028	0.067	0.036	<0.0170	
W182	<0.059	<0.156	0.21	<0.101	<0.090	<0.124	<0.096	<0.088	0.185	<0.109	<0.066	
Au197	<0.059	<0.093	<0.080	<0.090	<0.084	<0.092	<0.051	0.059	<0.090	<0.093	<0.062	
Hg202	<0.00	<0.00	<0.00	<0.00	<0.00	<0.00	<0.00	<0.00	<0.00	<0.00	<0.00	
Pb208	2.85	6.8	19.59	10.18	8.55	10.69	6.24	7.25	2.83	3.75	3.84	
Bi209	0.212	0.152	0.635	<0.032	<0.027	<0.030	<0.021	0.048	2.97	0.906	0.238	
Th232	<0.027	<0.023	0.164	2.63	1.44	0.291	0.143	10.42	0.511	0.95	1.36	
U238	0.021	0.028	0.258	1.38	0.96	0.353	0.044	0.063	0.44	0.234	0.956	

To be continued

LA-ICPMS data-FeOx analysis data (47) – 1 to 4 grains (2066166)

Rock	Calc-silicate -2066166			
Sample ID	166B-1	166B-2	166B-3	166B-4
Mineral	Magnetite			
Na23	59.58	29.91	361.27	3384.64
Mg25	17.13	21.29	1971.62	18214.35
Al27	115	204.37	5313.55	13211.82
Si29	1145.17	1574.85	122152.9	87175.3
P31	64.53	52.66	113.44	130.06
K39	64.61	23.37	183.54	209.92
Ca43	<150.12	<148.30	968.41	86902.57
Ti49	94.78	17.43	1177.96	1437.99
V51	37.15	8.92	103.53	70.9
Cr53	<3.11	<2.77	6.58	10.32
Mn55	783.77	821.49	2057.37	4417.07
Fe57	712794.1	712794.1	712794.1	712794.1
Co59	22.54	19.62	18.03	70.27
Ni60	13.41	14.39	60.83	69.68
Cu65	4.55	0.98	4.85	2199.55
Zn66	56.4	43.06	198.41	180.5
Ga69	0.475	0.283	3.69	6.78
Ge73	2.35	1.91	1.99	2.55
Rb85	0.55	0.238	1.46	0.81
Sr88	1.11	0.88	7.59	5.16
Y89	5.61	3.95	11.99	42
Zr90	0.56	0.13	6.94	14.25
Nb93	2.5	0.503	4.58	8.77
Mo95	0.58	0.52	1.26	0.6
Sn118	39.54	6.05	163.52	19.4
Sb121	15.48	13.64	9.59	6.15
Ba137	4.57	1.79	14.25	14.55
La139	1.25	0.427	4.21	18.68
Ce140	2.38	1	6.02	55.27
Pr141	0.271	0.143	0.86	8.54
Nd146	1.42	1.15	4.62	43.37
Sm147	0.71	0.38	1.6	11.68
Eu153	0.136	0.078	0.32	2.48
Gd157	0.62	0.44	2.05	9.21
Tb159	0.106	0.045	0.411	1.27
Dy163	1.04	0.74	2.31	9.86
Ho165	0.273	0.122	0.504	1.75
Er166	0.61	0.57	2.07	6.16
Tm169	0.128	0.09	0.181	0.75
Yb172	0.74	0.48	1.15	4.68
Lu175	0.068	0.078	0.167	0.73
Hf178	<0.065	0.052	0.198	0.26
Ta181	0.047	<0.0230	0.054	0.478
W182	16.78	2.28	17.96	7.59
Pb208	9.28	7.65	14	328.24
Bi209	0.65	0.48	0.25	14.47
Th232	0.168	0.086	0.62	5.67
U238	0.9	0.471	5.27	11.01

LA-ICPMS data-FeOx analysis data (47) – 5 to 14 grains (2066169-2066174)

Rock	Granite -2066169									2066174
Sample ID	169A-1	169A-2	169A-3	169A-4	169A-5	169B-1	169B-2	169B-3	169B-4	174C-02
Mineral	Hematite									
Na23	47.6	63.9	98.54	<4.21	12.13	183.79	98.93	351.5	243.42	581.6
Mg25	50.02	116.24	254.9	70.78	416.2	271.33	114.35	223.97	1866.33	9001.51
Al27	180.93	487.19	617.24	170.98	498.16	732	521.16	2951.94	1641.24	74677.95
Si29	1155.81	1931.06	2759.49	1109.45	10991.93	3252.23	3206.89	89512.84	4931.37	103960.8
P31	153.95	172.15	169.57	58.71	82.5	45.94	87.04	133.19	66.36	279.15
K39	18.94	42.65	50.5	34.81	212.16	59.44	52.71	325.45	309.97	36873.86
Ca43	253.03	424.84	243.28	<166.41	<183.34	463.11	389.35	421.86	364.07	1211.4
Ti49	110.03	574.28	100.12	1878.27	1559.25	119.8	76.72	171.14	6501.5	2061.11
V51	23.56	286.11	71.68	87.95	37.67	131.89	114.65	166.21	451.69	412.71
Cr53	3.15	<2.81	<2.42	3.33	<3.27	10.57	11.2	<3.07	<2.22	104.44
Mn55	462.95	474.11	391.3	4.58	10.71	356.79	549.53	336.55	50.69	801.05
Fe57	659936.9	659936.9	659936.9	659936.9	659937	671985.4	671985.4	671985.4	671985.4	635000.9
Co59	49.85	27.27	25.8	<0.21	0.42	43.92	39.04	29.24	1.32	10.75
Ni60	346.55	85.41	211.71	1.84	2.77	190.26	195.67	261.35	5.68	11.27
Cu65	307.49	43.44	4.71	<0.56	<0.68	173.93	114.84	136.45	1.17	14.86
Zn66	184.98	157.95	120.46	<3.41	<3.26	500.75	371.99	760.09	8.07	101.24
Ga69	10.13	15.51	12.69	5.38	5.12	11.49	10.07	8.4	9.45	29.3
Ge73	1.1	1.72	5.65	<0.56	<1.08	3.57	7.13	4.48	2.97	3.98
Rb85	0.12	0.391	0.334	0.53	3.09	0.285	0.208	2.88	4.95	429.78
Sr88	1.39	4.85	2.96	<0.039	0.049	3.49	2.34	6.26	1.81	11.73
Y89	2.84	5.67	9.67	0.059	0.267	18.24	9.6	9.73	2.14	6.14
Zr90	3.78	4	3.38	4.23	1.23	1.5	2.34	3.56	16.68	14.48
Nb93	0.246	0.212	0.275	16.95	6.19	0.404	0.227	0.338	17.01	33.27
Mo95	1.54	0.88	1.16	0.3	<0.26	2.85	2.39	6.87	2.82	1.82
Sn118	1.03	2.88	1.77	455.4	516.62	4.55	3.87	5.97	95.9	6.04
Sb121	8	7.37	7.57	0.61	1.25	4.62	3.86	12.07	43.98	11.75
Ba137	5.16	46.55	7.86	0.26	<0.29	10.81	8.99	42.49	7.9	575.06
La139	1.35	2.08	1.94	0.125	0.215	1.26	1.45	2.24	1.84	15.79
Ce140	2.17	4.1	3.48	0.089	0.369	2.06	2.35	3.77	2.99	32.69
Pr141	0.214	0.514	0.346	<0.0132	<0.024	0.282	0.264	0.344	0.389	3.81
Nd146	0.53	1.87	1.62	0.029	<0.159	1.36	1.11	1.37	1.26	13.22
Sm147	<0.149	0.5	0.7	<0.00	<0.096	0.55	0.138	0.38	0.2	3.06
Eu153	0.09	0.25	0.232	0.016	<0.043	0.158	0.083	0.28	0.038	0.628
Gd157	0.54	1.27	1.07	0.102	<0.132	1.03	0.57	0.65	0.49	3.47
Tb159	0.088	0.244	0.231	<0.0266	<0.0197	0.347	0.199	0.143	0.064	0.465
Dy163	0.63	1.25	1.49	<0.090	0.092	2.85	1.35	1.5	0.54	2.56
Ho165	0.133	0.291	0.446	<0.0136	0.011	0.77	0.454	0.344	0.119	0.322
Er166	0.45	0.75	1.41	<0.040	0.083	2.42	1.37	1.7	0.39	0.72
Tm169	0.056	0.092	0.184	<0.0216	<0.0131	0.44	0.228	0.226	0.045	0.102
Yb172	0.42	0.75	1.51	<0.074	<0.077	3.1	1.82	1.1	0.34	0.67
Lu175	0.105	0.072	0.181	<0.0125	0.0152	0.47	0.252	0.235	0.109	0.053
Hf178	0.107	<0.055	<0.060	0.121	<0.063	0.115	0.082	<0.099	1.04	0.75
Ta181	<0.025	<0.028	<0.0124	0.1	0.229	<0.0119	0.015	<0.028	0.88	0.39
W182	21.54	8.41	12.67	132.07	148.16	28.4	38.47	65.44	54.59	49.07
Pb208	97.94	58.14	82.43	0.62	0.294	70.84	80.23	136.45	15.22	66.45
Bi209	3.6	3.12	1.68	<0.010	<0.0126	18.38	11.25	11.87	0.51	1.35
Th232	0.17	0.332	0.221	0.138	0.094	0.13	0.088	0.154	0.365	58.01
U238	3.17	3.76	4.41	0.417	0.087	5.06	6.63	12.18	1.48	12.01

LA-ICPMS data-FeOx analysis data (47) – 15 to 23 grains (2066178)

Rock	Granite-2066178								
Sample ID	178A-1	178A-2	178B-2	178B-4	178B-5	178B-6	178F-03	178F-1	178F-2
Mineral	Hematite		Magnetite	Hematite		Magnetite		Hematite	
Na23	<5.76	15.34	1150.96	<5.49	522.25	973.36	133.21	<7.68	592.33
Mg25	16.33	17.53	221385.5	40.32	886.63	1563.08	17888.68	17.29	162.71
Al27	386.58	450.33	321419.4	310.45	8153.64	8667.27	22453.33	674.69	708.74
Si29	<394.84	567.62	562664.5	655.77	14619.69	12722.39	40561.8	1094.6	2471.38
P31	63.59	80.72	279.89	44.42	80.14	84.71	55.43	81.02	<49.33
K39	61.29	<4.73	203300.9	33.58	243.33	913.03	12706.68	<5.59	43.8
Ca43	<194.04	<185.32	16796.53	<164.36	7238.19	3967.48	1689.23	<274.63	502.78
Ti49	263.42	388.69	37946.54	105.56	254.2	68.99	3503.57	533.27	1120.41
V51	791.76	803.99	675.43	402.7	441.16	421.92	1011.94	1189.77	1239.78
Cr53	32.04	48.03	20.56	6.04	9.37	8.57	1397.44	1719.36	1711.99
Mn55	252.98	279.2	8292.49	181.59	329.47	221.26	724.53	313.14	482.41
Fe57	668409.8	668409.9	660000.9	660000.9	660000.9	711101.4	703200.8	686801.1	686801.1
Co59	20.72	21.88	253.12	21.25	18.86	23.39	37.18	22.69	21.89
Ni60	38.27	38.03	315.99	26.39	25.38	33.26	59.86	43.09	37.91
Cu65	0.78	<0.79	7.83	0.64	0.74	4.57	3.67	<0.99	5.46
Zn66	28.02	34.01	1996.64	27.48	38.19	40.93	178.98	201.41	216.69
Ga69	20.75	22.33	192.27	14.08	26.18	19.78	32.69	17.42	19.3
Ge73	3.42	3.74	13.59	1.89	4	3.12	3.48	2.28	3.71
Rb85	<0.112	<0.108	5242.42	0.61	2.04	14.83	365.32	<0.124	0.151
Sr88	<0.060	0.063	6.79	0.085	11.28	7.19	2.55	<0.068	0.323
Y89	<0.069	<0.073	36.32	<0.050	0.811	0.514	4.72	<0.087	0.094
Zr90	<0.136	<0.170	4.91	<0.057	<0.099	<0.140	9.9	<0.189	1.28
Nb93	<0.08	0.06	183.68	<0.063	<0.054	<0.049	13.22	<0.103	<0.105
Mo95	<0.32	0.33	<1.08	<0.29	<0.37	<0.45	<0.53	<0.38	<0.60
Sn118	1.14	<0.95	142.76	<0.84	1.18	<0.94	7.18	<1.04	3.16
Sb121	<0.164	0.19	1.39	<0.140	0.26	0.29	<0.29	0.15	<0.29
Ba137	0.57	<0.31	1139.12	0.48	1.47	10.48	135.66	<0.32	3.81
La139	<0.043	<0.040	2.16	<0.039	19.13	0.717	1.15	<0.057	<0.058
Ce140	<0.045	0.038	6.09	<0.023	24.81	1.14	3.33	<0.030	0.108
Pr141	0.022	0.026	1	0.027	2.18	0.056	0.482	<0.025	<0.044
Nd146	0.1	<0.172	5.46	<0.170	6.84	0.28	2.24	0.036	0.21
Sm147	<0.174	<0.32	1.23	<0.184	0.54	<0.22	0.39	<0.24	<0.21
Eu153	0.053	<0.052	<0.25	<0.051	1.08	0.067	<0.064	<0.042	0.052
Gd157	<0.138	<0.145	1.5	<0.156	0.5	0.18	1	<0.207	<0.27
Tb159	0.02	<0.043	0.63	<0.0212	0.064	<0.036	0.074	<0.047	<0.044
Dy163	<0.087	<0.172	5.12	<0.127	0.191	0.118	1.07	<0.130	<0.186
Ho165	0.019	<0.017	1.44	<0.029	0.045	<0.032	0.198	<0.038	<0.0194
Er166	<0.066	<0.130	4.42	0.043	0.065	<0.092	0.71	<0.137	<0.170
Tm169	<0.031	<0.043	0.68	<0.035	<0.020	0.022	0.048	<0.037	<0.042
Yb172	<0.151	<0.112	2.97	<0.141	<0.100	<0.154	0.38	<0.205	<0.209
Lu175	<0.036	<0.034	0.36	<0.0212	0.023	<0.043	0.074	<0.053	<0.041
Hf178	<0.071	<0.092	0.96	<0.104	<0.139	<0.101	0.98	<0.107	<0.089
Ta181	<0.041	<0.030	73.24	<0.038	<0.031	<0.034	0.91	<0.056	<0.030
W182	<0.21	<0.21	15.61	<0.14	<0.24	0.11	1	<0.22	<0.19
Pb208	0.396	0.82	8.81	0.356	0.86	1.22	2.51	0.235	4.6
Bi209	<Inf	<Inf	<Inf	<Inf	<Inf	<Inf	<Inf	<Inf	<Inf
Th232	<0.034	<0.032	0.86	<0.020	<0.020	<0.026	1.18	<0.037	0.064
U238	<0.0222	<0.030	1.15	<0.0162	0.0143	0.034	0.38	<0.028	0.026

LA-ICPMS data-FeOx analysis data (47) – 24 to 29 grains (2066635-2066641)

Rock	Calc-silicate-2066635	Metasediment-2066641				
Sample ID	635B-1	641B-1	641B-2	641C-2	641C-3	641C-4
Mineral	Hematite					
Na23	168.98	189.87	4340.7	242.71	437.48	3628.89
Mg25	26669.23	1448.54	4185.01	83.3	2768.15	488.33
Al27	20515.87	16462.38	10975.85	3661.8	30319.37	7298.36
Si29	29674.17	55533.04	27697.62	5696.89	71654.78	13265.03
P31	135.63	63.17	46.01	67.39	216.7	179.08
K39	161.19	8404.92	4400.58	486.27	15381.17	25969.79
Ca43	315.31	239.92	2910.55	376.63	776.28	2138.2
Ti49	5176.07	2340.25	412.59	860.78	3318.58	3880.57
V51	278.39	65.24	62.3	40.33	159.13	119.82
Cr53	18.13	19.08	16.11	9.24	27.73	20.61
Mn55	2252.27	15363.69	22219.6	20970.03	17614.6	660411.4
Fe57	642401.1	560000.4	600000.9	573001	592000.8	592000.8
Co59	58.43	303.22	208.13	291.65	261.29	956.38
Ni60	12.85	44.56	38.59	47.86	42.12	54.63
Cu65	84.96	756.15	3200.19	640.97	1400.9	1270.42
Zn66	225.07	762.8	1146.33	616.08	397.89	1374.34
Ga69	5.76	15.94	14.28	7.19	33.91	6532.85
Ge73	<1.52	1.52	1.78	0.77	3.38	4.33
Rb85	0.92	71.12	38.04	3.07	131.77	44.11
Sr88	4.48	7.92	7.25	13.09	28.52	464.42
Y89	8.53	3.57	2.68	1.43	9.34	11.36
Zr90	23.51	38.56	31.11	7.83	38.15	17.18
Nb93	17.91	10.97	1.88	8.94	18.2	15.3
Mo95	6.53	3.58	2.81	1.89	7.09	22.04
Sn118	16.48	3.64	7.97	0.68	2.28	3.21
Sb121	76.15	7.42	8.24	5.96	11.6	14.89
Ba137	25.04	260.51	234.98	131.26	570.74	169030.4
La139	40.25	4.66	2.36	2.58	15.86	11.56
Ce140	80.74	16.56	9.12	21.38	80.08	44.8
Pr141	8.4	1.265	0.846	1.175	6.82	4.9
Nd146	29.37	3.19	2.68	4.11	22.81	17.26
Sm147	5.11	0.49	0.48	0.5	3.61	3.25
Eu153	0.83	0.103	0.088	1.62	0.685	2.63
Gd157	2.84	0.58	0.304	0.47	2.76	3.75
Tb159	0.442	0.105	0.052	0.104	0.377	0.41
Dy163	2.19	0.67	0.542	0.342	2.31	2.05
Ho165	0.61	0.137	0.103	0.086	0.362	0.369
Er166	0.84	0.439	0.316	0.15	1.36	1.07
Tm169	0.168	0.077	0.05	0.024	0.158	0.142
Yb172	1.4	0.401	0.435	0.155	1.43	0.79
Lu175	0.18	0.068	0.058	<0.018	0.165	0.159
Hf178	0.91	0.87	0.597	0.16	1.09	0.371
Ta181	1.35	0.83	0.171	0.243	1.07	1.01
W182	27.67	8.28	9.86	3.93	13.92	38.04
Pb208	23.75	202.75	139.57	155.93	664.52	6794.37
Bi209	<Inf	5.56	5.59	6.88	24.45	34.44
Th232	16.78	13.22	7.05	5.76	21.18	12.84
U238	9.8	6.02	5.32	7.32	24.89	95.08

LA-ICPMS data-FeOx analysis data (47) – 30 to 42 grains (2066655)

Rock	Metasediment					
Sample ID	655A-18	655A-19	655A-2	655B-1	655B-2	655B-3
Mineral	Hematite			Magnetite		Hematite
Na23	312.79	408.09	1085.52	318.42	3645.31	1576.27
Mg25	20039.68	4595.53	24448.15	428.53	10100.47	647.38
Al27	26717.43	5057.44	35861.58	1358.38	15482.44	1575.99
Si29	36285.45	9771.59	44383.13	8068.01	124020.9	35960.52
P31	86.98	99.4	36.36	52.98	93.88	44.71
K39	412.64	737.97	290.09	280.25	692.38	775.25
Ca43	1219.79	7188.6	793.75	780.24	2819.45	1554.24
Ti49	172.33	1009.37	236.16	191.78	259.06	350.81
V51	86.74	81.87	101.09	58.15	85.28	93.59
Cr53	14.22	18.41	11.12	4.95	61.96	54.77
Mn55	805.33	2069.41	1356.36	174.45	431.45	202.97
Fe57	680001	680001	680001	692800.9	692800.9	669400.8
Co59	11.14	4.02	11.98	4.74	6.81	4.21
Ni60	13.13	5.38	13.6	7.69	11.32	4.19
Cu65	141.59	20.84	106.03	242.28	1687.68	145.47
Zn66	89.97	45.17	204.07	13.56	57.57	31.39
Ga69	34.72	16.69	37.49	15.04	25.84	14.27
Ge73	12.36	6.14	9.08	10.45	8.27	5.81
Rb85	1.28	8.15	2.28	1.82	6.96	7.04
Sr88	2.61	3.68	4.45	3.3	4.18	4.11
Y89	10.64	14.55	2.99	5.31	25.24	6.83
Zr90	0.289	49.63	0.245	2.22	113.52	20.08
Nb93	1.11	3.26	0.84	0.82	1.07	1.99
Mo95	14.6	9.06	0.72	0.68	4.44	3.42
Sn118	1.39	2.64	1.49	1.33	3.52	2.76
Sb121	2.18	4.26	2.08	4.58	6.32	9.01
Ba137	5.75	6.15	4.85	6.67	14.04	12.65
La139	0.066	0.932	0.23	0.396	0.604	0.452
Ce140	0.087	1.94	0.744	0.733	1.66	1.139
Pr141	0.057	0.286	0.076	0.079	0.162	0.118
Nd146	0.241	0.99	0.28	0.142	1.6	0.33
Sm147	<0.29	0.68	0.29	<0.19	0.69	0.34
Eu153	0.083	0.46	0.069	<0.067	0.338	0.177
Gd157	<0.29	1.7	<0.23	<0.22	1.32	0.82
Tb159	0.139	0.379	0.072	0.084	0.604	0.187
Dy163	1.16	2.27	0.369	0.63	4.79	1.07
Ho165	0.266	0.538	0.151	0.118	1.025	0.299
Er166	1.67	1.8	0.225	0.63	3.37	1.17
Tm169	0.321	0.249	0.07	0.09	0.72	0.128
Yb172	1.75	2.38	0.46	0.56	3.75	1.19
Lu175	0.311	0.347	<0.035	0.146	0.74	0.218
Hf178	<0.134	1.33	<0.125	<0.110	4.46	0.48
Ta181	0.157	0.301	0.075	<0.043	0.152	0.402
W182	0.51	1.92	0.39	0.78	0.77	3.94
Pb208	12.86	39.93	24.32	9.01	17.85	20.84
Bi209	0.6	0.25	0.12	4.52	4.8	3.54
Th232	<0.038	6.63	0.305	0.615	14.47	2.3
U238	0.147	3.41	0.346	0.505	7.58	2.45

To be continued

Rock	Metasediment -2066655						
Sample ID	655B-4	655B-5	655B-6	655E-1	655E-2	655E-3	655E-4
Mineral	Hematite						
Na23	704.14	137.64	379.82	1810.72	8495.34	787.04	804.57
Mg25	451.39	135	252.54	3966.94	3632.53	2309.3	2782.85
Al27	2335.09	2037.65	1576.31	7226.64	4368.86	5703.07	6135.54
Si29	6916.64	1989.77	10646.97	21405.93	37145.37	12604.99	12543.75
P31	74.14	87.17	179.61	98.42	90.42	47.11	83.11
K39	438.48	124.06	332.23	1511.92	1147.82	1288.1	901.42
Ca43	1218.64	272.06	590.64	1868.66	5830.56	1526.97	1309.77
Ti49	123.34	10086.54	1984.54	358.68	723.9	560.15	608.38
V51	71.1	176.82	125.04	76.31	120.73	90.45	102.72
Cr53	8.7	42.32	84.23	10.8	22.04	11.92	16.38
Mn55	193.44	210.1	269.36	383.61	292.68	321.19	378.45
Fe57	669400.8	678101.3	678101.2	660000.8	660000.8	660000.8	660000.7
Co59	4.04	2.49	2.13	4.27	2.77	3.14	3.73
Ni60	6.33	<0.63	2.14	8.94	7.6	8.31	8.6
Cu65	167.79	0.94	<0.80	3.54	28.54	38.7	47.15
Zn66	16.6	17.51	20.07	49.81	59.45	47.67	61.82
Ga69	16.91	12.65	13.69	19.98	18.3	19.57	20.4
Ge73	8.97	3.16	6.18	9.41	10.66	8.86	8.55
Rb85	2.12	1.37	3.19	18.95	10.66	14.57	8.87
Sr88	4.39	2.37	3.9	3.31	6.8	2.97	2.54
Y89	11.15	1.82	4.94	9.42	8.29	7.15	17.75
Zr90	29.45	2.43	4.85	37.06	25.35	10.52	20.69
Nb93	1.41	30.72	13.39	1.99	3.34	2.53	2.95
Mo95	<0.46	4.32	5.32	14.5	2.37	1.08	1.75
Sn118	2.53	24.2	9.53	2.64	4.93	3.67	4.62
Sb121	3.84	27.72	19.38	2.31	6.3	2.74	3.79
Ba137	9.05	12.14	50.35	9.8	16.82	6.08	7.14
La139	<0.037	1.233	2.91	0.455	1.97	0.398	0.316
Ce140	0.134	2.32	5.52	0.891	11.34	0.654	2.13
Pr141	0.039	0.284	0.671	0.117	0.98	0.092	0.098
Nd146	<0.180	0.81	3.03	0.37	98.42	0.179	0.3
Sm147	<0.22	0.27	0.73	0.126	0.43	<0.17	<0.169
Eu153	0.094	0.2	0.572	0.099	0.167	0.152	0.083
Gd157	0.22	0.47	1.14	0.43	1.1	0.42	0.31
Tb159	0.146	0.117	0.326	0.163	0.165	0.163	0.11
Dy163	1.28	0.58	1.55	1.44	0.93	0.88	0.93
Ho165	0.387	0.082	0.303	0.307	1.22	0.283	0.204
Er166	1.47	0.315	0.552	1.32	1.16	1.1	0.8
Tm169	0.26	0.034	0.072	0.185	0.129	0.145	0.12
Yb172	2.13	0.203	0.58	1.8	0.74	1.07	0.69
Lu175	0.5	0.032	0.138	0.31	0.163	0.216	0.175
Hf178	0.73	0.273	0.249	1.45	0.81	0.473	0.35
Ta181	0.176	1.86	0.86	0.251	0.45	0.348	0.532
W182	0.69	59.46	11.75	0.2	2.77	0.99	1.46
Pb208	7.87	27.83	15.71	7.22	14.28	12.89	16.03
Bi209	2.09	0.67	1.24	0.64	0.24	0.21	0.12
Th232	1.48	17.49	9.09	2.46	2.57	2.02	1.37
U238	0.698	7.88	7.62	1.78	2.26	1.5	1.16

LA-ICPMS data-FeOx analysis data (47) – 42 to 47 grains (2066656)

Rock	Granite-2066656				
Sample ID	656A-06	656B-05	656B-06	656B-08	656B-09
Mineral	Hematite				
Na23	194.41	116.46	224	256.66	291.52
Mg25	2201.23	124.34	1356	2045.66	2299.89
Al27	19788.76	1679.97	29935	32311.05	45385.57
Si29	28211.06	2683.77	39825	44232.33	92342.09
P31	198.71	78.96	163	176.83	133.98
K39	8266.15	292.79	13438	13994.87	21135.06
Ca43	813.49	153.51	#VALUE!	412.56	656.28
Ti49	4018.14	810.03	1275	86599.04	738.55
V51	860.82	1187.13	1104	1165.47	697.49
Cr53	1061.5	1382.19	1843	1225.16	317.71
Mn55	3560.09	169.64	471	804.61	365.31
Fe57	650000.6	650000.6	650000	650000.6	650000.6
Co59	27.85	8.83	13	9.39	10.29
Ni60	28.37	35.05	26	23.4	34.44
Cu65	189.51	8.37	34	56.65	15.78
Zn66	73.24	15.85	49	44.97	47.92
Ga69	18.31	14.75	25	22.38	26.09
Ge73	5.31	4.42	5	3.66	10.1
Rb85	88.68	3.35	118	136.98	188.75
Sr88	4.18	2.4	4	6.85	3.66
Y89	7	0.505	2	26.74	1.84
Zr90	4.76	<0.103	3	5.22	2.17
Nb93	10.99	1.99	2	351.25	1.3
Mo95	3.83	3.35	4	3.19	0.94
Sn118	5.68	4.67	3	26.15	5.34
Sb121	51.68	53.37	45	85.05	19.28
Ba137	158.83	17.21	229	154.12	149.49
La139	4.05	0.445	8	16.99	0.758
Ce140	10.36	0.762	14	25.78	1.12
Pr141	1.047	0.097	2	2.66	0.109
Nd146	4.11	0.235	6	9.28	0.41
Sm147	1.76	0.158	2	3.11	<0.18
Eu153	0.647	<0.035	0	1.28	0.164
Gd157	3.36	0.248	1	4.1	0.73
Tb159	0.592	0.048	0	0.93	0.129
Dy163	2.79	<0.097	1	6.73	0.296
Ho165	0.444	0.033	0	1.47	0.091
Er166	0.95	0.093	0	4.28	0.216
Tm169	0.094	<0.0192	0	0.66	<0.025
Yb172	1.18	0.082	0	5.23	0.46
Lu175	0.151	<0.019	#VALUE!	0.73	0.029
Hf178	0.08	<0.049	0	0.183	0.171
Ta181	0.86	0.027	0	23.87	0.092
W182	34	40.04	20	109.38	5.45
Pb208	134.37	31.98	83	102.84	29.17
Bi209	2.21	0.84	2	2.38	0.56
Th232	28.2	20.91	41	53.13	9.26
U238	7.68	7.95	7	10.05	3.8

Notes: the Fe oxide analysis have been done for 100 spots. The spots have been failed to the low Fe contents due to the small inclusions, for example, 19 spots in 2066177 has the 41-58Fe%. The only 47 of 100 spot have been listed here for magnetite and hematite.

LA-ICPMS data-S mineral data (51) -1 to 5 grains (2066166)

Rock	Calc-silicate-2066166				
Sample ID	166B-1	166B-2	166B-3	166E-1	166E-2
Mineral	Chalcopyrite			Pyrite	
Na23	<3.21	202.31	88.92	12.81	483.79
Si29	<0.00	<0.00	<0.00	<0.00	<0.00
S33	381644.4	341508.6	74176.4	460493.3	488143.8
S34	378882.4	351916	70374.59	498067.2	497556
V51	0.29	10.45	143.49	0.227	0.215
Cr52	<2.95	<2.51	3.1	<1.07	<1.08
Mn55	<0.93	10.35	4472.32	<0.33	1.23
Fe57	304317.3	304317.3	304317.3	463899.3	463899.3
Co59	<0.109	<0.101	13.77	271.45	85.3
Ni60	<0.45	<0.44	7.47	674.38	350.76
Cu65	309684.7	280159.4	50978.44	6	2.86
Zn66	8.08	13.07	199.71	<1.26	5.17
Ga69	<0.082	0.135	6.74	<0.036	<0.044
As75	<0.71	4.58	40.94	208.63	54.83
Se82	55.78	34.86	5.66	236.94	168.86
Mo95	20.04	0.29	0.96	<0.110	<0.065
Ag107	2.7	4.31	2.8	<0.022	<0.021
Cd111	<0.38	<0.34	<0.204	<0.118	<0.134
In115	12.72	10.01	2.66	<0.0109	0.0087
Sn118	<0.51	15.61	181.96	<0.185	0.59
Sb121	<0.091	0.46	3.33	<0.031	<0.037
Te125	0.42	<0.31	<0.175	5.45	3.88
Ba137	1.38	12.96	54.88	<0.33	9.3
W184	<0.079	1.24	10.47	<0.029	<0.036
Ir193	<0.0182	<0.0098	<0.0123	<0.0060	<0.0052
Au197	<0.038	<0.042	0.026	<0.021	<0.0164
Hg202	0.34	0.28	0.083	0.039	0.06
Tl205	<0.0219	0.075	0.054	<0.0046	<0.0041
Pb208	2.16	5.68	40.18	1.65	0.739
Bi209	4.76	8.83	6.04	0.353	0.056

LA-ICPMS data-S mineral data (51) - 6 to 14 grains (2066169)

Rock	Granite - 2066169								
Sample ID	169A-01	169A-02	169A-03	169B-1	169B-2	169B-3	169B-1	169B-2	169B-3
Mineral	Pyrite						Chalcopyrite		
Na23	<1.15	<1.20	1.37	<0.94	<0.93	<0.96	8.52	136.97	19.65
Si29	<0.00	<0.00	<0.00	<0.00	<0.00	<0.00	<0.00	<0.00	<0.00
S33	485784.9	485375.6	461690.2	437807	416091.6	435447.5	296605.4	189260.4	318479.8
S34	490959.3	478992.3	473135.4	429420.2	418973.1	447938	303884.5	192001.2	308457.3
V51	0.205	0.237	0.237	0.16	0.242	0.263	0.157	63.27	0.701
Cr52	<1.02	<1.04	<1.05	<0.79	<0.77	<0.80	<0.62	1.82	<0.88
Mn55	0.59	0.38	<0.33	0.57	0.26	0.49	2.54	127.75	1.92
Fe57	474937.1	474937.1	474937.1	414928.7	414928.7	414928.7	294290	294290	294290
Co59	1053.31	1227.89	532.85	5784.58	5580.72	3674.42	3352.39	27.48	5266.26
Ni60	2586.26	2715.63	3006.2	1323.08	926.66	1700.34	918.82	25.33	104.55
Cu65	0.49	0.65	1	0.41	0.72	0.46	11154.68	117173.2	46189.26
Zn66	<1.89	<1.71	<1.68	<0.94	<0.96	<0.93	21.63	215411.2	70.37
Ga69	<0.030	<0.034	<0.033	<0.022	<0.0200	<0.021	0.11	1.94	0.153
As75	96.08	71.09	61.39	61.56	123.99	169.34	66.04	5.11	297.36
Se82	42.68	39.01	50.17	23.35	34.69	47.2	26.08	34.24	14.58
Mo95	<0.126	0.059	<0.061	<0.085	<0.089	<0.033	<0.076	4.8	<0.104
Ag107	<0.0159	<0.0167	<0.0082	<0.0195	<0.0147	<0.0153	0.43	144.69	65.11
Cd111	<0.135	<0.147	<0.121	<0.104	<0.088	<0.092	<0.071	360.56	0.53
In115	<0.0075	<0.0083	<0.0065	<0.0053	<0.0047	<0.0049	0.339	3.31	0.0077
Sn118	<0.168	<0.168	<0.178	<0.131	<0.126	<0.124	0.539	0.94	<0.144
Sb121	<0.033	<0.018	<0.018	<0.0178	<0.0228	<0.022	0.051	4.78	0.163
Te125	<0.110	0.61	<0.146	<0.147	<0.135	<0.165	3.33	3.75	105.49
Ba137	<0.33	<0.45	<0.40	<0.43	<0.34	<0.28	17.27	67.57	0.36
W184	<0.019	<0.0251	0.0068	<0.0218	0.016	<0.0144	<0.0169	13.87	0.229
Ir193	<0.0068	<0.0071	<0.0057	<0.0052	<0.0041	<0.0037	<0.0033	<0.0104	<0.0045
Au197	<0.0170	<0.0195	<0.018	<0.0083	<0.0058	<0.0134	0.037	0.245	0.026
Hg202	0.101	0.073	0.081	0.039	0.038	0.038	0.029	0.36	0.103
Tl205	<0.0043	<0.0055	<0.0050	<0.0033	0.004	<0.0029	0.0082	3.43	0.243
Pb208	0.045	0.075	0.381	0.088	0.309	0.313	0.434	71080.46	43.75
Bi209	0.0073	0.067	<0.0045	<0.0048	0.0076	<0.0041	1.23	402.13	19.46

LA-ICPMS data-S mineral data (51) - 15 to 21 grains (2066203)

Rock	Calc-silicate - 2066203						
Sample ID	203D-01	203D-02	203D-03	203D-04	203D-06	203C-01	203C-03
Mineral	Chalcopyrite						
Na23	12.97	769.19	1319.43	12.83	6217.19	2930.24	1428.73
Si29	<0.00	<0.00	<0.00	<0.00	<0.00	<0.00	<0.00
S33	414269.9	416666.6	225783.3	408208.3	225275.3	253152.8	306226.8
S34	410091.3	409586.8	225464.8	415998.5	214966.1	256077.5	301433.5
V51	0.203	0.38	46.8	0.34	74.03	59.57	27.15
Cr52	<2.68	<4.49	18.63	<2.74	24.27	33.22	5.39
Mn55	<1.01	7.51	41149.93	45.18	5565.36	11938.08	4422.76
Fe57	293000.4	293000.3	293000.4	293000.4	293000.4	293000.4	293000.4
Co59	<0.139	1.36	19	<0.129	12.55	15.64	3.44
Ni60	<0.71	<1.00	348.94	<0.67	164.96	207.23	49.91
Cu65	317540.3	321162.5	154544.1	323531.9	142004.3	187100.8	251364.5
Zn66	7.72	<6.45	889.67	13.55	151.62	431.38	88.95
Ga69	<0.098	17.69	2.09	<0.130	21.45	16.64	6
As75	<0.69	<1.32	7.7	<0.72	2.01	5.74	2.41
Se82	71.86	63.64	<21.49	81.82	<12.16	15.87	45.63
Mo95	<0.37	<0.85	<0.90	<0.37	<0.37	0.4	<0.28
Ag107	0.7	0.25	0.47	0.89	0.62	1.24	0.99
Cd111	<0.68	<0.90	<1.03	<0.53	<0.56	<0.42	<0.57
In115	4.96	4.37	5.34	4.99	3.62	2.94	2.57
Sn118	<0.51	0.97	6.4	<0.52	23.67	26.84	8.38
Sb121	<0.105	0.48	9.63	<0.120	3.87	4.68	2.78
Te125	0.92	<1.38	<1.19	1.01	<0.91	<0.77	<0.81
Ba137	<3.48	5401.89	16.29	<3.87	608.27	404.28	157.62
W184	<0.127	<0.21	<0.233	<0.098	<0.137	<0.124	<0.110
Ir193	<0.030	<0.044	<0.074	<0.029	<0.021	<0.042	<0.029
Au197	<0.081	<0.146	<0.195	<0.078	<0.095	<0.097	<0.083
Hg202	0.37	0.4	0.4	0.3	0.24	0.078	<0.072
Tl205	0.051	2.2	1.26	0.027	2.71	0.79	0.616
Pb208	5.41	38.48	71.88	6.69	711.83	16.43	100.51
Bi209	2.36	33.87	63.79	1.69	28.08	39.2	29.76

LA-ICPMS data-S mineral data (51) - 22 to 39 grains (2066635)

Rock	Calc-silicate -2066635								
Sample ID	635B-1	635B-2	635B-3	635B-4	635B-5	635B-6	635B-7	635B-8	635G-1
Mineral	Chalcopyrite								Bornite
Na23	6864.43	22036.65	5140.36	115.63	7198.88	20604.25	369.03	918.77	97.99
Si29	<0.00	<0.00	<0.00	<0.00	<0.00	<0.00	<0.00	<0.00	<0.00
S33	578708.9	14861.78	513303.8	599894.2	223808.7	5363.79	151895.9	1728.96	281962.1
S34	562410.1	8634.42	504131.8	610896.3	219687.8	3716.74	152905.5	763.83	286567.2
V51	5.56	136.14	4.77	13.16	4.58	43.2	2	37.43	2.63
Cr52	3.71	25	2.06	3.83	3.45	7.64	1.28	4.51	3.67
Mn55	778.88	14590.71	180.63	66.55	807.86	14370.99	156.28	2697.85	4940.76
Fe57	426000.7	426000.7	426000.7	426000.7	120000.5	120000.5	120000.5	120000.5	102000.3
Co59	175.57	637.87	91.46	72.73	88.4	89.01	68.11	98.45	7.59
Ni60	10.01	101.71	2.91	1.5	6.33	13.9	1.66	14.19	1.47
Cu65	261807.3	40412.91	93703.83	124299.7	237140.7	6198.53	76872.2	1734.46	487663.1
Zn66	68.71	2226.17	58214.62	319355.8	65.18	328.33	11.35	202.95	59586.44
Ga69	1.59	26.44	0.668	0.108	1.81	9.67	0.271	4.5	1.03
As75	3518.55	59.85	173.55	209.41	632.77	17.51	281.03	19.18	<0.72
Se82	<6.87	<17.85	<5.40	12.17	7.68	<7.56	5.27	<2.43	<10.02
Mo95	0.47	10	0.72	1.33	0.258	2.16	0.096	2.22	<0.34
Ag107	7.32	0.16	15.42	49.21	6.31	0.049	5.42	<0.021	12.81
Cd111	<0.38	3.27	143.57	825.28	<0.182	<0.34	<0.080	<0.114	142.04
In115	0.088	0.884	4.66	32.21	0.0177	0.494	0.018	0.21	1.55
Sn118	4.83	18	3.88	2.31	3.25	9.44	0.79	3.25	0.77
Sb121	16.94	35.51	9.82	21.6	6.09	7.61	3.61	10.35	0.87
Te125	5.17	<1.12	0.93	1.74	1.4	<0.55	1.16	<0.189	<0.71
Ba137	142.29	610.88	109.12	41.2	112.5	381.25	28.4	76.18	8.61
W184	0.422	21.17	1.12	3.57	0.84	4.8	0.302	8.39	<0.097
Ir193	<0.0120	<0.045	<0.0122	<0.0228	<0.0099	<0.0133	<0.0036	0.0036	0.024
Au197	0.133	<0.092	0.139	0.43	0.06	<0.059	0.1	<0.0168	<0.080
Hg202	0.054	<0.126	0.146	0.5	0.029	<0.053	0.013	<0.0172	0.21
Tl205	6.85	0.092	2.01	6.63	3.89	0.022	2.17	0.0074	1.22
Pb208	230.24	57.71	552.36	906.48	83.13	10.47	237.18	10.29	107.95
Bi209	382.81	60.94	205.08	435.39	339.16	1.98	181.04	3.18	706.36

To be continued

Rock	Calc-silicate -2066635								
Sample ID	635G-2	635G-3	635G-6	635G-7	635J-1	635J-2	635F-1	635F-3	635F-2
Mineral	Bornite				Chalcopyrite		Sphalerite	Bornite	Sphalerite
Na23	1442.05	25.74	<6.91	9100.12	198.65	1121.76	142.3	50.37	4.7
Si29	<0.00	<0.00	<0.00	<0.00	<0.00	<0.00	<0.00	<0.00	<0.00
S33	300465.4	279947.8	280969.6	265274.4	69301.95	86193.38	619927.7	260771.3	47093.22
S34	297941.3	283034.5	273935.5	269561.6	69794.84	85488.79	634453	259568.3	48348.24
V51	0.63	0.56	<0.189	1.7	0.095	0.414	44.63	23.28	1.33
Cr52	3.62	<3.19	<3.22	2.8	0.72	1.03	26.12	14.38	0.87
Mn55	17.31	91.86	<1.19	440.12	3.59	5.35	5611.43	244.88	316.1
Fe57	102000.3	102000.3	102000.3	102000.3	22370.23	22370.23	112000.4	112000.4	7864.83
Co59	<0.184	1.96	<0.168	5.41	0.047	0.218	183.1	5.6	6.84
Ni60	<0.76	<0.79	<0.86	<0.68	<0.171	<0.186	26.58	1.08	0.97
Cu65	535738.3	541270.3	531370.8	516164.7	121222.4	117781.9	202274	374679.6	24787.41
Zn66	8.76	31824.98	<4.38	57.77	10850.44	48491.47	1121268	112019.1	81994.94
Ga69	<0.176	<0.19	<0.162	0.96	0.039	0.076	12.33	1.01	0.436
As75	<0.99	<0.98	<0.92	<0.70	<0.196	<0.176	3.66	2.64	0.51
Se82	<13.22	<13.24	<13.13	<10.86	3.56	5.39	<20.19	<8.60	<1.46
Mo95	<0.41	<0.47	<0.45	<0.36	<0.106	<0.078	<0.70	1.01	<0.053
Ag107	8.94	9.4	11.88	16.98	5.82	10.4	53.79	19.99	4.26
Cd111	<0.74	33.88	<0.60	<0.46	34.22	115.18	2207.97	349.88	175.88
In115	0.037	0.166	<0.037	0.087	0.694	1.51	106.57	2.67	12.38
Sn118	4.98	1	<0.58	3.61	0.488	0.84	2.74	0.62	0.758
Sb121	0.128	0.71	<0.125	1.24	0.165	2.07	13.03	3.98	1.39
Te125	<0.70	<0.77	<1.03	<0.64	<0.155	<0.179	<1.25	<0.36	<0.107
Ba137	63.66	<4.88	<3.50	148.85	8.49	34.58	24.97	187.61	2.57
W184	0.37	<0.115	<0.121	<0.082	0.104	0.066	<0.142	2.85	0.0264
Ir193	<0.038	<0.019	<0.044	<0.024	<0.0078	<0.0057	<0.051	<0.0245	<0.0038
Au197	<0.116	<0.096	<0.089	<0.084	<0.0194	0.034	0.31	<0.083	0.025
Hg202	0.22	0.105	0.16	0.103	0.088	0.18	6.46	0.12	0.22
Tl205	1.48	1.4	1.76	0.79	0.143	0.219	5.69	0.85	0.9
Pb208	27.78	24.13	27.82	21.94	4.95	21.79	346.31	45.95	170.25
Bi209	744.15	1480.33	710.12	678.41	156.83	4251.84	522.59	608.14	109.27

LA-ICPMS data-S mineral data (51) - 40 to 51 grains (2066655)

Rock	Metasediment -2066655											
Sample ID	655A-1	655A-2	655A-3	655A-4	655A-1	655A-2	655A-3	655A-4	655A-5	655B-1	655B-2	655B-3
Mineral	Chalcopyrite				Pyrite					Chalcopyrite		
Na23	101.38	4641.32	400.85	1007.58	6.56	3.86	40.01	6.27	3.74	1362.16	3754.54	1087.17
Si29	<0.00	<0.00	<0.00	<0.00	<0.00	<0.00	<0.00	<0.00	<0.00	<0.00	<0.00	<0.00
S33	480148.2	338106.4	478781.8	474007.5	431613	434667.9	450154.5	426577.1	418135.4	79261.43	80437.63	77137.15
S34	464251.3	327220.3	478206.8	455229.9	429051.9	419426.8	425458.9	429019	427685.5	79000.48	80904.99	75199.2
V51	0.17	2.6	0.255	10.68	0.119	0.144	0.093	0.128	0.101	0.595	0.26	0.055
Cr52	<0.58	2.83	1.15	7.15	<0.59	<0.57	<0.62	<0.62	<0.61	0.81	0.57	0.51
Mn55	11.14	272.5	14.45	1249.52	1.62	0.46	6.22	0.71	1.02	23.15	9.09	1.89
Fe57	414400.8	269360	419060.8	419060.8	414400.8	418700.9	418700.9	419060.8	419060.8	47400.43	47400.43	47400.43
Co59	570.44	247.37	677.97	21.68	768.62	381.15	208.09	380.4	397.45	<0.0167	0.021	0.0215
Ni60	64.83	21.85	67.23	10.08	81.58	39.11	57.34	265.82	623.97	<0.091	0.22	0.103
Cu65	38437.21	107500.7	32966.45	335769	9.73	96.98	221.71	11.73	82.83	52945.38	53427.34	49883.64
Zn66	8.34	68.51	9.03	259.48	<1.15	<1.11	4.85	<1.16	<1.13	4.37	7.06	3.03
Ga69	0.041	10.19	0.512	49.3	<0.027	<0.025	<0.034	0.632	<0.035	0.21	0.263	0.072
As75	314.98	155.4	361.77	360.72	529	253.6	501.34	580.6	841.96	<0.095	<0.111	<0.109
Se82	14.63	11.05	15.18	14.02	12.41	19.31	29.4	9.54	12.94	2.26	1.96	3.59
Mo95	0.13	3.57	0.153	4.31	<0.084	<0.075	<0.097	<0.098	0.155	<0.054	<0.057	<0.054
Ag107	8.83	8.31	13.79	8.77	0.541	1.063	2.3	0.826	0.118	0.418	0.677	0.472
Cd111	<0.150	<0.181	<0.132	<0.45	<0.161	<0.176	<0.161	<0.122	<0.130	<0.085	<0.100	<0.074
In115	0.754	0.702	0.579	0.216	<0.0097	<0.0085	0.0293	<0.0103	0.0221	0.811	0.81	0.979
Sn118	<0.137	0.92	0.29	1.05	<0.132	<0.135	<0.153	0.152	<0.150	19.12	2.1	0.375
Sb121	0.734	40	1.85	211.88	<0.026	0.048	0.076	0.042	0.081	0.053	0.115	0.05
Te125	14.93	18.58	43.89	<0.70	2.86	1.77	4.48	3.63	2.51	<0.110	0.206	<0.124
Ba137	3.64	57.06	8.15	31.81	1.89	0.74	6.44	224.6	<0.75	50.31	61.06	17.29
W184	<0.032	<0.046	<0.030	<0.110	<0.028	<0.032	<0.030	<0.032	<0.030	0.04	<0.0177	<0.0150
Ir193	<0.0065	<0.0106	<0.0090	<0.020	<0.0076	<0.0087	<0.0089	<0.0090	<0.0102	<0.0054	<0.0039	<0.0045
Au197	0.369	0.197	0.254	<0.085	0.136	0.05	0.362	3.52	1.49	<0.0161	<0.0160	<0.0116
Hg202	0.052	0.071	0.025	0.109	<0.025	0.035	<0.026	<0.025	<0.024	0.0258	0.0303	0.0438
Tl205	0.36	5.6	0.846	12.6	0.0304	<0.0094	0.0248	<0.0093	0.0196	0.0062	0.0094	<0.0051
Pb208	68.28	110.65	76.25	92.81	13.79	7.01	17.69	13.81	3.31	4.67	8.16	1.676
Bi209	61.41	84.86	83.81	14.07	6	15.62	37.33	22.12	5.39	1.009	4.81	1.511

Appendix 5: The multiple elements of minerals contributed to whole rock assay

➤ *Metasediments*

Two samples represent the altered protoliths of metasediments, hematite altered 2066641 and chlorite altered 2066655 (Table VIII). Ten elements are S-Cu-Ag-Sb-Bi-Ta-Ce-Pb-Th-U as ore related elements. Hematite-biotite-manganite (2066641) contain the weighted average S-Cu-Ag-Sb-U, roughly equal to assay. Hematite contributed major Cu-Sb-U to whole rock and manganite contribute major Ag to. The weight average Bi-Pb are 2-5 times of the assay with some uncertain but believed hematite-biotite-magnetite contributed major Bi and Pb to whole rock. The weight average Ta-Ce-Th contributed 27-38% of assay.

Table VI. Multiple elements of minerals contributed to whole rock assay in metasediments (2066641 and 2066655).

2066641 Hematite altered metasediment (HSCC)													
Minerals	%	S	S contribution	Cu	Ag	Sb	Bi	Ta	Ce	Pb	Th	U	n
Quartz	35												
Kfeldspar	10												
Chlorite	20												
Hematite	25			1454		9.62	15.4	0.66	34.4	1591	12.0	27.7	5
Apatite	1												
Biotite	5	269.44	13.47	1308	0.06	4.12	17.9	1.33	69.9	675	19.6	26.4	1
Manganite	4	138.57	5.54	270.2	3.7	0.5	9.95		9.09	3637	1.32	26.7	2
Weighted Average		19.01		439.6	0.15	2.63	5.14	0.23	12.5	577.1	4.03	9.32	
Assay		25		483	0.21	2.45	2.59	0.6	45.8	144	11.1	12.5	
2066655 Chlorite altered metasediment (CAM)													
Minerals	%	S	S contribution	Cu	Ag	Sb	Bi	Ta	Ce	Pb	Th	U	n
Quartz	25												
Kfeldspar	15												
Chlorite	30	314.82	94.45	633.9	0.26	0.40	0.62	0.04	0.30	7.3	2.22	1.30	14
Hematite	20			35.75		6.87	0.86	0.63	3.24	19.3	5.49	3.51	8
Magnetite	1			242.3		12.9	4.52	0.04	0.73	9.0	0.62	0.51	1
Dolomite	5	296.05	14.8	122.3	0.04	0.35	0.82	0.03	51.2	6.8	3.31	0.2	3
Calcite	2												
Pyrite	0.2	426128	852	85	0.97	0.05	17.3			11.1			5
Chalcopyrite	0.2	280001	560	95847	5.9	4	678			21.9			7
Weighted Average			1522	398	0.09	1.65	1.84	0.14	3.31	6.6	1.93	1.11	
Assay			1600	797	0.29	1.57	1.24	7.2	93.9	5	7	3.2	

n=the number of grains. Element value is at ppm. Whole rock assay is for one meter interval.

Unaltered vs altered granite

Three minerals have been considered the important in the unaltered (2066178) and altered granite (2066178, 2066656 and 2066169) in Table IX. Three minerals are K-feldspar, chlorite, hematite. Ten elements are determined for enrichments/remobilize during alteration of the granite.

K-feldspar-anorthoclase-biotite (magnetite-hematite) contains the weight average S-Pb, roughly equal to whole rock assay (2066178) in Table II. K-feldspar contributed major S to assay in unaltered granite. These contain the weight average Cu-Ag-Bi-Ta-Ce-Th-U, contributed 0.4-53% of assay. Hematite contributed major Sb to whole rock.

K-feldspar-hematite-muscovite contains the weight average Bi-Th-U contributed 59-63% of assay U in muscovite-altered granite (2066656). Hematite contributed the major Bi-Th-U to whole rock. These contributed 1.6-10 times of assay with some uncertain. Believed hematite contributed major Sb-Ta-Pb to whole rock. These contributed 16-33% of assay with the weighted average.

K-feldspar-biotite-dolomite-apatite contains the weighted average S-Th contributed 66-86% of assay (2066174). These contributed 1.3-3.8 times of assay Sb-Bi-Pb-U with the weighted average with some uncertain, but believed hematite-apatite contributed major Sb-Pb-U to whole rock. These contributed 32-46% of assay with the weighted average. Apatite contribute the major Ce to whole rock, biotite contribute major Ta to whole rock.

Chlorite-hematite contains the weighted average Pb-U, contributed 45% of assay in hematite-altered-granite (2066169). Hematite contributed the major Pb-U to whole rock. These contains 2.8-9.3 times of assay with uncertain. Chalcopyrite contributed major Cu-Bi to whole rock, pyrite contributed major S, and hematite contribute major Sb-Bi. These contributed 0.5-9% of assay Ag-Ta-Ce-Th with the weighted average.

K-feldspar contains low contents S-Cu-Ce-Sb-Th-U in unaltered granite (2066178) in Table II. The K-feldspar contains high value S-Cu-Ce-Sb-Th-U in altered granite (2066656 and 2066174). The K-feldspar of altered granite has the 6-30 times Cu of the unaltered granite K-feldspar, 94-197 time Ce, 696-1740 time Th and 80-823 time U. This imply that the Cu, Ce, Th, U elements have been enriched greatly during alteration accompanying the S-Sb-Bi increasing. The Ag is decreasing; and Pb and Ta are up and down.

Chlorite contains S-Cu-Sb-Pb in unaltered granite (2066178) in Table II. The altered chlorite contains S-Cu-Ce-Sb-Pb in altered granite (2066169). The chlorite of altered granite has the 8.2 times Cu of the unaltered granite chlorite. This imply that the Cu element have been enriched during alteration accompanying the S, Ag, Bi and U increasing. The Sb, Ta, Ce, Pb and Th is decreasing.

Hematite contains Cu-Ce-Sb-Th-U in unaltered granite (2066178) in Table II. The hematite contains Cu-Ce-Sb-Th-U in altered granite (20666169). The hematite of altered granite has the 7.7 times Cu of the unaltered granite hematite accompanying the chalcopyrite and pyrite forms. This imply that the Cu elements has been enriched greatly during alteration accompanying the Sb-Pb increasing. The Ce-Th are extremely decreasing with U content down.

Table VII. Multiple elements of minerals contributed to of whole rock assay in granite (2066178 unaltered and 2066656 muscovite-altered, 2066174 dolomite-altered and 2066169 hematite-altered granite).

2066178 Unaltered granite													
Minerals	%	S ppm	S contribution	Cu	Ag	Sb	Bi	Ta	Ce	Pb	Th	U	n
Quartz	35												
K-feldspar	30	233	69.9	1.7	0.04	0.3	0	0.08	0.54	52.6	0.04	0.03	2
Anorthoclase	5	417	20.85	2.08	0	0.13		0	6.09	6.38	0.04	0.04	5
Biotite	25	344	86	3.09	0	0.44	0.04	0	2.71	3.14	21.44	1.61	2
Chlorite	2	456	9.12	2.39	0	0.29	0	0	0	3.16	0	0	1
Magnetite	1			4.12		0.29		0.47	2.24	1.87	0.6	0.21	2
Hematite	1			14.6		10.97		0	27.3	71.7	47	11.8	4
Apatite	1												
Weighted Average			185.9	1.62	0.01	0.32	0.01	0.03	1.44	17.68	5.85	0.53	
Assay			195	43	0.1	0.6	2.83	7.2	105.4	22	20.9	4.99	
2066656 Muscovite-altered granite													
Quartz	10												
K-feldspar	20	401	80.2	11	0.07	1.07	0.07	0.58	106.37	13.78	20.5	2.4	1
Chlorite	10												
hematite	15			95		58.3	1.44	106	18.96	71.05	27.85	6.64	4
Muscovite	40	298	119.2	47	0.06	3.99	0.2	0	10.05	45.15	17.5	3.24	4
Ilmenite	5												
Weighted Average			199	35.25	0.04	10.56	0.31	16.02	28.14	31.47	15.28	2.77	
Assay			600	178	0.25	2.51	0.49	1.6	131.9	19.8	25.9	4.7	
2066174 Dolomite-altered granite													
Quartz	30												
K-feldspar	15	586	87.9	52	0.09	15	2.1	0.09	51	133	69.6	24.7	1
Biotite	10	70	7	50	0.05	8.24	1.8	1.99	28.86	122	38	15.7	1
Chlorite	20												
hematite	5			14.86		11.8		0.39	32.69	66.5	58.0	12.0	1
Dolomite	15	237	35.55	44	0.03	1.89	0.6	0.01	18.3	11.1	9.21	1.24	3
Apatite	5	397	19.85	34.6	0.16	10.2	1.0	0.51	572.7	144	57.7	84.6	1
Weighted Average			150.3	21.9	0.03	4.46	0.64	0.26	43.6	44.3	21.4	10.3	
Assay			174	48	0.08	1.17	0.49	0.8	101	24	32.4	3.62	
2066169 Hematite-altered granite													
Quartz	20												
K-feldspar	5												
Muscovite	5												
Chlorite	35	279	97.65	14	0.09	0.13	0.03	0.02	0.09	9.97	0.01	0.05	5
hematite	30			112		12.5	7.2	0.14	2.99	77.3	0.21	5.24	7
Pyrite	5	454000	22700	0.62	0.09	0.13	0.026			0.31			6
Chalcopyrite	0.1	318000	318	46000	65	0.16	19	105		43			1
Weighted Average			23018	84.53	0.10	3.80	2.19	0.15	0.93	26.74	0.07	1.59	
Assay			9840	397	1.1	1.13	0.77	1.6	136.1	57	15.13	3.49	

Low to high altered calc-silicate

Alteration intensity of calc-silicate rock are considered from low (2066166) via mid (2066199 and 2066635) to high (2066203) in Table X.

Chlorite-magnetite-garnet (pyrite-chalcopyrite) contains the weighted average 0.06 ppm Ag, contributed 60% to the whole rock assay 0.1 ppm Ag (2066166) in Table III. Chalcopyrite contributed major Ag to whole rock (2066166). These contain 2-20 times of assay S-Cu-Sb-Pb with the weighted average with some uncertain. Believed chlorite contributed the major Pb to assay and magnetite contributed the major Sb. Chalcopyrite contributed the major Cu to assay; pyrite and chalcopyrite contribute the major S to. These contain 3-24% of assay Bi-Ta-Ce-Th with the weighted average.

K-feldspar-biotite contributed 51-60% of assay Th-U with the weighted average (2066199). These contain 1.2 times of assay 67 ppm Ce with the weighted average 80 ppm, believed K-feldspar contributed the major Ce to whole rock. These contain 2-4% of assay S-Cu-Ag-Bi; and contributed 19-39% of assay Sb-Ta-Pb.

Chlorite-hematite-dolomite (chalcopyrite-gypsum) contributed 55-93% assay S-Cu-Ce-Pb-U (2066635). Chalcopyrite contribute the major Cu-S to whole rock; chlorite-hematite contributed the major Ce-U-Pb to. These contain 3.2 times of assay 6.3 ppm Sb uncertain, but believed hematite contributed the major Sb to. These contain 17-32% of assay Ag-Bi-Ta-Th.

K-feldspar-pyroxene (biotite-chalcopyrite) contributed 50-70% of assay S-Cu-Ta. Chalcopyrite contributed the major Cu-S to whole rock and K-feldspar contributed the major Ta to. These contain 0.2-7% of assay Ag-Sb-Bi-Ce-Pb-Th and U.

Table VIII. Multiple elements of minerals contributed to of whole rock assay in unaltered calc-silicate (2066166) and carbonate-altered (2066199), hematite-altered (2066635) and chlorite-altered granite (2066203).

2066166 Calc-silicate (CAM)													
Minerals	%	S	S contribution	Cu	Ag	Sb	Bi	Ta	Ce	Pb	Th	U	n
Quartz	30												
Chlorite	30	290.74	87.22	180.28	0.09	0.13	0.02	0.02	0.66	67.46	0.014	0.33	1
Hematite	10												
Magnetite	20			3.46		9.59	0.46	0.04	3.13	10.31	0.29	2.21	3
Pvrite	1	497811	4978.12	4.43	0.01	0.02	0.20			1.19			2
Chalcopyrite	1	267057	2670.58	213608	3.3	1.28	6.54			16.01			3
Garnet	8	296.89	23.75	539.53	0.04	0.98	0.19	0.08	38.92	10.39	1.73	4.33	2
Weighted Average		7759		2234	0.06	2.05	0.18	0.02	3.94	23.30	0.20	0.89	
Assav		1716		113	0.1	1.08	0.75	0.2	82	2.5	5.79	6.82	
2066199 Carbonate altered calc-silicate (CAM)													
Minerals	%	S	S contribution	Cu	Ag	Sb	Bi	Ta	Ce	Pb	Th	U	n
Quartz	10												
Kfeldspar	20	386.38	77.28	12.19	0.07	4.49	0.21	1.59	392.6	8.96	37.5	10.9	6
Chlorite	20												
Hematite	9												
Dolomite	20												
Calcite	10												
Apatite	4												
Biotite	1	360.43	3.60	9.10	0.05	3.67	0.31	1.10	100.7	9.24	21.41	8.92	8
Muscovite	1												
Rutile	5												
Weighted Average		80.88		2.53	0.01	0.94	0.05	0.33	79.54	1.88	7.72	2.27	
Assav		3537		120	0.23	2.44	2.08	0.9	67.1	10	12.85	4.47	
2066635 Hematite altered Calc-silicate (HSCC)													
Minerals	%	S	S contribution	Cu	Ag	Sb	Bi	Ta	Ce	Pb	Th	U	n
Quartz	25												
Kfeldspar	10												
Chlorite	15	340.89	51.13	2231	0.12	32	8.88	0.56	153.7	40.41	23.53	9.85	5
Hematite	20			84.96		76.15	0.12	1.35	80.74	23.75	16.78	9.8	1
Dolomite	20	450.27	90.05	456.76	0.07	0.90	3.00	0.06	64.40	10.77	2.66	0.67	3
Bornite	2	296073	5921	359849	9.5	5.6	505.9			104.7			6
Apatite	3												
Gypsum	5	261.38	13.07	3.53	0.04	0.04	0.03	0.01	3.61	2.55	0.71	0.23	1
Weighted Average		6076		7640.21	0.22	20.32	12.08	0.37	52.27	15.19	7.45	3.58	
Assav		9700		8173	0.68	6.3	72.46	1.7	94.7	26.1	23.6	4.3	
2066203 Chlorite altered calc-silicate (HSCC)													
Minerals	%	S	S contribution	Cu	Ag	Sb	Bi	Ta	Ce	Pb	Th	U	n
Quartz	25												
Kfeldspar	15	412.1	61.81	1281.81	0.09	1.28	0.42	2.22	3.67	5.56	0.58	2.55	2
Biotite	0.1	304.4	0.30	262.31	0.06	2.11	0.03	0.09	0.11	30.37	0.211	0.18	1
Chlorite	20												
Hematite	8												
Calcite	10												
Pvrite	2												
Chalcopyrite	3	321369	9641	242464	0.74	3.08	28.39	0.52		135.89			7
Apatite	1												
Pvroxene	15	423.24	63.49	288.53	0.06	3.49	0.32		7.11	73.56	1.30	3.14	4
Sphalerite	1												
Weighted Average		9766.67		7509.74	0.05	0.81	0.96	0.35	1.62	15.97	0.28	0.85	
Assav		19439		10692	10	11.98	19.7	0.6	1005	1330	17.38	42.1	

Amphibolite

Amphibolite is at low intensity alteration with dolomite-hematite alteration veins in Table XI. Hematite contained a great number of other mineral inclusions 1-10 μm . Great care I could not avoid the inclusions for 11 spots which is consistent with the Electron Probe. Believed hematite contributed Sb-Th-U and possible Cu-S with fine inclusions to whole rock.

Table IX. Multiple elements of minerals contributed to of whole rock assay in amphibolite (2066177).

Amphibole (CAM)													
Minerals	%	S ppm	S contribution	Cu	Ag	Sb	Bi	Ta	Ce	Pb	Th	U	n
Quartz	10												
Kfeldspar	10												
Chlorite	20	260.36	52.07	25.69	0.07	0.17	0.04	0.03	7.24	1.88	0.20	0.12	7
Hematite	9												
Magnetite	1												
Amphibole	30												
Dolomite	20	249.80	49.96	5.27	0.07	0.18	0.05	0.02	221.27	6.85	0.83	0.15	2
Weighted Average			102	6.19	0.03	0.07	0.02	0.01	45.70	1.75	0.20	0.05	
Assay			797	36	0.37	1.87	3.41	1.6	87	22	7.45	5.33	

Eleven hematite grains analysis failed here due to 47 wt % Fe only with 1-10 μm inclusions of quartz-biotite-chlorite.

Appendix 6: The element substitution of sulphur minerals, hematite, chlorite, muscovite and K-feldspar

Mineral	Ions	Possible ionic substitutions						
Pyrite		negative charge	Same positive charge	More positive charge	Less positive charge	Common substitution	≥5 times of crust abundance in study areas	
	Fe ²⁺		Mg ²⁺ , Ca ²⁺ , Sr ²⁺ , Co ²⁺ , Ni ²⁺ , Cu ²⁺ , Zn ²⁺ , Mn ²⁺ , V ²⁺ , Ti ²⁺ , Ag ²⁺ , Hg ²⁺ , Pb ²⁺ and Ba ²⁺ .	Al ³⁺ , Au ⁵⁺ , As ³⁺ , Ga ³⁺ , Tl ³⁺ and Mo ³⁺ ,		Li ⁺ , Ag ⁺ , K ⁺ and Rb ⁺	Ni, Co, As, Cu, Zn, Ag, Au, Tl, Se and V	Co, Ni, Cu, Ag, Au, As, Bi, Se and Te
	S	OH, O ²⁻ , Se ²⁻ , Te ²⁻						
Chalcopyrite	Cu ⁺		Li ⁺ , Na ⁺ , Ag ⁺ and K ⁺	Au ³⁺ , Sb ³⁺ , In ³⁺ , Ga ³⁺ , Ni ²⁺ , Mg ²⁺ , Co ²⁺ , Zn ²⁺ , Fe ²⁺ , Mn ²⁺ , Hg ²⁺ and Pb ²⁺			Ag, Au, In, Tl, Se and Te	Ba, Mo, Co, Ni, Ag, Au, Zn, Hg, In, Tl, Sn, Pb, As, Sb, Bi, Se and Te.
	Fe ³⁺		Ga ³⁺ , Al ³⁺ , Sb ³⁺ , Ag ³⁺ , Au ³⁺ and In ³⁺	Mo ⁶⁺ , W ⁶⁺ , Te ⁶⁺ , V ⁵⁺ , Ge ⁴⁺ , Mn ⁴⁺ , Co ⁴⁺ , Ti ⁴⁺ , Sn ⁴⁺ , Pb ⁴⁺ and Te ⁴⁺	Mg ²⁺ , Ca ²⁺ , Sr ²⁺ , Co ²⁺ , Ni ²⁺ , Cu ²⁺ , Zn ²⁺ , Mn ²⁺ , V ²⁺ , Ti ²⁺ , Ag ²⁺ , Hg ²⁺ , Pb ²⁺ and Ba ²⁺ .			
	S ²⁻	OH, O ²⁻ , Se ²⁻ , Te ²⁻						
Hematite	Fe ³⁺		Ga ³⁺ , Al ³⁺ , Sb ³⁺ , Ag ³⁺ , Au ³⁺ and In ³⁺	Mo ⁶⁺ , W ⁶⁺ , Te ⁶⁺ , V ⁵⁺ , Ge ⁴⁺ , Mn ⁴⁺ , Co ⁴⁺ , Ti ⁴⁺ , Sn ⁴⁺ , Pb ⁴⁺ and Te ⁴⁺	Ni ²⁺ , Cu ²⁺ , Mg ²⁺ , Co ²⁺ , Zn ²⁺ , Mn ²⁺ , Hg ²⁺ , Pb ²⁺ , Li ⁺ , Cu ⁺ , Na ⁺ and K ⁺ .	Ti, Al, Mn, H ₂ O	Ba, U, Nb, Ta, Mo, W, Co, Cu, Zn, Ga, Sn, Pb, Sb and Bi	
	O ²⁻	S ²⁻ , Se ²⁻ , Te ²⁻						
Chlorite	Fe ²⁺		Mg ²⁺ , Co ²⁺ , Zn ²⁺ , Mn ²⁺ , Ca ²⁺ , Hg ²⁺ , Sr ²⁺ , Pb ²⁺ and Ba ²⁺ .	Ta ⁵⁺ , Pb ⁴⁺ , V ⁴⁺ , Ti ⁴⁺ , Sn ⁴⁺ , Sc ³⁺ , In ³⁺ , Ce ³⁺ , La ³⁺ , Bi ³⁺ and Cr ³⁺		Li ⁺ , Ag ⁺ , K ⁺ and Rb ⁺	Mn, Ca, Na, K and Cr	Th, U, Mo, W, Co, Ni, Cu, Ag, Zn, Ga, Ge, Sn, As, Sb, Bi and LREE
	Mg ²⁺		Fe ²⁺ , Co ²⁺ , Zn ²⁺ , Mn ²⁺ , Ca ²⁺ , Hg ²⁺ , Sr ²⁺ , Pb ²⁺ and Ba ²⁺ .	V ⁴⁺ , Ta ⁵⁺ , Ti ⁴⁺ , Fe ³⁺ , Sn ⁴⁺ , Sc ³⁺ , In ³⁺ , Pb ⁴⁺ , Ce ³⁺ , La ³⁺ , Bi ³⁺ and Cr ³⁺		Li ⁺ , Ag ⁺ , K ⁺ and Rb ⁺		
	Al ³⁺		Ga ³⁺ , Fe ³⁺ , In ³⁺ , Sb ³⁺ , Ag ³⁺ and Au ³⁺ .	Mn ⁷⁺ , S ⁶⁺ , Mn ⁶⁺ , Mo ⁶⁺ , W ⁶⁺ , Te ⁶⁺ , Se ⁶⁺ , Mo ⁵⁺ , Mn ⁵⁺ , As ⁵⁺ , V ⁵⁺ , Ge ⁴⁺ , Mn ⁴⁺ , Co ⁴⁺ , Ti ⁴⁺ , Sn ⁴⁺ , Pb ⁴⁺ , Te ⁴⁺ and Si ⁴⁺	Ni ²⁺ , Cu ²⁺ , Mg ²⁺ , Co ²⁺ , Zn ²⁺ , Fe ²⁺ , Mn ²⁺ , Hg ²⁺ , Pb ²⁺ , Na ⁺ , Li ⁺ , K ⁺ and Cu ⁺			
	Si ⁴⁺		Ge ⁴⁺ , Mn ⁴⁺ , Co ⁴⁺ , Ti ⁴⁺ , Sn ⁴⁺ , Pb ⁴⁺ and Te ⁴⁺	Mn ⁷⁺ , S ⁶⁺ , Fe ⁶⁺ , Se ⁶⁺ , Mo ⁶⁺ , W ⁶⁺ , Te ⁶⁺ , As ⁵⁺ and V ⁵⁺	Ni ²⁺ , Cu ²⁺ , Mg ²⁺ , Co ²⁺ , Zn ²⁺ , Fe ²⁺ , Hg ²⁺ , Pb ²⁺ , Ag ²⁺ , Li ⁺ , Cu ⁺ , Na ⁺ , K ⁺ , Ag ⁺ and Ag ⁺			
	O ²⁻	OH, S ²⁻ , Se ²⁻ , Te ²⁻						
Muscovite	K ⁺		Li ⁺ , Na ⁺ , Rb ⁺ , Cs ⁺ , Ag ⁺ , Au ⁺ , Cu ⁺ and Hg ⁺	Ba ²⁺ , Pb ²⁺ , Sr ²⁺ , Ca ²⁺ , Mn ²⁺ , Fe ²⁺ , Zn ²⁺ , Co ²⁺ , Mg ²⁺ , Ge ²⁺ , Ni ²⁺ , Cr ³⁺ , La ³⁺ , Ce ³⁺ , Bi ³⁺ , In ³⁺ , Sc ³⁺ , V ³⁺ , Al ³⁺ , Sb ³⁺ and Ga ³⁺		Cr, Li, Fe, V, Mn, Na, Cs, Rb, Ca, Mg and H ₂ O.	Cr, Li, Fe, V, Mn, Na, Cs, Rb, Ca, Mg and H ₂ O.	Rb, Ba, Th, U, Zr, Mo, W, Co, Ni, Cu, Zn, Ga, Ge, Sn, Pb, As, Sb, Bi, Se and LREE
	Al ³⁺		Cr ³⁺ , Ga ³⁺ , In ³⁺ , Tl ³⁺ ,	Mn ⁷⁺ , S ⁶⁺ , Fe ⁶⁺ , Mn ⁶⁺ , Mo ⁶⁺ , W ⁶⁺ ,	Ni ²⁺ , Cu ²⁺ , Mg ²⁺ , Co ²⁺ ,			

			U ³⁺ , Nb ³⁺ , Ta ³⁺ , V ³⁺ , Mo ³⁺ , Cr ³⁺ , Mn ³⁺ , Fe ³⁺ , Co ³⁺ , Ni ³⁺ , Sb ³⁺ , Cu ³⁺ , Ag ³⁺ and Au ³⁺	Te ⁶⁺ , Se ⁶⁺ , Mo ⁵⁺ , As ⁵⁺ , V ⁵⁺ , Ge ⁴⁺ , Ti ⁴⁺ , Sn ⁴⁺ , Pb ⁴⁺ , Te ⁴⁺ and Si ⁴⁺	Zn ²⁺ , Fe ²⁺ , Mn ²⁺ , Hg ²⁺ , Pb ²⁺ , Na ⁺ , Li ⁺ and K ⁺		
	Si ⁴⁺		Ti ⁴⁺ , Ge ⁴⁺ , Mn ⁴⁺ , Co ⁴⁺ , Sn ⁴⁺ , Pb ⁴⁺ and Te ⁴⁺	Mn ⁷⁺ , S ⁶⁺ , Fe ⁶⁺ , Se ⁶⁺ , Mo ⁶⁺ , W ⁶⁺ , Te ⁶⁺ , As ⁵⁺ and V ⁵⁺	Ni ²⁺ , Cu ²⁺ , Mg ²⁺ , Zn ²⁺ , Fe ²⁺ , Mn ²⁺ , Hg ²⁺ , Li ⁺ , Cu ⁺ , Na ⁺ , K ⁺ and Ag ⁺		
	O ²⁻	F ⁻ , S ²⁻ , Se ²⁻ , Te ²⁻					
K-feldspar	K ⁺		Na ⁺ , Cs ⁺ , Rb ⁺ , Cu ⁺ , Hg ⁺ , Ag ⁺ and Au ⁺	Fe ²⁺ , Ca ²⁺ , Cr ²⁺ , Mn ²⁺ , Co ²⁺ , Ni ²⁺ , Zn ²⁺ and Cd ²⁺		Na, Fe, Ba, Rb, Ca, Li, Cs, Rb, Pb and H ₂ O.	Rb, Ba, Th, U, Ta, W, Co, Cu, Zn, Ga, Ge, Sn, Pb, Sb, As and Bi
	Al ³⁺		Cr ³⁺ , Ga ³⁺ , In ³⁺ , Tl ³⁺ , U ³⁺ , Nb ³⁺ , Ta ³⁺ , V ³⁺ , Mo ³⁺ , Mn ³⁺ , Fe ³⁺ , Co ³⁺ , Ni ³⁺ , As ³⁺ , Sb ³⁺ , Ce ³⁺ , Bi ³⁺ , Cu ³⁺ , Ag ³⁺ and Au ³⁺	As ⁵⁺ , Sb ⁵⁺ and Bi ⁵⁺	Ni ²⁺ , Cu ²⁺ , Mg ²⁺ , Co ²⁺ , Zn ²⁺ , Fe ²⁺ , Mn ²⁺ , Hg ²⁺ , Pb ²⁺ , Na ⁺ , Li ⁺ and K ⁺		
	Si ⁴⁺		Ti ⁴⁺ , Ge ⁴⁺ , Mn ⁴⁺ , Co ⁴⁺ , Sn ⁴⁺ , Pb ⁴⁺ and Te ⁴⁺	Mn ⁷⁺ , S ⁶⁺ , Fe ⁶⁺ , Se ⁶⁺ , Mo ⁶⁺ , W ⁶⁺ , Te ⁶⁺ , As ⁵⁺ and V ⁵⁺	Ni ²⁺ , Cu ²⁺ , Mg ²⁺ , Zn ²⁺ , Fe ²⁺ , Mn ²⁺ , Hg ²⁺ , Pb ²⁺ , Li ⁺ , Cu ⁺ , Na ⁺ , K ⁺ and Ag ⁺		
	O ²⁻	OH ⁻ , S ²⁻ , Se ²⁻ , Te ²⁻					

Notes: Element occurred in low and high positive charge and did not show in high positive charge. For example, Co³⁺ and Ni³⁺ did not show in Fe²⁺ in pyrite because Co²⁺ and Ni²⁺ showed in the same charge. In hematite, Ag occurred in Ag³⁺ so that we did not show in Ag⁺ and Ag²⁺. Fe, Ce, Mn, Ag and Mo has multiple positive charge so that more chance to substitute other elements. References are the webs; radii (Shannon, 1976) and mindat.org and Shao et al., 1979.

Element substitution in minerals lattices involved in Sb⁵⁺ oxidation state has a similar ionic radius to W⁵⁺ and Ti⁴⁺ (Graham and Morris, 1973; Hans 1985) in chapter 3.4.2. Firstly, mineral web mindata.org showed the elements could be substituted each other in the minerals. Then the ionic radius database showed the potential for substitution for the elements of minerals. The minerals were chosen to pyrite, chalcopyrite, hematite, chlorite and muscovite and K-feldspar because important. The charge balance is important as the Li, Na, K, Rb, Cs in the first column as +1. Ga, In and Tl is the same column for Al as +3, and the Ge, Sn and Pb are the same column with Si for 4+. The REE is most with +3 charge. The radius of ionic are mostly increase from the top of period to bottom and also increase from the sequence of atom (see Table Appendix 6).

Sulphur minerals had chosen pyrite and chalcopyrite as important for the study. Pyrite had the chemistry formula FeS₂ and elements listed as Fe, S with common Impurities: Ni, Co, As, Cu, Zn, Ag, Au, Tl, Se and V. Chalcopyrite had Ag, Au, Cd, Co, Ni, Pb, Sn, and Zn which can be measured (at part per million levels), likely substituting for Cu and Fe. Se, Bi, Te, and As may substitute for sulfur without charge balance with uncertainty. Chalcopyrite elements listed as Cu, Fe, S; and common impurities: Ag, Au, In, Tl, Se and Te.

Hematite had elements listed as Fe, O and had common impurities: Ti, Al, Mn, H₂O. Hematite was important for Ba, U, Nb, Ta, Mo, W, Co, Cu, Zn, Ga, Sn, Pb, Sb and Bi substitute

of Fe^{3+} in eastern Gawler Craton with lots of uncertainty such as Abraitis (2004). Basically, chlorite (mindata.org) had two groups of chlorite as chamosite and clinochlore. The chamosite composition are Fe^{2+} , Mg^{2+} , Al^{3+} , Fe^{3+} and Si^{4+} , Al^{4+} , O_2^- , OH^- . Chamosite has elements listed as Al, Fe, H, Mg, O and Si, and common impurity Mn, Ca, Na, K. The clinochlore composition are Mg^{2+} , Al^{3+} , Si^{4+} , O^{2-} and OH^- . Clinochlore has elements listed as Al, H, Mg, O, Si and common impurity Cr and Ca. The K-feldspar has three groups of microcline, orthoclase and sanidine. Microcline has elements listed as Al, K, O and Si, and common impurity Fe, Ca, Na, Li, Cs, Rb, H_2O and Pb. Orthoclase has elements listed as Al, K, O and Si and common impurity Na, Fe, Ba, Rb and Ca. Sanidine has elements listed as Al, K, O, Si - search for minerals with similar chemistry and common impurity Fe, Ca, Na and H_2O . Muscovite had the same chemistry format with K-feldspar but muscovite had $\text{KAl}_3\text{Si}_3\text{O}_{10}(\text{OH})_{1.8}\text{F}_{0.2}$ and monoclinic system two dimensional platy forms with aggregates being flaky and K-feldspar had the triclinic system crystal often plate-like, prism-like crystal form. Muscovite had more Fe, Mg, Ba and Si substitution with different trace element patterns. Muscovite had elements listed as Al, H, K, O, Si and Common impurity Cr, Li, Fe, V, Mn, Na, Cs, Rb, Ca, Mg and H_2O . The charge were complicated by combination of elements to replace one elements. The radius are complicated to match by two element substitute one elements. The muscovite had the wide substitution as $\text{Ba} \leq 10\%$, $\text{Na} \leq 2.9\%$, $\text{Rb} \leq 1.4\%$, $\text{Fe}^{3+} \leq 6.6\%$, $\text{Cr} \leq 4.8\%$, $\text{V} \leq 3.5\%$, $\text{Fe}^{2+} \leq 3.2\%$, $\text{Mg} \leq 2.8\%$, $\text{Li} \leq 1.8\%$, $\text{Ca} \leq 1.1\%$ and $\text{F} \leq 2.1\%$ (Shao et al., 1979).

Appendix 7: Fluid components and symbols used in HCh models

Table X. fluid compositions used in HCh models

Components	A	B	B1	C
wt %	35	16.2	16,2	30
Unit	g/l			
KCl	60	38	38	31
CaCl ₂	80	55	55	4.6
FeCl ₂	100	40	45	139.6
MgCl ₂				80
MnCl ₂	10	23	23	5.4
NaCl	70			
CuCl	15	1	1	32.1
FeSO ₄	15	5		

Table XI. The important symbols and their meanings used in the construction of an HCh control file algorithm, from Cleverley et al. (2005).

Symbol Variable
T Current temperature (°C)
P Current pressure (bars)
i Current step number
N Current wave number
[1] Input composition (1 ¼ first, 2 ¼ second, etc.)
[A] Bulk composition of aqueous phase in system from current wave, previous step
[S] Bulk composition of solid phase in system from current wave, previous step
[*] Current total system bulk composition (all phases)
{A} Bulk composition of aqueous phase in system from previous wave, current step
{S} Bulk composition of solid phase in the system from the previous wave, current step
{A(i)1} Bulk composition of aqueous phase in the system from the previous wave, step number i) 1